ENGINEERING DESIGN FILE

FORM L-0431.2#
(05-96 - Rev. #02)

Project File Number
EDF Serial Number ER-WAG 7-82
Functional File Number INEL-95/282
EDF Page 1 of

Project/Task WAG 7 Groundwater

Subtask

Title: Evaluation of the Mobility of Am, Cs, Co, Pu, Sr, and U through INEL Basalt and Interbed Materials: Summary Report of the INEL/Clemson University Laboratory Studies.

SUMMARY: The summary briefly defines the problem or activity to be addressed in the EDF, gives a summary of the activities performed in addressing the problem and states the conclusions, recommendations, or results arrived at from this task.

Equilibrium distribution coefficients were determined for americium (Am), cesium (Cs), cobalt (Co), strontium (Sr), uranium (U), plutonium (Pu) V, and Pu (VI) with interbed and crushed basalt materials collected from the Idaho National Engineering Laboratory (INEL). Both batch and column tests were conducted using solution chemistries similar to those observed in the Snake River Plain aquifer beneath the INEL. The values obtained by the two techniques were in reasonable agreement and did not vary greatly from values reported in the literature for similar, though not identical, conditions. However, a fraction of the Am, Co, and Pu applied to crushed basalt and interbed material packed columns was transported at a faster rate than the bulk of these three radionuclides. Sorption rate constants were determined using batch tests and were generally observed to be greater for interbed than for crushed basalt materials. Tests were also conducted to evaluate the use of laboratory determined sorption parameters for more complex conditions such as those in the field. Results indicated that, although variations in solids concentration can affect measured distribution coefficients, lab-obtained distribution coefficients measured at lower solid/liquid ratios compared favorably with those measured at solid/liquid ratios similar to those found in the field. Also, results indicated that distribution coefficients measured under saturated conditions may be used to estimate retardation under unsaturated conditions.

Distribution (complete package): B. N. Burton, S. L. Barrie, K. J. Dooley

Distribution (summary package only):

Author Dept.	Reviewed Date	Approved Date
Kit Dooley for MN. Meredith Newman	N/A	N/A
	LITCO Review Date	LITCO Approval Date
	T. P. Shea by mp 9/18/95 J. P. Shea 10-31-95	K. J. Dooley 9-18-95 K. J. Dooley

See Management Control Procedure (MCP) 6 for instructions on use of this form.

ER-WAG7-82
INEL-95/282

Evaluation of the Mobility of Am, Cs, Co, Pu, Sr, and U through INEL Basalt and Interbed Materials: Summary Report of the INEL/Clemson University Laboratory Studies

Meredith E. Newman, Indrek Porro, Rick Scott, and Frank M. Dunnivant

Idaho National Engineering Laboratory
Integrated Earth Sciences, LITCO
P.O. Box 815, MS 2107
Idaho Falls, ID 83415

Russell W.Goff, Matthew D. Blevins, Steve M. Ince, John D. Leyba, Timothy A. DeVol, Alan W. Elzerman, and Robert A. Fjeld

Environmental Systems Engineering
Rich Labs
Clemson University
Clemson, SC 29656

Abstract

Equilibrium distribution coefficients were determined for americium (Am), cesium (Cs), cobalt (Co), strontium (Sr), uranium(U), plutonium (Pu) V, and Pu (VI) with interbed and crushed basalt materials collected from the Idaho National Engineering Laboratory (INEL). Both batch and column tests were conducted using solution chemistries similar to those observed in the Snake River Plain aquifer beneath the INEL. The values obtained by the two techniques were in reasonable agreement and did not vary greatly from values reported in the literature for similar, though not identical, conditions. However, a fraction of the Am, Co, and Pu applied to crushed basalt and interbed material packed columns was transported at a faster rate than the bulk of these three radionuclides. Sorption rate constants were determined using batch tests and were generally observed to be greater for interbed than for crushed basalt materials. Tests were also conducted to evaluate the use of laboratory determined sorption parameters for more complex conditions such as those in the field. Results indicated that, although variations in solids concentration can affect measured distribution coefficients, lab-obtained distribution coefficients measured at lower solid/liquid ratios compared favorably with those measured at solid/liquid ratios similar to those found in the field. Also, results indicated that distribution coefficients measured under saturated conditions may be used to estimate retardation under unsaturated conditions.

Executive Summary

- Equilibrium distribution coefficients (K_d's) were determined for americium (Am), cesium (Cs), cobalt (Co), strontium (Sr), uranium (U), plutonium (Pu) V, and Pu (VI) with interbed and crushed basalt materials collected from the Idaho National Engineering Laboratory (INEL). Both batch and column tests were conducted using solution chemistries similar to those observed in the Snake River Plain aquifer beneath the INEL. The values obtained by the two methods were in reasonable agreement and did not vary greatly from values reported in the literature for similar though not identical conditions.

- A fraction of the Am , Co, and Pu applied to both crushed basalt and interbed material packed columns was transported at a much faster rate than the bulk of these three radionuclides. This enhanced mobility may alter predicted arrival time and peak concentrations of these three radionuclides downgradient from their source. Evaluation of the frequency, magnitude and mechanisms controlling enhanced transport was not an objective of the laboratory studies reported here, and remains unresolved.

- Equilibration of Pu with synthetic groundwater indicated that within 24 hours the majority of plutonium remaining in solution was Pu (V). Also within this time frame, the plutonium activity in the solution phase decreased to 60 to 70 % of the initial value, due primarily to a decline in Pu (IV) attributed to settling of polymerized or precipitated Pu (IV). Because the majority of Pu (IV) was removed from solution by polymerization or precipitation, Pu(IV) is not expected to be mobile (other than possibly through colloidal transport).

- Sorption rate constants were determined for Cs, Co, Sr, and U using batch tests. Comparison of the estimated time required to reach equilibrium with basalt (61 to 329 hr.) to the average flow velocity estimated by Porro and Bishop (1995) from the Large-Scale Aquifer Pumping and Infiltration Tests (LPIT) (5 m/day), indicates that these elements might not be in equilibrium with basalt surfaces under LPIT conditions. The shorter time required to reach equilibrium estimated for interbed materials (4 to 219 hr.) coupled with the slower average flow velocities observed for sedimentary interbeds indicate that the assumption of equilibrium may be valid for sedimentary interbeds.

- Tests were conducted to evaluate the use of batch tests (which typically use solid/liquid ratios much lower than those occurring in the field) in predicting distribution coefficients at solid/liquid ratios occurring in the field. Results from this study indicate that, although variation in solids concentration can affect measured K_d's, batch tests results at lower solid/liquid ratios compared favorably with K_d's measured at solid/liquid ratios equivalent to those in the field. Results from an additional test indicated that K_d's measured under saturated conditions may be used to estimate retardation under unsaturated conditions. The results from both of these tests indicate that laboratory determined K_d values may be applicable under field subsurface conditions.

Acknowledgments

We would like to acknowledge DOE-ID for funding this work. We would also like to acknowledge Gary Mecham, Scott Barrie, and Kirk Dooley for project management.

Table of Contents

Abstract ii

Executive Summary iii

Acknowledgments iv

List of Tables viii

List of Figures ix

1.0 Introduction 1

1.1 General Overview 1

1.2 Review of Relevant Previous Sorption Studies 1

1.3 Review of Environmental Geochemistry of Am, Cs, Co, Pu, Sr, and U 3

1.3.1 Americium 3

1.3.2 Cesium 3

1.3.3 Cobalt 4

1.3.4 Plutonium 4

1.3.5 Strontium 5

1.3.6 Uranium 5

1.4 Review of Previously Established Methods and Theory 5

1.4.1 Column Tests 6

1.4.2 Batch Tests 10

1.5 Objectives 11

2.0 Materials and Methods 12

2.1 Solid and Groundwater Composition 12

2.2 Saturated Column Tests 14

2.2.1 Crushed Basalt and Interbed Columns 14

2 2.2 Intact Basalt Cores 17

2.3 Unsaturated Column Tests 17

2.4 Batch Tests 20

2.7 Plutonium Oxidation States 21

2.8 Liquid Scintillation Analysis 21

2.9 Bromide, pH, Specific Conductivity and Atomic Adsorption Analysis 22
3.0 Results and Discussion 22
3.1 Clemson University Studies 22
3.1.1 Initial Column Tests 22
3.1.1.1 Crushed Basalt Packed Columns 22
3.1.1.2 Interbed Material Packed Columns 30
3.1.2 The Enhanced Mobility Fraction 36
3.1.3 Initial Batch Tests 39
3.1.4 Plutonium Oxidation State 49
3.1.5 Effects of pH and Ionic Strength 52
3.1.5.1 Crushed Basalt 52
3.1.5.2 Interbed Material 55
3.2 INEL Studies 58
3.2.1 Comparison of Distribution Coefficients Determined at Clemson University and at the INEL 58
3.2.2 Effects of the Solid/Liquid Ratio on Determination of Distribution Coefficients by Batch Methods 59
3.2.3 Comparison of Distribution Coefficients Determined by Batch, Crushed Basalt Packed Columns, and Intact Basalt Cores 62
3.3.3 Effects of Moisture Content on Distribution Coefficients Determined by Column Methods 68
4.0 Conclusions 77
5.0 References 80
Appendix A - Preparation of Synthetic Groundwater A-1
Appendix B - Characteristics of Packed Columns Used at Clemson University B-1
Appendix C - Radionuclide Sources Used in the Preparation of Spike Solutions for Column and Batch Tests C-1
Appendix D - Plutonium Oxidation State Analyses D-1
Appendix E - ^{3}H Breakthrough in Crushed Basalt and Interbed Material Packed Columns E-1
Appendix F - Breakthrough Curves for Am, Cs, Co, Pu, Sr, and U in Crushed Basalt and Interbed Material Packed Columns F-1

Appendix G - Distribution of Gamma-Emitting Radionuclides in Crushed Basalt and Interbed Material Packed Columns G-1

Appendix H - Results from Batch Tests Conducted at Clemson University Using Crushed Basalt and Interbed Materials from the INEL H-1

Appendix I - Results from Batch Tests Designed to Evaluate the Effects of Variations in pH and Ionic Strength on Measured Distribution Coefficients I-1

Appendix J - Breakthrough of Bromide and Strontium in Crushed Basalt Packed Columns and Intact Basalt Cores J-1

Appendix K - Breakthrough of Bromide and Strontium from Crushed Basalt Packed Columns of Varying Moisture Content K-1

List of Tables

Table 1. Distribution Coefficients Measured as Part of the WRIT Program 2

Table 2. Comparison of the Snake River Plain Aquifer and the Synthetic Groundwater Compositions 12

Table 3. Physical and Chemical Characteristics of the Crushed Basalt Composite Interbed Material Collected Near the Radioactive Waste Management Complex 13

Table 4. Mineralogy of the Clay Size Fraction of Composite Interbed Material Collected Near the Radioactive Waste Management Complex 13

Table 5. Mineralogy of the Sand Size Fraction of Crushed Basalt and Composite Interbed Material Collected Near the Waste Management Complex 14

Table 6. Results of Fitted Parameters and Percent Recovery for Crushed Basalt Column Tests at Clemson University 29

Table 7. Results of Fitted Parameters and Percent Recovery for Interbed Material Packed Column Tests at Clemson University 37

Table 8. Summary of Experimental Conditions and Model Results for Batch Studies at Clemson University Where the K_d is Determined from the Mass Balance, the Single Rate and the Dual Rate Models 48

Table 9. Summary of Average Plutonium Distribution Coefficient Values 51

Table 10. Comparison of Distribution Coefficients Measured Using Column Tests at the INEL and Clemson University 58

Table 11. Comparison of Distribution Coefficients Measured Using Batch Tests at the INEL and Clemson University 59

Table 12. Results of Batch Tests Varying Crushed Basalt/Synthetic Groundwater Ratios 60

Table 13. Comparison of Distribution Coefficients Measured Using Batch and Column Methods at Clemson University 62

Table 14. Summary of Crushed Basalt Packed Column and Intact Basalt Core Results Completed at the INEL 67

Table 15. Summary of Unsaturated Crushed Basalt Column Results Completed at the INEL 70

Table 16. Summary of K_d Values Obtained Using Both Batch and Column Tests 77

List of Figures

Figure 1. Predictions of breakthrough curves for various contaminant retardation factors based on equation (2) 8

Figure 2. Saturated column experimental setup 16

Figure 3. Unsaturated column experimental setup 19

Figure 4. Breakthrough Curve for ^{3}H (96.9% recovery) in crushed basalt packed column B08 for a reduced pulse time of 1.1 23

Figure 5. Breakthrough of two distinct fractions of ^{60}Co (2.9 and 63% recovery) in crushed basalt packed column B02 24

Figure 6. Breakthrough of ^{239}Pu (33.5% recovery) in crushed basalt packed column B08 25

Figure 7. Breakthrough of ^{137}Cs (94.3% recovery) in crushed basalt packed column B10 26

Figure 8. Breakthrough of ^{233}U (89.9 % recovery) in crushed basalt packed column B02 27

Figure 9. Distribution of ^{137}Cs and ^{241}Am activity in crushed basalt packed column B07 as determined by a gamma-scan 31

Figure 10. Breakthrough curve for ^{3}H (101.5% recovery) in interbed material packed column IB07 for a reduced pulse time of 1.14 32

Figure 11. Breakthrough curve of ^{239}Pu (0.1% recovery) in interbed material packed column IB06 33

Figure 12. Breakthrough curve of ^{137}Cs (2.7% recovery) in interbed material packed column IB05 34

Figure 13. Breakthrough curve of ^{233}U (90.3 % recovery) in interbed material packed column IB01 35

Figure 14. Distribution of ^{137}Cs and ^{241}Am activity in interbed material packed column IB05 as determined by a gamma-scan 38

Figure 15. Enhanced breakthrough of ^{239}Pu at varying eluent total alkalinity (0.05 to 1.1 g/L as $CaCO_3$) 40

Figure 16. Enhanced breakthrough of ^{241}Am at varying flowrates (0.1 to 10 mL/min.) 41

Figure 17. Aqueous phase concentration of ^{60}Co as a function of time in a crushed basalt batch test 42

Figure 18. Aqueous phase concentration of ^{137}Cs as a function of time in a crushed basalt batch test 43

Figure 19. Aqueous phase concentration of ^{233}U as a function of time in a crushed basalt batch test 44

Figure 20. Aqueous phase concentration of ^{60}Co as a function of time in an interbed material batch test 45

Figure 21. Aqueous phase concentration of ^{137}Cs as a function of time in an interbed material batch test 46

Figure 22. Aqueous phase concentration of ^{233}U as a function of time in an interbed material batch test 47

Figure 23. Oxidation state of plutonium during a 14 day equilibration in synthetic groundwater (pH 8) 50

Figure 24. Cesium K_d's versus pH and ionic strength (controlled with Ca^{2+}) for crushed basalt 53

Figure 25. Cesium K_d's versus pH and ionic strength (controlled with K^+) for crushed basalt 54

Figure 26. Uranium K_d's versus pH and ionic strength (controlled with Ca^{2+}) for crushed basalt 56

Figure 27. Uranium K_d's versus pH and ionic strength (controlled with K^+) for crushed basalt 57

Figure 28. Strontium distribution coefficient versus solid/liquid ratio of crushed basalt 61

Figure 29. Bromide breakthrough (98.96% recovery) in crushed basalt column CB5 63

Figure 30. Strontium breakthrough (100.44% recovery) in crushed basalt column CB5 64

Figure 31. Bromide breakthrough (100.16% recovery) in intact basalt core I1 65

Figure 32. Strontium breakthrough (94.98% recovery) in intact basalt core I1 66

Figure 33. Bromide breakthrough in a crushed basalt column with a volumetric moisture content of 0.180 cm^3/cm^3 (33% saturation) 71

Figure 34. Bromide breakthrough in a crushed basalt column with a volumetric moisture content of 0.157 cm^3/cm^3 (29% saturation) 72

Figure 35. Strontium breakthrough in a crushed basalt column with a volumetric moisture content of 0.22 cm^3/cm^3 (40% saturation) 73

Figure 36. Strontium breakthrough in a crushed basalt column with a volumetric moisture content of 0.25 cm^3/cm^3 (45% saturation) 74

Figure 37. Estimated distribution coefficient of bromide as a function of volumetric moisture content 75

Figure 38. Estimated distribution coefficient of strontium as a function of volumetric moisture content 76

1.0 Introduction

1.1 General Overview

The laboratory studies performed at the Idaho National Engineering Laboratory (INEL) and Clemson University (CU) are part of a series of tests, including the Large-Scale Aquifer Pumping and Infiltration Test (LPIT), whose objectives are to provide much needed, defensible, site-specific subsurface parameters, including distribution coefficients (K_d's) and sorption rate constants for americium (Am), cesium (Cs), cobalt (Co), plutonium (Pu), strontium (Sr), and uranium (U). Equilibrium distribution coefficients and sorption rate constants are input parameters for risk assessment models and therefore must be known with a high degree of accuracy in order to make valid risk-based decisions.

The objectives of the INEL and CU laboratory tests complement the objectives of the LPIT. The CU tests were designed to determine distribution coefficients and reaction rate constants for a large set of radioactive contaminants (^{3}H, ^{241}Am, ^{137}Cs, ^{60}Co, ^{239}Pu, ^{90}Sr, and ^{233}U) using relatively fast, well established techniques which may or may not be directly applicable to actual field conditions. The INEL laboratory tests involved progressively more complex techniques to allow extrapolation of distribution coefficients determined under relatively simple conditions to more complex conditions more closely approximating those in the field. The LPIT was designed to measure hydrological parameters such as flow patterns and dispersion coefficients which can not be determined at the laboratory scale.

1.2 Review of Relevant Previous Sorption Studies

INEL specific K_d values are few but do exist for ^{90}Sr (Hawkins and Short, 1965; Schmalz, 1972; Del Debbio and Thomas, 1989) and ^{137}Cs (Hawkins and Short, 1965; Schmalz, 1972). Del Debbio and Thomas (1989) studied the sorption of strontium and other hazardous metals on basalt, interbed materials, and alluvium from near the Idaho Chemical Processing Plant at the INEL. The groundwater used in experiments was taken from wells near the INEL's Test Reactor Area. Strontium distribution coefficients were determined in batch tests and sorption isotherms were developed. Strontium sorption was greatest in the interbed material (K_d = 110-186 mL/g) and weakest in basalt (K_d = 1.1 mL/g).

Schmaltz (1972) performed limited batch tests with cobalt, strontium, and cesium in alluvial material taken from the INEL's Test Reactor Area. The water used in the batch tests was surface water from a pond at the Test Reactor Area. Schmaltz then developed equations to predict strontium and cesium distribution coefficients based on the chemical composition of the aqueous solution. The mean K_d for strontium was 24 mL/g , and the mean K_d for cesium was 950 mL/g.

Hawkins and Short (1965) studied the sorption of strontium and cesium to alluvial soil from the INEL using batch tests. A solution for use in these tests was synthesized to simulate INEL groundwater. The solution chemistry was varied (specifically $[Ca^{2+}]$, $[Mg^{2+}]$, $[Sr^{2+}]$, $[Cs^{+}]$, $[K^{+}]$, $[Na^{+}]$, and $[NH_4^{+}]$) and equations were developed to predict the sorption of strontium and cesium at varying solution chemistries. K_d values measured for strontium ranged from 8.3 to 16.6 mL/g. K_d values measured for cesium ranged from 75 to 225 mL/g.

A number of studies were conducted with Columbia River basalts as part of investigations for citing a national repository for high level waste (Ames et al., 1981; Barney, 1981, Salter et al., 1981a and b; Serne et al., 1979; Serne and Relyea 1982; Seitz et al., 1979; Routson et al., 1981). The experimental conditions for most of these studies are similar though not identical to the hydrogeologic system at the INEL (i.e. alkaline pH, high carbonate concentrations, oxidizing conditions, and similar though not identical basalt mineral compositions). The results from these studies are summarized in Table 1.

Table 1. Distribution Coefficients Measured as Part of the WRIT Program

Element	Umtanum K_d (mL/g)	Basalts Flow E K_d (mL/g)	Pomona K_d (mL/g)	Smectite K_d (mL/g)
U^{3}	1-15			76
U^{5}	3			
U^{1}	20	2.9	5.8	76
U^{1}	2.5	0.19	0.42	22
Pu^{1}	20			13900
Pu^{3}	20-25			2572
Pu^{5}	40			
Pu^{4}	8-1078			
Pu^{2}	35-125	107-1269		1066-9417
Am^{3}	230-600			1355

Am[5]	50			
Am[2]	50-315			
Co[7]				3000
Sr[2]	174-984			563-5258
Sr[4]	41-92			
Sr[5]	100			
Cs[1]	1084	498	1281	25000
Cs[2]	40-187			1657-5355
Cs[3]	200-900			>10000
Cs[4]	265-453			
Cs[5]	300			
Cs[6]	350-500			

[1]Ames et al., 1981
[2]Barney, 1981
[3]Salter et al., 1981a and b
[4]Serne et al., 1979
[5]Serne and Relyea, 1982
[6]Seitz et al., 1979
[7]Routson et al., 1981

1.3 Review of the Environmental Geochemistry of Am, Cs, Co, Pu, Sr and U

1.3.1 *Americium*

The predicted americium species in solution under oxidizing conditions and alkaline pH are $Am(CO_3)_2^-$, $Am(CO_3)_3^{-3}$, and $AmCO_3^+$ (Early, 1984). The pH of water in the Snake River Plain (SRP) aquifer beneath the INEL has been observed to range from 7.0 to 9.1. Fried et al. (1974) found the distribution coefficient for americium to decrease with increasing Na^+, Ca^{+2}, Sr^{+2}, La^{+3}, and Zr^{+4}, suggesting ion exchange as a sorption mechanism. Other researchers have found americium to be associated with colloidal material, and in some instances appeared to be irreversibly sorbed to these colloids (Means et al., 1978; Travis and Nuttall, 1985; Penrose et al., 1990) . Moulin et al., (1991) and Nash et al., (1988) suggest that sorption on SiO_2 and formation of silicate pseudo-colloids may be an important mechanism in controlling americium distribution.

1.3.2 *Cesium*

In natural waters, cesium in solution exists primarily as the monovalent cation Cs^+ with little tendency to form complexes. The solubility of most cesium compounds in aqueous solutions is quite high. The mechanism of cesium sorption is believed to be ion exchange, and other monovalent ions such as K^+, Na^+, and NH_4^+ compete with Cs^+ for available sites (Barney, 1982; Salter et al., 1981a and b; Hawkins and Short, 1965).

1.3.3 *Cobalt*

Two oxidation states have been observed for cobalt in nature, Co(II) and Co(III), where Co(II) predominates in most natural waters. In soil/water systems, sorption of ^{60}Co has been shown to increase with increases in pH between pH 6 and 9 (James and Healy, 1972; Tewari et al., 1972). Additionally, the solubility of cobalt decreases with increasing pH primarily due to the precipitation of $Co(OH)_2$ ($Ksp = 1.09x10^{-15}$) (Dean, 1985). The aforementioned increase in ^{60}Co sorption with increasing pH may be explained by the hydrolysis of Co^{+2} and the subsequent formation of cobalt colloids (Sorathesm et al., 1960; Tewari et al., 1972). In sorption studies, Means et al. (1987) found that cobalt was associated with particles from 0.2 to 2 μm in diameter. The cobalt was correlated with organic and/or manganese oxide coatings of clay minerals within this size range. Killey et al. (1984) proposed that ^{60}Co was sorbing to iron oxide coatings and that the ^{60}Co sorption mechanism was ion exchange. However, 80% of the sorbed ^{60}Co in his study was "fixed" and was not removed in desorption experiments, thus contradicting the proposed mechanism of ion exchange.

1.3.4 *Plutonium*

The aqueous speciation of plutonium is complex in that it may coexist in solution in different oxidation states (III, IV, V, and VI). Since the environmental behavior of plutonium depends on its oxidation state, it is critically important to know the oxidation state(s) of plutonium for determination of its distribution coefficient(s). In aqueous solutions plutonium exists as the hydrated ions Pu^{3+}, Pu^{4+}, PuO_2^{+}, and PuO_2^{2+}. The III and IV states (Pu^{3+} and Pu^{4+}) of plutonium predominate under reducing and low pH conditions, and the V and VI states (PuO_2^{+} and PuO_2^{2+}) predominate under oxidizing and alkaline pH conditions (Ames and Rai, 1978). The Pu(IV) oxidation state is insoluble at high pH where it tends to hydrolyze and form polymers. These polymers may be either neutral or positively charged and may remain in solution for significant time periods. Penrose et al. (1990) showed that plutonium exists in solution as predominately uncharged (91-99%) or anionic (2-10%) species in groundwater migrating from the Los Alamos National Laboratory, NM. Furthermore, this research showed plutonium was tightly or irreversibly associated with colloidal material 25 to 450 μm in size.

Carbonate complexation of actinides including plutonium may lead to increased solubility and formation of anionic species (Guillaumont and Adloff, 1992; Nash et al., 1988). The transuranics in general tend to form stable neutral and anionic carbonate complexes. The Pu(IV) carbonate complexes in particular neither undergo disproportionation nor redox reactions (IAEA, 1991; Sanchez et al., 1985). Pu(V) and Pu(VI) may form carbonate complexes as well (Yamaguchi, 1993; Salter et al., 1981a and b).

1.3.5 *Strontium*

The average content of stable strontium in basaltic rock is 465 ppm (Ames and Rai, 1978). This concentration is high considering the amount of ^{90}Sr that may come in contact with the basalt from waste sites. Therefore, the resident stable strontium concentration must be considered in regards to the concentration of strontium used in distribution coefficient determinations. Strontium shows little tendency to form colloidal or anionic species (Ames and Rai, 1978). The mechanism of strontium sorption is believed to be ion exchange, and Ca^{+2} has been shown to compete for sorption sites with Sr^{+2} (Barney, 1982; Salter et al., 1981a and b) as their ionic radii are similar, 1.18 and 1.32 Å, respectively (Huheehy, 1983).

1.3.6 *Uranium*

Uranium has three stable oxidation states: IV, V, and VI. The divalent uranyl cation, UO_2^{2+}, is the most stable form of uranium in neutral aerated aqueous solutions (Langmuir, 1978; Seaborg and Katz, 1957). Under these conditions uranium is believed to form anionic or neutral species (Early et al., 1984; Jensen, 1980; Ames et al., 1981). At alkaline pH's the uranyl ions may become hydrolyzed to form uranyl hydroxides and carbonates. Negative surface charges, such as those found on most subsurface materials, can repel these negatively charged ions and reduce the extent of sorption.

1.4 Review of Previously Established Methods and Thoery

Batch or column tests are the two most commonly used methods for determining equilibrium distribution coefficients. Batch tests have the advantage of being relatively fast and simple. They are generally the method of choice for strongly sorbing contaminants due to the extremely long time requirements of column test for such

contaminants. Batch methods are currently the only method available for determining sorption rate constants, because chemical processes cannot be completely separated from physical processes in column tests (see section 1.4.1 of this report). Batch tests have the disadvantage of being conducted under conditions far removed from those observed in the field (see section 3.2.2 of this report). Specifically they are carried out under static conditions (no advective flow), at solid/liquid ratios much lower than present in the field, and only under saturated conditions.

Column tests have the advantage of being conducted under conditions approximating those observed in the field. Specifically, (1) columns may be packed to have bulk densities and porosities (and thus solid/liquid ratios) similar to those observed in the field, (2) column tests are conducted under advective and dispersive flow conditions similar to those in the field, and (3) column tests may be conducted under a variety of different moisture contents. Column tests have the disadvantage of being quite time consuming and of commingling chemical and physical transport processes.

1.4.1 *Column Tests*

Subsurface contaminant transport is generally assumed to be controlled by advection, dispersion, and contaminant-subsurface material interactions. In this report the contaminant-subsurface material interactions are collectively referred to as sorption. The effect of linear, equilibrium sorption on contaminant migration is quantified through the retardation factor (R), which is the ratio of the pore water velocity to the contaminant velocity. It is given by

$$R = 1 + \rho \frac{\rho K_d}{\theta}, \qquad (1)$$

where ρ is the bulk soil density (g/cm^3), θ is the volumetric water content (cm^3/cm^3) which is equal to the porosity (n) under saturated conditions, and K_d is the distribution coefficient (mL/g). The distribution coefficient is the ratio of the contaminant concentration sorbed to the solid phase to the aqueous phase contaminant concentration. One of the simplest mathematical models for subsurface transport is one-dimensional advection-dispersion with linear, equilibrium sorption, and is given by

$$R \frac{\partial C}{\partial t} = D \frac{\partial^2 C}{\partial x^2} - u \frac{\partial C}{\partial x}, \qquad (2)$$

where C is the aqueous phase concentration (Bq/mL or mg/mL), D is the dispersion coefficient (cm^2/sec), t is time (sec), u is average linear pore water velocity (cm/sec), and x is distance along the axis of flow (cm).

Analytical solutions to equation (2) applicable to column tests for semi-infinite and finite-step inputs are given in Parker and van Genuchten (1984) and incorporated in their FORTRAN program CXTFIT. Presented in Figure 1 are CXTFIT predictions using the equilibrium model for the experimental apparatus described in sections 2.2 and 2.3 of this report. Shown in Figure 1 are predicted effluent concentrations as a function of time (expressed as displaced pore volumes) for a cylindrical column (15.2 cm in length and 5.07 cm^2 cross-sectional area) for a finite-step input of one displaced pore volume, u = 0.007 cm/sec, and D = 0.001 cm^2/sec. Predictions are given for retardation factors of 1 (K_d = 0 mL/g), 10 (K_d = 2 mL/g), and 100 (K_d = 25 mL/g). The effluent concentration is expressed in reduced form, C/C(0). When the effluent concentration is equivalent to the influent concentration, C/C(0) is unity. Time is expressed as displaced pore volumes (DPV) and is normalized to the volume of pore water within the column, called the volumetric water content. For example, if the volumetric water content of a column is 35 mL, and 70 mL have been collected in the column effluent, this corresponds to two DPV. For a conservative tracer (Kd = 0 mL/g) 50% of the input concentration should be observed in the column effluent after elution of one DPV (see Figure 1). If C/C(0) reaches 0.5 prior to one DPV, then this is an indication that channeling may be occurring within the column.

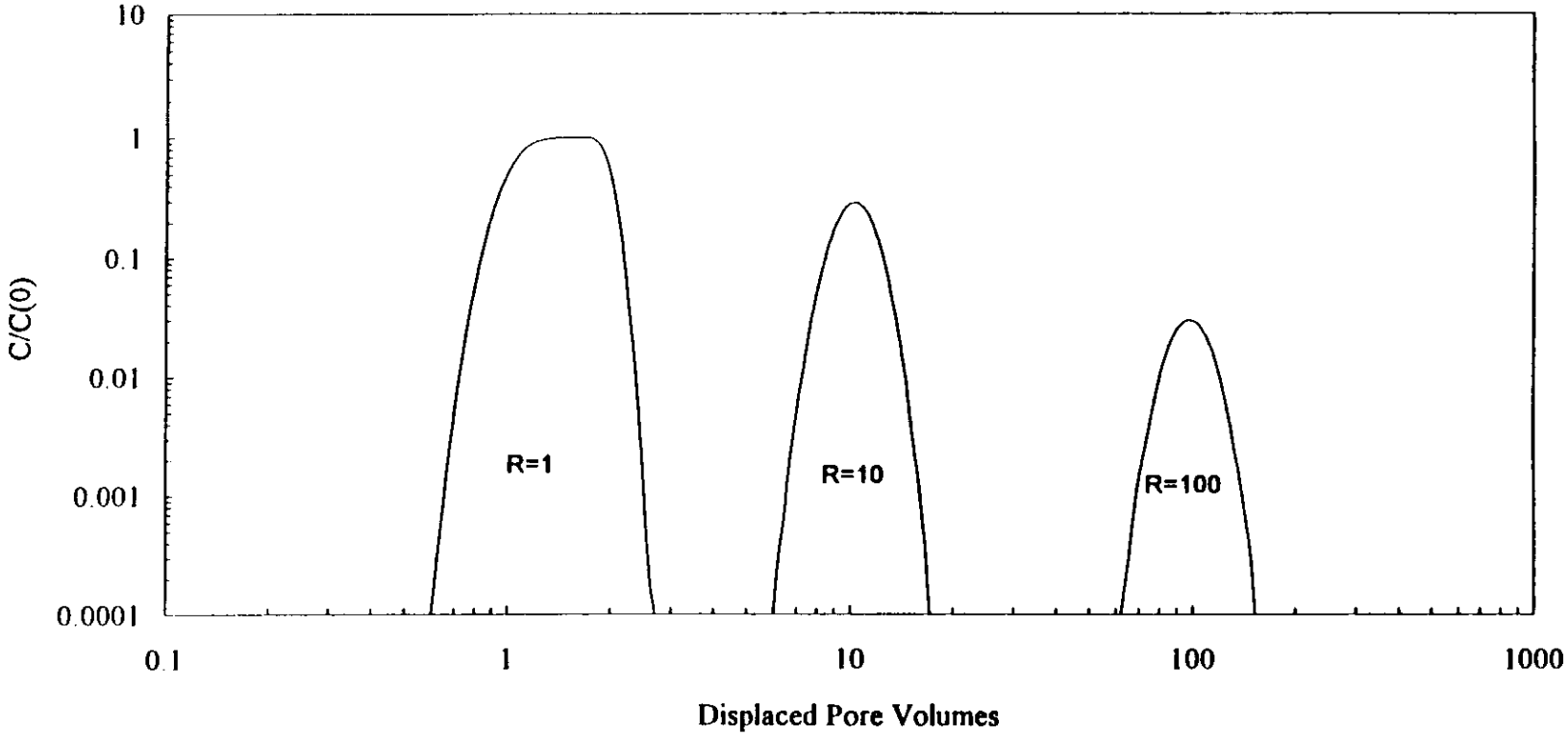

Figure 1. Predictions of breakthrough curves for various contaminant retardation factors based on equation (2).

Unfortunately, the simple model described above is not appropriate for all situations. For the case of slow sorption kinetics and/or rapid advective flow the non-equilibrium (or kinetic), first order sorption model may be appropriate. The governing equations for this model are

$$\frac{\partial C}{\partial t} + \frac{\rho}{\theta}\frac{\partial S}{\partial t} = D\frac{\partial^2 C}{\partial x^2} - u\frac{\partial C}{\partial x} \tag{3}$$

$$\frac{\partial S}{\partial t} = \alpha(K_d C - S), \tag{4}$$

where S is the contaminant concentration sorbed to the solid phase and α is a first order rate constant (1/sec).

Researchers have observed accelerated transport followed by tailing under a variety of different conditions including strong sorption interactions, fractured material, and unsaturated materials (Gupta et al., 1973; Gaudet, et al., 1977; van Genuchten and Cleary, 1979). van Genuchten (1981) attempted to model this observed behavior by incorporating solute transport between mobile and immobile regions of water. Immobile regions may be caused by secondary porosity or internal pores whose access is limited by mass diffusion. The governing equations for these interactions are

$$(\theta_m + \rho f k)\frac{\partial C_m}{\partial t} + [\theta_{im} + (1-f)\rho K_d]\frac{\partial C_{im}}{\partial t} = \theta_m D\frac{\partial^2 C_m}{\partial x^2} - \theta_m u\frac{\partial C_m}{\partial x} \tag{5}$$

$$[\theta_{im} + (1-f)\rho K_d]\frac{\partial C_{im}}{\partial t} = \alpha(C_m - C_{im}), \tag{6}$$

where, C_m is the concentration in the mobile water (Bq/mL or mg/mL), C_{im} is the concentration in the immobile water (Bq/mL or mg/mL), θ_m is the mobile volumetric water content, θ_{im} is the immobile volumetric water content, f is the fraction of sorption sites available to mobile water, and α is the mass transfer coefficient between the mobile and immobile water. This problem is mathematically identical to the case of two different types of sorption sites; sorption to one type of these sites is assumed to be instantaneous, while sorption to the other type of site is assumed to be time-dependent. Thus this model is referred two as the two-site/two-region model. Analytical solutions to equations (3 - 6) are also incorporated in CXTFIT.

CXTFIT can be used in two ways: (1) to predict effluent concentrations for specified transport parameters or, (2) to fit transport parameters (by least squares) for measured effluent concentrations. In this work average pore water velocity, and initial aqueous concentration, C(0), were specified and, pulse duration, retardation factors, dispersion coefficients, rate constants, and the immobile volumetric water content were fit to the data. Distribution coefficients were calculated from the estimated retardation factors using equation (1).

1.4.2 *Batch Tests*

One of the simplest mathematical models for describing contaminant partitioning between two phases at equilibrium is the empirically derived Freundlich isotherm,

$$C_s = K_d C^{1/n}, \tag{7}$$

where C_s is the solid phase concentration (Bq/g or mg/g), C is the aqueous phase concentration (Bq/mL or mg/mL), and n is the Freundlich constant, frequently assumed to be one. When n is one K_d values can be calculated from batch tests by

$$K_d = \frac{C(0) - C}{C}\left(\frac{V}{m}\right), \tag{8}$$

where V is volume of the aqueous phase (mL), C(0) is the initial aqueous phase concentration (Bq/mL or mg/mL), C is the final aqueous phase concentration (Bq/mL or mg/mL), and m is the mass of the solid phase (g).

Equation (7) is only valid when contaminant partitioning between the aqueous and solid phases is in equilibrium. In situations where the solid/groundwater system is not in equilibrium, a first order rate equation can be used to approximate the contaminant distribution and estimate the sorption rate constant. As a solid/groundwater system approaches steady-state, the change in the solid phase concentration may be represented by

$$\frac{\partial C_s}{\partial t} = \alpha(K_d C - C_s), \tag{9}$$

where α is a sorption rate constant (1/sec) and C is the aqueous concentration. The solution for the aqueous phase concentration for the initial condition C = C(0) at t = 0, is

$$C(t) = C(0)\frac{\left[1 + K_d\left(\frac{m}{V}\right)e^{-\alpha\left(C + K_d\frac{m}{V}\right)t}\right]}{1 + K_d\left(\frac{m}{V}\right)} \qquad (10).$$

Dzombak and Morel (1987) observed that contaminant sorption kinetics are often not adequately modeled as a single, first-order process, but rather as the combination of two first-order processes, one fast and one slow. They developed a so called "two box" model to incorporate dual sorption rates. Wilczak (1988) adapted Dzomback and Morel's model to include an asymptotic approach to equilibrium. In order to accomplish this, Wilczak added two new parameters, p_c, the percent deviation of the observation from equilibrium, and τ, the length of time required to reacn p_c. The resulting equation is (Wilczak, 1988)

$$C(t) = C_{eq} + p_c C_{eq} e^{\lambda_2(\tau - t)} + C(0)\left[e^{-\lambda_1 t} - e^{-\lambda_2(\tau - t) - \lambda_1}\right], \qquad (11)$$

where λ_1 and λ_2 are sorption rate constants (1/sec) and C_{eq} is the equilibrium concentration (Bq or mg/mL).

1.5 Objectives

The objectives of the CU laboratory tests were to:

- determine defensible distribution coefficients for Am, Cs, Co, Pu, Sr and U applicable to the INEL using both batch and column methods to insure as accurate and field representative results as possible,
- determine sorption rate constants so that the applicability of distribution coefficients under interstitial fluid velocities observed in the field can be evaluated, and
- determine the effects of variation in pH and ionic strength on distribution coefficients so that the applicability of the distribution coefficients measured to variations in groundwater chemistry caused by natural heterogeneity or waste inputs can be assessed.

The objectives of the INEL laboratory tests were to:

- verify that results obtained at the two laboratories are comparable,
- evaluate the applicability of distribution coefficients measured at the low solid/liquid ratios normally used in batch tests to distribution coefficients measured at solid/liquid ratios observed in the field,

- evaluate the applicability of distribution coefficients measured using crushed basalt, where surface characteristics may have been altered, to distribution coefficients measured using intact basalt cores, and
- evaluate the applicability of distribution coefficients measured under saturated conditions in predicting contaminant transport under unsaturated conditions.

2.0 Materials and Methods

2.1 Solid and Groundwater Composition

All column and batch tests were conducted using a synthetic groundwater formulated to approximate the composition observed in SRP aquifer field samples (Wood and Low, 1986). The compositions of the synthetic groundwater and field samples are compared in Table 2. The synthetic groundwater had an ionic strength of 4.8 mM and a total dissolved solids concentration of 212.4 mg/L. The equilibrium speciation model, MINTEQ, estimated that much of the groundwater in the SRP aquifer is supersaturated with respect to dolomite. Although the kinetics of dolomite precipitation are slow, it was decided to keep the calcium, magnesium, and carbonate composition of the synthetic groundwater below that at which dolomite is expected to precipitate, in order to assure that the synthetic groundwater composition remained constant over time and between tests. The synthetic groundwater was made by adding accurately weighed (± 0.001 mg) amounts of reagents to distilled, deionized water with the final pH adjusted to 8.00 ± 0.05 using either 1.0 N HCl or 0.5 N NaOH. The procedure for making synthetic groundwater is presented in Appendix A.

Table 2. Comparison of the Snake River Plain Aquifer and the Synthetic Groundwater Compositions

Component	Synthetic Groundwater	Snake River Plain Aquifer (Wood and Low, 1986)		
	Base Chemistry (mg/L)	average (mg/L)	max. (mg/L)	min. (mg/L)
Ca^{2+}	11.5	51	120	5.0
K^{+}	9.8	4	12	0
Mg^{2+}	8.3	18	54	0.2
Na^{+}	19.7	26	140	4.0
Cl^{-}	18.9	28	230	1.8
SO_4^{2-}	23.4	41	218	1.8
HCO_3^{-}	96.6	220	510	52
F^{-}	0.5	0.6	11	0.03

SiO_2	10.0	50	138	5.8
pH	8.0	7.8	9.1	7.0
I (mole/L)	0.0048	0.008	0.02	0.004

Both batch and column tests were carried out using interbed and basalt materials collected from the INEL. The interbed material used was a composite of samples from five uncontaminated well cores collected near the Radioactive Waste Management Complex. The material was composited to assure that all results obtained were comparable. The characteristics and mineral composition of the composite interbed material are given in Tables 3, 4 and 5. The interbed material was dry sieved and the fraction smaller than 250 μm was used in batch and column tests. This size fraction was chosen because it provided uniform hydraulics in packed columns. The basalt used came from a boulder collected near the Radioactive Waste Management Complex. Intact basalt cores were drilled from the boulder and the remainder of the boulder was crushed for use in batch and column tests. The characteristics and mineral composition of the crushed basalt are given in Tables 3 and 5. The crushed basalt was dry sieved and the fraction larger than 250 μm used in batch and column tests. Again, this size fraction was chosen because it provided uniform hydraulics in packed columns.

Table 3. Physical and Chemical Characteristics of the Crushed Basalt and Composite Interbed Material Collected Near the Radioactive Waste Management Complex

Characteristic	Crushed Basalt	Composite Interbed
DCB Extractable Fe oxide ($\%Fe_2O_3$)	ND	1.77
NH_4OAc Extractable Mn (ppm)	1.0	1.99
Total CEC (meq/100g)	6.05	17.39
Particle Size Used (mm)	0.25-2.0	<0.25
Major Minerals	Pyroxene Plagioclase Olivine	Montmorillonite Mica Vermiculite

Table 4. Mineralogy of the Clay Size Fraction of Composite Interbed Material Collected Near the Radioactive Waste Management Complex

Mineral	Composite Interbed Material[1]
Mica	30%
Montmorillonite	20%

Vermiculite	40%
Chlorite	10%

[1]Composite of 11 samples from 5 cores.

Table 5. Mineralogy of the Sand Size Fraction of Crushed Basalt and Composite Interbed Material Collected Near the Waste Management Area

Mineral	Composite Interbed Material[1]	Basalt
Pyroxene	30-50%	30-50%
Plageoclase	30-50%	30-50%
Quartz	15-30%	ND
Olivine	10-15%	15-30%
Magnetite	<10%	<10%

[1]Composite of 11 samples from 5 cores

2.2 Saturated Column Test

2.2.1 *Crushed Basalt and Interbed Columns*

Column dimensions were selected based on design recommendations by Relyea (1982) for minimum channeling along column walls. The columns were constructed of polycarbonate cylinders, 2.5 cm in diameter and 15.1 cm in length, with bolted flanges at each end. At CU crushed basalt columns were wet packed to insure complete saturation by adding crushed basalt in approximately 5 g increments and tapping lightly with a rod. At the INEL crushed basalt columns were dry packed again by adding approximately 5 g increments and tapping lightly. Saturation was insured by eluting the column with degassed synthetic groundwater. At both CU and at the INEL interbed material columns were dry packed 1 cm at a time while lightly tapping the column. After each interbed material addition, the top interbed layer was agitated to avoid "bands" of fine material forming . The amount of material added to each tared column was recorded, as well as the weight of the saturated column. The bulk density of the column was calculated as the amount of solid added to the column per unit of column volume. The porosity of the column was calculated as the difference in the column mass before and after saturation, divided by the total packed column volume. The characteristics of packed columns are listed in Appendix B.

The column apparatus consisted of reservoirs for synthetic groundwater or the

spiked synthetic groundwater solutions, peristaltic pump or HPLC pump (Masterflex, model 7550-90 at CU, Eldex, model AA-100-S at the INEL), soil column, and fraction collector (Eldex Universal Fraction Collector) (Figure 2).

Synthetic groundwater was pumped up through the column until the column was saturated. Saturation was defined as the point at which the column weight did not change with time by more than 5%. Columns were generally pumped at a flowrate of 1 mL/min which corresponds to an average pore water velocity of 0.007 cm/sec. However, flowrates as low as 0.1 and as high as 10 mL/min were tested. The pH and specific conductivity of the column effluent were monitored during column saturation. After the column was saturated and the pH and specific conductivity of the column had stabilized, the column influent was switched to the spiked synthetic groundwater solution. The spiked synthetic groundwater was produced by the addition of measured amounts of either bromide, stable strontium, or acidic radiotracers, including ^{241}Am, ^{60}Co, ^{137}Cs, ^{239}Pu, ^{90}Sr, ^{233}U, and ^{3}H to synthetic groundwater. The pH of the spiked synthetic groundwater was then readjusted to 8.0 ± 0.05 by the addition of 0.1 N NaOH. The composition of spike solutions is given in Appendix C.

The spiked synthetic groundwater was introduced as a finite-step input. At CU a step input of one pore volume was used to reduce the amount of radioactivity required for the column tests. The column was then washed with approximately 200 pore volumes of unspiked synthetic groundwater. At the INEL the spiked input was maintained until the effluent concentration had reached that of the input. The influent was then switched to unspiked synthetic groundwater. The volumes of effluent fractions were adjusted to insure that at least 10 data points were obtained on the rising portion of the breakthrough curve (BTC). Volumes collected ranged from 0.5 mL to 20 mL.

A conservative tracer, either ^{3}H or bromide, was applied to all columns for three reasons: (1) to evaluate channeling within the column, (2) as an intercolumn control for caparison of column dispersion, and (3) as a control for CXTFIT determinations of retardation factors. As pointed out previously the retardation factor for a conservative tracer is one. An observed retardation factor less than one for a conservative tracer indicates channeling within the column.

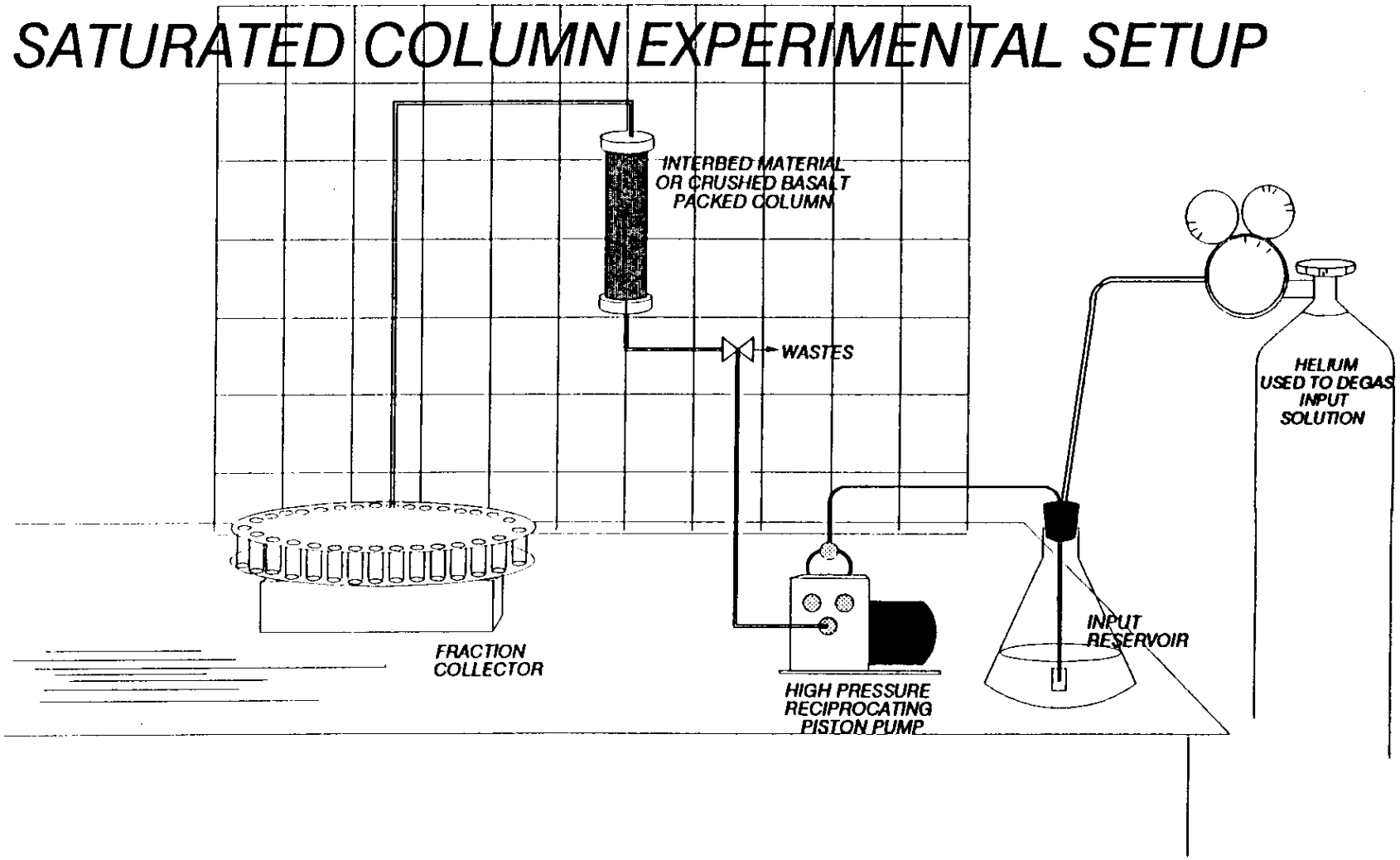

Figure 2. Saturated column experimental setup.

2.2.2 *Intact Basalt Cores*

Intact basalt cores were sealed in a polymeric resin (Master Bond Inc., EPL1LV and EP21HTAR-1). This was accomplished by first painting the cores with the resin and allowing the resin to dry in order to minimize penetration of the core porosity by the resin. The painted core was then centered in a polycarbonate cylinder and resin was pored into the annular space between the core and cylinder. The ends of the resin coated core were removed with a rock saw. End caps containing a water distribution system to insure even distribution of the eluent across the core surface as well as input and output fittings were then sealed to the column ends, again using polymeric resin. Intact basalt cores had internal diameters of 3.8 cm and were approximately 20.3 cm in length. The intact basalt cores were saturated and operated as described in section 2.2.1.

2.3 Unsaturated Column Tests

Figure 3 depicts the general setup for the unsaturated column experiments. Columns for the unsaturated flow experiments were constructed of Plexiglas (2.77 cm internal diameter by 25.4 cm in length) with bolted flanges at both ends and two tensiometers approximately 2.5 cm from each end (soil Measurement Systems catalog number CL-021). Columns were filled with air-dry crushed basalt (>250 μm) by adding the basalt in approximately 1-cm increments and tapping lightly. Care was taken to avoid obvious layering or segregation of basalt by particle size. The oven-dry weight of the crushed basalt was also determined. The bulk density of the column was calculated as the weight of solid added to the column per unit of column volume.

Synthetic groundwater was pumped up through the column using a syringe pump (Soil Moisture Measurement Systems catalog number CL-010) until the column was saturated. Flow was stopped and a wettable porous plastic disk and nylon mesh filter were installed in the bottom of the column. The input solution line was switched to the top of the column and the bottom of the column was connected to a vacuum chamber (Soil Measurement Systems catalog number CL-040). Synthetic groundwater flow was established to the top of the column at the desired rate for the experiment, with vacuum applied to the bottom of the column through the vacuum chamber. The vacuum was adjusted using a pressure regulator (Soil Measurement Systems catalog number CL-041)

until tensions in the column tensiometers were equal. Tensions were measured using a Tensiometer (Soil Measurement Systems catalog number SW-010). The input solution then was switched from synthetic groundwater to spiked synthetic groundwater. Bromide and strontium were used as spikes in this set of experiments. Thymol (168 ppm) was used in all input solutions (except column 1) to inhibit biological activity within the column and porous disk. In general, this input solution was applied to the column until the level of bromide or strontium in the effluent solution matched the level of the input solution. At that point, the input solution was switched back to unspiked synthetic groundwater. Unspiked synthetic groundwater continued to be applied to the column until the bromide or strontium level in the column effluent was at or near background levels. Initial column and input bromide and strontium levels are listed in Appendix C.

The same column, without repacking, was used for all six unsaturated flow experiments, and one saturated flow experiment. At the conclusion of a given experiment, a different flow rate was applied to the top of the column and vacuum adjusted, as described above, to establish flow at a different moisture content. The saturated flow experiment was run by pumping input solution to the bottom of the column and collecting effluent from the top of the column. The porous disk and nylon filter were removed from the bottom of the column and replaced with glass wool.

The pore volume of the column at each moisture content (unsaturated and saturated) was calculated as the difference in column weight before water was applied to the column and after steady flow conditions were established for each experiment. Column effluent was collected in relatively small (< 12 mL) increments using a fraction collector (Soil Measurement Systems catalog number CL-050) installed inside the vacuum chamber (the vacuum chamber was not required for the saturated experiment). Selected effluent samples (enough to define the tracer breakthrough curve) were chosen for tracer analysis. Input flow rates were monitored continually by weighing the input reservoir.

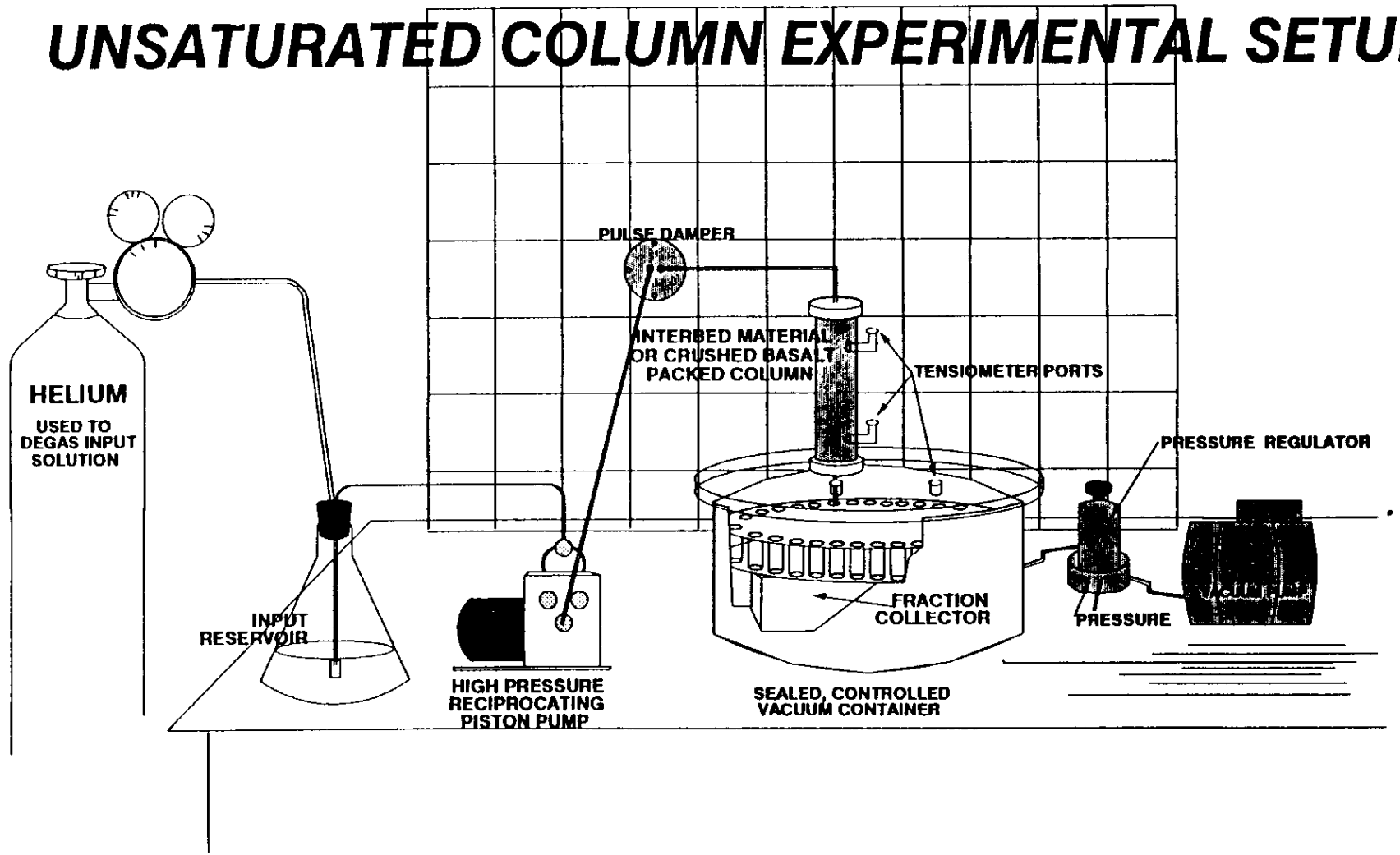

Figure 3. Unsaturated column experimental setup.

2.4 Batch Test

The batch test design was adapted from ASTM method D4319, Standard Test Method for Distribution Ratios by the Short-Term Batch Method (ASTM, 1990). The solid/liquid ratios used in batch tests were generally selected to decrease the aqueous phase concentration of the element under study by a factor of approximately two; thus insuring a sufficient aqueous phase concentration for accurate measurement while insuring a sufficient change in concentration to accurately determine the difference. Solids concentrations used at Clemson University ranged from 3.5 to 150 g/L for interbed material and from 20 to 500 g/L for basalt. Crushed basalt solids concentrations used at the INEL ranged from 100 to 700 g/L. The aqueous phase concentration was defined as the activity passing through a 0.2 μm cellulose acetate filter or remaining in suspension after centrifugation for 20 minutes at 3200 rpm in a Sorvall RC-5C centrifuge with a GSA rotor.

Batch tests were conducted in either 15 or 50 mL polystyrene or polycarbonate screw cap centrifuge tubes (Scientific Products or Fisher Brand). Polycarbonate tubes were used for ^{241}Am and ^{239}Pu, while polystyrene tubes were used for all other elements. Basalt or interbed material was added to a tared centrifuge tube and weighed to + 0.0002 g (Sartorius AG, model MC1, or Mettler model H33AR). The appropriate volume of synthetic groundwater was added to each tube and the tubes tumbled at 10 rpm for two consecutive 12 hour periods. At the conclusion of the first 12 hour period, the tubes were centrifuged and the synthetic groundwater was siphoned off, discarded, replaced with fresh synthetic groundwater, and returned to the tumbler for an additional 12 hours. At the conclusion of the second 12 hour wash, the same procedure was followed. The final weight of the centrifuge tubes was measured prior to the addition of the spike for determination of the amount of synthetic groundwater in each tube.

Duplicate centrifuge tubes were prepared for all sampling times. Additionally, one tube blank (no solid present) was taken at each sampling time and three soil blanks (no spike present) were taken throughout the test period. Tube blanks were taken to account for any loss of the spiked element to the container walls, and soil blanks were taken to

account for any isotope that may already have been present in the basalt or interbed material.

Generally a small volume and high concentration were required for batch test spike solutions so that small increments (0.1 mL) could be added to each centrifuge tube without having a significant effect on the aqueous volume. Centrifuge tubes were spiked in reverse order of that used for sampling. At the designated sampling times, samples and tube blanks were removed from the tumbler and allowed to settle for a few seconds. Sampling was accomplished by siphoning. The supernatant was subsequently filtered through a 0.2 μm cellulose acetate syringe filter.

2.5 Plutonium Oxidation States

Plutonium oxidation state was determined using both the thenoyltriflouracetone (TTA) (Kobashi and Choppin, 1988) and the bis (2-ethylhexyl) hydrogen phosphate (HDEHP) (Neu et al., 1994) extraction techniques. Both of these extraction techniques are described in Appendix D. These techniques were verified by extracting mixtures of radionuclides with known oxidation states, such as uranium and thorium, and by comparison of the results from the two techniques for the same plutonium solution.

Plutonium was converted to and maintained in the VI oxidation state using a 10^{-4} M solution of potassium permanganate, $KMnO_4$, in synthetic groundwater. Plutonium was converted to the V oxidation state using a TTA back-extraction method described by Saito et al., 1985 and in Appendix D.

2.6 Liquid Scintillation Analysis

Liquid scintillation counting was used to determine aqueous concentrations of all radionuclides used in laboratory experiments. The Wallac 1415 LSC used here has the ability to distinguish between alpha and beta emissions by pulse shape discrimination. Typically, 1 mL aliquots of sample were added to 10 mL of Highsafe 2 cocktail (Wallac Inc.) for activity determination. Quench curves for ^{3}H, ^{60}Co, ^{90}Sr, and ^{137}Cs were prepared with National Institute of Standards and Technology traceable standards. The alpha efficiency was assumed to be 100 percent and no quench curves were prepared for alpha emitting radionuclides. Samples were initially counted for 10 min. If the activity in the sample was less than ~2 dpm the sample was recounted for 30 min.

2.7 Bromide, pH, Specific Conductivity and Atomic Adsorption Analysis

Bromide, pH and specific conductivity were measured using a Fisher Scientific Accumet 50 meter with, combination, reference, and ion selective electrodes, and conductivity cells. The meter and electrodes were calibrated with at least three solutions covering the range of pH or bromide concentration expected in the sample. The meter and electrodes were calibrated before each use and calibration was checked every two hours during use. The cell constant and temperature compensation for conductivity were checked by analyzing a standard solution before each use.

Stable strontium was measured using a Perkin-Elmer model 5100 atomic absorption spectrophotometer with a Zeeman 5100 graphite furnace. All stable strontium samples were preserved by acidification (pH < 2) with nitric acid. The spectrophotometer was calibrated using 4 standard solutions covering the concentration range expected in the samples prior to each use. All samples and standards were run in triplicate.

3.0 Results and Discussion

3.1 Clemson University Studies

3.1.1 *Initial Column Test*

3.1.1.1 *Crushed Basalt Packed Columns.* As stated previously ^{3}H was used as a conservative tracer to assure that all columns were properly constructed and wall channeling was not occurring. Channeling was not observed in the column runs reported here based on the retardation values estimated for ^{3}H . A typical ^{3}H breakthrough curve (BTC) is shown in Figure 4. The remaining ^{3}H BTCs are presented in Appendix E. A summary of the percent breakthrough, as well as the dispersion coefficient, D, and retardation factor, R, estimated by CXTFIT for each ^{3}H run is also listed in Appendix E.

Typical BTCs for ^{60}Co, ^{239}Pu, ^{137}Cs, and ^{233}U are presented in Figures 6-9. The remaining BTCs are presented in Appendix F. In general the BTCs are similar to those expected based on the equilibrium adsorption model (Figure 1). However, there are three significant differences.

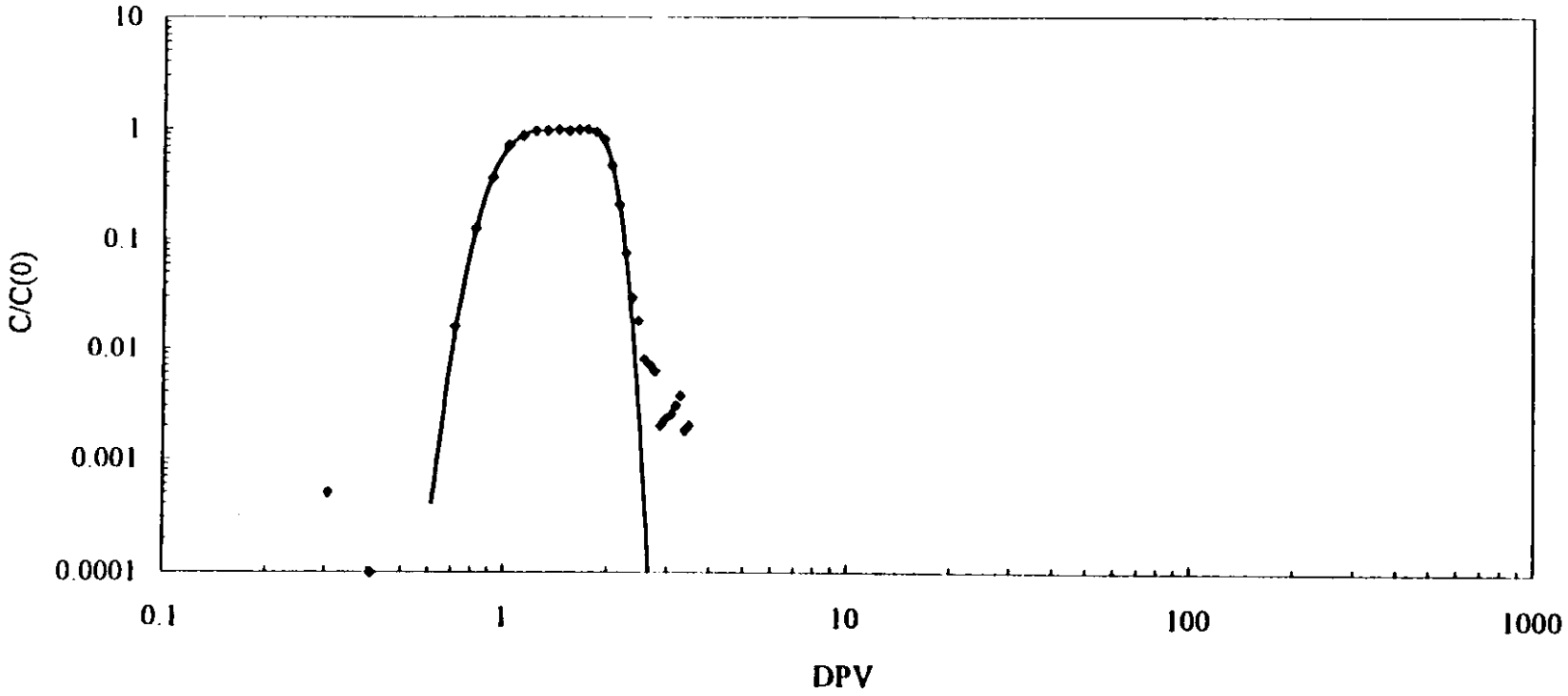

Figure 4. Breakthrough Curve for ^{3}H (96.9% recovery) in crushed basalt packed column B08 for reduced pulse time of 1.1. The solid diamond shapes represent data points and the line represents the equilibrium CXTFIT model fit.

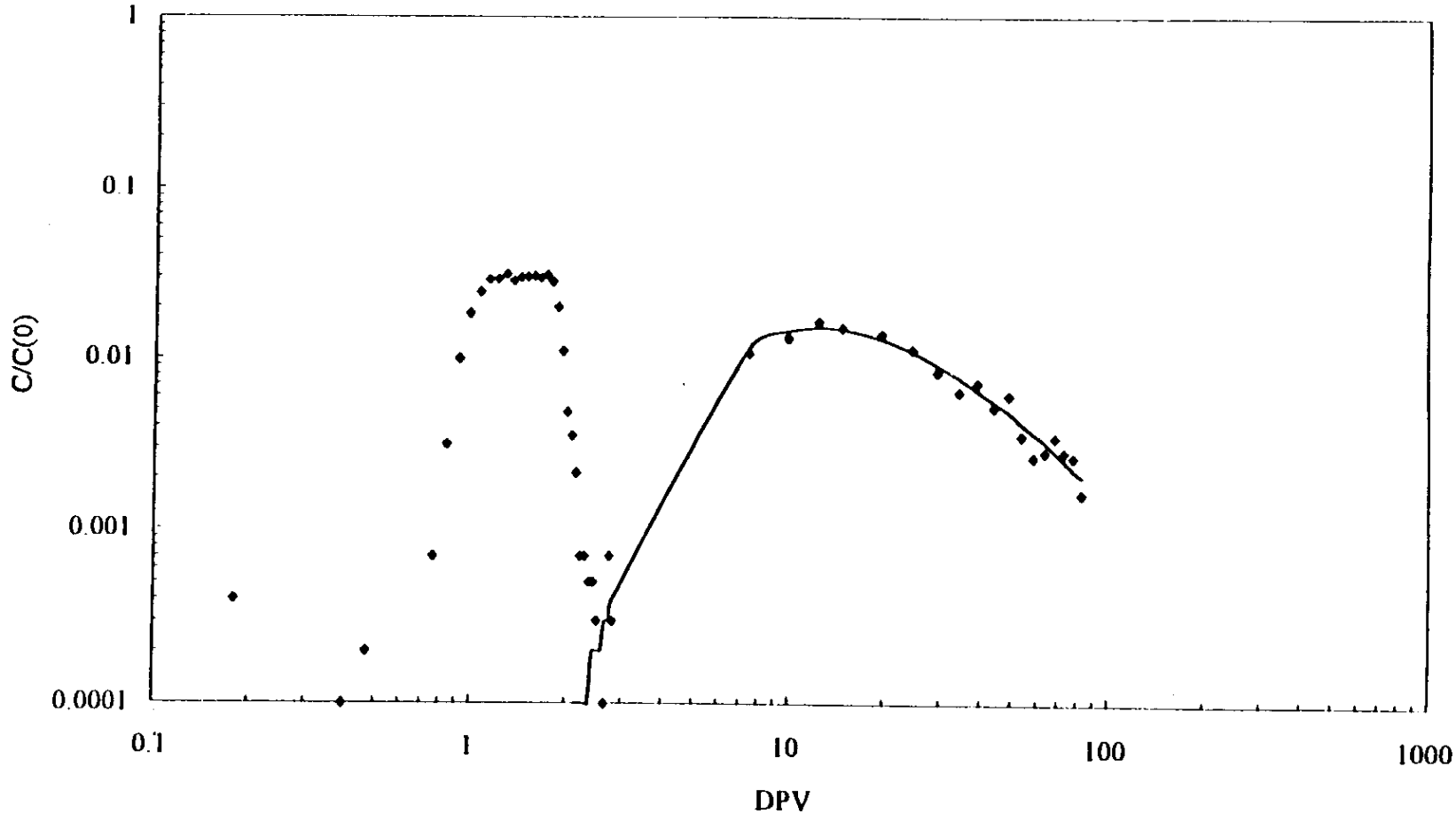

Figure 5. Breakthrough of two distinct fractions of ^{60}Co (2.9 and 63% recovery) in crushed basalt packed column B02. The diamond shapes represent data points while the line represents the fit of the equilibrium CXTFIT model.

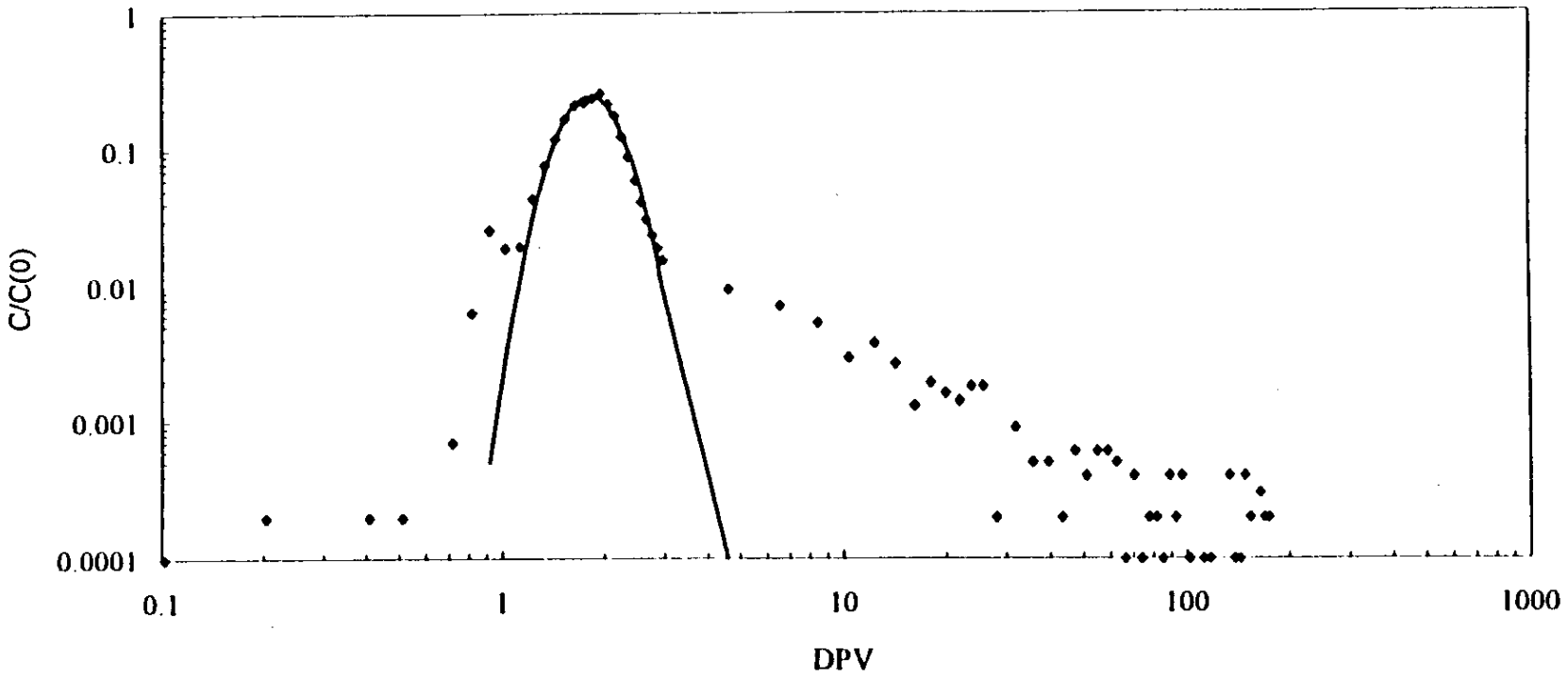

Figure 6. Breakthrough of ^{239}Pu (33.5% recovery) in crushed basalt packed column B08. The diamond shapes represent data points while the line represents the fit of the equilibrium CXTFIT model.

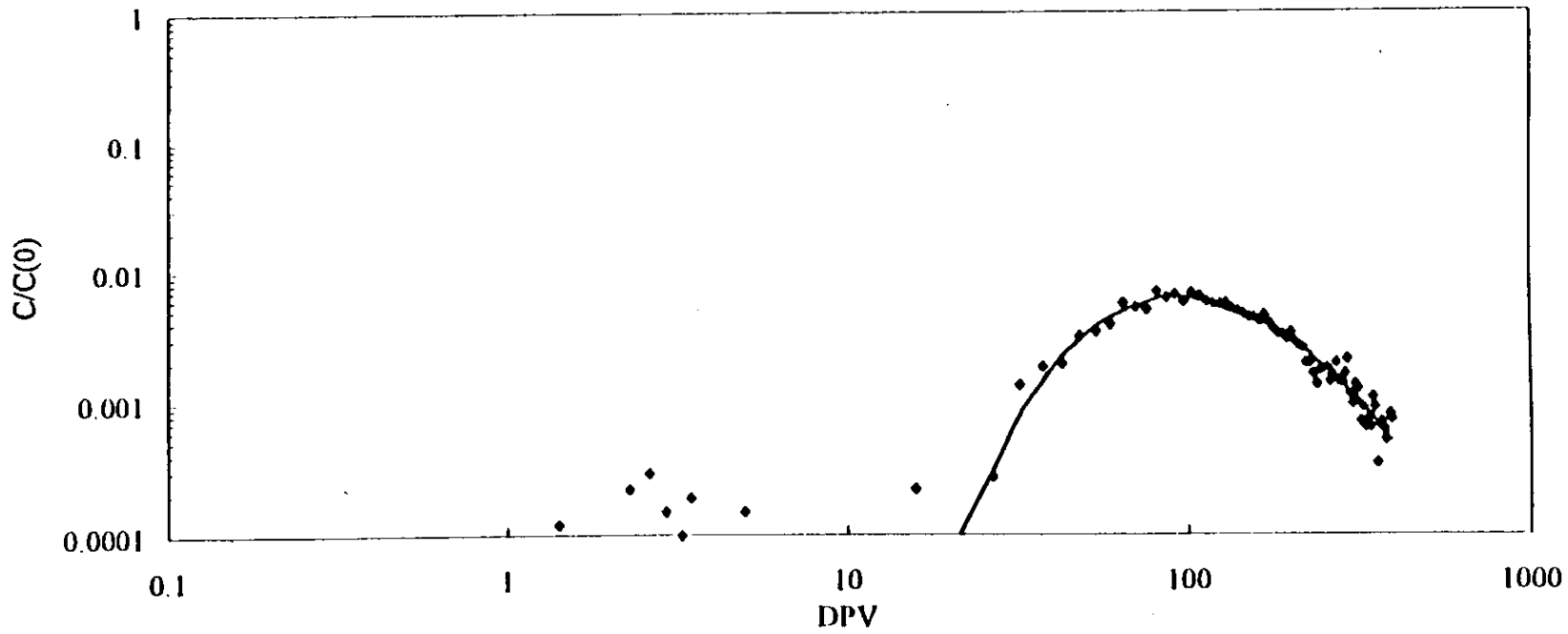

Figure 7. Breakthrough of ^{137}Cs (94.3% recovery) in crushed basalt packed column B10. The diamond shapes represent data points while the line represents the fit of the equilibrium CXTFIT model.

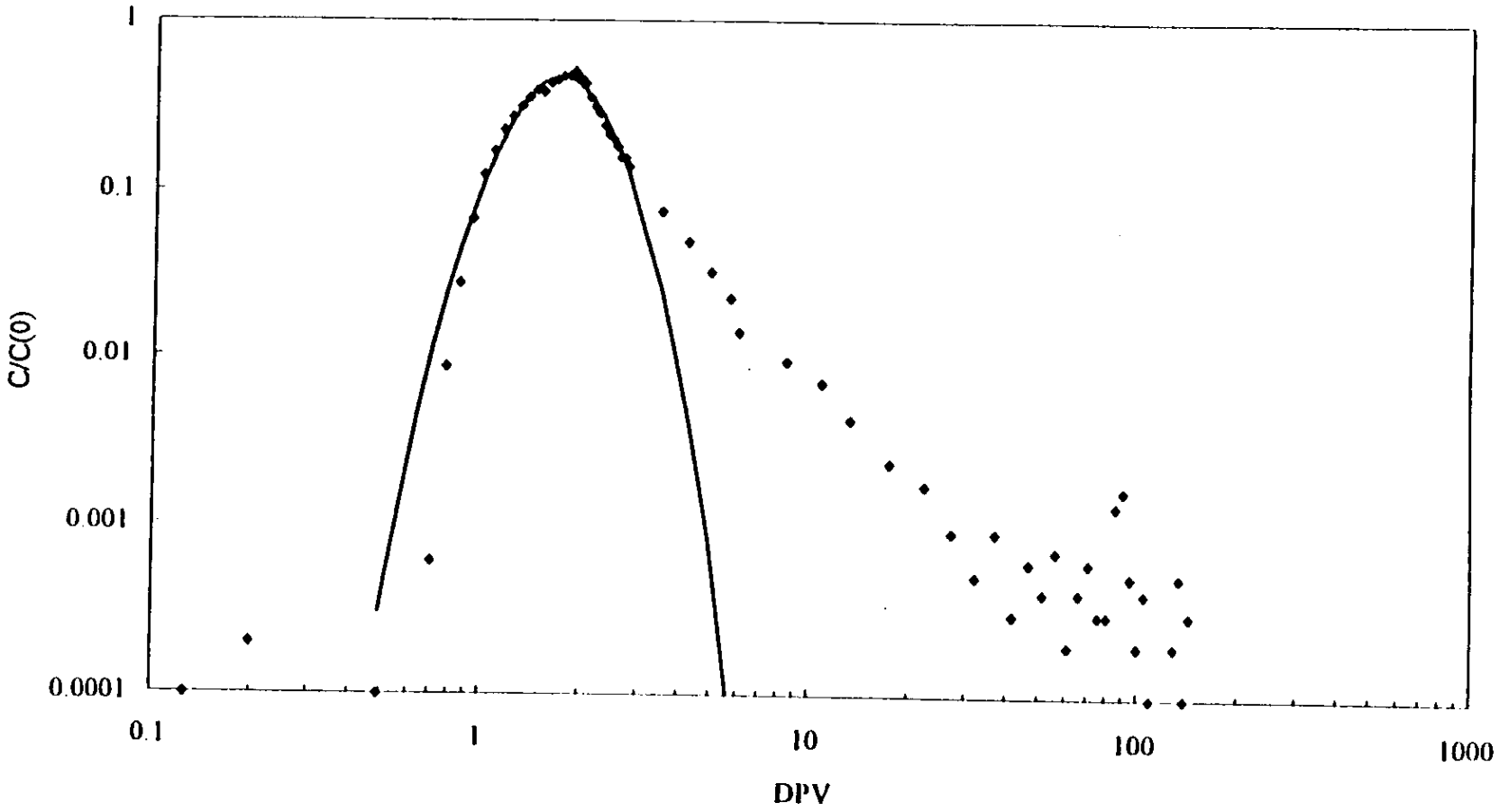

Figure 8. Breakthrough of ^{233}U (89.9 % recovery) in crushed basalt packed column B02. The diamond shapes represent data points while the line represents the fit of the equilibrium CXTFIT model.

First, percent recovery was less than 100% for ^{60}Co (~69%), ^{90}Sr (~50%), ^{239}Pu (~33%), and ^{241}Am (~10%). Incomplete recovery suggests that some fraction of the radionuclide either had a retardation factor greater than 200 (corresponding to the maximum number of pore volumes eluted during these column runs) or was irreversibly immobilized by the basalt.

Second, the BTCs were generally broader than predicted by the equilibrium model and were sometimes skewed toward higher pore volumes. This difference between theoretical equilibrium predictions and column data suggests that one or more processes collectively referred to as "non-equilibrium" by Parker and van Genuchten (1984) may be important. The fact that the two-site/two region model generally fit the data better than the equilibrium model, based on the correlation coefficient, supports this observation. "Non-equilibrium" processes may include the presence of two different types of adsorption sites, one of which may not have reached equilibrium, or the presence of secondary porosity whose access is limited by mass transport. Secondary porosity is present in the crushed basalt. However, it is not possible to conclude which of these mechanisms is most probable from the results reported here.

Finally, enhanced mobility fractions of ^{60}Co, ^{239}Pu and ^{241}Am were observed within the first 5 pore volumes eluted (Figures 6 and 7). The percentages of the total radionuclide observed in the enhanced mobility fractions were 3% for ^{60}Co, 9 to 13% for ^{241}Am, and 10 to 55% for ^{239}Pu. Three possible explanations for the observed enhanced mobility fractions are: 1) association of these elements with a mobile colloidal phase, 2) formation of a more mobile complex, or 3) kinetically limited sorption. All three of these radionuclides have been observed to form or be associated with colloidal material (Sorathesm et al., 1960; Tewari et al., 1972; Means et al., 1978; Travis and Nuttall, 1985; Nash et al., 1988; Penrose et al., 1990; Moulin et al., 1991). ^{239}Pu and ^{241}Am are thought to form neutral or negatively charged complexes with carbonate (see section 1.3 of this report). It is not possible to conclude which of these three mechanisms is most probable from the results reported here.

Percent recovery and parameter estimates based on CXTFIT are summarized in Table 6. Breakthrough curves from both the crushed basalt and interbed material packed

Table 6. Results of Fitted Parameters and Percent Recovery for Crushed Basalt Column Tests at Clemson University

			Equilibrium Model				Two Site/Two Region Model				
Isotope	Column ID	Percent Recovery	D (cm^2/sec)	R	Enhanced Mobility Fraction R	r^2	D (cm^2/sec)	R	θ_{im}	α	r^2
^{60}Co	B02	66.5	0.0017	22.2	1.49						
	B03	57.5	0.0021	24.9	1.52						
^{90}Sr	B08	43	0.0176	20.8		0.957	0.0009	31.32	0.238	2.791	0.774
	B11	57.8	0.0013	16.5		0.429	0.0013	28.86	0.382	1.791	0.880
^{137}Cs	B07	67.1	0.0008	119.1			0.008	138.75	0.313	4.275	0.970
	B10	94.3	0.0012	67.7			0.0012	151.97	0.255	4.485	0.923
^{233}U	B02	89.8	0.0017	1.6		0.675	0.017	2.73	0.409	1.105	0.990
	B03	104	0.0021	2		0.726	0.0021	3.30	0.406	1.388	0.985
^{239}Pu	B08	33.5	0.0009	>200	1.8	0.907					
	B11	10	0.0013	>200	2	0.964					
	B12	17.1	0.0018	>200	2						
	B13	24.1	0.0026	>200	2						
^{241}Am	B07	13.8	0.0029	>200	1.6						
	B10	9.0	0.0012	>200	1.7	0.815					

column tests were fit using the equilibrium, non-equilibrium and two-site/two-region models described in section 1.4.1. Of the three models tested the two-site/two-region model generally provided the best fit to the data based on the correlation coefficient (Tables 6 and 7). Therefore, the parameter estimates from both the equilibrium model, the simplest, and the two-site/two-region model, which provided the best fit, are presented for all column tests. Retardation of the radionuclides (excluding the enhanced mobility fractions of ^{60}Co, ^{239}Pu, and ^{241}Am) in basalt increased in the following order $^{3}H<^{233}U<^{90}Sr<^{60}Co<^{137}Cs<^{239}Pu$ and ^{241}Am.

In an attempt to account for activity not recovered in the column, effluent gamma scans of columns eluted with gamma-emitting radionuclides [^{60}Co (1.173 and 1.332 MeV), ^{137}Cs (0.662 MeV) and ^{241}Am(0.060 MeV)] were conducted. A gamma scan of the crushed basalt packed column eluted with ^{137}Cs and ^{241}Am is shown in Figure 9. The remaining scans are presented in Appendix G. ^{60}Co, ^{137}Cs, and ^{241}Am appear to be distributed throughout the crushed basalt columns.

3.1.1.2 *Interbed Material Packed Columns.* Again, channeling was not observed in the column runs reported here based on retardation factors estimated for ^{3}H. A typical ^{3}H breakthrough curve (BTC) is shown in Figure 10. The remaining ^{3}H BTCs are presented in Appendix E. A summary of the percent breakthrough, as well as the dispersion coefficient, D, and retardation factor, R, estimated by CXTFIT for each ^{3}H run is also listed in Appendix E.

Typical BTCs for ^{239}Pu, ^{137}Cs, and ^{233}U are presented in Figures 11-14. The remaining BTCs are presented in Appendix F. ^{233}U, which had a 95 percent, recovery was the only radionuclide observed in the column effluent at relatively high concentrations. Again, there was evidence for an enhanced mobility fraction. Small (<1%) but detectable amounts of ^{60}Co, ^{239}Pu, and ^{241}Am were observed in the column effluent within the first five pore volumes eluted. The transport of enhanced mobility fractions of ^{60}Co, ^{239}Pu, and ^{241}Am is consistent with observations of mobile fractions in crushed basalt packed columns. However, percent recovery in the mobile fraction for the three radionuclides in interbed material packed columns was smaller than in crushed basalt packed columns. The net concentrations of ^{90}Sr and ^{137}Cs in the colum effluent were

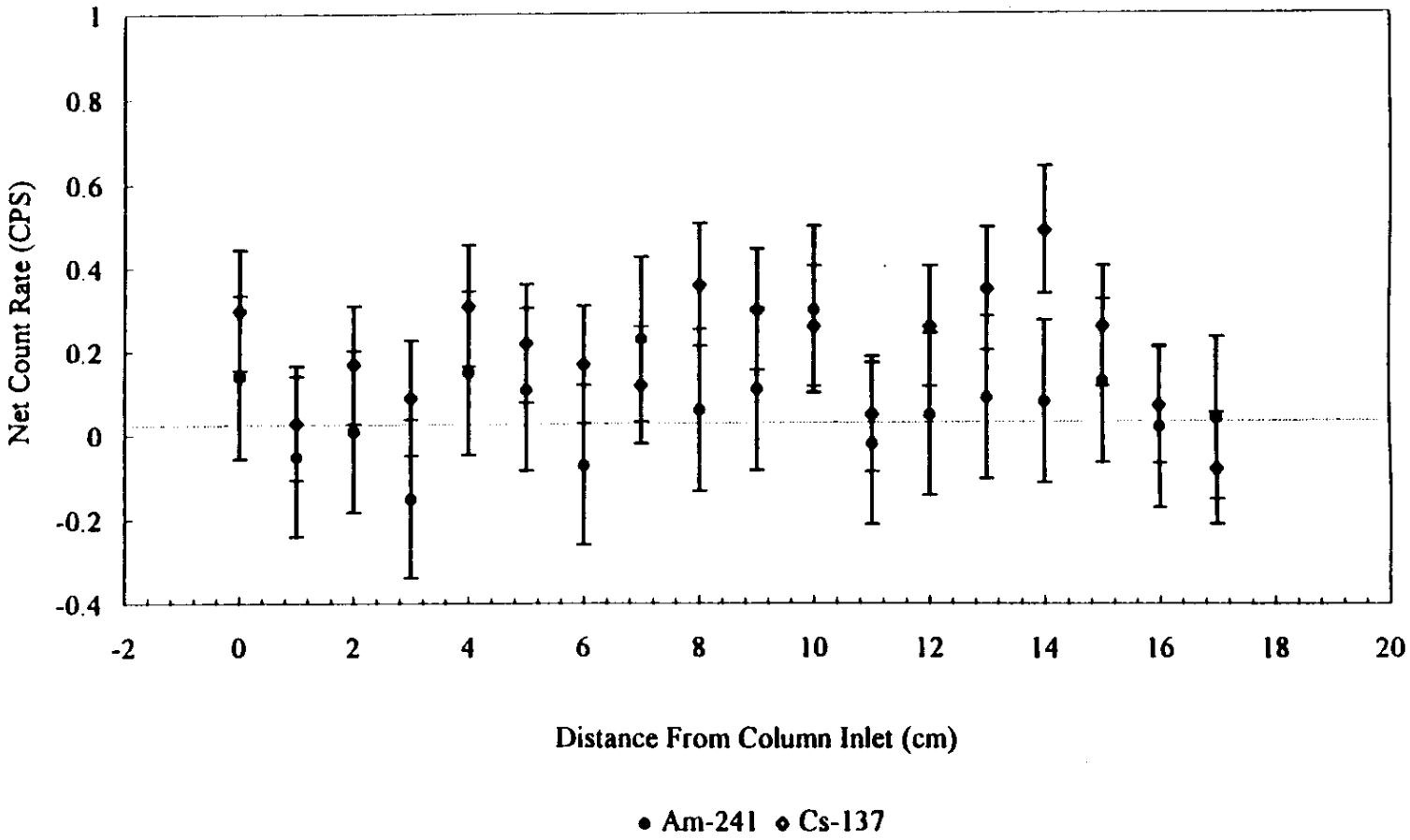

Figure 9. Distribution of 137Cs and 241Am activity in crushed basalt packed column B07 as determined by a gamma-scan.

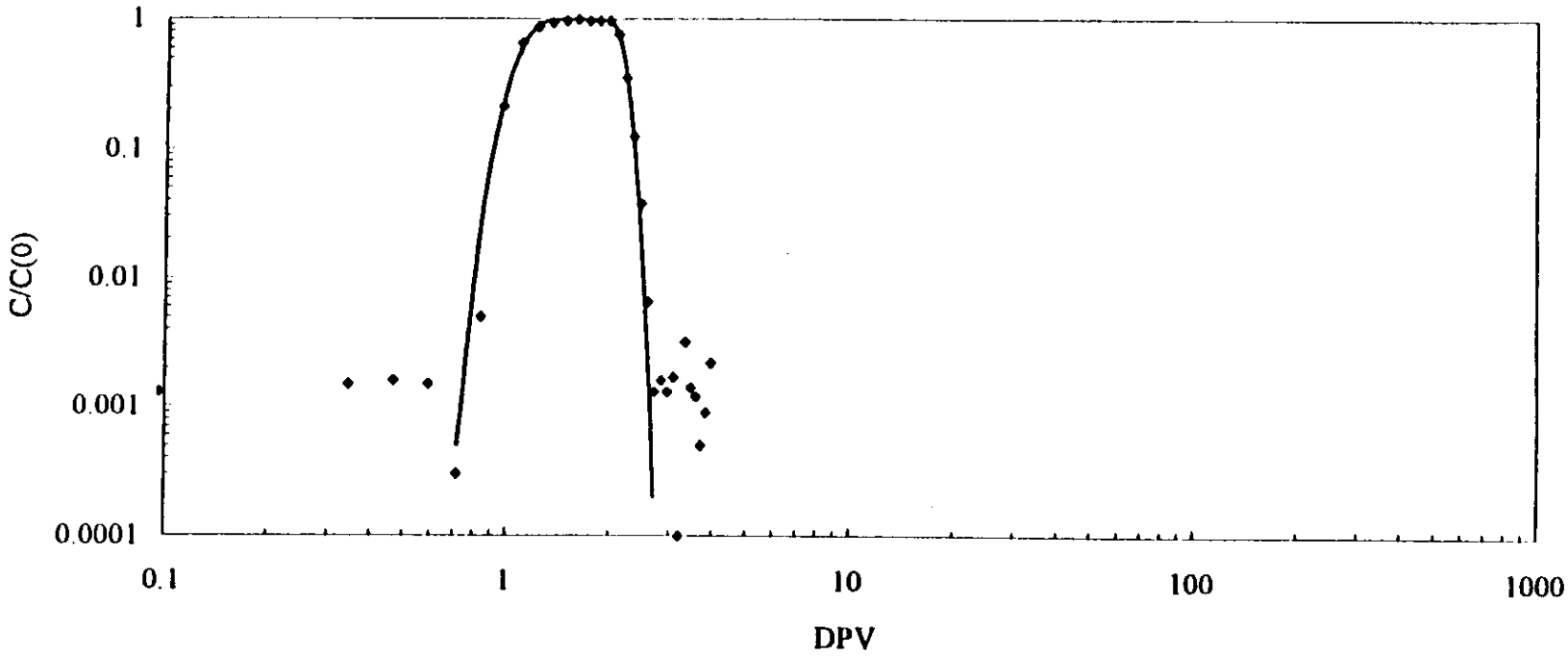

Figure 10. Breakthrough curve for ^{3}H (101.5% recovery) in interbed material packed column IB07 for a reduced pulse time of 1.14. The solid diamond shapes represent data points and the line represents the equilibrium CXTFIT model fit.

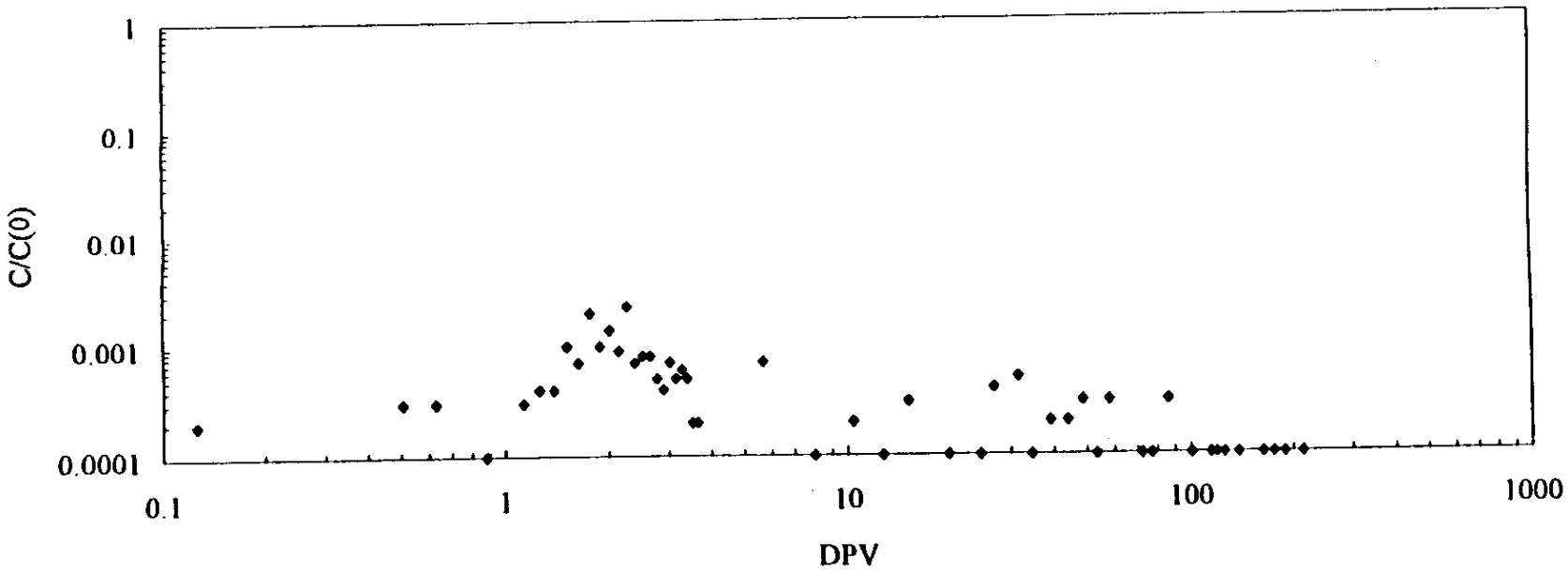

Figure 11. Breakthrough curve for ^{239}Pu (0.1% recovery) in interbed material packed column IB06. The solid diamond shapes represent data points and the line represents the equilibrium CXTFIT model fit.

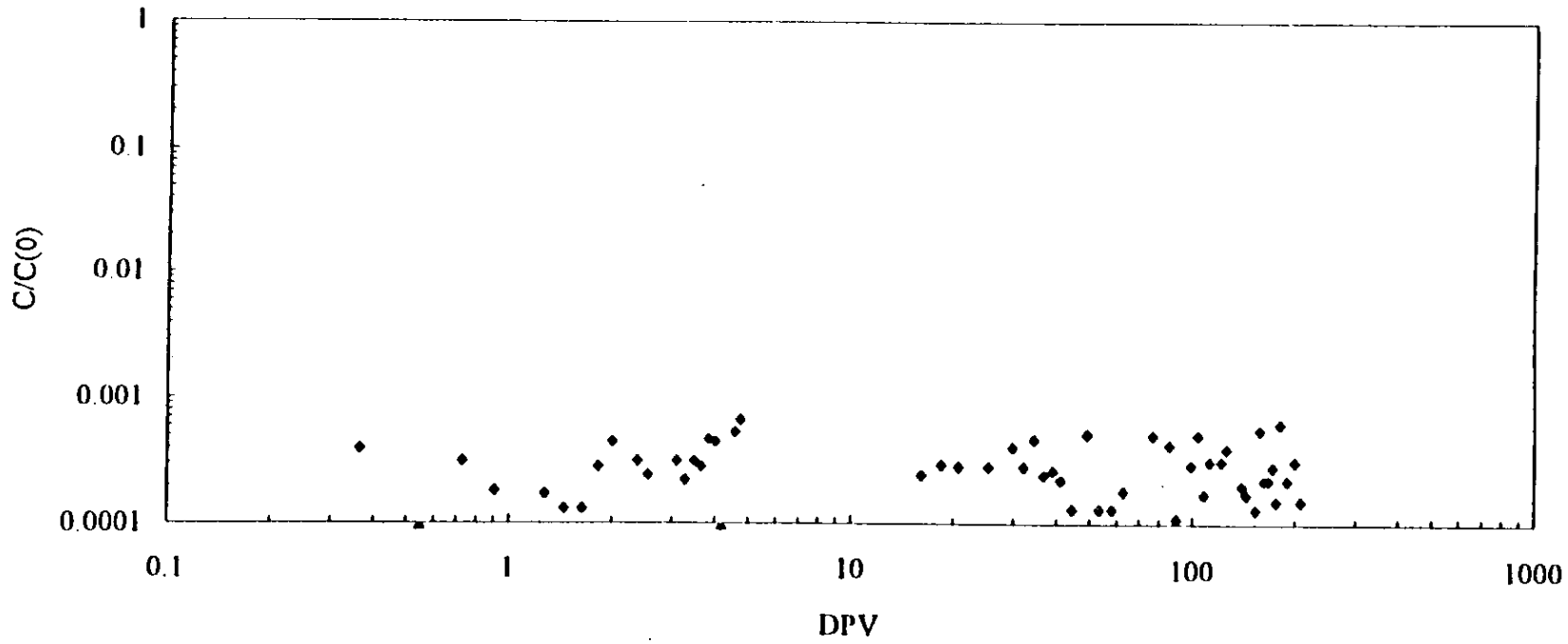

Figure 12. Breakthrough curve for ^{137}Cs (2.7% recovery) in interbed material packed column IB05. The solid diamond shapes represent data points and the line represents the equilibrium CXTFIT model fit.

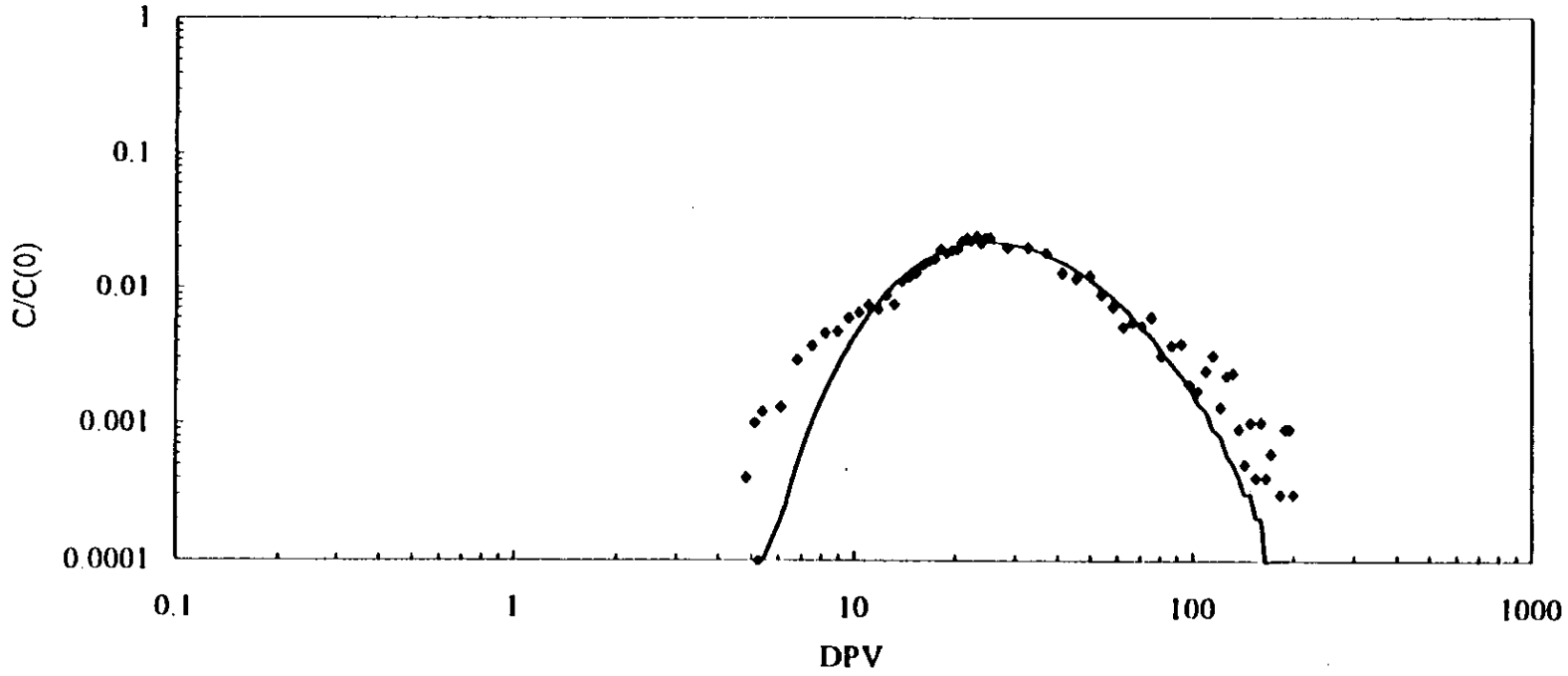

Figure 13. Breakthrough curve for ^{233}U (90.3% recovery) in interbed material packed column IB01. The solid diamond shapes represent data points and the line represents the equilibrium CXTFIT model fit.

were distributed about zero after background correction, indicating they were not present in the column effluent at concentrations above the detection limit.

The advective-dispersive model was only applied to the ^{233}U data because the percent recovery of the other radionuclides was too small to model. Percent recovery and parameter estimates based on CXTFIT are listed in Table 7. The lack of recovery of the other radionuclides in the column effluent after elution of 200 pore volumes implies a retardation factor greater than 200.

Again, in an attempt to account for activity not recovered in the column effluent, gamma scans of columns eluted with gamma-emitting radionuclides were conducted. A gamma scan of an interbed material packed column eluted with ^{137}Cs and ^{241}Am is shown in Figure 14. The remaining gamma scans are presented in Appendix G. ^{60}Co, ^{137}Cs, and ^{241}Am were concentrated within 3 cm of the interbed material packed column inlet.

3.1.2 *The Enhanced Mobility Fraction*

A fraction of ^{241}Am, ^{60}Co, or ^{239}Pu moving at a much faster rate than predicted by use of a single, equilibrium based, distribution coefficient may significantly alter predicted arrival times and peak concentrations of these three radionuclides downgradient from their source. Enhanced transport may change risk calculations or the importance of perceived risk. Consequently, the frequency and magnitude of enhanced transport, as well as the mechanisms controlling enhanced transport were explored.

The enhanced mobility fraction observed in column tests was greatest for plutonium. Therefore, initial efforts to elucidate the mechanism causing this enhanced transport were directed at plutonium. Studies were performed to test each of the three possible mechanisms for enhanced mobility identified in section 3.1.1.1. Oxidation state analyses of plutonium equilibrated with synthetic groundwater showed that colloidal plutonium can be formed under the conditions in the INEL subsurface (see section 3.1.3 of this report). Also, Estes and McCurry (1994) found 2.3 to 9.8 ppm of colloidal material (< 0.45 μm) in three wells near the Idaho Chemical Processing Plant. This colloidal material was made up primarily of calcium, magnesium, and silica. Both plutonium (Choppin and Stout, 1989) and americium (Moulin et al., 1991; Nash et al., 1988) have been shown to sorb strongly to silica. Both of these facts support but do not

Table 7. Results of Fitted Parameter and Percent Recovery for Interbed Material Packed Column Tests at Clemson University

			Equilibrium Model				Two Site/Two Region Model				
Isotope	Column ID	Percent Recovery	D (cm^2/sec)	R	Enhanced Mobility Fraction	r^2	D (cm^2/sec)	R	θ_{im}	α	r^2
^{60}Co	IB01	0.88		>200	*						
	IB02	3.8		>200	*						
^{90}Sr	IB06	0.0		>200							
	IB07	0.0		>200							
	IB09	0.0		>200							
^{137}Cs	IB05	2.7		>200							
	IB08	0.0		>200							
^{233}U	IB01	90.3	0.0219	43.4	0.971		0.0008	37.92	0.2015	5.659	0.94
	IB02	98.7	0.0121	30	0.949		0.0005	33.44	0.44055	2.950	0.952
^{239}Pu	IB06	1.1		>200	*						
	IB07	0.58		>200	*						
	IB09	1.35		>200	*						
^{241}Am	IB05	1.8		>200	*						
	IB08	1.9		>200	*						

* Enhanced transport was observed. However, the mobile fraction (~1%) was too samll to model using CXTFIT.

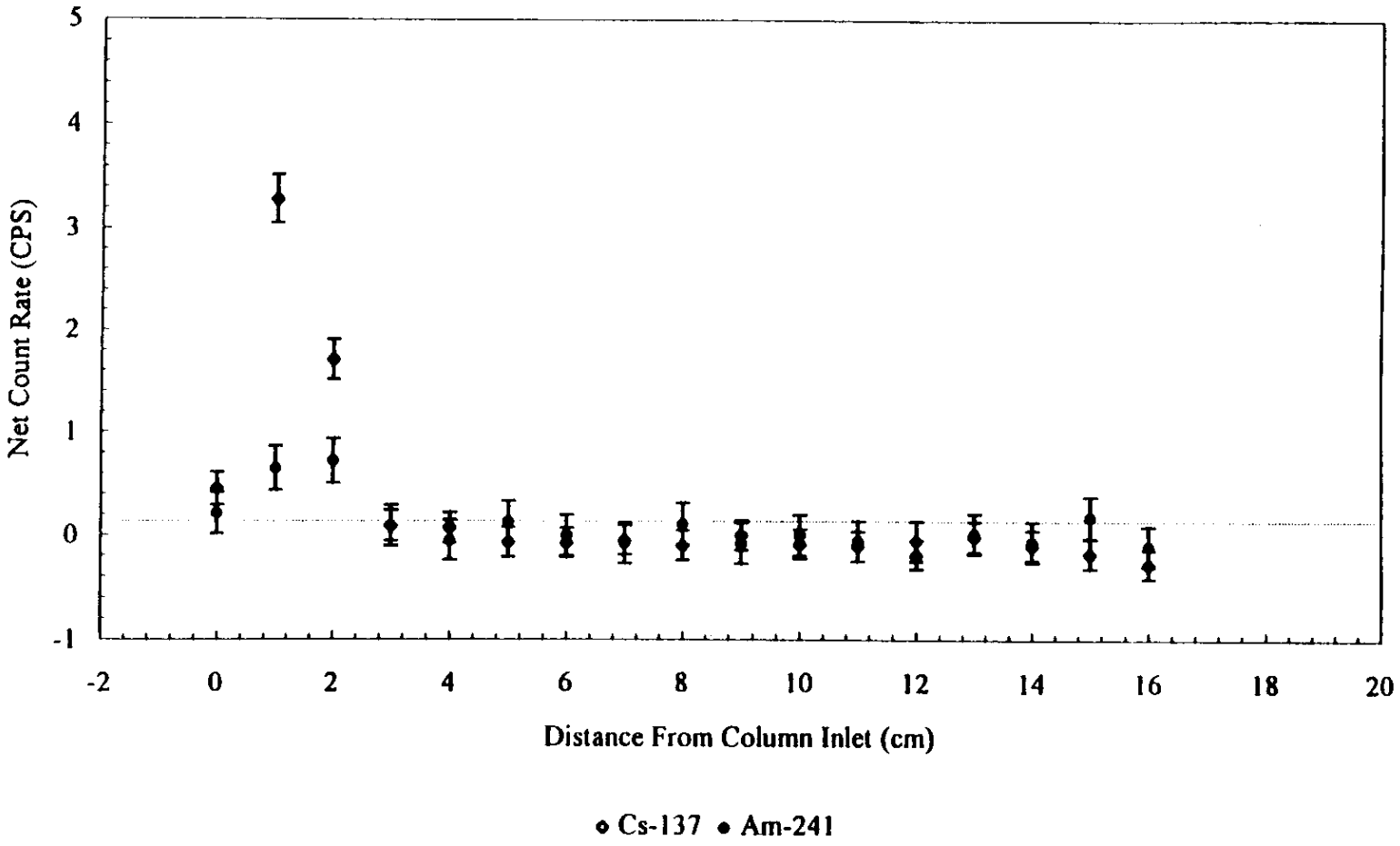

Figure 14. Distribution of ^{137}Cs and ^{241}Am activity in interbed material packed column IB05 as determined by a gamma-scan. The diamond shapes represent data points and the error bars represent the variation between replicate analyses.

prove the hypothesis of colloid associated transport as a mechanism for the observed enhanced transport.

In order to examine the possibility of enhanced transport due to the formation of negatively charged carbonate complexes, the total alkalinity of the plutonium spiked synthetic groundwater applied to a crushed basalt packed column was varied. The results of this study are presented in Figure 15. An increase in total alkalinity from 0.05 to 1.1 g/L as $CaCO_3$ increased the apparent enhanced mobility fraction from 52.2 to 78.0%. This supports the hypothesis that carbonate complexation may result in enhanced transport of plutonium.

Finally, the effect of flowrate on enhanced transport of americium was examined. Figure 16 shows americium breakthrough in the column effluent at varying flowrates. An increase in flowrate from 0.1 mL/min to 10 mL/min increased the apparent enhanced mobility fraction from 1.3 to 42.9%. Increased flowrates may increase the mass of mobilized colloidal material and/or reduce the fraction of contaminant which is in equilibrium with the solid surfaces (by decreasing the contact time).

Although these initial studies indicate enhanced transport can occur in laboratory columns, they do not clearly elucidate either the mechanism(s) causing the apparent enhanced transport or the significance of this phenomena under field conditions. Further study is needed in this area in order to provide an effective assessment of the frequency and magnitude of enhanced transport and resulting risk.

3.1.3 *Initial Batch Test*

Typical batch test results for ^{60}Co, ^{137}Cs, and ^{233}U with crushed basalt and interbed materials are presented in Figures 17-22. The remainder of the batch tests results are presented in Appendix H. Distribution coefficients were determined from partitioning of the radionuclide at 400 hours and from first-order and dual rate models. Results are presented in Table 8. Distribution coefficients based on concentrations at 400 hours were generally higher than values determined from the other two methods. The dual rate model appears to provide a better approximation to the data than the single rate model (see Figures 17-19), indicating heterogeneity among sorption sites. It appears that incorporation of an additional rate may be needed to explain ^{60}Co sorption to interbed

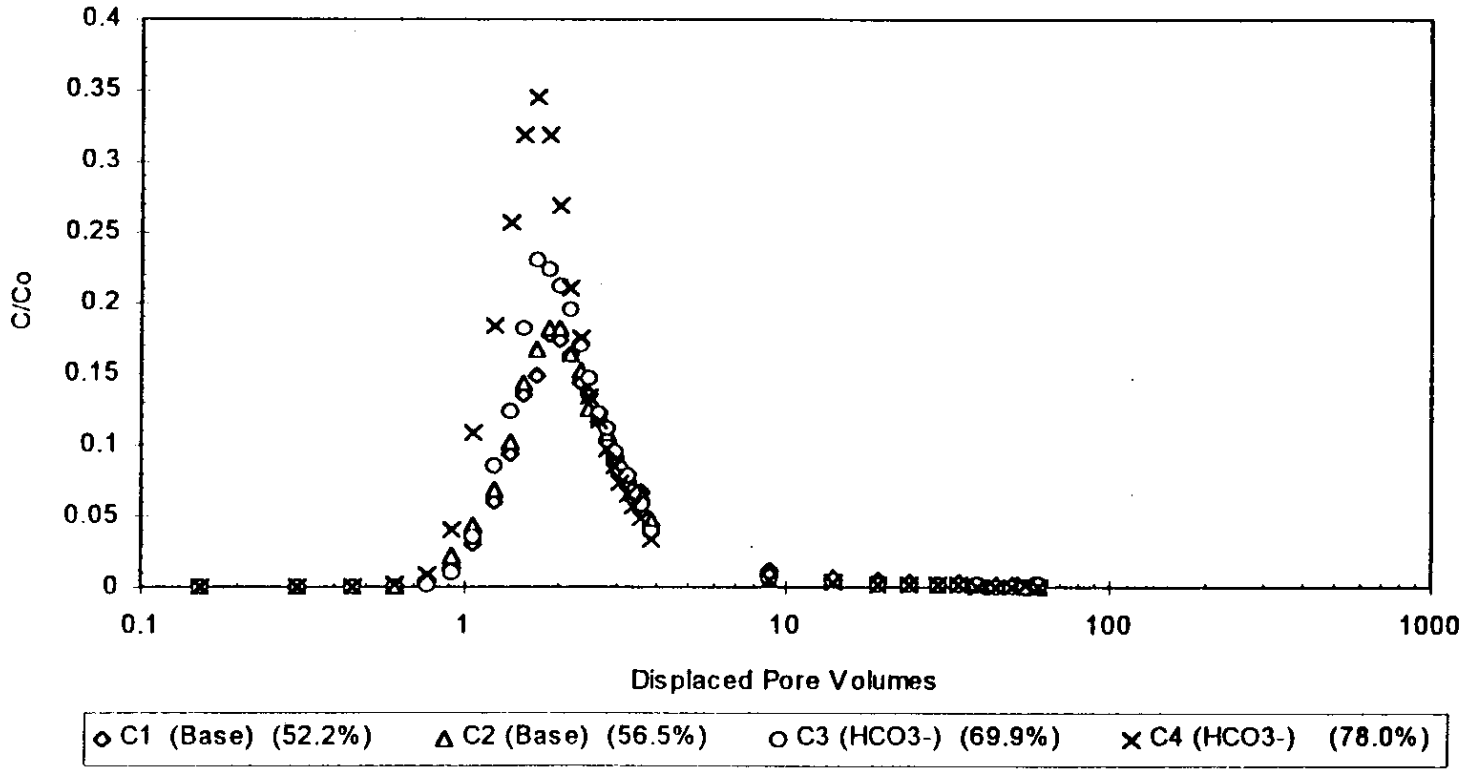

Figure 15. Enhanced breakthrough of ^{239}Pu at varying eluent total alkalinity (0.05 to 1.1 g/L as $CaCO_3$).

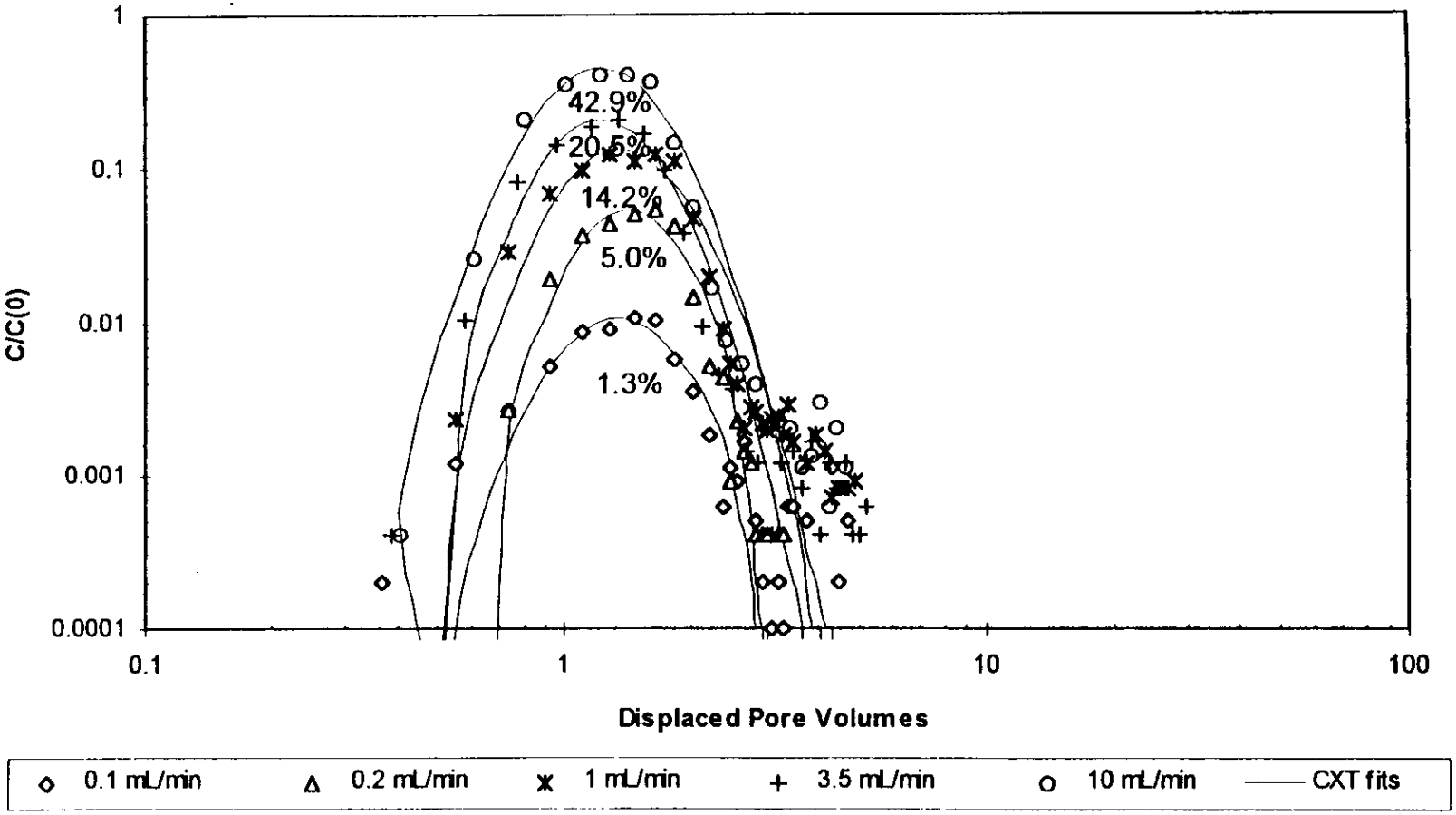

Figure 16. Enhanced breakthrough of ^{241}Am at varying flowrates (0.1 to 10 mL/min). The lines represent the fit of the equilibrium CXTFIT model.

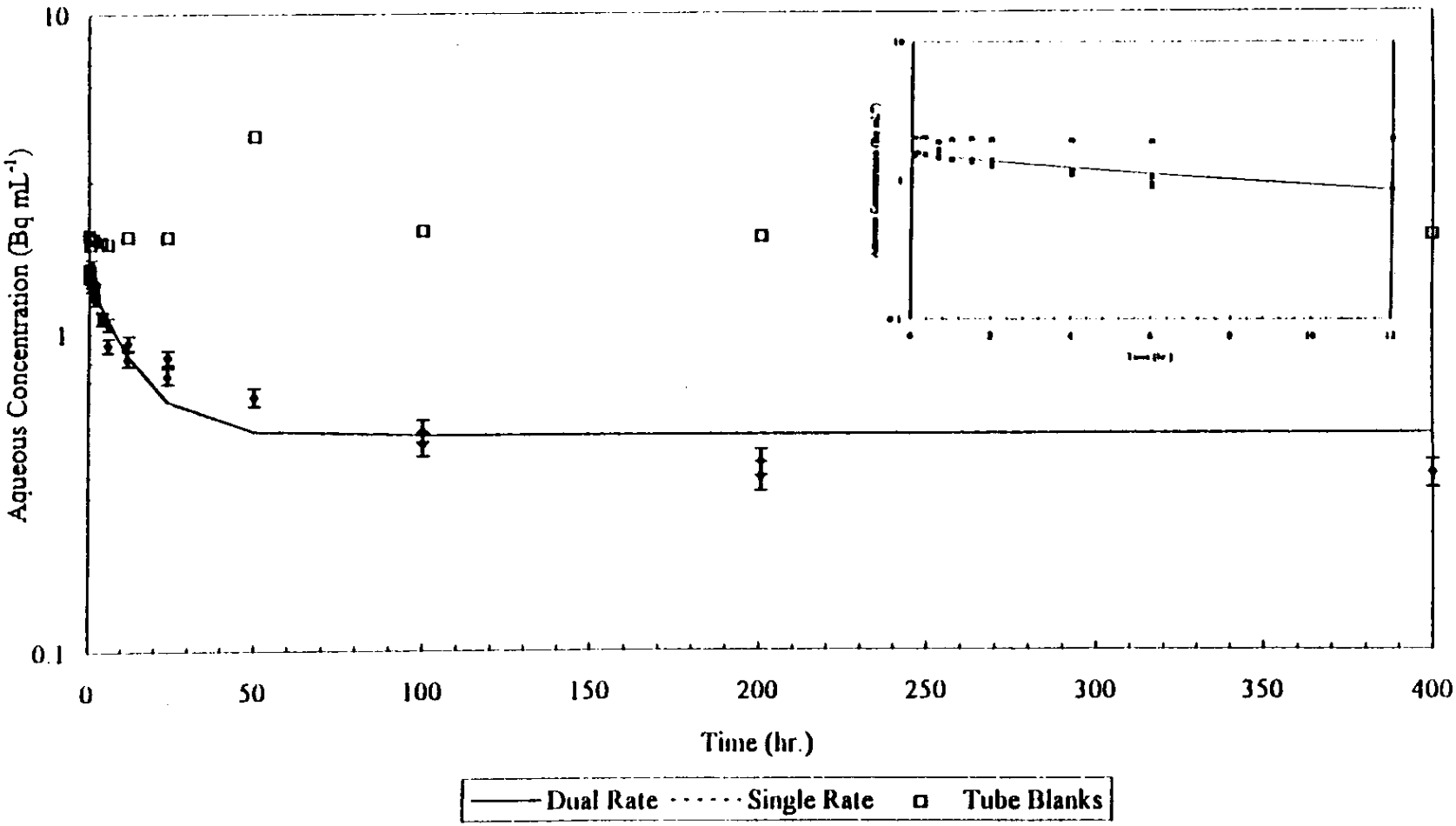

Figure 17. Aqueous phase concentration of ^{60}Co as a function of time in a crushed basalt batch test. The solid diamond shapes represent data points and the error bars represent the variation between replicate analyses.

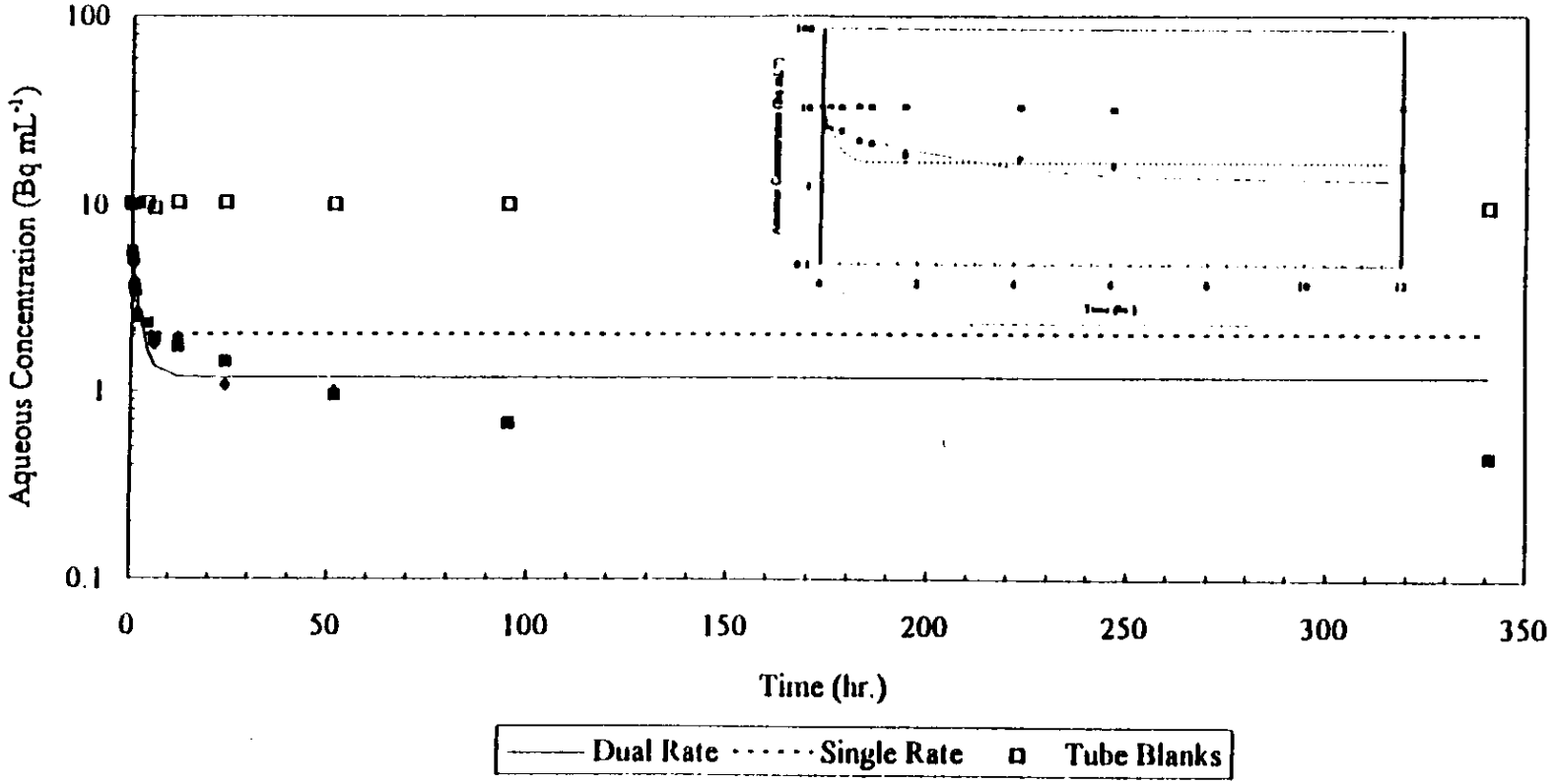

Figure 18. Aqueous phase concentration of ^{137}Cs as a function of time in a crushed basalt batch test. The solid diamond shapes represent data points and the error bars represent the variation between replicate analyses.

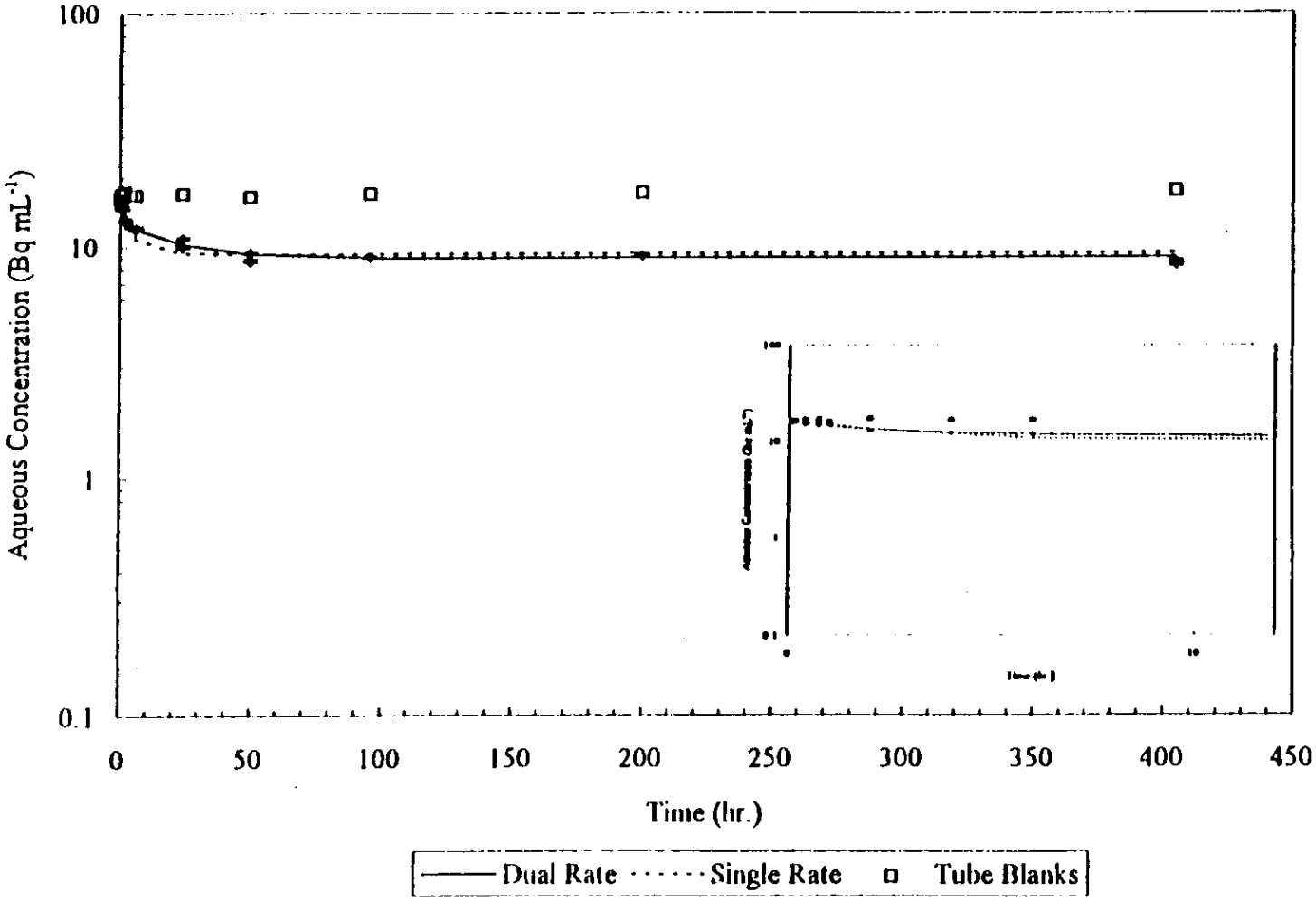

Figure 19. Aqueous phase concentration of ^{233}U as a function of time in a crushed basalt batch test. The solid diamond shapes represent data points and the error bars represent the variation between replicate analyses.

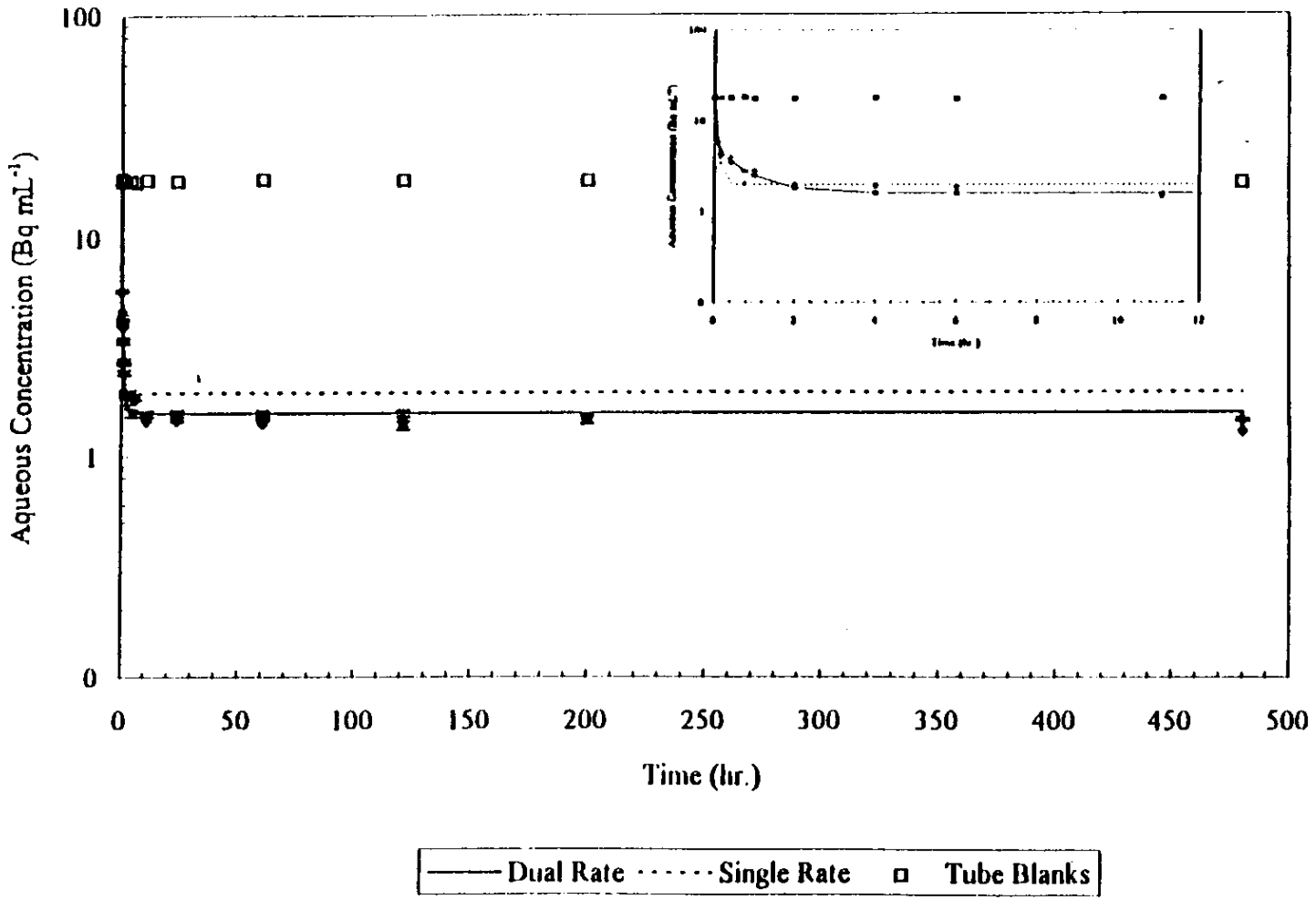

Figure 20. Aqueous phase concentration of ^{60}Co as a function of time in interbed material batch test. The solid diamond shapes represent data points and the error bars represent the variation between replicate analyses.

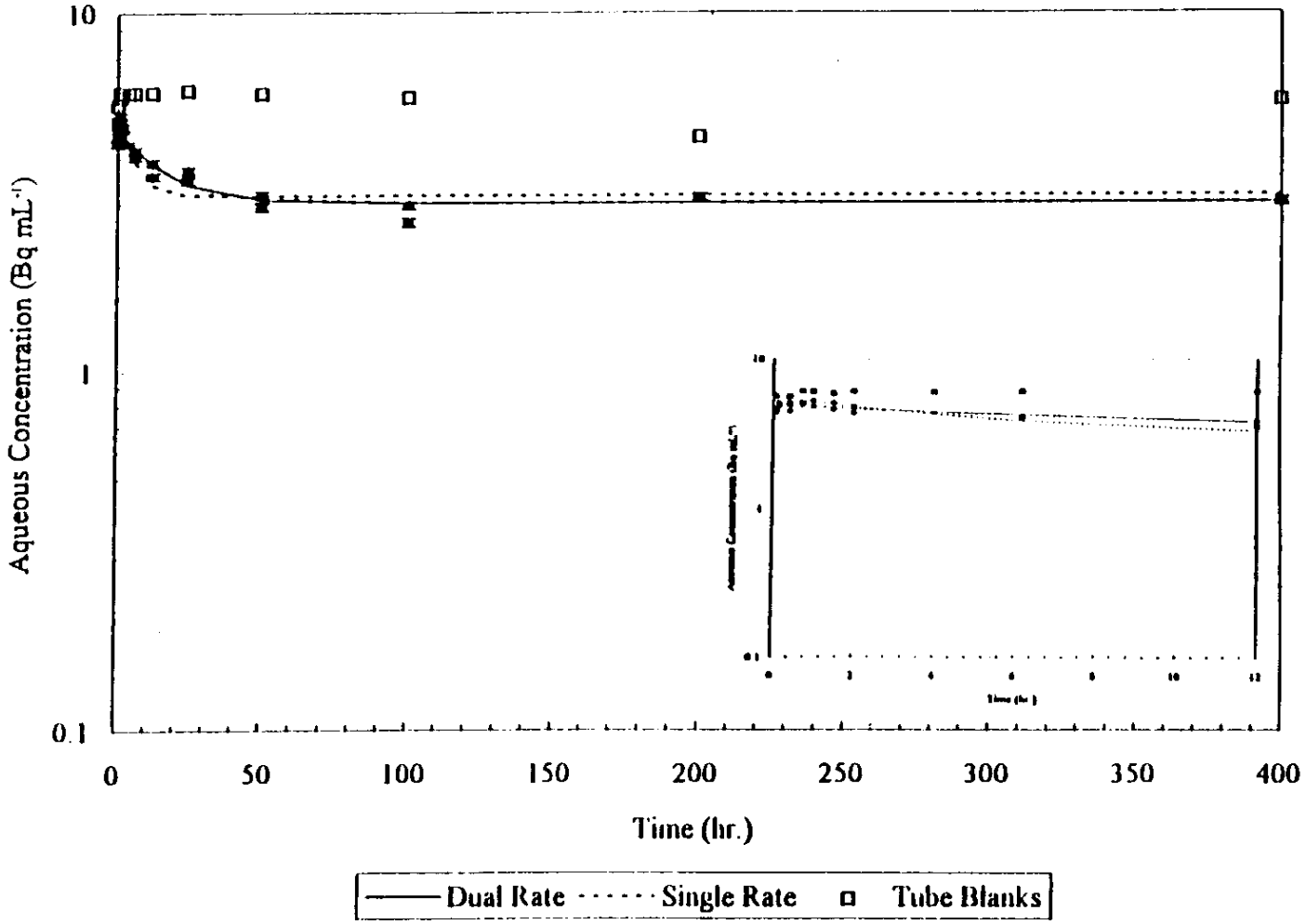

Figure 21. Aqueous phase concentration of ^{137}Cs as a function of time in an interbed material batch test. The solid diamond shapes represent data points and the error bars represent the variation between replicate analyses.

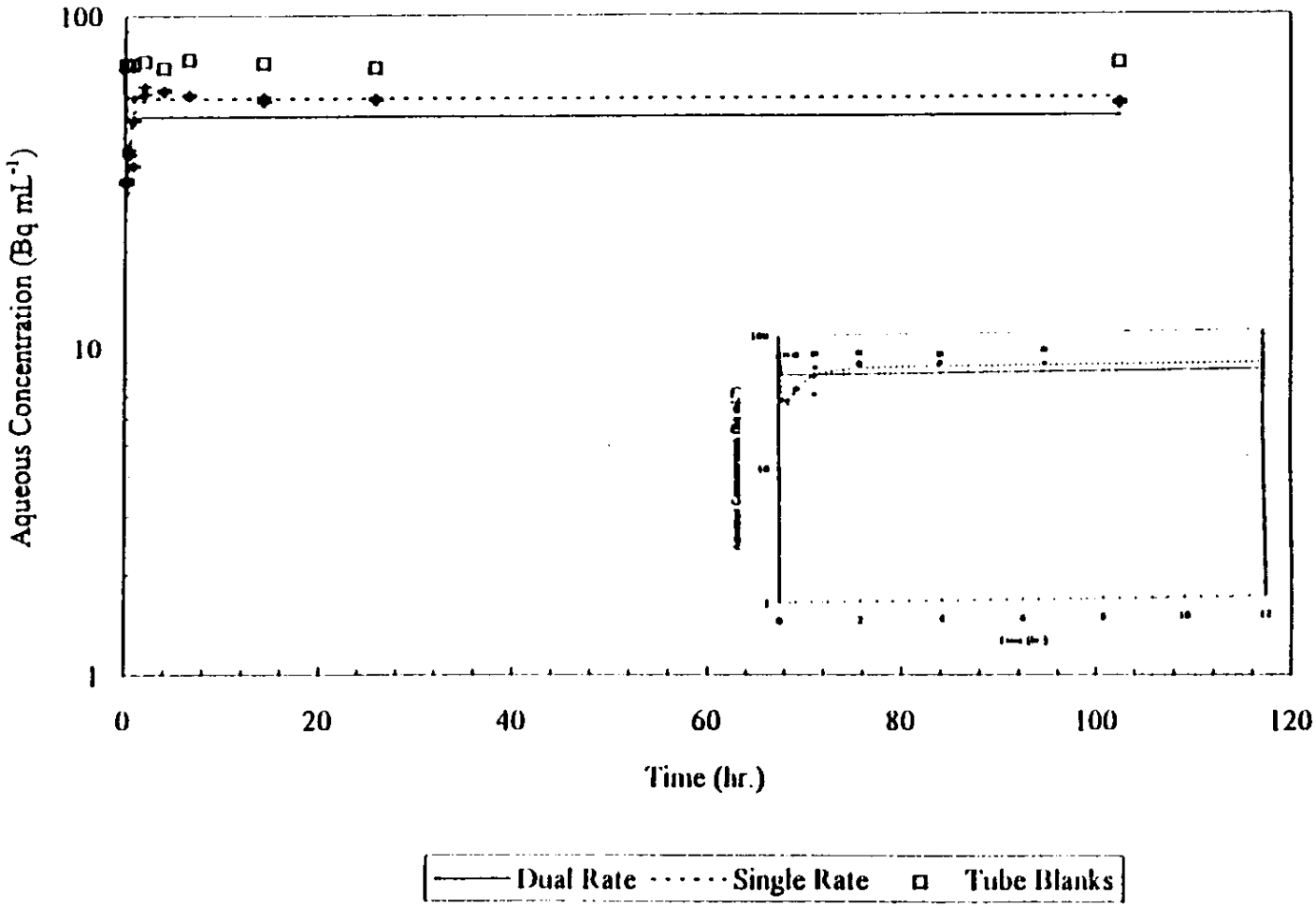

Figure 22. Aqueous phase concentration of ^{233}U as a function of time in an interbed material batch test. The solid diamond shapes represent data points and the error bars represent the variation between replicate analyses.

Table 8. Summary of Experimental Conditions and Model Results for Batch Studies Conducted at Clemson University Where the K_d is Determined from the Mass Balance, the Singel Rate, and the Dual Rate Models.

		Equilibrium Mass Balance				Langmuir First-Order Rate			Two Box, Dual First-Order Rates				
Isotope	Media	C(0) (Bq/mL)	C(t) (Bq/mL)	K_d (mL/g)	SS (g/L)	C(0) (Bq/mL)	K_d (mL/g)	α (hr)	K_d (mL/g)	λ_1 (hr)	λ_2 (hr)	τ (hr)	Final pH
^{60}Co	Basalt	1.57	0.47	53.6	64.5	1.55	30.4	0.033	36.5	0.086	0.001	71	7.93
^{60}Co	Interbed	10.1	0.68	3912	3.49	10.1	1148	6.15	2158	315	0.537	8	8.16
^{90}Sr	Basalt	18.3	12.9	12	34.4	18.3	9	0.820	12.9	1.15	0.0087	329	8.01
^{90}Sr	Interbed	15.2	12.9	63	3.3	15.2	41.9	0.438	56.3	0.84	0.008	219	8.06
^{137}Cs	Basalt	16.6	8.7	41	20.3	16.6	38.5	0.258	42.9	0.669	0.044	87	7.85
^{137}Cs	Interbed	17.2	1.4	3255	3.47	17.1	2228	14.40	2978	26.85	1.37	4	8.01
^{233}U	Basalt	5.94	3.1	4.7	200	5.6	4.4	0.084	5.2	24.5	0.065	61	7.79
^{233}U	Interbed	69.05	51	5.1	6.8	69.1	3.4	2.20	6.0	149.9	0	103	8.23
^{241}Am	Basalt	1.38-7.34		70-280	12.5								
^{241}Am	Interbed	3.5-15		450-1100	2.5								

SS = Suspended Solids Concentration

$K_d = (C_i-C_f)V/(mC_f)$

τ = Time to within 1% of equilibrium

α, λ_1, λ_2 = Reaction rate constants

(Figure 17). This observation may be due to a change in the redox state of cobalt possibly mediated by a subsurface component.

Generally, the sorption rate constant was larger with interbed than basalt. ^{90}Sr appeared to sorb slowly to both basalt and interbed. This apparent slow sorption may have been caused by large amounts of naturally occurring strontium in the basalt and interbed material which reached equilibrium with the synthetic groundwater during the washes prior to spike addition (Ames and Rai, 1978).

3.1.4 *Plutonium Oxidation States*

Because of its important role in subsurface transport, plutonium oxidation states were measured in the synthetic groundwater solution. This was accomplished by allowing plutonium to equilibrate in the synthetic groundwater solution for 14 days and monitoring the oxidation state(s) over time. The results from this equilibration are shown in Figure 23. Within the first 24 hr. the majority of plutonium remaining in solution was Pu(V) with smaller amounts of Pu(IV), Pu(VI), and Pu(III). Also within this time frame the total plutonium activity in the solution phase decreased to 60 to 70% of the initial value, due primarily to a decline in Pu(IV). However, when the container was shaken at the end of the 14 day period, the solution phase activity increased to 90% of the initial value. Thus, the initial decline in solution phase activity was attributed to settling of polymerized or precipitated Pu(IV). The distribution of plutonium between the oxidation states remained relatively constant throughout the remainder of the 14 day period.

These results indicate that colloidal plutonium can be formed under the conditions in the INEL subsurface. Also, because the majority of Pu(IV) was removed from solution by polymerization or precipitation, Pu(IV) is not expected to be mobile (other than possibly through colloidal transport) and a distribution coefficient is not appropriate for this form of plutonium. Therefore, it was decided to concentrate on determining distribution coefficients for Pu(V) and (VI), the forms of plutonium expected to predominate in solution and to be most mobile.

Batch tests as described in sections 2.4 and 2.5 of this report were used to determine distribution coefficients for Pu(V) and Pu(VI). The results (Table 9) at the highest suspended solids concentrations are highlighted because they most closely

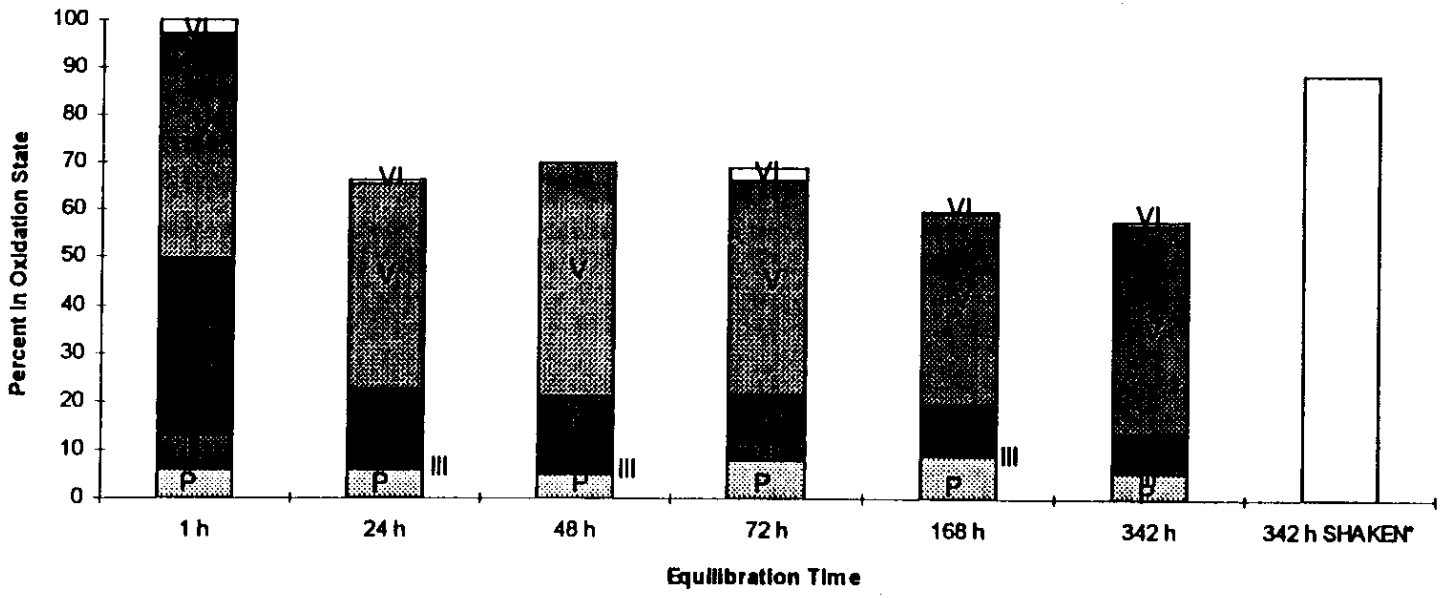

Figure 23. Oxidation state of plutonium during a 14 day equilibration in synthetic groundwater (pH 8). The decrease in total plutonium activity with time is attributed to the settling of polymeric Pu(IV). When the reaction vessel was shaken at the end of the 14 days, the majority of the initial plutonium activity was recovered.

approximate subsurface conditions in the field. The following observations can be made regarding the magnitudes of the distribution coefficients. First, distribution coefficients were higher in surface soil (collected near the Radioactive Waste Management Area) and interbed material than in basalt. This was expected due to the higher content of clay, iron and manganese minerals in surface soils and interbed material which can sorb and/or reduce plutonium to the least mobile IV state. Second, results are consistent with the belief (Choppin, 1983) that Pu(VI) complexes most strongly with carbonate, which yields a negatively charged ion. Finally, plutonium K_d values were over an order of magnitude lower in the presence of EDTA. EDTA is a strong chelating agent that forms (negative or neutral) complexes with metals.

Table 9. Summary of Average Plutonium Distribution Coefficient Values

Media	Suspended Solids (mg/L)	Pu(V)	Pu(VI)	Pu(EDTA)
Basalt	50000	70	24	0.5
	100000	110	14	0.5
	300000	280	12	0.4
	500000	130	16	0.4
Interbed[1]	25000	6600	130	5
	50000	5100	110	5
	100000	7900	320	5
	150000	6400	690	4
Surface Soil[2]	25000	22000	4900	40
	50000	17000	4000	400
	100000	10000	2600	490
	150000	7800	1800	430

[1]Composite of 11 samples from 5 cores collected near the Radioactive Waste Management Complex

[2]Surface soil was collected near the Radioactive Waste Management Complex

An important observation was made regarding the oxidation state of the solution phase plutonium in interbed material batch tests. At the low suspended solids concentrations, plutonium remained in the initial state (either V or VI). However, at high suspended solids concentrations, transformation from V to IV and from VI to V and IV was observed. This was likely due to reduction mediated by iron and/or manganese minerals. Since actual solid to liquid ratios in the subsurface are much higher than those in

batch tests, it is likely that plutonium will be in reduced forms in the field, i.e. IV and V. Plutonium (IV), as discussed previously, does not stay in solution but tends to form polymers or precipitates, and to stick to surfaces. In this form it is highly immobile unless colloidal forms are transported.

3.1.5 *Effects of pH and Ionic Strength*

Both pH and ionic strength (I) are subject to variability due to subsurface heterogeneity and alteration by buried waste. Many researchers have reported pH and ionic strength effects on solution chemistry and sorption (Hawkins and Short, 1965; Dosch and Lynch, 1978; Rai and Serne, 1978; Bondietti, 1982; Bell and Bates, 1988; and Ticknor, 1993). Therefore, pH and ionic strength effects on the sorption of cesium and uranium to INEL subsurface materials were examined through a series of batch tests as described in section 2.4 of this report. The synthetic groundwater solution described in section 2.1 of this report was used as the "base" chemistry. The ionic strength of the synthetic groundwater was adjusted to 0.01 and 0.02 M by the addition of either KCl or $CaCl_2$. The initial pH of the synthetic groundwater was adjusted to 6 and 10 by the addition of either 0.1 N HCl or 0.1 N NaOH. Although the initial pH was adjusted to 6 and 10, at the conclusion of all experiments the pH of the aqueous phase was nearly 8. This suggests the subsurface materials beneath the SRP have a high buffering capacity.

3.1.5.1 <u>*Crushed Basalt.*</u> The effects of $[Ca^{2+}]$, $[K^+]$, and pH on cesium K_ds with basalt are illustrated in Figures 24 and 25. Based on visual examination of these figures there appears to be little, if any, effect of pH or $[Ca^{2+}]$ and a large effect of $[K^+]$. Significance, or p, tests with a confidence level of 0.05 verified this visual analysis. The null hypothesis that the K_d for a given aqueous phase chemistry was equal to that of the base chemistry failed to be rejected for $[Ca^{2+}]$ for all cases except pH 10 and I = 0.02 M. However, for $[K^+]$ the null hypothesis was rejected in all cases and it was concluded that K_d decreased at elevated $[K^+]$. For pH variation the null hypothesis failed to be rejected in all cases, and it was concluded that the K_d for cesium with basalt was not effected by variations in initial groundwater pH over the range tested. These observations are reasonable when examined with respect to the expected cesium speciation (see section 1.3.2 of this report). Cesium is generally found in solution as the monovalent cation, Cs^+,

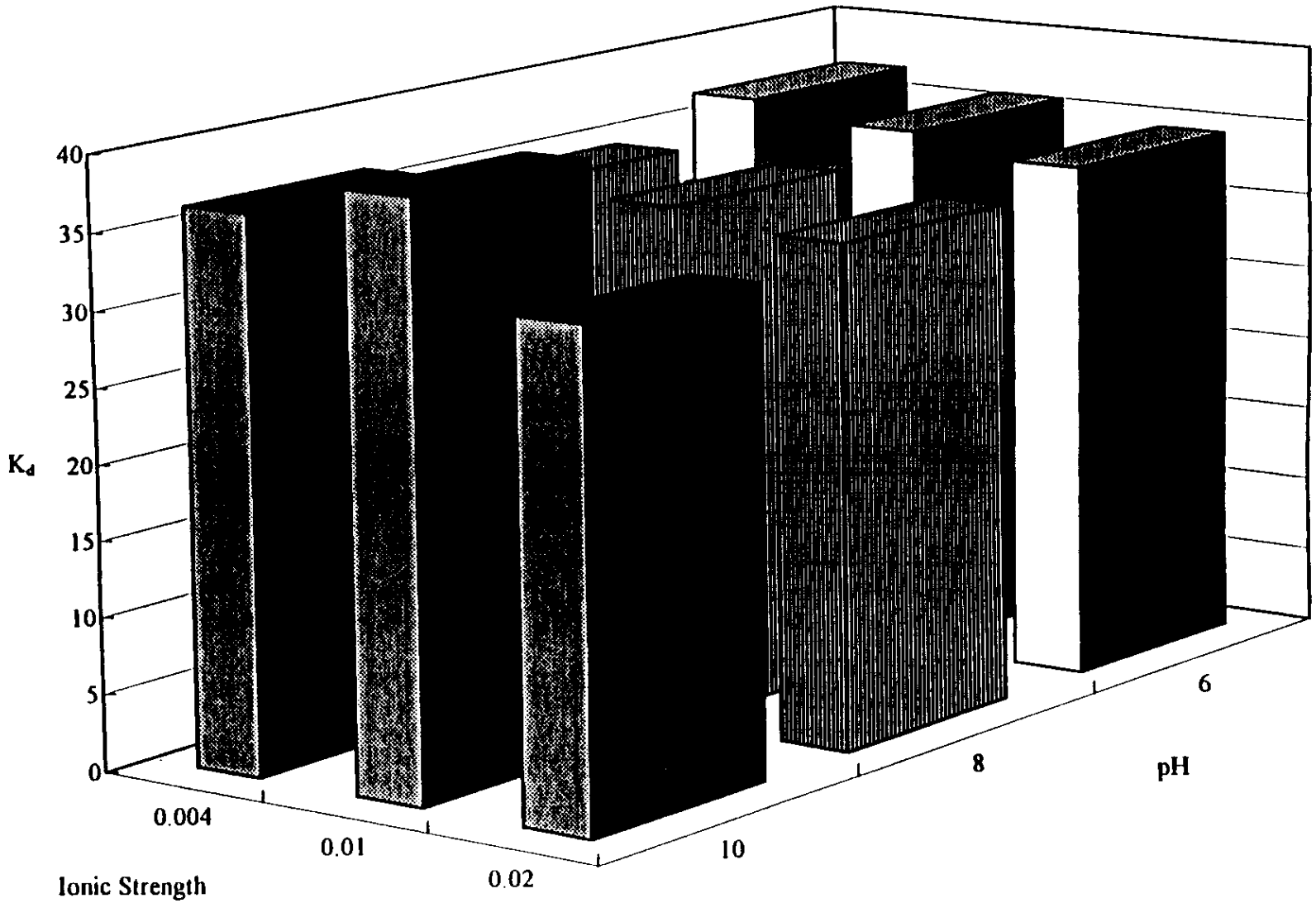

Figure 24. Cesium K_d's versus pH and ionic strength (controlled with Ca^{2+}) for crushed basalt.

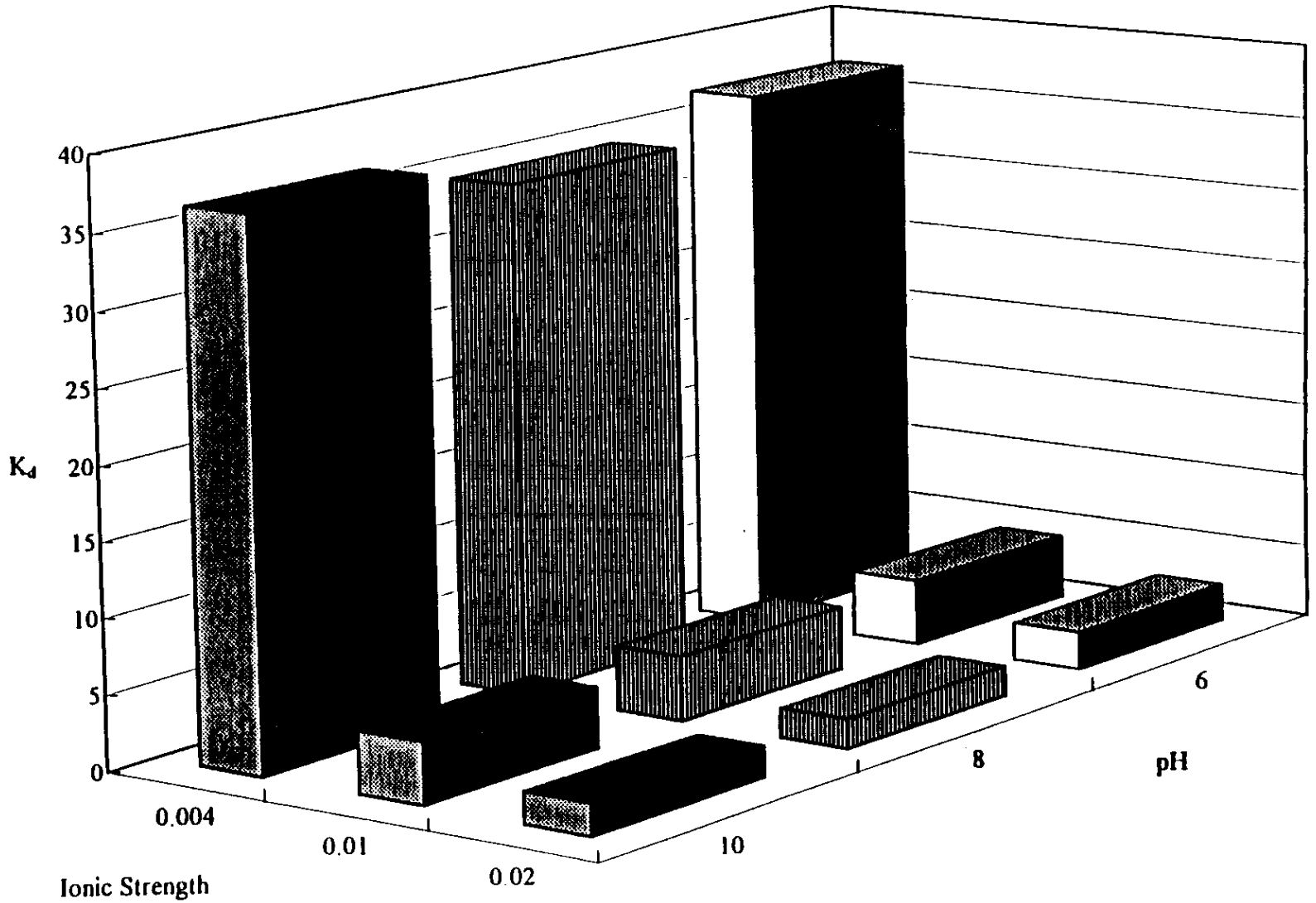

Figure 25. Cesium K_d's versus pH and ionic strength (controlled with K^+) for crushed basalt.

and the mechanism of cesium sorption is believed to be ion exchange. Therefore, K^+ is expected to compete with Cs^+ for sorption sites due to its similar charge and ionic radius.

The effects of $[Ca^{2+}]$, $[K^+]$, and pH on uranium K_ds with basalt are illustrated in Figures 26 and 27. Based on visual examination of these figures there appears to be some effect of pH, $[Ca^{2+}]$, and maybe $[K^+]$. Again p tests were used to verify this subjective judgment. The null hypothesis that the K_d for a given aqueous phase chemistry was equal to that of the base chemistry was rejected for all $[Ca^{+2}]$ except at pH 10. It was concluded that Kd decreased at elevated $[Ca^{2+}]$, except at pH 10, where elevated $[Ca^{2+}]$ had no effect. The null hypothesis failed to be rejected for all $[K^+]$, and it was concluded that the K_d of uranium with basalt was not affected by $[K^+]$. For pH variation the null hypothesis was rejected in all cases. These observations seem reasonable when examined with respect to the expected UO_2^{2+} speciation under these conditions (see section 1.3 of this document). The uranyl cation complexes strongly with carbonate. The concentration of carbonate in solution increases as pH increases. Thus, the K_d of uranium is expected to decrease with increasing pH. Also, because Ca^{2+} and UO_2^{2+} have similar charges, Ca^{2+} is expected to compete with UO_2^{2+} for adsorption sites. However, at pH 10, UO_2^{2+} is no longer found as the free cation but is complexed with carbonate and therefore $[Ca^{2+}]$ no longer affects the K_d.

3.1.5.2 *Interbed Material.* The effects of $[Ca^{2+}]$, $[K^+]$, and pH on cesium K_ds with interbed material are illustrated in Appendix I. For all $[Ca^{2+}]$ the null hypothesis that the K_d for a given aqueous phase chemistry was equal to that for the base chemistry failed to be rejected, while for all $[K^+]$ the null hypothesis was rejected. It was concluded that $[Ca^{2+}]$ had no effect on the K_d of cesium with interbed material while K_d decreased with increasing $[K^+]$. For all pH values tested the null hypothesis failed to be rejected and it was concluded that the K_d of cesium with interbed material was not affected by variations in initial groundwater pH. These observations agree with those observed for basalt and the expected speciation of cesium.

The effects of $[Ca^{2+}]$, $[K^+]$, and pH on uranium K_ds with interbed material are illustrated in Appendix I. For all $[Ca^{2+}]$ and $[K^+]$ the null hypothesis that the K_d for a

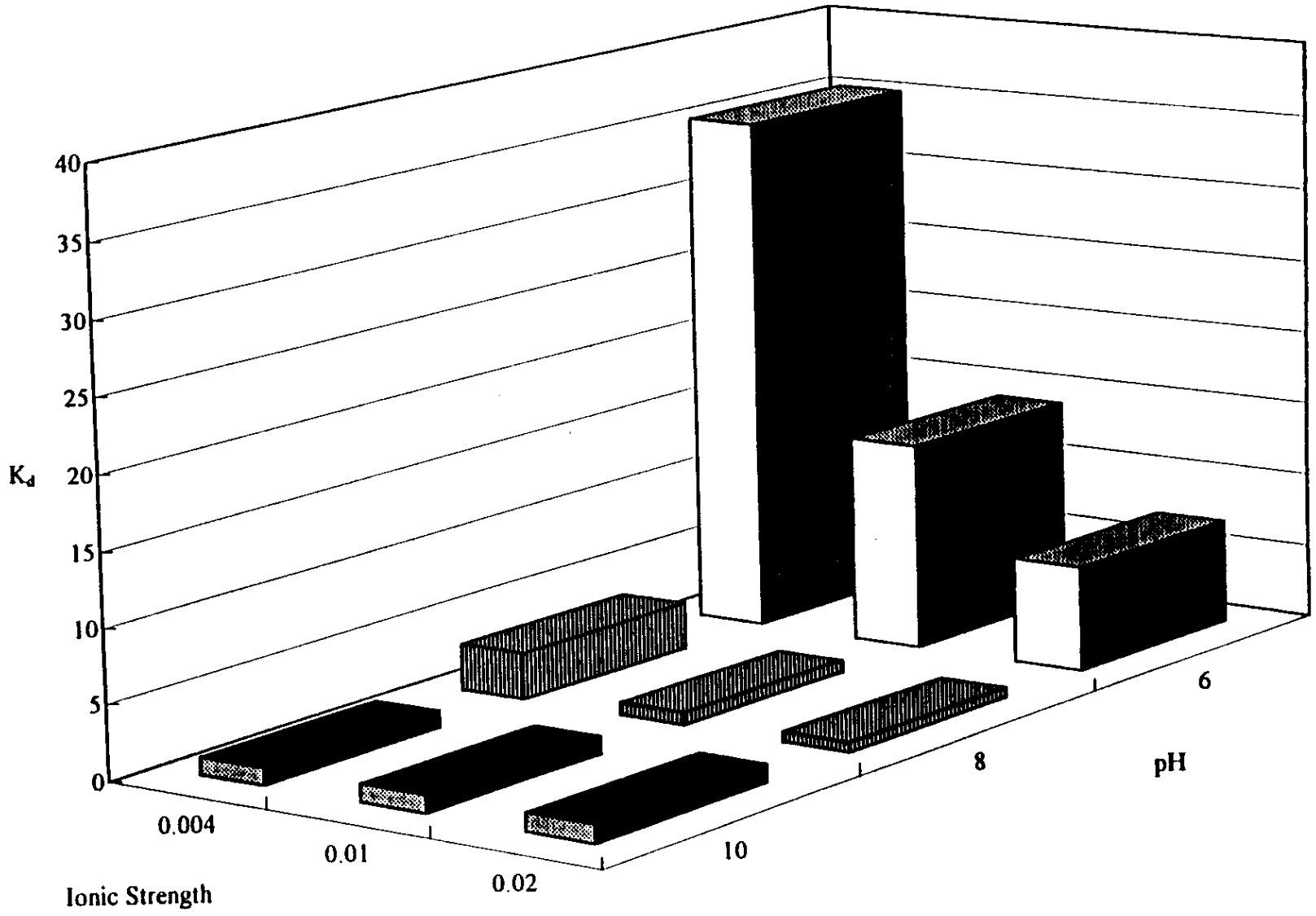

Figure 26. Uranium K_d's versus pH and ionic strength (controlled by Ca^{2+}) for crushed basalt.

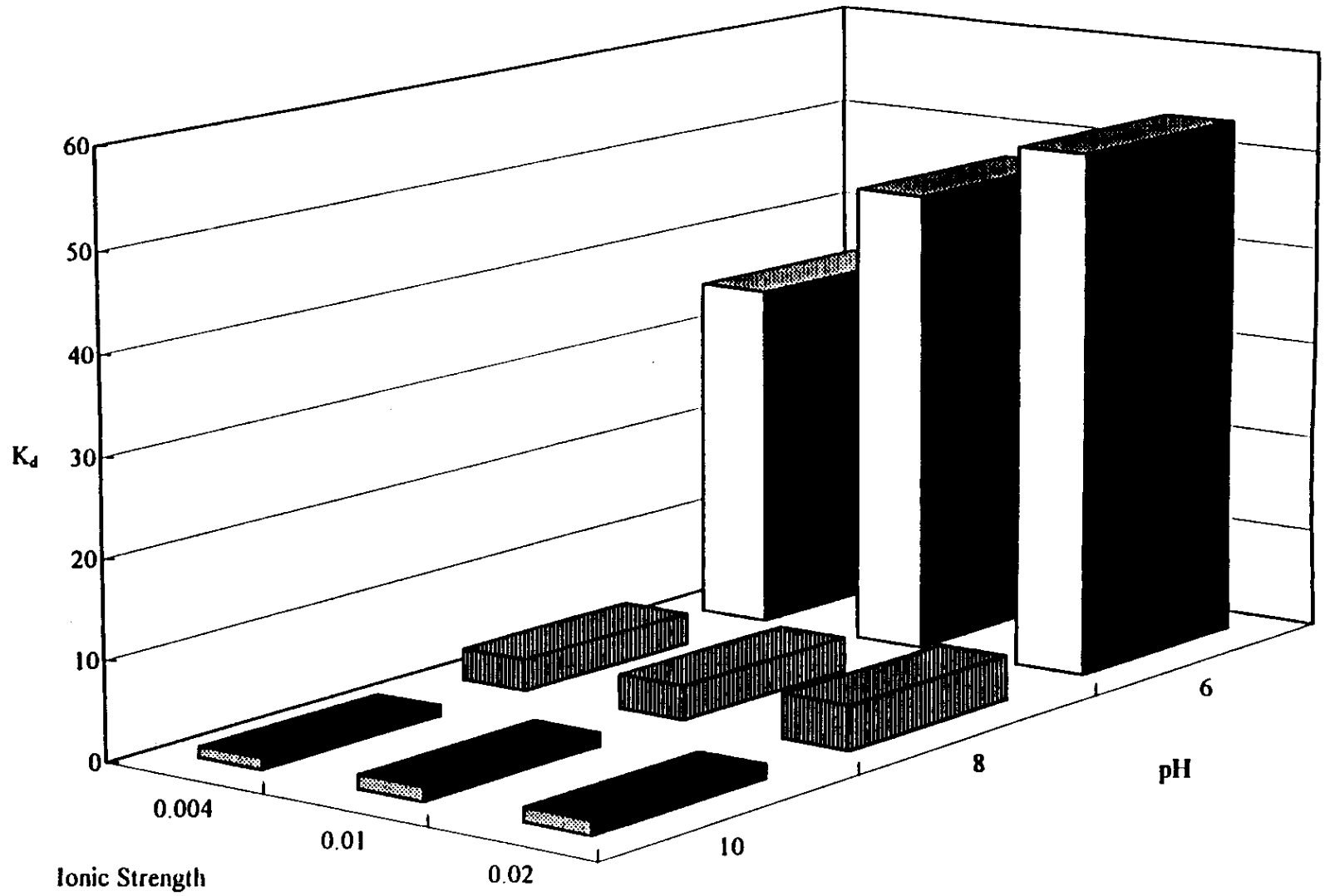

Figure 27. Uranium K_d's versus pH and ionic strength (controlled by K^+) for crushed basalt.

given aqueous phase chemistry was equal to that for the base chemistry was rejected, except at pH 10, and I = 0.02 M. It was concluded that K_d for U increased at elevated $[Ca^{2+}]$ and decreased at elevated $[K^+]$. These observations may result from the effects of Ca^{2+} and K^+ on the surface charge and structure of expandable clays. Ca^{2+} expands the space between the clay layers while K^+ reduces or collapses the space between the clay layers. The p tests for pH results were mixed. Although some statistically significant differences were observed, there were no consistent trends.

3.2 INEL Studies

3.2.1 *Comparison of Distribution Coefficients Determined at Clemson University and at the INEL*

Distribution coefficients for strontium with crushed basalt were determined at the INEL and CU using both batch and column methods to verify that results obtained at the two locations were comparable. Table 10 compares distribution coefficients obtained from saturated column tests at both the INEL and Clemson University. The differences observed in the column test distribution coefficients measured by the two laboratories can be solely attributed to the differing concentrations of strontium used by the two laboratories. Friedam and Kelmers (1990) observed the distribution coefficient to decrease at higher strontium concentrations. At the INEL a relatively high stable strontium concentration (500 μg/L) was necessary to insure adequate detection of the strontium spike above natural background strontium concentrations. CU was able to use much lower ^{90}Sr concentrations (3.6×10^{-3} μg/L) because ^{90}Sr is not naturally occurring. The distribution coefficients measured by the two laboratories are well within an acceptable range of agreement considering the 6 order-of-magnitude difference in the concentrations of strontium used. The concentration of strontium used by CU more closely approximates ^{90}Sr concentrations observed in the INEL subsurface.

Table 10. Comparison of Distribution Coefficients Measured Using Column Tests at the INEL and Clemson University

	INEL	Clemson University
Eluent Used	Synthetic Groundwater	Synthetic Groundwater
Solid Used	Crushed INEL Basalt	Crushed INEL Basalt
Packed Column Bulk Density	1.62-1.65 g/cm^3	1.50 g/cm^3
Packed Column Porosity	0.465-0.492	0.457

Initial Strontium Concentration, C(0)	500 µg/L	$3.6x10^{-3}$ µg/L (18.3 Bq/mL)
Measured Distribution Coefficient	3.37-3.68 mL/g	6.3-9 mL/g

Table 11 compares distribution coefficients obtained from batch tests at both the INEL and CU. Here, both the concentration of strontium and of suspended solids (34.4 g/L at CU, and 100 to 700 g/L at the INEL) varied between the two laboratories. Again, however, the distribution coefficients measured by the two laboratories are well within an acceptable range of agreement considering the differences in strontium and suspended solids concentration used by the two laboratories.

Table 11. Comparison of Distribution Coefficients Measured Using Batch Tests at the INEL and Clemson University

	INEL	Clemson University
Suspended Solids (g/L)	100-700	34.4
Initial Strontium Concentration, C(0)	500 µg/L	$3.6x10^{-3}$ µg/L (18.3 Bq/L)
Measured Distribution Coefficient	1.92-3.12 mL/g	9-12.9 mL/g

3.2.2 *Effects of the Solid/Liquid Ratio on Determination of Distribution Coefficients by Batch Methods*

It has been observed by other researchers that distribution coefficients measured in batch tests decrease as the suspended solids concentration used increases (DiToro and Horzempa, 1982; Voice et al., 1983). Several explanations have been proposed for this phenomenon. First, as suspended solids concentration is increased, all solid material may not be available for sorption due to the closer proximity of the solids, i.e. the ratio of available surface area to mass does not increase linearly with total solids concentration. Second, as the mass of solid increases, the time required to reach steady-state increases due to the increased time necessary for sorbing ions to diffuse into secondary pores and reach all available sites. If the experiment is not continued for a sufficient time, an apparent decrease in K_d with increasing solids concentration will result. Finally, the proportion of colloidal material increases as the total mass of solid increases. These colloids may not be removed from solution by standard filtration or centrifugation procedures and therefore will result in apparent decreases in K_d with increasing solids concentration. Because of the potential mechanisms discussed above and the fact that the

solid/liquid ratios used in batch tests are generally significantly lower than those observed in the field, there has been considerable debate concerning the representativness of batch test to field conditions. However, batch tests have the advantage of being a relatively fast and inexpensive technique, especially when strongly sorbing contaminants are of concern.

In order to test the applicability of batch tests for solid/liquid ratios observed in the field, we performed a series of batch tests with solid/liquid ratios varying from 1/10 (100 g/L) to 7/10 (700 g/L). A solid/liquid ratio of 7/10 corresponds to a porosity of approximately 0.3, which is representative of column tests (see Appendix B) and also corresponds to many unconsolidated field conditions. The distribution coefficients measured for the varying solid/liquid ratios are presented in Figure 28 and Table 12. The distribution coefficients measured at the varying solid/liquid ratios varied from 1.92 to 3.12 mL/g and did not show a clear trend with solid's concentration.

Table 12. Results from Batch Tests with Varying Crushed Basalt/Synthetic Groundwater Ratios

Crushed Basalt Added (g)	Synthetic Groundwater Added (mL)	[Sr] Added (μg/L)	Distribution Coefficient[1] (mL/g)
3.000	27	500	
3.000	27	500	2.845
6.000	24	500	
6.000	24	500	3.12
8.999	21	500	
9.001	21	500	3.09
12.000	18	500	
12.000	18	500	2.78
15.000	15	500	
14.998	15	500	2.71
17.999	12	500	
17.999	12	500	2.39
21.000	9	500	
21.000	9	500	1.92

[1]Values are averages of two duplicates

Distribution coefficients determined at CU using batch tests with relatively low suspended solids concentrations compared reasonably well with distribution coefficients estimated at CU from column tests (Table 13). The columns used had porosities similar to those observed in unconsolidated field conditions. The fact that distribution coefficients

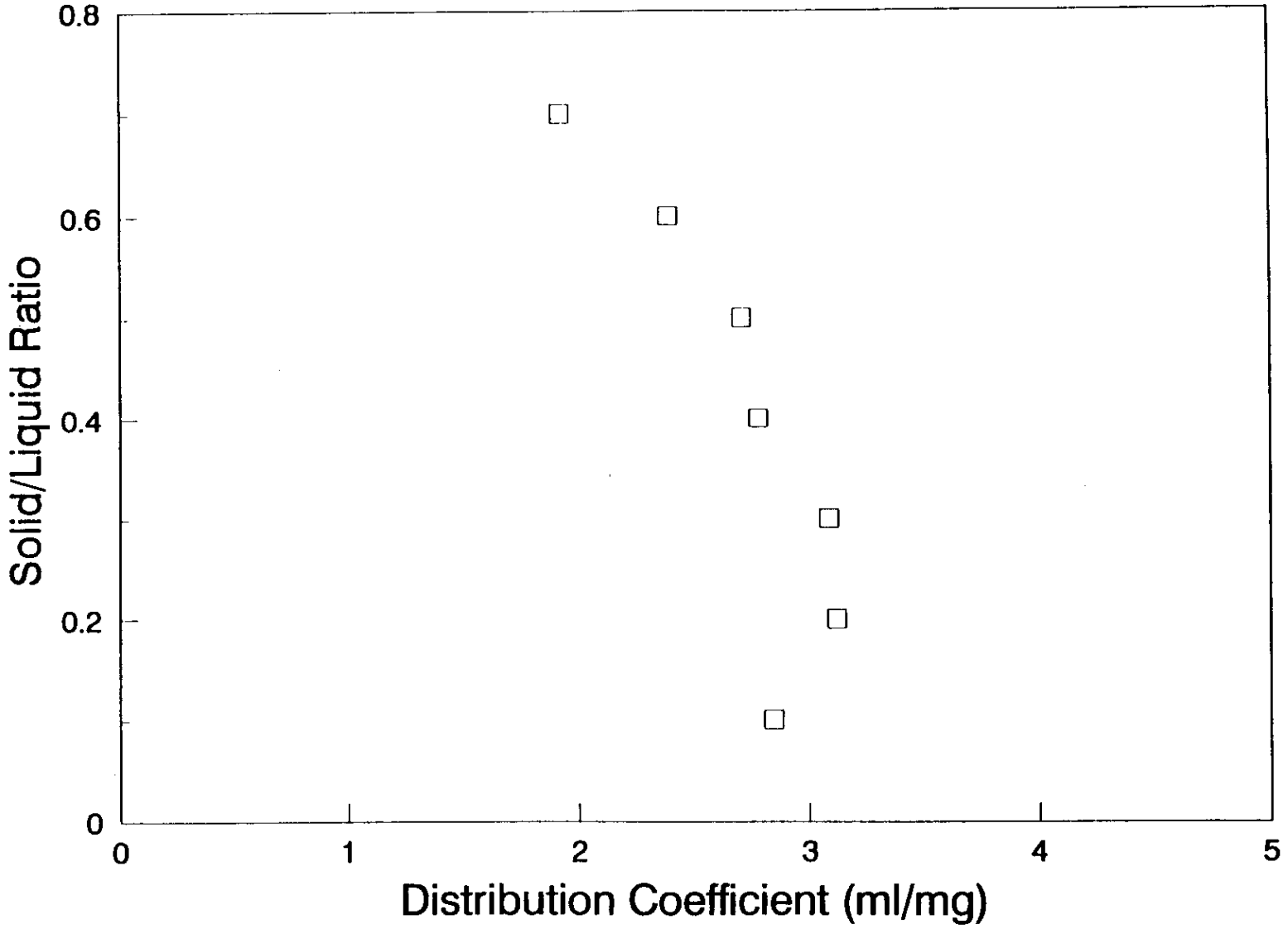

Figure 28. Strontium distribution coefficient versus solid/liquid ratio of crushed basalt.

determined using both batch and column methods are comparable indicates that, although variations in suspended solids concentrations can affect measured distribution coefficients, K_d's measured at lower suspended solids concentrations compare favorably with K_d's measured at solid/liquid ratios equivalent to those observed in the field.

Table 13. Comparison of Distribution Coefficients Measured Using Batch and Column Methods at Clemson University

Isotope	Media	Batch Test K_d (mL/g)	Column Test K_d (mL/g)[1]
237Cs	Basalt	39-43	39-44
60Co	Basalt	30-54	11-16
90Sr	Basalt	9-13	6.3-6.5
233U	Basalt	4-6	0.2-0.3
233U	Interbed	3-6	9

[1]Distribution coefficients are calculated from R values estimated using the two-site/two-region CXTFIT model.

3.2.3 *Comparison of Distribution Coefficients Determined by Batch, Crushed Basalt Packed Columns, and Intact Basalt Core Methods*

Typical breakthrough curves of bromide and strontium in crushed basalt packed columns and intact basalt cores are shown in Figures 29-32. The remaining BTCs are presented in Appendix J. The breakthrough curves observed in crushed basalt packed columns roughly resemble those anticipated for advective-dispersive flow with equilibrium sorption. However, as discussed in section 3.1.1.1 of this report, observed BTCs were generally broader than predicted and were frequently skewed toward higher pore volumes. This difference between theoretical predictions and column data suggests either the presence of more than one type of sorption site, one of which may not have reached equilibrium, or the presence of secondary porosity whose access is limited by mass transport. Because bromide does not sorb to basalt surfaces its transport is not influenced by the occurrence of heterogeneous sorption sites. Fitting data from bromide BTCs with the two site/two region CXTFIT model indicated that approximately 10% of the saturated porosity was immobile or not readily available for advective transport (see Table 14). Strontium distribution coefficients estimated from crushed basalt packed columns (3.37 to 3.68 mL/g) agreed reasonably well with distribution coefficients measured in batch tests (1.92 to 3.12 mL/g) (see Tables 12 and 14).

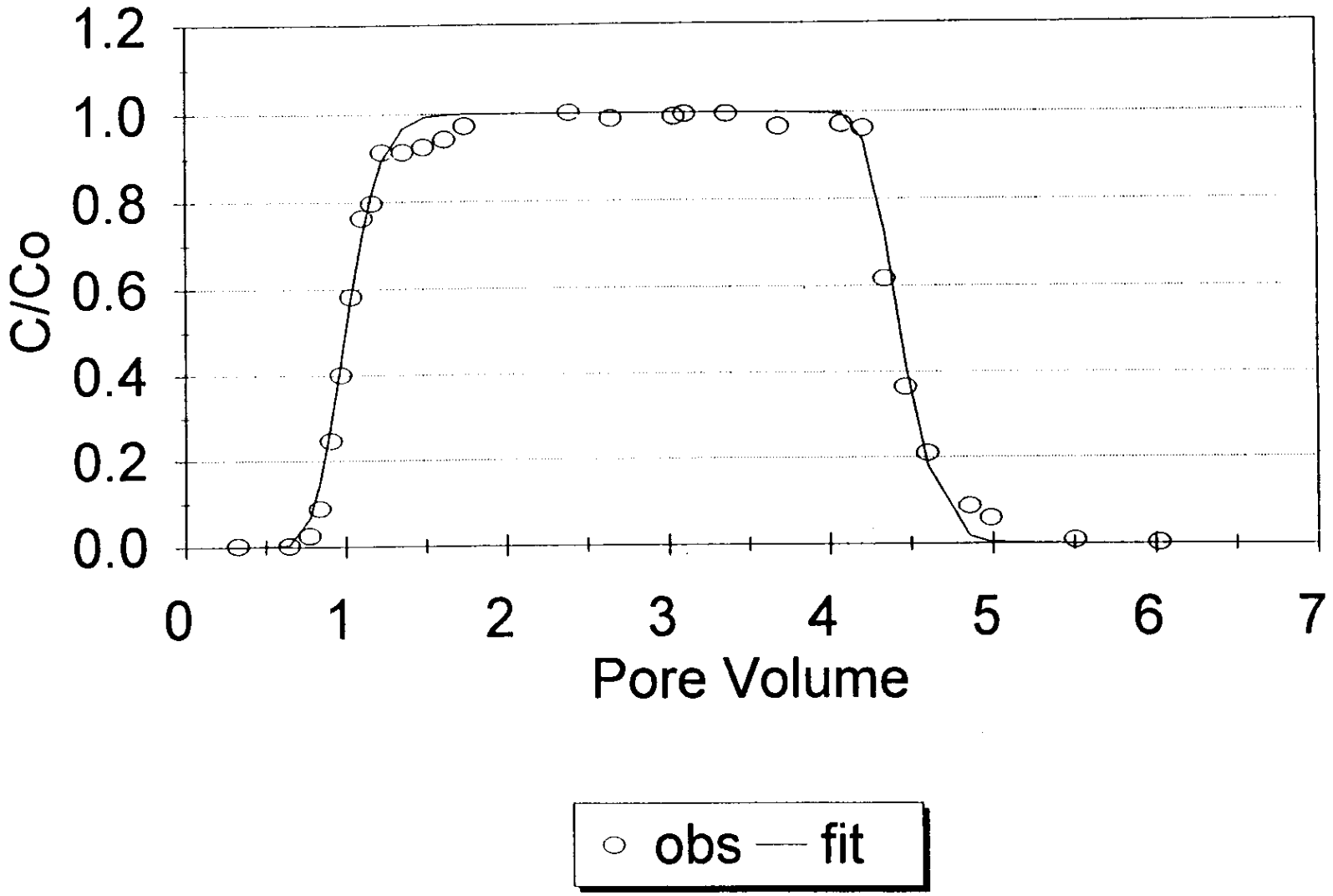

Figure 29. Bromide breakthrough (98.96 % recovery) in crushed basalt column CB5. The solid line represents the equilibrium CXTFIT model fit.

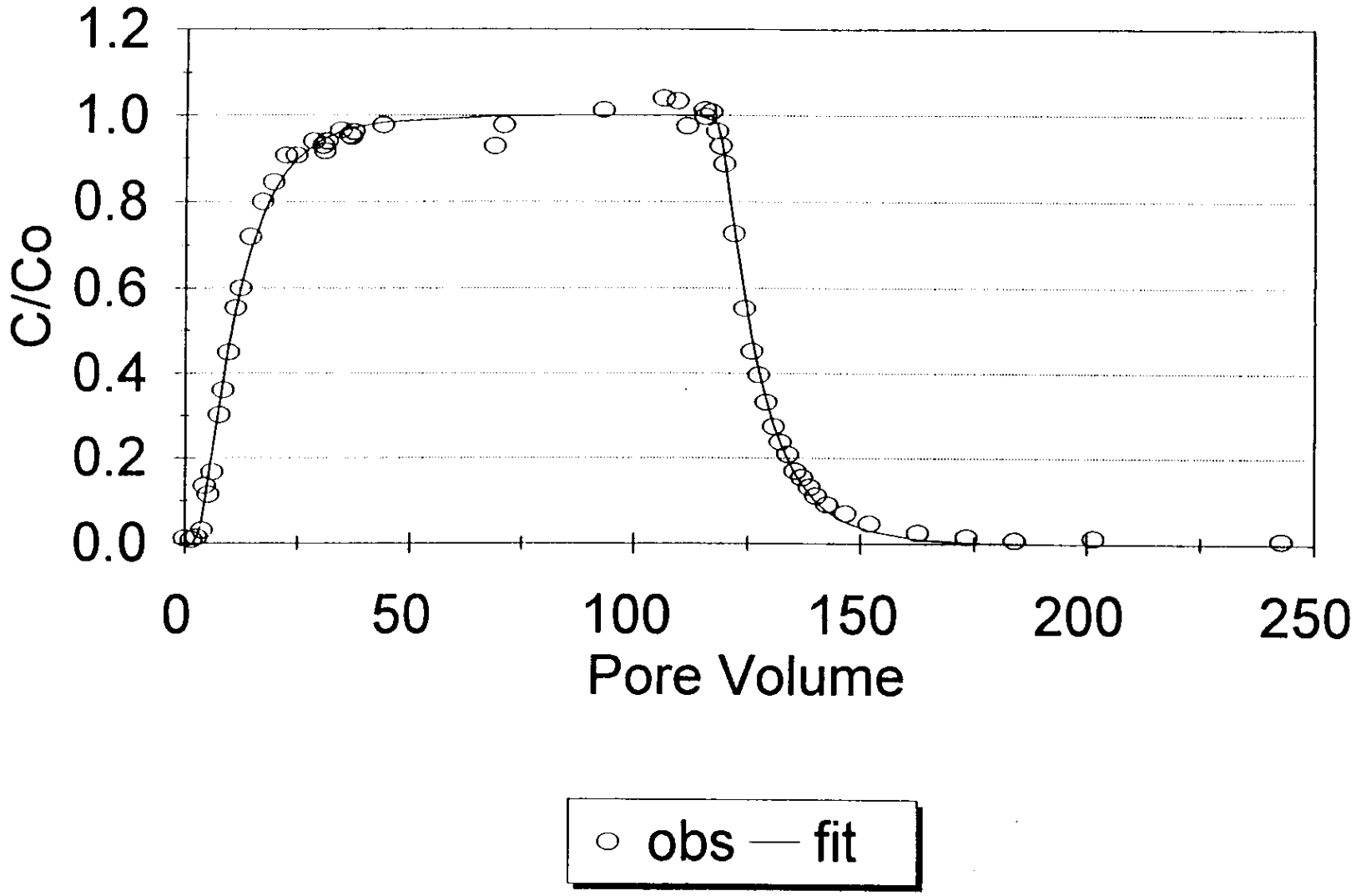

Figure 30. Strontium breakthrough (100.44 % recovery) in crushed basalt column CB5. The solid line represents the equilibrium CXTFIT model fit.

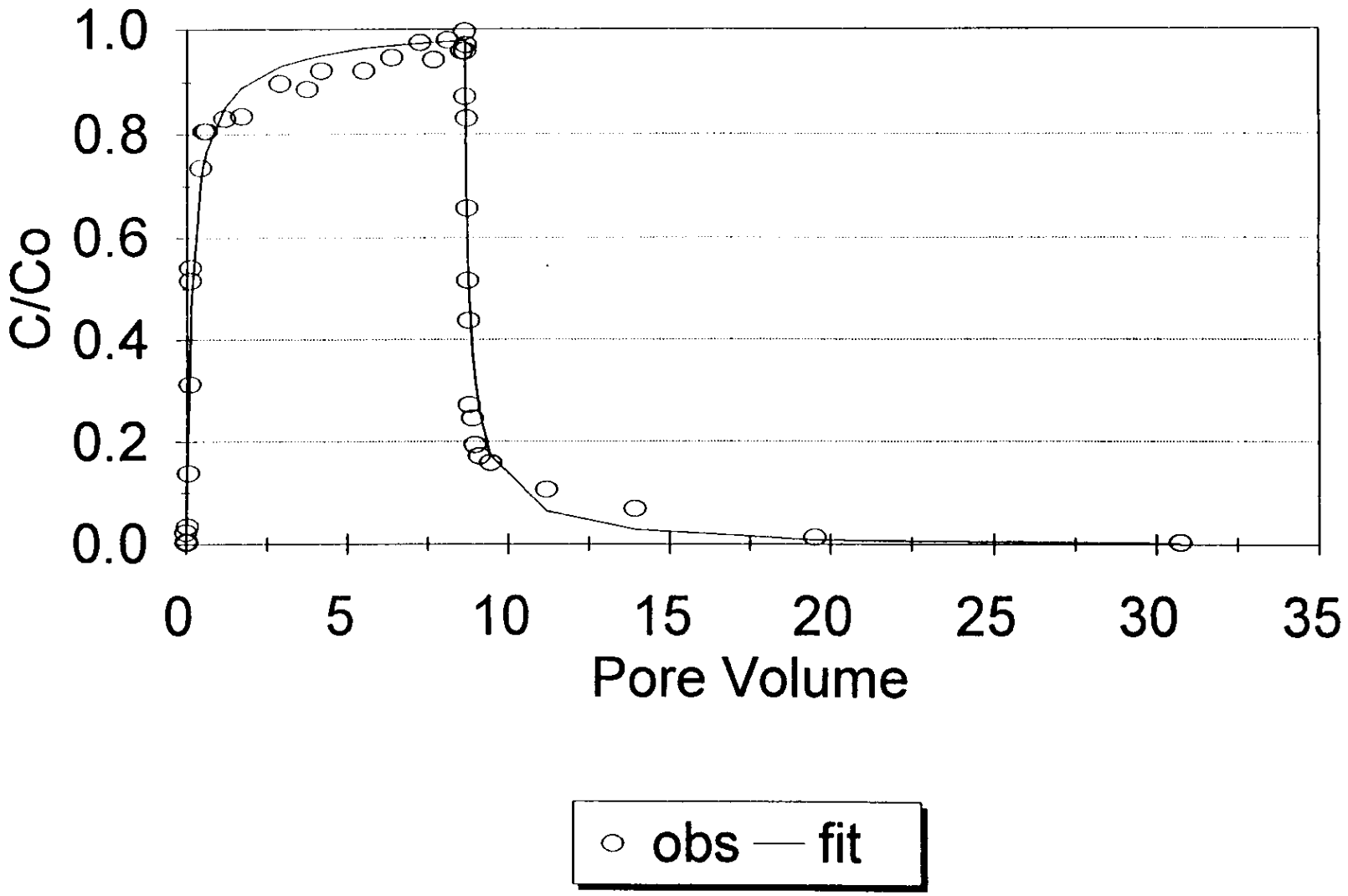

Figure 31. Bromide breakthrough (100.16 % recovery) in intact basalt core I1. The solid line represents the equilibrium CXTFIT model fit.

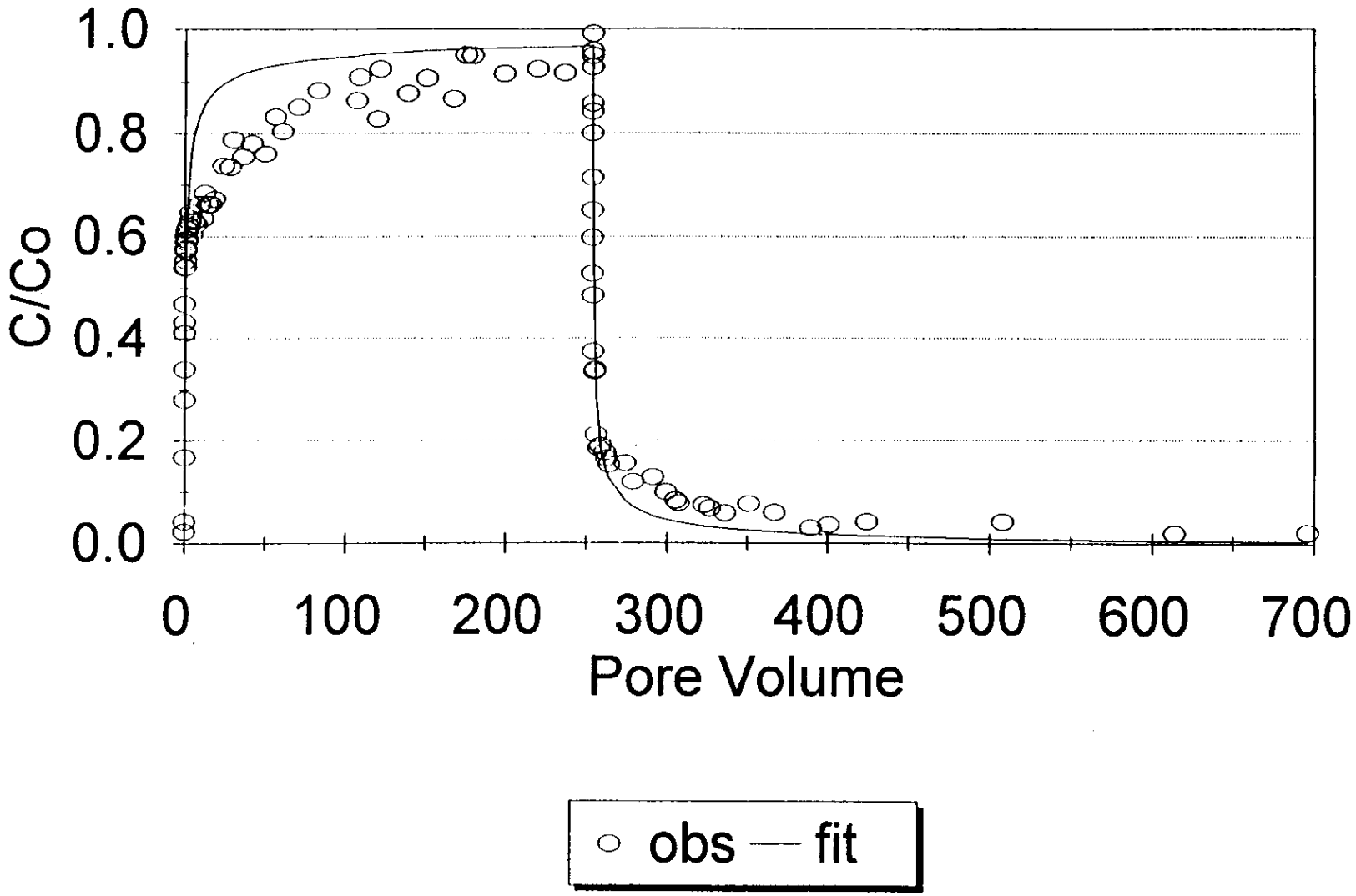

Figure 32. Strontium breakthrough (94.98 % recovery) in intact basalt core I1. The solid line represents the equilibrium CXTFIT model fit.

Table 14. Summary of Crushed Basalt Packed Column and Intact Basalt Core Results Completed at the INEL

						Equilibrium Model			Two Site/Two Region Model				
Column ID	u (cm/min)	Pulse Duration (DPV)	θ (cm^3/cm^3)	bulk density (g/cm^3)	% Recovery	D (cm^2/min)	R	r^2	D (cm^2/min)	R	θ_{im}	α	r^2
CB5BR1	0.48	3.46	0.457	1.497	98.96	0.1026	1.01	0.9918	0.0586	1.05	0.917	0.197	0.9954
CB5BR2	0.93	3.54	0.457	1.497	103.50	0.2270	0.99	0.9934	0.2299	0.99	0.948	875.8	0.9936
CB5SR1	0.40	115.4	0.457	1.497	100.44	1.6201	12.99	0.9970	1.7076	13.4	0.915	22243	0.9973
CB5SR2	0.91	78.2	0.457	1.497	103.48	4.3949	12.07	0.9951	1.6929	12.2	0.640	0.561	0.9963
I1BR2	0.51	8.65	0.1493		100.58	33.069	0.929	0.9726	68.681	1.24	0.10	1.511	0.9955
I1BR3	0.26	8.97	0.1493		100.16	12.97	1.034	0.9805	11.956	1.00	0.895	****	0.9833
I2BR1	0.73	7.65	0.1293		99.42	38.85	1.022	0.9863	2.7567	0.80	0.171	0.606	0.9942
I1SR1	0.52	254.4	0.1493		94.60	*****	****	0.9286	454856	35531	1.00	****	0.9570
I1SR2	0.30	487.0	0.1493		94.98	*****	****	0.9571	24.5362	93.6	0.041	1.161	0.9872

**** = number too large for CXTFIT formatted output

The BTCs observed for intact basalt cores do not resemble those expected based on advective-dispersive flow through a uniform porous media. The BTCs obtained from the intact basalt cores show rapid breakthrough of approximately 60% of the input concentration (C/C(0) = 0.6) followed by extensive tailing (or extremely slow breakthrough) (Figures 32 and 33). Fitting data from bromide BTCs with the two site/two region CXTFIT model indicated that up to 90% of the saturated porosity was immobile (Table 14). However, these estimates were highly variable.

Strontium retardation factors estimated from intact basalt cores were significantly higher than those estimated from either crushed basalt packed columns or batch tests (Tables 12 and 14). These estimates may be misleading, however, as it is difficult to estimate a distribution coefficient from the intact basalt cores using traditional techniques. As previously discussed, the retardation factor is estimated as the number of pore volumes at which 50% of the influent concentration has been eluted. This assumes a symmetrical BTC. The intact basalt core BTCs are asymmetrical and it is not visually obvious at what pore volume 50% of the influent concentration has been eluted. Estimation of the number of pore volumes corresponding to 50% breakthrough is also difficult using curve fitting techniques such as CXTFIT. Therefore, it is not possible to conclude whether the retardation factor is actually greater for the intact basalt cores or whether the flow through the intact basalt cores is sufficiently different from that assumed by the model that the intact basalt cores cannot be interpreted using traditional techniques. It is possible that contaminant transport in the intact cores is controlled by diffusion into and out of the basalt matrix rather than by sorption reactions.

3.2.4 *Effects of Moisture Content on Distribution Coefficients Determined by Column Methods*

The effect of moisture content on contaminant sorption and retardation has traditionally been incorporated into subsurface transport models through equation (1). However, the distribution coefficients input into this equation have almost exclusively been measured under saturated conditions. A series of crushed basalt packed column tests were performed at varying moisture contents in order to evaluate the validity of using distribution coefficients measured under saturated conditions for estimating retardation

under unsaturated conditions. Column characteristics and parameters estimated by CXTFIT for these column tests are listed in Table 15. Typical BTCs for bromide at volumetric moisture contents of 0.18 cm^3/cm^3 (33 % saturation) and 0.157 cm^3/cm^3 (29 % saturation) and strontium at moisture contents of 0.22 cm^3/cm^3 (49 % saturation) and 0.25 cm^3/cm^3 (45 % saturation) are shown in Figures 33-36.

BTCs observed for unsaturated crushed basalt columns closely resemble those observed for saturated crushed basalt columns (Figures 29, 30 and 33-36). The excluded volume estimated by the two site/two region CXTFIT model from unsaturated bromide BTCs ranged from 20 to 33%, intermediate between the excluded volumes estimated for saturated crushed basalt packed columns and intact basalt cores. The strontium distribution coefficients estimated at the varying moisture contents (K_d = 2.37 to 3.35 based on the equilibrium model) agreed reasonably well with those obtained from saturated crushed basalt packed columns (K_d = 3.37 to 3.68 mL/g) and batch tests (K_d = 1.92 to 3.09 mL/g).

Figures 37 and 38 shows the measured strontium and bromide distribution coefficients as a function of volumetric moisture content. Measured K_d values appear to oscillate randomly around means of 3.59 and 0 mL/g for bromide and strontium, respectively, with no apparent relationship to moisture content. The evidence accumulated from these tests indicates that distribution coefficients measured under saturated conditions can be used in equation (1) to estimate contaminant retardation under unsaturated conditions.

Table 15. Sumarry of Unsaturated Crushed Basalt Column Results Completed at the INEL

					Equilibrium Model			Two Site/Two Region Model				
Column ID	u (cm/min)	θ (cm^3/cm^3)	% Sat.	bulk density (g/cm^3)	D (cm^2/sec)	R	r^2	D (cm^2/sec)	R	θ_{im}	α	r^2
BR3	0.041	0.157	29	1.674	0.0940	1.00	0.9872	0.0138	1.03	0.679	1.108	0.9923
BR1	0.373	0.180	33	1.674	0.8387	0.81	0.9902	0.3032	0.99	0.687	0.228	0.9989
BR2	0.744	0.218	40	1.674	1.4328	0.85	0.9539	0.7426	0.94	0.809	0.147	0.9615
	0.033	0.20	37	1.674	0.2765	29.08	0.9713	0.0531	33.51	0.481	0.750	0.9825
SR5	0.295	0.22	40	1.674	3.9738	19.04	0.9916	4.3221	19.78	0.408	339.1	0.9900
SR6	0.644	0.25	45	1.674	14.199	22.32	0.9839	5.1876	29.50	0.478	0.176	0.9916
SR7	0.388	0.546	100	1.674	4.2566	12.08	0.9972	2.6708	12.15	0.768	0.205	0.9978

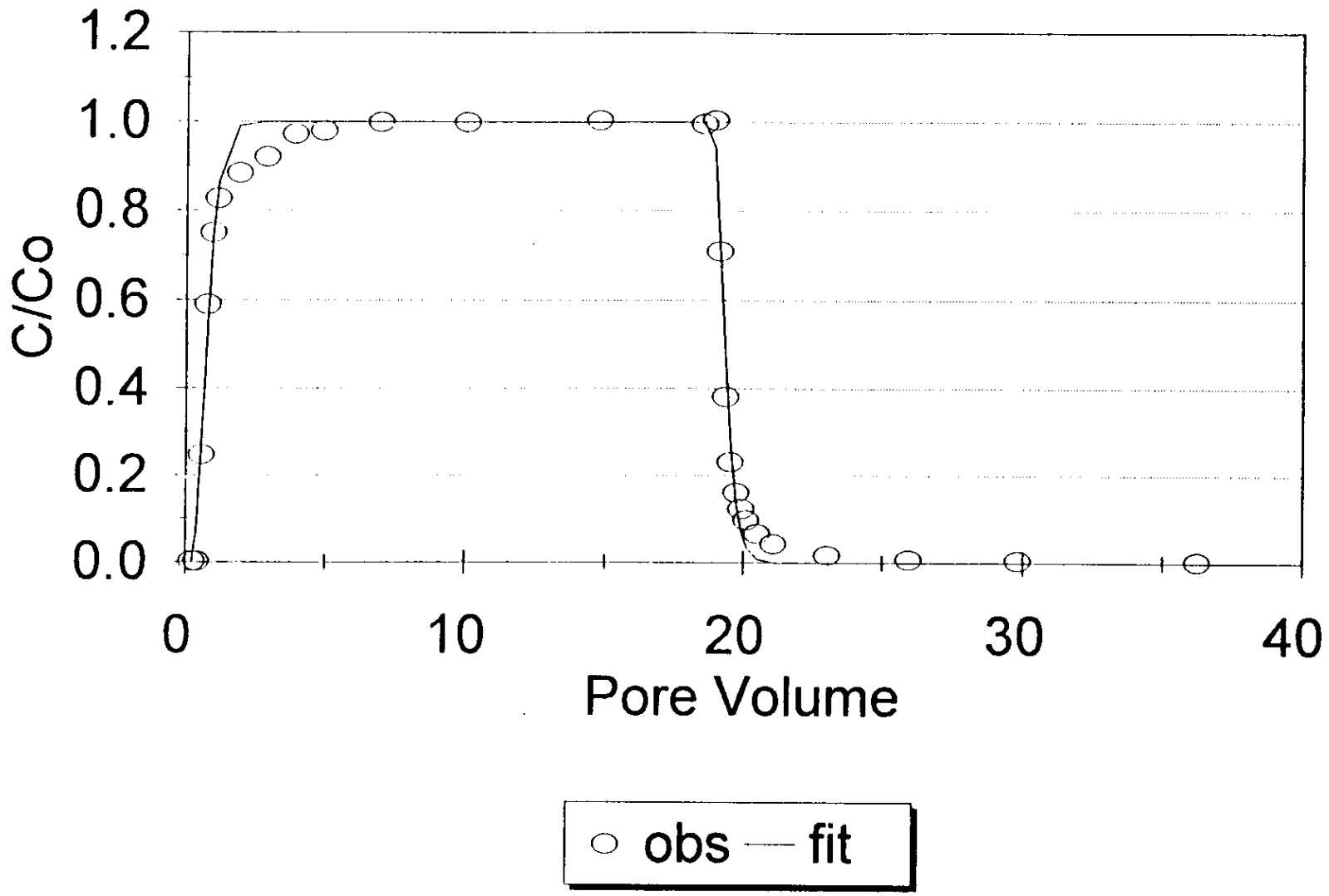

Figure 33. Bromide breakthrough in a crushed basalt column with a volumetric moisture content of 0.18 cm^3/cm^3 (33 % saturation). The solid line represents the equilibrium CXTFIT model fit.

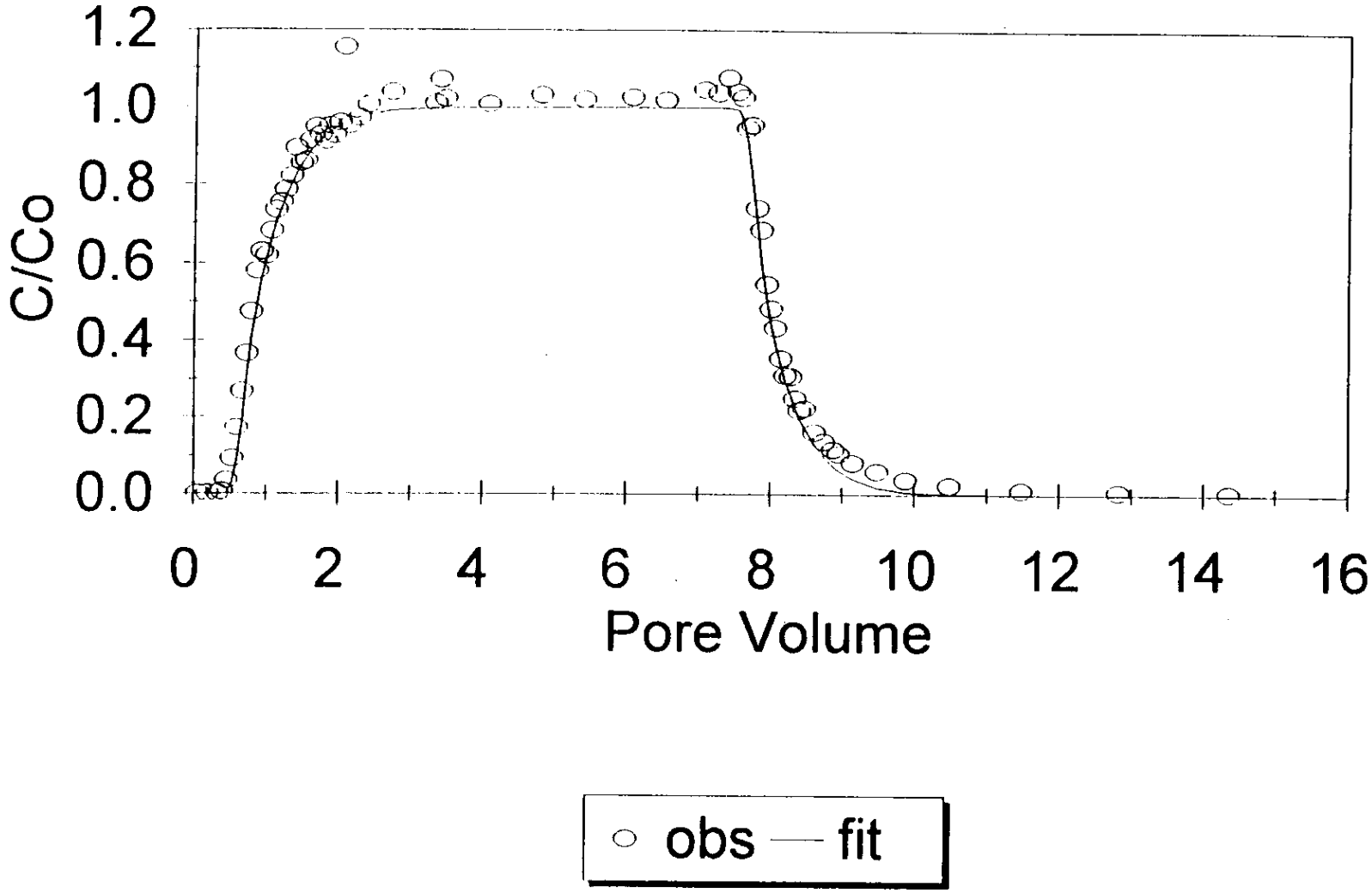

Figure 34. Bromide breakthrough in a crushed basalt column with a volumetric moisture content of 0.157 cm^3/cm^3 (29 % saturation). The solid line represents the equilibrium CXTFIT model fit.

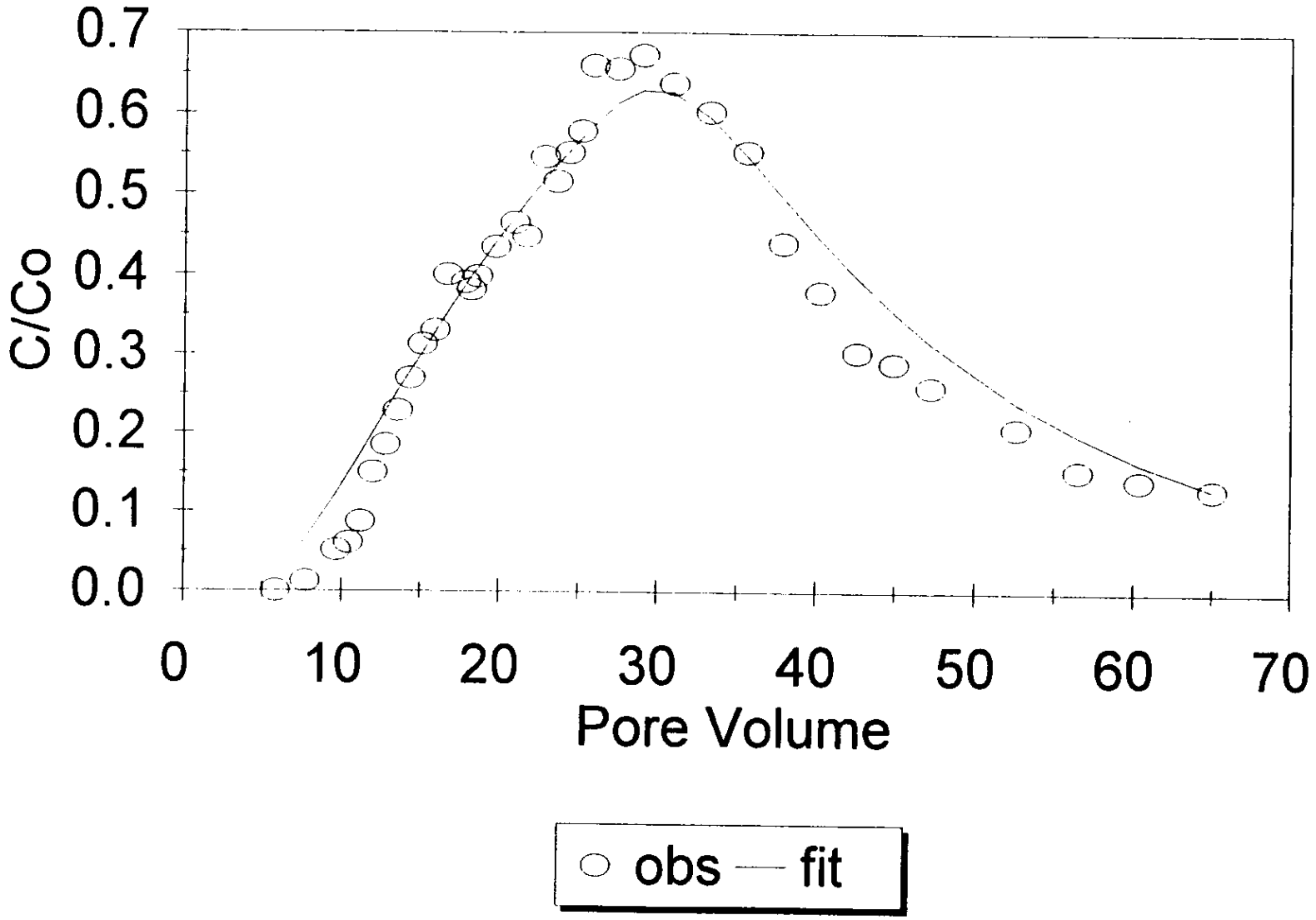

Figure 35. Strontium breakthrough in a crushed basalt column with a volumetric moisture content of 0.22 cm^3/cm^3 (40 % saturation). The solid line represents the equilibrium CXTFIT model fit.

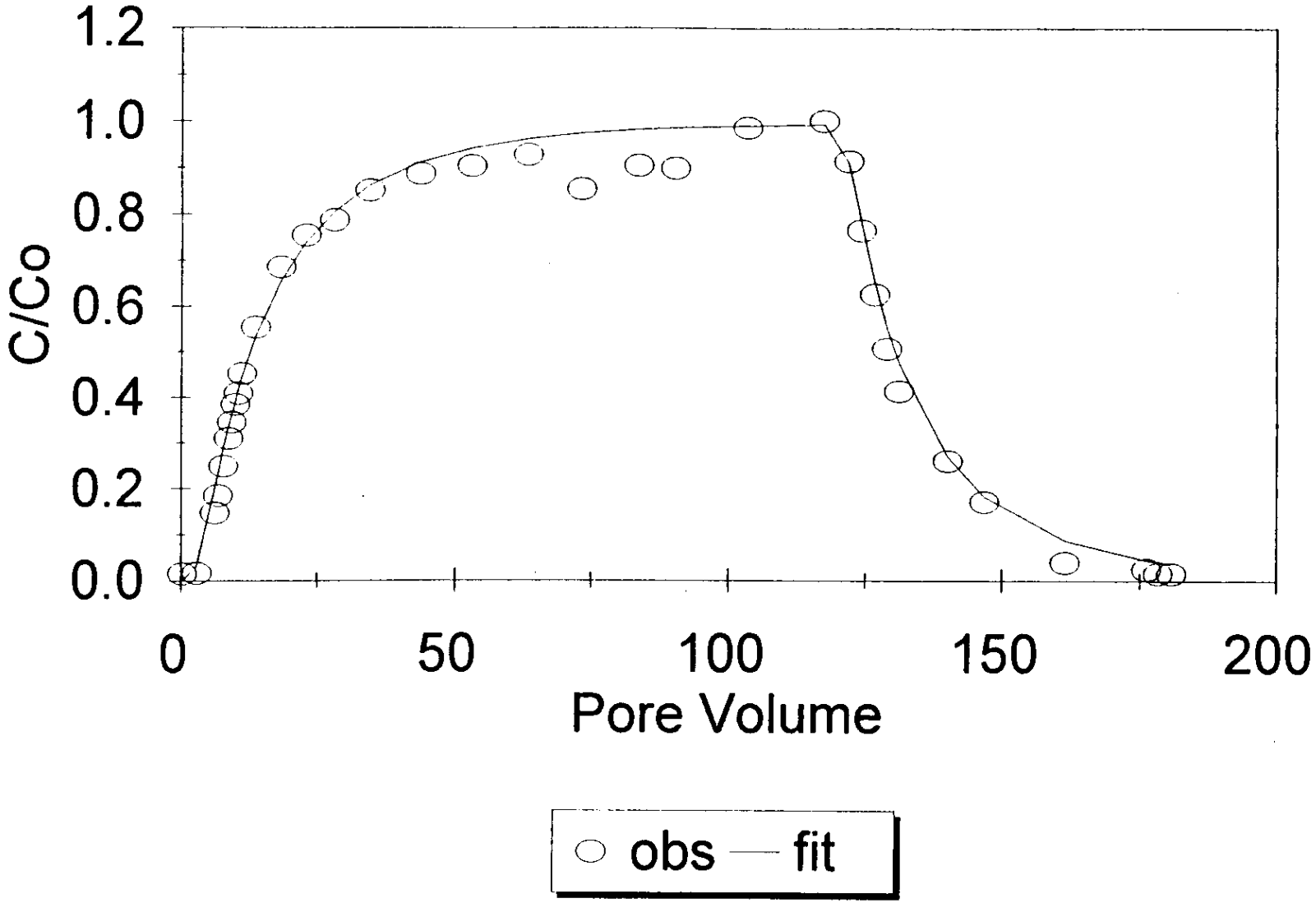

Figure 36. Bromide breakthrough in a crushed basalt column with a volumetric moisture content of 0.25 cm^3/cm^3 (45 % saturation). The solid line represents the equilibrium CXTFIT model fit.

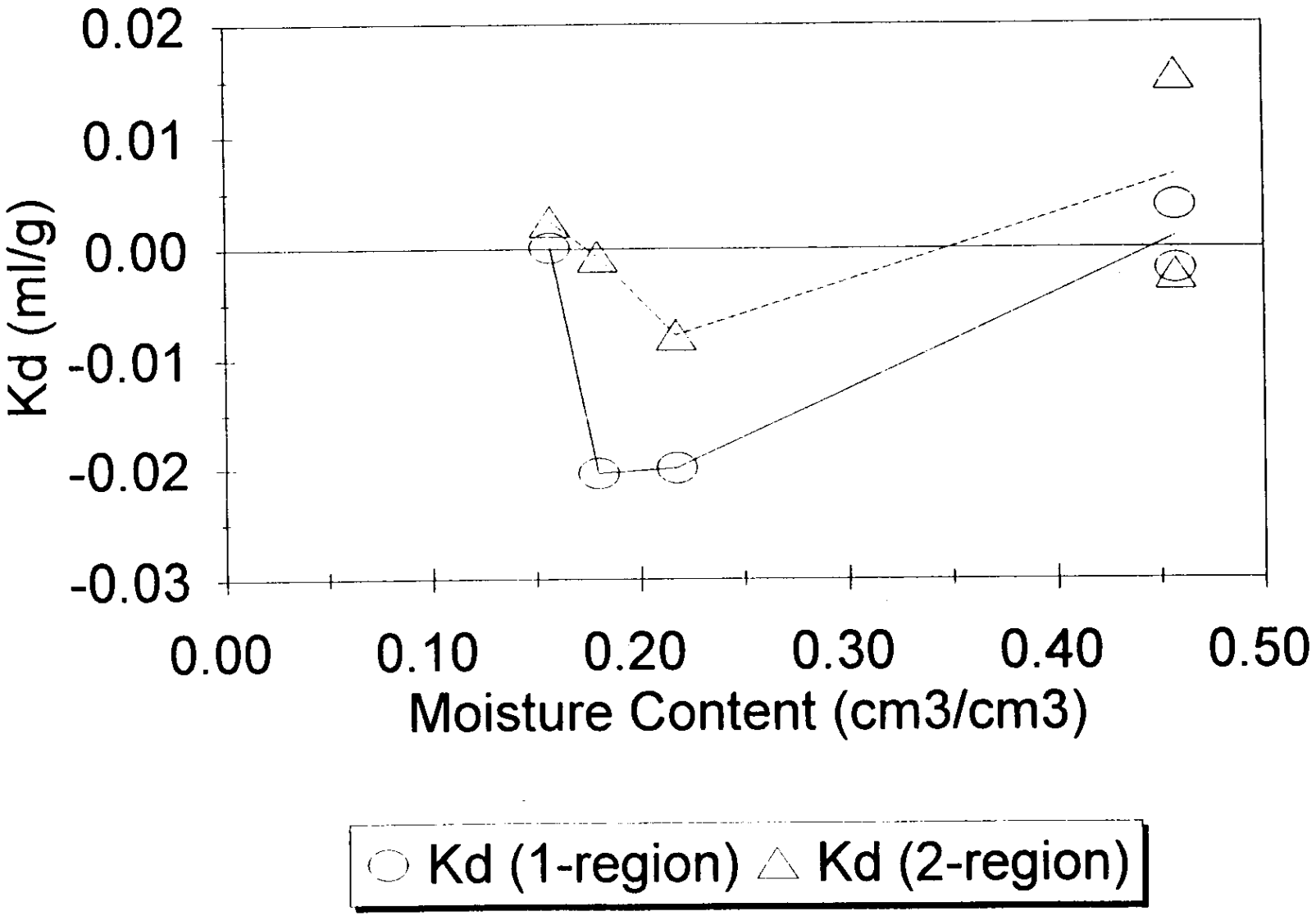

Figure 37. Estimated distribution coefficient of bromide as a function of volumetric moisture content.

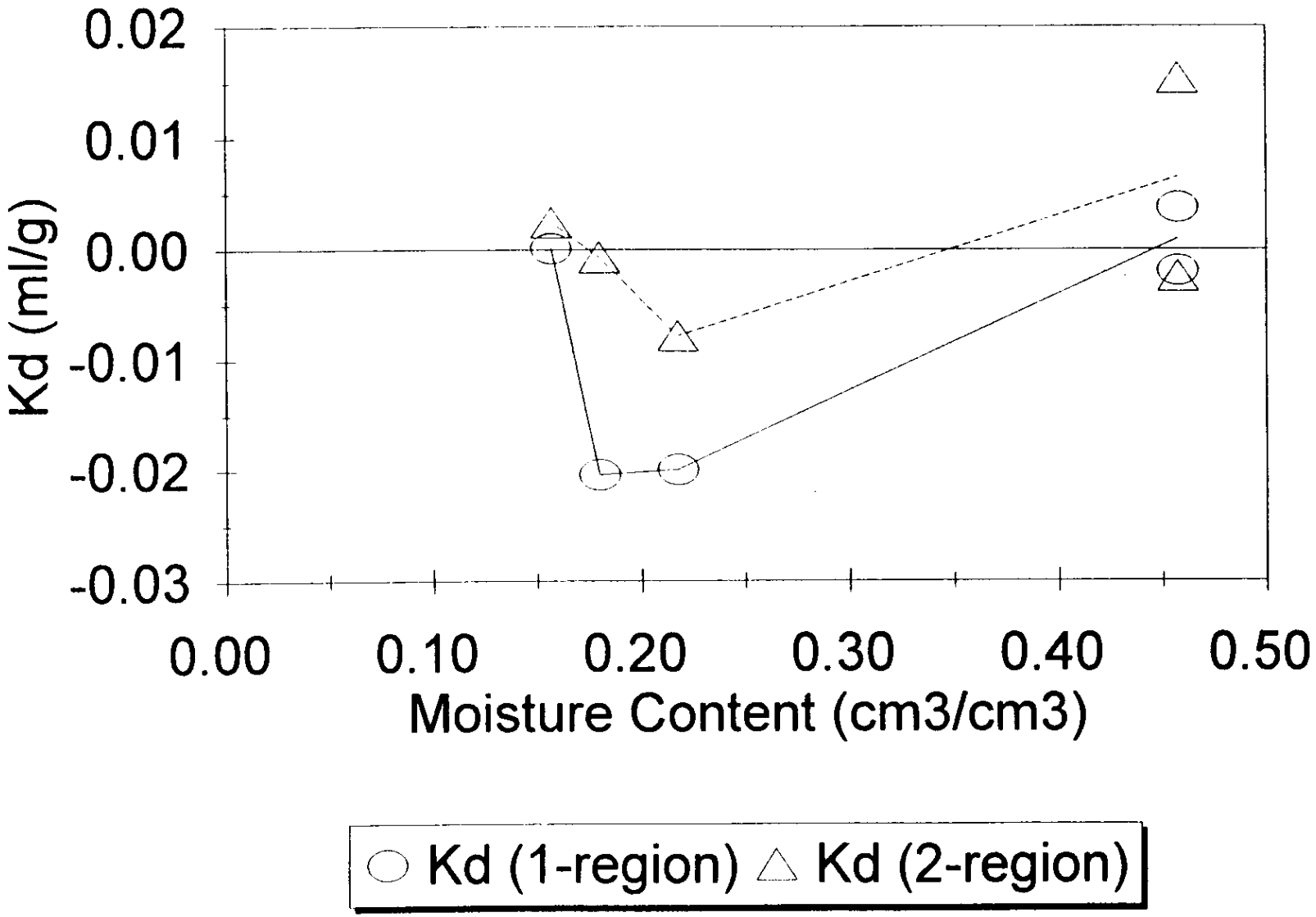

Figure 38. Estimated distribution coefficient of strontium as a function of volumetric moisture content.

4.0 Conclusions

Equilibrium distribution coefficients were determined for Am, Cs, Co, Sr, U, Pu (V) and Pu(VI) with interbed and crushed basalt materials collected from the INEL. Both batch and column tests were conducted using solution chemistries similar to those observed in the SRP aquifer beneath the INEL. Distribution coefficients were determined using both batch and column techniques in order to insure that the values obtained were as applicable as possible to field conditions. The values obtained by the two techniques were in reasonable agreement (Table 16) and did not vary greatly from values reported in the literature for, similar though not identical, conditions (Tables 1 and 16).

Table 16. Summary of K_d Values Obtained Using Both Batch and Column Tests

		Batch Test	Column Test	Enhanced Mobility
Isotope	Media	K_d (mL/g)	K_d (mL/g)[1]	K_d (mL/g)
^{241}Am	Basalt	70-280		0.18
^{241}Am	Interbed	450-1100		*
^{137}Cs	Basalt	39-43	39-44	
^{137}Cs	Interbed	2230-3260		
^{60}Co	Basalt	30-54	11-16	0.17
^{60}Co	Interbed	1150-3900		*
^{239}Pu (total)	Basalt			0.25
^{239}Pu (total)	Interbed			*
Pu(V)	Basalt	70-130		
Pu(V)	Interbed	5100-7900		
Pu(V)	Surface Soil	7800-22000		
Pu(VI)	Basalt	12-24		
Pu(VI)	Interbed	110-690		
Pu(VI)	Surface Soil	1800-4900		
Pu(EDTA)	Basalt	0.04-0.05		
Pu(EDTA)	Interbed	4-5		
Pu(EDTA)	Surface Soil	40-490		
^{90}Sr	Basalt	9-13	6.3-6.5	
^{90}Sr	Interbed	42-63		
^{233}U	Basalt	4-6	0.2-0.3	
^{233}U	Interbed	3-6	9	

[1]Distribution coefficients are calculated from retardation factors estimated using the two-site/two-region CXTFIT model.

*Although an enhanced mobility fraction was observed, it was too small (~1%) too be modeled using CXTFIT.

However, a fraction of the ^{241}Am (9-13%), ^{60}Co (3 %) and ^{239}Pu (10-55%) applied to crushed basalt packed columns was transported at a much faster rate than the bulk of these three radionuclides. The enhanced mobility fractions of ^{241}Am, ^{60}Co, and ^{239}Pu were observed to a lessor degree (~1%) in interbed material packed columns. This phenomena would not have been observed with batch tests alone. This enhanced mobility may alter predicted arrival times and peak concentrations of these three radionuclides downgradient from their source. Thus enhanced mobility may change risk calculations. Evaluation of the frequency, magnitude and mechanisms controlling enhanced transport was not an objective of the laboratory studies reported here, and thus its relevance in the field remains unresolved.

Equilibration of plutonium with synthetic groundwater indicated that within 24 hours the majority remaining in solution was Pu (V). Also within this time frame the total plutonium activity in the solution phase decreased to 60 to 70% of the initial value. This was due primarily to a decline in Pu (IV) and was attributed to settling of polymerized or precipitated Pu (IV). Because the majority of Pu (IV) was removed from solution by polymerization or precipitation, it is not expected to be mobile (other than possibly through colloidal transport) and a distribution coefficient is not appropriate for this form of plutonium. Finally, in batch studies using high interbed material suspended solids concentrations, Pu (V) was reduced to Pu (IV), and Pu (VI) was reduced to Pu (V) and Pu (IV). This reduction indicates that at the high suspended solids concentrations found in the field, plutonium may be present in its reduced and less mobile forms (again, with the possible exception of colloidal transport).

Batch studies indicated that the buffering capacity of both interbed and crushed basalt materials from the INEL are sufficiently high to make significant variations in subsurface pH at distances more than a few meters from perturbations (waste sources) unlikely. Therefore, pH variations are not expected to be a significant factor in predicting subsurface transport. However, ionic strength and specific ion effects on the sorption of cesium and uranium were observed. Specifically, increasing K^+ concentrations were shown to reduce sorption of cesium to both crushed basalt and interbed materials. Increasing Ca^{2+} concentrations were observed to decrease uranium sorption to basalt

surfaces, while increasing sorption to interbed surfaces. Increasing K^+ concentrations decreased uranium sorption to interbed surfaces. The effects of K^+ and Ca^{2+} on the sorption of uranium to interbed materials may result from the effects of these two cations on the surface charge and structure of expandable clays.

Sorption rate constants were determined for Cs, Co, Sr, and U. Comparison of the estimated times required to reach equilibrium with basalt (61 to 329 hr.), based on the "two-box" model (see section 1.2.2 of this report), to the average flow velocity estimated by Porro and Bishop (1995) from the Large-Scale Aquifer Pumping and Infiltration Test (5 m/day), indicates that these elements might not be in equilibrium with basalt surfaces under LPIT conditions. The times required to reach equilibrium estimated for interbed materials were considerably shorter (4 to 219 hr.). The faster sorption rates for interbed materials coupled with the much slower average flow velocities observed for sedimentary interbeds indicate that the assumption of equilibrium may be valid for sedimentary interbeds.

Tests were conducted to evaluate the use of batch tests (which typically use solid/liquid ratios much lower than those occurring in the field) in predicting distribution coefficients at solid/liquid ratios occurring in the field. Results from this study indicate that, although variation in solids concentration can affect measured K_d's, strontium batch tests results at lower solid/liquid ratios compare favorably with strontium K_d's measured at solid/liquid ratios equivalent to those observed in the field. Comparisons of batch and column tests results support this conclusion. Tests to evaluate the validity of using distribution coefficients measured under saturated conditions for estimating retardation under unsaturated conditions were also designed and completed. The results indicated that distribution coefficients measured under saturated conditions may be used in equation (1) to estimate retardation under unsaturated conditions. The results from both of these tests indicate that laboratory determined distribution coefficients may be applicable under field subsurface conditions.

Experiments were conducted using intact basalt cores as well as crushed basalt packed columns. Results indicated that contaminant transport in intact basalt cores, and possibly in fractured basalt, did not follow traditional patterns assume by advective-

dispersive flow models and may be dominated by prfered flow paths and diffusion into and out of the basalt matrix rather than by sorption reactions. These last results indicate the complexity of field conditions and emphasize the need for caution in data interpretation and application.

5.0 References

Ames, L.L. and D. Rai, Radionuclide Interactions with Soil and Rock Media, Battelle Pacific Northwest Laboratories, Richland, WA, EPA 520/6-78-007-A, 1978.

Ames, L.L., J.E. McGarrah, and B.A. Walker, Basalt Radionuclide Reactions: FY-1981 Annual Report, Pacific Northwest Laboratories, Richland, WA, US DOE Report RHO-BW-CR-127-P, (1981)

ASTM, Standard Methods for Distribution Ratios by the Short-Term Batch Method, ASTM D4319, 1990.

Barney, G.S., Radionuclide Reactions with Groundwater and Basalts from Columbia River Basalt Formations, Rockwell International, Richland, WA, US DOE Report RHO-SA-217, 1981.

Barney, G.S., Radionuclide Sorption on Basalt-Interbed Materials: FY 1981 Annual Report, Rockwell International, Richland, WA, US DOE Report RHO-BW-ST-35-P, 1982.

Bell, J. and T.H. Bates, Distribution Coefficients of Radionuclides Between Soils and Groundwaters and Their Dependence on Various Test Parameters, *Sci. Total Environment*, 69: 297-317, 1988.

Bondietti, E.A., Mobile Species of Pu, Am, Cm, Np, and Tc in the Environment, IAEA-Sm-257/42, International Atomic Energy Agency, Vienna, Austria, 1982.

Choppin, G.R., Aspects of Plutonium Solution Chemistry, *Plutonium Chemistry*, American Chemical Society, 1983.

Choppin, G.R., and B.E. Stout, Actinide Behavior in Natural Waters, *The Science of the Total Environment*, 83: 203-216, 1989.

Dean, J.A., *Lange's Handbook of Chemistry*, Thirteenth Edition, McGraw Hill, Inc., New York, NY, 1985.

Del Debbio, J.A., and T.R. Thomas, Transport Properties of Radionuclides and Hazardous Chemical Species in Soils at the Idaho Chemical Processing Plant, Westinghouse Idaho Nuclear Company, Inc., Idaho Falls, ID, WINCO-1068, 1989.

DiToro, D.M., and L.M. Horzempa, Reversible and Resistant Components of PCB Adsorption-Desorption: Isotherms, *Environ. Sci. Technol.*, 16: 594-810, 1982.

Dosch, R.G., and A.W. Lynch, Interaction of Radionuclides with Geomedia Associated with the Waste Isolation Pilot Plant (WIPP) Site in New Mexico, Sandia Laboratories, Albuquerque, NM, SAND 78-0297, 1978.

Dzombak, D.A., and F.M.M. Morel, Adsorption of Inorganic Pollutants in Aquatic Systems, *J. Hydraulic Engr., Proc. Am. Soc. Civ. Engr.*, 113: 430-475, 1987.

Early, T.O., G.K. Jacobs, and D.R. Drewes, Geochemical Controls on Radionuclide Releases from a Nuclear Waste Repository in Basalt, *Geochemical Behavior of Radioactive Waste,* American Chemical Society, 1984.

Estes, M. and M. McCurry, Concentrations and Compositions of Colloidal Particles in Groundwater Near the ICPP, Idaho National Engineering Laboratory, Idaho, Hydrogeology, Waste Disposal, Science and Politics, Proceedings 30th Symposium, Engineering Geology and Geotechnical Engineering, 165-179, 1994.

Fried, S., A.M. Friedman, and R. Weeber, Studies of the Behavior of Plutonium and Americium in the Lithosphere, Argonne National Laboratory, Chicago, IL, ANL-8096.

Friedman, H.A., and A.D. Kelmers, Laboratory Measurement of Radionuclide Sorption in Solid Waste Storage Area 6 Soil/Groundwater Systems, Oak Ridge National Laboratory, Oak Ridge, TN, ORNL/TM-10561, 1990.

Gaudet, J.P., H. Jegat, G. Vachaud, and P.J. Wierenga, Solute Transfer with Exchange Between Mobile and Stagnant Water, Through Unsaturated Sand, *Soil Sci. Soc. Am. J.*, 41: 665-671, 1977.

Guillaumont, R., and J.P. Adolf, Behavior of Environmental Plutonium at Vary Low Concentrations, *Radiochem. Acta,* 58/59: 53-60, 1992.

Gupta, R.K., R.J. Millington, and A Klute, Hydrodynamic Dispersion in Unsaturated Porous Media: II. The Stagnant Zone Concept and the Dispersion Coefficient. *J. India Soc. Soil Sci.* 21: 121-128, 1973.

Hawkins, D.B., and H.L. Short, Equations for the Sorption of Cesium and Strontium on Soil and Clinoptilolit, Atomic Energy Commission, Idaho Operations Office, Idaho Falls, ID, IDO-12046, 1965.

Hoeffner, S.L. Laboratory Simulation of Radionuclide Migration Through Basalt: Applications to the Proposed radioactive Waste Repository Near Richland, Washington, Ph.D. Dissertation, University of Missouri-Columbia, 1983.

Huheey, J.E., *Inorganic Chemistry,* Third Edition, Harper and Row Publishers, New York, NY, 1983.

IAEA, Geochemistry of Long Lived Transuranic Actinides and Fission Products, International Atomic Energy Agency, Vienna, Austria, IAEA-TECDOC-637, 1992.

James, R.O., and T.W. Healy, Adsorption of Hydrolyzable Metal Ions at the Oxide-Water Interface, *J. Colloid Interface. Sci.*, 40: 65-81, 1972.

Jensen, B.S., The Geochemistry of Radionuclides with Long Half-Lives: Their Expected Migration Behavior, Riso National Laboratory report Riso-R-430, Roskilde, Denmark, 1980.

Killey, R.W., J.O. McHugh, D.R. Champ, E.L. Cooper, and J.L, Young, Subsurface Cobalt-60 Migration from a Low-Level Waste Disposal Site, *Environ. Sci. Technol.* 18: 148-157, 1984.

Kobashi, A., and G.R. Choppin, A Study of Techniques for Separating Plutonium in Different Oxidation States, *Radiochim. Acta.* 43: 211-215, 1988.

Kreft, R.W., and A. Zuber, On the Physical Meaning of the Dispersion Equation and its Solution for Different Initial and Boundary Conditions, *Chem. Eng. Sci.* 33: 1471-1480, 1978.

Langmuir, D. Uranium Solution-Mineral Equilibria at Low Temperatures with Applications to Sedimentary Ore Deposits, *Geochim. Cosmochim. Acta*, 42: 547-569, 1978.

Means, J.L., D.A. Crerar, and J.O. Duguid, Migration of Radioactive Wastes: Radionuclide Mobilization by Complexing Agents, *Science*, 200: 1477-1481, 1978.

Moulin, V., N. Labonne, and M. Theyssier, Retention Properties of Silica Colloids for Actinides, Migration '91, Abstracts: 77, 1991.

Nash, K.L., J.M. Cleveland, and T.F. Rees, Speciation Patterns of Actinides in Natural Waters: A Laboratory Investigation, *J. Environ. Radioactivity*, 7: 131-157, 1988.

Neu, M.P., D.C. Hoffman, K.E. Roberts, H. Nitsche, and R.J. Silva, Comparison of Chemical Extractions and Laser Photoacustic Spectroscopy for the Determination of Plutonium Species in Near-Neutral Carbonate Solutions, *Radiochem. Acta*, 66/67: 261-268, 1994.

Parker, J.C., and Van Genuchten, M.T., Determining Transport Parameters from Laboratory and Field Tracer Experiments, Virginia Polytechnic Institute and State University, Blacksburg, VA, Virginia Agricultural Experiment Station, Bulletin 84-3, ISSN 0096-6088, 1984.

Penrose, W.R., W.L. Polzer, et al., Mobility of Plutonium and Americium Through a Shallow Aquifer in a Semiarid Region, *Environ. Sci. Tech.* 24: 228-234, 1990.

Porro, I., C.W. Bishop, and J.D. Burgess, Vadose Zone Water Movement at the INEL Large-Scale Infiltration Test, *Water Resources Research,* submitted, 1995.

Rai, D. and R.J. Serne, Solid Phases and Solution Species of Different Elements in Geologic Environments, Pacific Northwest Laboratories, Richland, WA, PNL-2651, UC-70, 1978.

Relyea, J.F., Theoretical and Experimental Considerations for the Use of the Column Method for Determining Retardation Factors, *Radioactive Waste Management and the Nuclear Fuel Cycle*, 3: 151-166, 1982.

Routson, R.C., G.S. Barney, et al., Fission Product Parameters for Hanford 200 Area Sediment Types, Rockwell International, Richland, WA, US DOE Report RHO-SR-35, 1981.

Saito, A., R.A. Roberts, G.R. Choppin, Preparation of Solutions of Tracer Level Plutonium (V), *Anal. Chem.*, 57: 390-391, 1985.

Salter, O.F., L.L. Ames, and J.E. McGarrah, Sorption of Selected Radionuclides on Secondary Minerals Associated with the Columbia River Basalts, Rockwell International, Richland, WA, US DOE Report RHO-BWI-LD-43, 1981a.

Salter, O.F., L.L. Ames, and J.E. McGarrah, The Sorption Behavior of Selected Radionuclides on Columbia River Basalts, Rockwell International, Richland, WA, US DOE Report RHO-BWI-LD-48, 1981b.

Sanchez, A.L., J.W. Murray, and T.H. Sibley, The Adsorption of Plutonium IV and V on Geothite, *Geochim. Cosmochim. Acta.*, 49: 2297-2307, 1985.

Schmalz, B.L. Radionuclide Distribution in the Soil Mantle of the Lithosphere as a Consequence of Waste Disposal at the National Reactor Testing Station, US Atomic Energy Commission, IDO-10049, 1972.

Seaborg, G.T., and J.J. Katz, *The Chemistry of the Actinide Elements,* John Wiley and Sons, Inc., New York, NY, 1957.

Seitz, M.G., P.G. Rickert, R.A. Coutoure, et al., Studies of Nuclear Waste Migration in Geologic Media, Argonne National Laboratory, Chicago, IL, US DOE Report ANL-80-36, 1979.

Serne, R.J., and J.F. Relyea, Waste Rock Interactions Technology Program: The Status of Radionuclide Sorption-Desorption Studies Performed by the WRIT Program, Pacific Northwest Laboratory, Richland, WA, US DOE Report PNL-3997, 1982.

Serne, R.J., D. Rai, and J.F. Relyea, Preliminary Results of Comparison of Adsorption-Desorption Methods and Statistical Techniques to Generate K_d Predictor Equations, Pacific Northwest Laboratory, Richland, WA, US DOE Report PNL-SA-7245, 1979.

Sorathesm, A., G. Bruscia, T. Tamura, and E.G. Struxness, Mineral and Sediment Affinity for Radionuclides, CF-60-6-93, 1960.

Tewari, P.H., A.B. Cambell, and W. Lee, Adsorption of Cobalt(II) by Oxides from Aqueous Solution, *Can. J. Chem.* 50: 1642-1648, 1972.

Ticknor, K.V., Actinide Sorption by Fracture-Infilling Minerals, *Radiochim. Acta*, 60: 33-42, 1993.

Travis, B.J., and H.E. Nuttall, *Analysis of Colloid Transport*, L.O. Werme, ed., Materials Research Society Symposium Proceedings, Scientific Basis for Nuclear Waste Management-IX, Pittsburgh, PA, MRS:737-745.

van Genuchten, M.Th. and R.W. Cleary, Movement of Solutes in Soil: Computer-Simulated and Laboratory Results. *Soil Chemistry, B. Physico-Chemical Models*, G.H. Bolt, ed., Elsevier Scientific Publishers, Inc., NY, 349-386, 1979.

van Genuchten, M.Th., Non-Equilibrium Transport parameters from Miscible Displacement Experiments, USDA, US Salinity Laboratory, Riverside, CA, Research Report 119, 1981.

Wilczak, A., Sorption of Heavy Metal Cations on Activated Carbon, Ph.D. Dissertation, Clemson University, Clemson, SC, 1988.

Wood, W.W., and W.H. Low, Aqueous Geochemistry and Diagenesis in the Eastern Snake River Plain Aquifer System, Idaho, *Geological Society of America Bulletin*, 97: 1456-1466, 1986.

Yamaguchi, T., Y. Sakamoto, and T. Ohnuki, Effect of Complexation on Solubility of Pu(IV) in Aqueous Carbonate System, *Radiochimica Acta*, 1994.

Appendices

Appendix A

Appendix A

Preparation of Synthetic Groundwater

The following chemicals were weighed to an accuracy of ±0.001 g, dissolved independently in approximately 250 mL of distilled, deionized water, combined, and adjusted to a final volume of 20L.

1. 0.500 g calcium chloride ($CaCl_2 * 2H_2O$)
2. 0.200 g calcium nitrate ($Ca(NO_3)_2 * 4H_2O$)
3. 0.500 g potassium bicarbonate ($KHCO_3$)
4. 0.300 g magnesium chloride ($MgCl_2 * 6H_2O$)
5. 0.100 g magnesium nitrate ($Mg(NO_3)_2 * 6H_2O$)
6. 1.200 g magnesium sulfate ($MgSO_4 * 7H_2O$)
7. 0.020 g sodium fluoride (NaF)
8. 1.200 g sodium bicarbonate ($NaHCO_3$)
9. 40 mL of standard calcium carbonate solution (1 mL = 1 mg Ca)
10. 200 mL of standard Si solution (1 mL = 1 mg Si)

The pH of the resulting solution was then adjusted to 8.00 ± 0.05 using either 0.5 N HCl or 0.5 NaOH.

Appendix B

Appendix B

Characteristics of Packed Columns Used at Clemson University

Table B-1. Summary of Conditions for Crushed Basalt Packed Columns

Column ID	ρ (cm^3/cm^3)	n	u (cm/sec)	Effluent pH	Effluent Specific Conductivity (μS/cm)
B02	1.50	0.518	0.0123	8.02	345
B03	1.73	0.436	0.0073	8.09	338
B07	1.60	0.485	0.0066	8.12	351
B08	1.62	0.492	0.0065	8.04	383
B10	1.62	0.464	0.0069	8.12	305
B11	1.65	0.465	0.0069	8.05	327
B12	1.69	0.434	0.0074	8.13	336
B13	1.64	0.443	0.0072	8.09	325
SGW				8.00	300

Table B-2. Summary of Conditions for Interbed Material Packed Columns

Column ID	ρ (g/cm^3)	n	u (cm/sec)	Eluent pH	Eluent Specific Conductivity (μS/cm)
IB01	1.65	0.446	0.0072	8.48	345
IB02	1.69	0.428	0.0075	8.46	333
IB05	1.69	0.413	0.0072	8.62	368
IB06	1.78	0.399	0.008	8.36	421
IB07	1.74	0.405	0.0079	8.57	354
IB08	1.72	0.413	0.0077	8.72	323
IB09	1.78	0.389	0.0082	8.51	355
SGW				8.00	300

Appendix C

Appendix C

Radionuclide Sources Used in the Preparation of Spike Solutions for Column and Batch Tests at Clemson University

Isotope	Chemical Form	Solution
^{3}H	HTO	H_20
^{60}Co	$CoCl_2$	0.5 N HCl
^{90}Sr	$SrCl_2$	0.5 N HCl
^{137}Cs	CsCl	0.1 N HCl
^{233}U	$UO_2(NO_3)_2$	0.1 NHCl
^{239}Pu	$Pu(NO_3)_4$	4.0 N HNO_3
^{241}Am	$AmCl^3$	0.1 N HCl

Initial Column and Input Tracer Levels for the Unsaturated Flow Experiments

Column ID	Tracer	Background Tracer Level (C)	Input Tracer Level (C0)	Initial C/C(0)
BR1	Br	0.0685 mg/L	24.90 mg/L	0.0028
BR2	Br	0.074 mg/L	24.33 mg/L	0.003
BR3	Br	0.042 mg/L	23.35 mg/L	0.0018
SR4	Sr	2.20 µg/L	469.37 µg/L	0.0047
SR5	Sr	7.71 µg/L	496.53 µg/L	0.0155
SR6	Sr	18.10 µg/L	495.56 µg/L	0.0365
SR7	Sr	2.60 µg/L	476.68 µg/L	0.0055

Appendix D

Appendix D

Plutonium Oxidation State Analyses

Thenoyltriflouracetone (TTA) Extraction Method

Preparation

1. Dissolve 2.22 g of the 99% TTA in 20 mL of toluene in a glass scintillation vial that has been covered in aluminum foil to prevent exposure of the solution to light. This will yield a solution of 0.5 M TTA. This solution will photo-decompose, turning from pale yellow to copper in color, so it should be made just prior to use and stored in a drawer away from light.

2. Prepare five 20 mL plastic liquid scintillation vials by filling each with 10 mL of Highsafe 2, or an appropriate scintillation cocktail. These should be analyzed using two separate protocols due to the difference in quench for the solutions. One protocol should be used for the TTA/organic samples and another for the aqueous samples.

Procedure

3. Transfer a 0.5 mL aliquot of the sample solution to each of two, 2 dram vials.
4. Add 0.5 mL of 0.75 M HNO_3 to one vial (pH = 0.6) and 0.5 mL of 0.5 M acetate buffer solution to the other vial (pH = 4.5), taking care to mark the vials accordingly. It is important to move rapidly through the following steps, since oxidation state changes may begin to occur once the pH is adjusted.
5. Gently swirl the liquids in each vial to ensure mixing.
6. Add 1.0 mL of 0.5 M TTA to each vial, cap tightly and shake vigorously for 5 minutes.
7. Centrifuge both vials to facilitate phase separation.
8. Working with one vial at a time, transfer 250 µL of the organic phase (TTA: the upper most liquid layer in the vial) to a 20 mL scintillation vial containing 10 mL of Highsafe 2, or an appropriate scintillation cocktail. Cap and mix well.
9. Using a micro-pipettor, transfer about 0.5 mL of the aqueous phase (the bottom most liquid layer in the vial) from the original reaction vial to a clean 2 dram vial. It is best to depress the pipettor piston while probing through the organic layer, thus using the air bubble stream to keep the organic phase from wetting and contaminating the inside of the pipette tip. After retrieving the aqueous phase sample, purge a small amount back into the original vial to remove any organic phase which may have attached to the end of the pipette tip.
10. Transfer 250 µL of the freshly separated aqueous phase to another of the scintillation vials containing Highsafe 2 for counting. Cap and mix well.
11. Repeat steps 6 through 8 for the second reaction vial.
12. Transfer 250 mL of the original sample solution to a scintillation vial containing Highsafe 2. This will serve as the reference to ensure that all activity is accounted for.
13. Count the scintillation vials.

Di-(2-ethylhexyl)-orthophosphoric acid (HDEHP) Extraction Method

Description

This process involves four separate extractions, which when combined will yield an oxidation state distribution for an aqueous sample of plutonium solution. The four extractions are as follows:

1. Extraction of Pu (IV) into an organic phase.
2. Extraction of Pu(III) and Pu(IV) into an organic phase.
3. Extraction of Pu(IV) and Pu(VI) into an organic phase.
4. Extraction of Pu(III), Pu(IV), Pu(V), and Pu(VI) into an organic phase. The Pu remaining in the aqueous phase is termed "unextractable" and is assumed to be in the Pu (IV) polymeric form.

Preparation

1. Dissolve 2.22 g of the 99% TTA in 20 mL of toluene in a glass scintillation vial that has been covered in aluminum foil to prevent exposure of the solution to light. This will yield a solution of 0.5 M TTA. This solution will photo-decompose, turning from pale yellow to copper in color, so it should be made just prior to use and stored in a drawer away from light.

2. Transfer 3.225 g (3.3 mL) of HDEHP solution into 20 mL of toluene to yield a solution of 0.5 M HDEHP.

3. Add 0.02354 g of $K_2Cr_2O_7$ to 20 mL of 1.0 M HCl to yield a solution that is 1.0 M HCL and 4.0 mM $K_2Cr_2O_7$ (8.0 mM Cr (VI)).

4. Prepare nine 20 mL plastic liquid scintillation vials by filling each with 10 mL of Highsafe 2, or an appropriate scintillation cocktail. These should be analyzed using two separate protocols due to the difference in quench for the solutions. One protocol should be used for the TTA/organic samples and another for the aqueous and HDPEHP/organic samples.

Procedure

1. Transfer a 0.25 mL aliquot of the plutonium solution to one of the scintillation vials filled with Highsafe 2 to determine the total plutonium concentration in the original sample.

Extraction 1 - Determination of Pu(IV)

2. Transfer 0.5 mL of the TTA/toluene solution to one of the 2 dram vials.
3. Add 0.5 mL of 1.0 M HCL solution to this 2 dram vial.

4. To a second 2 dram vial, add 0.1 mL of 5.0 M HCL solution.
5. Add 0.5 mL of the plutonium sample solution to the vial containing the 5.0 M HCL and gently swirl to ensure complete mixing.
6. Pour the contents of the vial containing the TTA solution into the vial containing the plutonium sample solution. Be sure to completely empty both the aqueous and organic phases for the vial. Cap the vial and shake gently for 2 min. and 20 sec to ensure complete extraction.
7. Centrifuge the vial to facilitate phase separation. Be sure to carefully counterbalance the centrifuge.
8. Place 0.25 mL of the organic phase (Pu(IV)) into one of the scintillation vials filled with Highsafe 2.
9. Transfer 0.5 mL of the aqueous phase into a clean 2 dram vial. Depress the pipettor as the tip travels through the organic phase, so that the air stream prevents the introduction of any organic phase into the sample. Now transfer 0.25 mL of this aqueous solution (Pu(III), Pu(V), Pu(VI), and polymeric plutonium) into one of the scintillation vials filled with Highsafe 2, again being cautious to avoid drawing any of the thin film of organic phase from the top of the sample.

Extraction 2 - Determination of Pu(III and IV)
Note extraction 2 is identical to extraction 1, with the exception of substituting a 1.0 M HCl/4.0 mM $K_2Cr_2O_7$ solution for the 1.0 M HCL solution from step 2 in step 11. This serves to oxidize any Pu(III) to Pu(VI), which will subsequently be extracted into the TTA/organic phase.

10. Transfer 0.5 mL of the TTA/toluene solution to one of the 2 dram vials.
11. Add 0.5 mL of 1.0 M HCL/4.0 M $K_2Cr_2O_7$ solution to this 2 dram vial.
12. To a second 2 dram vial, add 0.1 mL of 5.0 M HCL solution.
13. Add 0.5 mL of the plutonium sample solution to the vial containing the 5.0 M HCL and gently swirl to ensure complete mixing.
14. Pour the contents of the vial containing the TTA solution into the vial containing the plutonium sample solution. Be sure to completely empty both the aqueous and organic phases for the vial. Cap the vial and shake gently for 2 min. and 20 sec to ensure complete extraction.
15. Centrifuge the vial to facilitate phase separation. Be sure to carefully counterbalance the centrifuge.
16. Place 0.25 mL of the organic phase (Pu(IV)) into one of the scintillation vials filled with Highsafe 2.
17. Transfer 0.5 mL of the aqueous phase into a clean 2 dram vial. Depress the pipettor as the tip travels through the organic phase, so that the air stream prevents the introduction of any organic phase into the sample. Now transfer 0.25 mL of this aqueous solution (Pu(III), Pu(V), Pu(VI), and polymeric plutonium) into one of the scintillation vials filled with Highsafe 2, again being cautious to avoid drawing any of the thin film of organic phase from the top of the sample.

Extraction 3 - Determination of Pu (IV and VI)

Note that extraction 3 is identical to extraction 1 except for the substitution of a 0.5 M HDEHP/toluene solution for the TTA/toluene solution from steps 1 in step 18. The HDEHP will extract both Pu(IV) and Pu (VI) from the aqueous phase.

18. Transfer 0.5 mL of the HDEHP/toluene solution to one of the 2 dram vials.
19. Add 0.5 mL of 1.0 M HCL solution to this 2 dram vial.
20. To a second 2 dram vial, add 0.1 mL of 5.0 M HCL solution.
21. Add 0.5 mL of the plutonium sample solution to the vial containing the 5.0 M HCL and gently swirl to ensure complete mixing.
22. Pour the contents of the vial containing the TTA solution into the vial containing the plutonium sample solution. Be sure to completely empty both the aqueous and organic phases for the vial. Cap the vial and shake gently for 2 min. and 20 sec to ensure complete extraction.
23. Centrifuge the vial to facilitate phase separation. Be sure to carefully counterbalance the centrifuge.
24. Place 0.25 mL of the organic phase (Pu(IV)) into one of the scintillation vials filled with Highsafe 2.
25. Transfer 0.5 mL of the aqueous phase into a clean 2 dram vial. Depress the pipettor as the tip travels through the organic phase, so that the air stream prevents the introduction of any organic phase into the sample. Now transfer 0.25 mL of this aqueous solution (Pu(III), Pu(V), Pu(VI), and polymeric plutonium) into one of the scintillation vials filled with Highsafe 2, again being cautious to avoid drawing any of the thin film of organic phase from the top of the sample.

Extraction 4 - Determination of Pu (III, IV, V, and VI)
Note extraction 4 is identical to extraction 2 except for the substitution of HDEHP/toluene for the TTA/toluene solution from step 10 in step 26. In this extraction, the dichromate solution oxidizes the Pu(III to Pu(IV) and the Pu(V) to Pu(VI), both of which are subsequently extracted by the HDEHP.

26. Transfer 0.5 mL of the HDEHP/toluene solution to one of the 2 dram vials.
27. Add 0.5 mL of 1.0 M HCL/4.0 M $K_2Cr_2O_7$ solution to this 2 dram vial.
28. To a second 2 dram vial, add 0.1 mL of 5.0 M HCL solution.
29. Add 0.5 mL of the plutonium sample solution to the vial containing the 5.0 M HCL and gently swirl to ensure complete mixing.
30. Pour the contents of the vial containing the TTA solution into the vial containing the plutonium sample solution. Be sure to completely empty both the aqueous and organic phases for the vial. Cap the vial and shake gently for 2 min. and 20 sec to ensure complete extraction.
31. Centrifuge the vial to facilitate phase separation. Be sure to carefully counterbalance the centrifuge.
32. Place 0.25 mL of the organic phase (Pu(IV)) into one of the scintillation vials filled with Highsafe 2.
33. Transfer 0.5 mL of the aqueous phase into a clean 2 dram vial. Depress the pipettor as the tip travels through the organic phase, so that the air stream prevents the

introduction of any organic phase into the sample. Now transfer 0.25 mL of this aqueous solution (Pu(III), Pu(V), Pu(VI), and polymeric plutonium) into one of the scintillation vials filled with Highsafe 2, again being cautious to avoid drawing any of the thin film of organic phase from the top of the sample.

34. Count each sample for 10 minutes using the Wallac liquid scintillation detector. Determination of the oxidation state distribution may be obtained via a mass balance on plutonium during each extraction step.

Appendix E

Appendix E

Fitted Parameters from the CXTFIT Equilibrium Model for ^{3}H in Crushed Basalt and Interbed Material Packed Columns at Clemson University

Isotope	Media	Column ID	Percent Recovery	D (cm^2/sec)	R
^{3}H	Basalt	B02	91.0	0.0017	0.931
		B03	101	0.0021	0.936
		B07	101.8	0.0008	1.06
		B08	96.9	0.0009	0.968
		B10	99.3	0.0012	1.04
		B11	96.2	0.0013	1.02
		B12	111	0.0009	1.03
		B13	124	0.0009	0.972
		mean	103.2	0.0013	0.985
^{3}H	Interbed	IB01	110	0.0008	1.0
		IB02	106	0.0005	0.99
		IB05	90.2	0.0018	1.06
		IB06	99.4	0.0008	1.05
		IB07	101.5	0.0008	1.06
		IB08	100	0.0005	1.05
		IB09	95.7	0.0012	1.06
		mean	101.5	0.0008	1.035

Breakthrough of ^{3}H in Crushed Basalt and Interbed Material Packed Columns at Clemson University

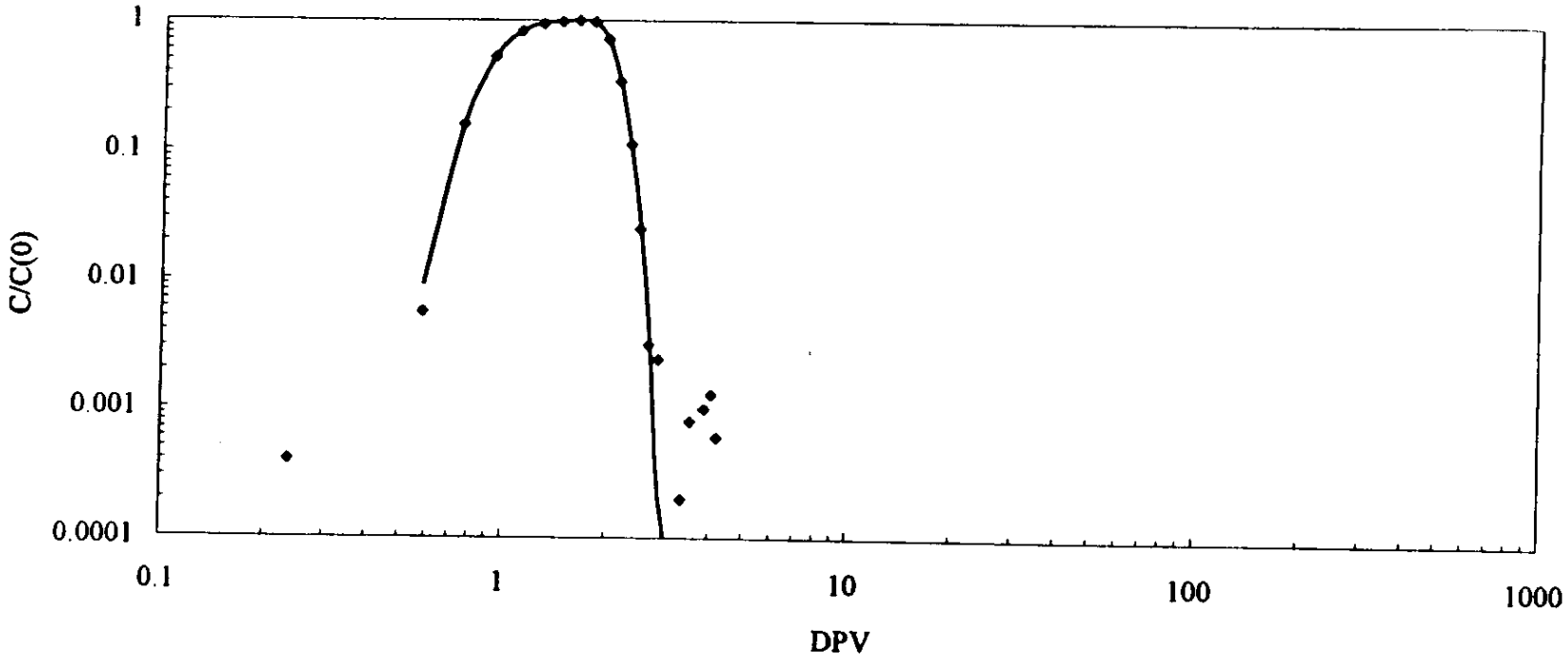

Figure E-1. Breakthrough of ^{3}H (91% recovery) in crushed basalt packed column B03. The diamond shapes represent data points and the line represents the CXTFIT equilibrium model fit.

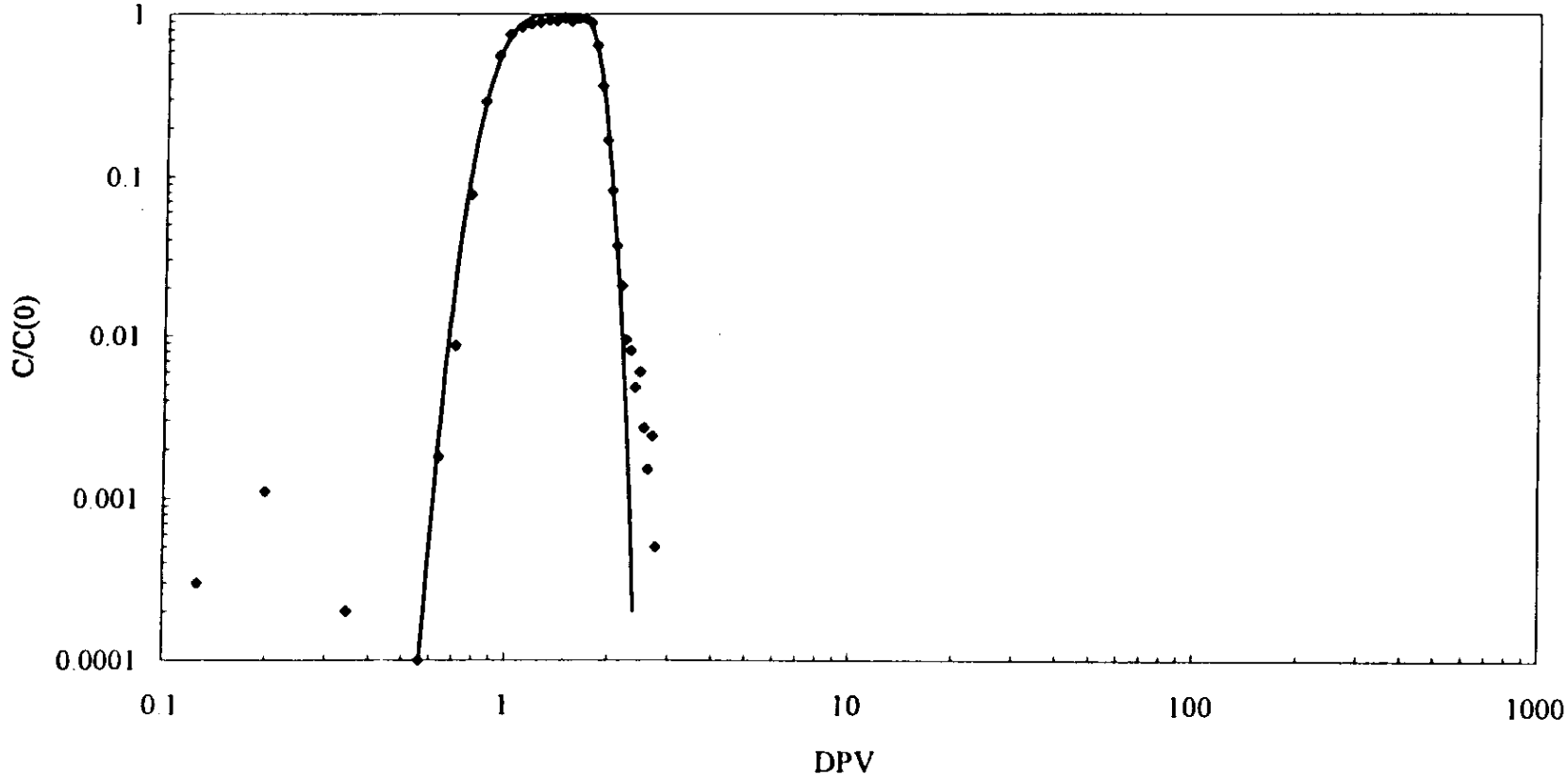

Figure E-2. Breakthrough of ^{3}H (91% recovery) in crushed basalt packed column B02. The diamond shapes represent data points and the line represents the CXTFIT equilibrium model fit.

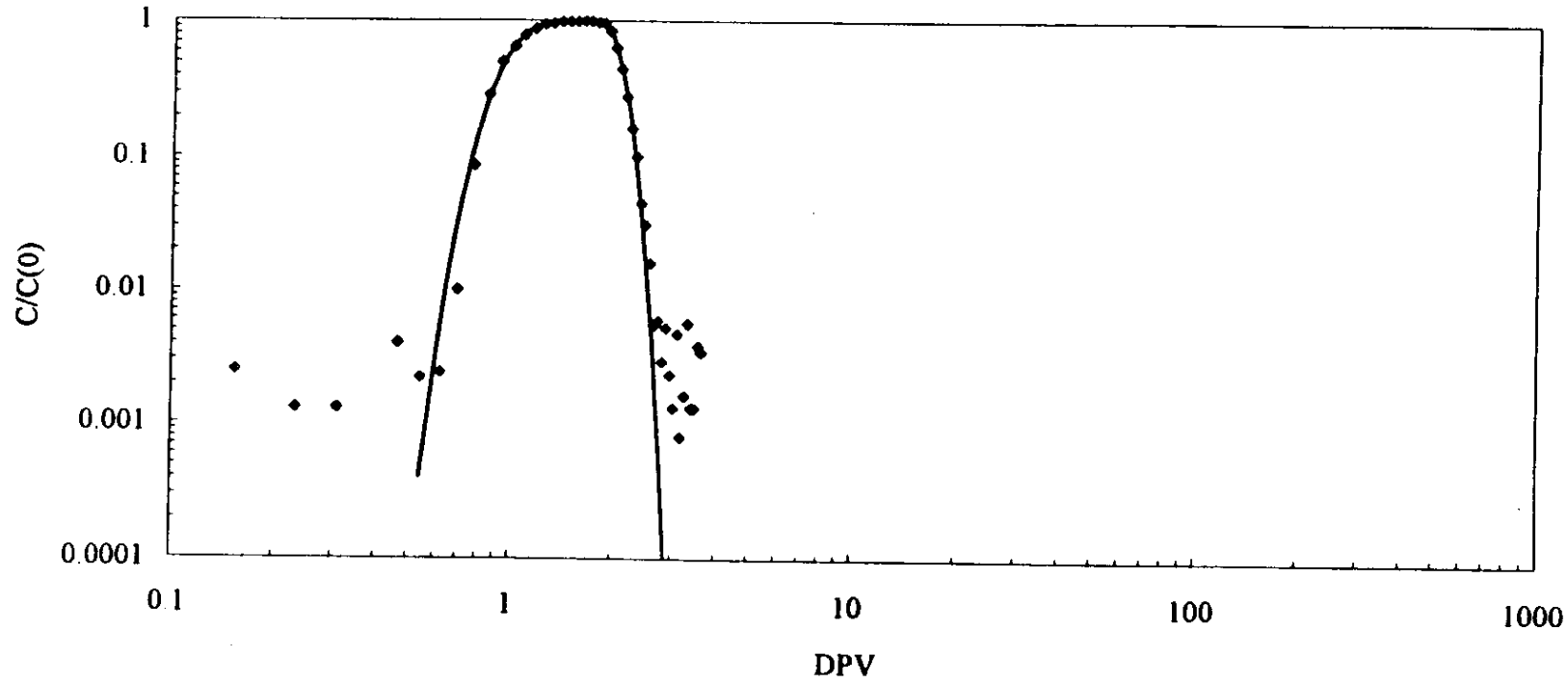

Figure E-3. Breakthrough of ^{3}H (101.8% recovery) in crushed basalt packed column B07. The diamond shapes represent data points and the line represents the CXTFIT equilibrium model fit.

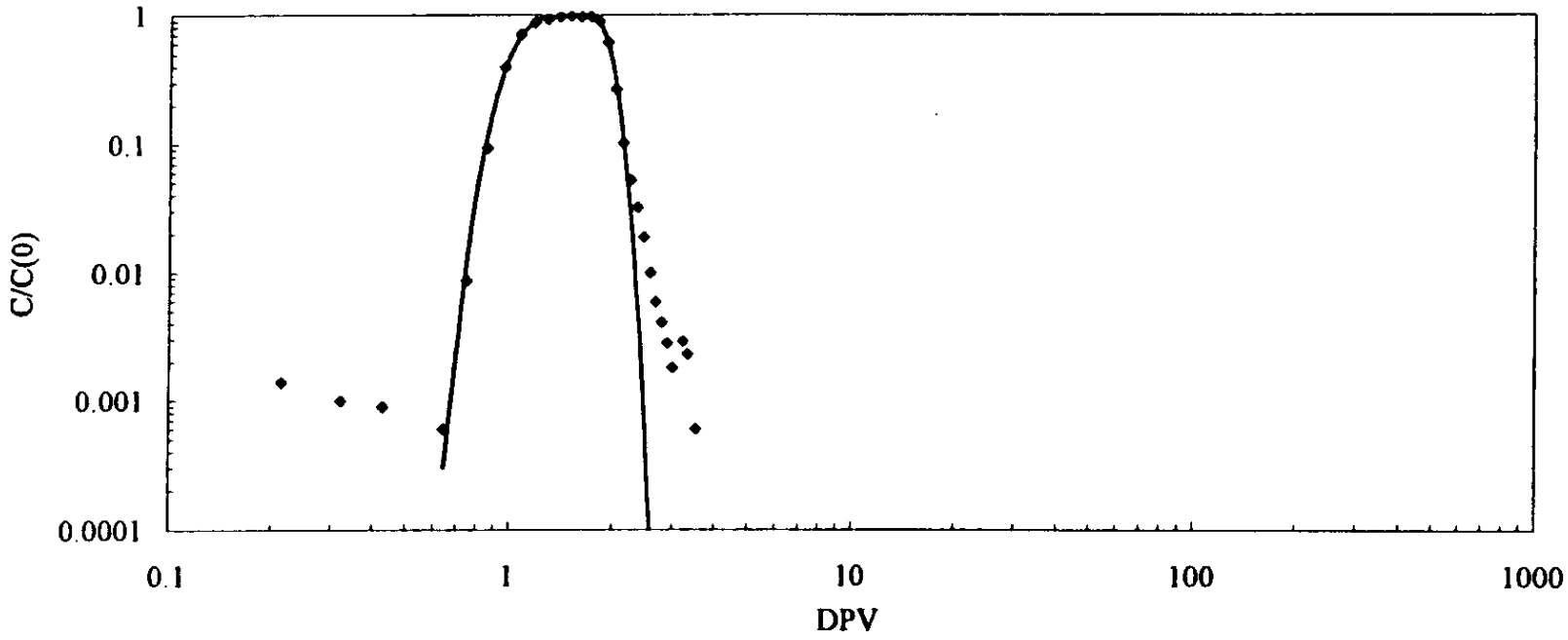

Figure E-4. Breakthrough of ^{3}H (102.2% recovery) in crushed basalt packed column B09. The diamond shapes represent data points and the line represents the CXTFIT equilibrium model fit.

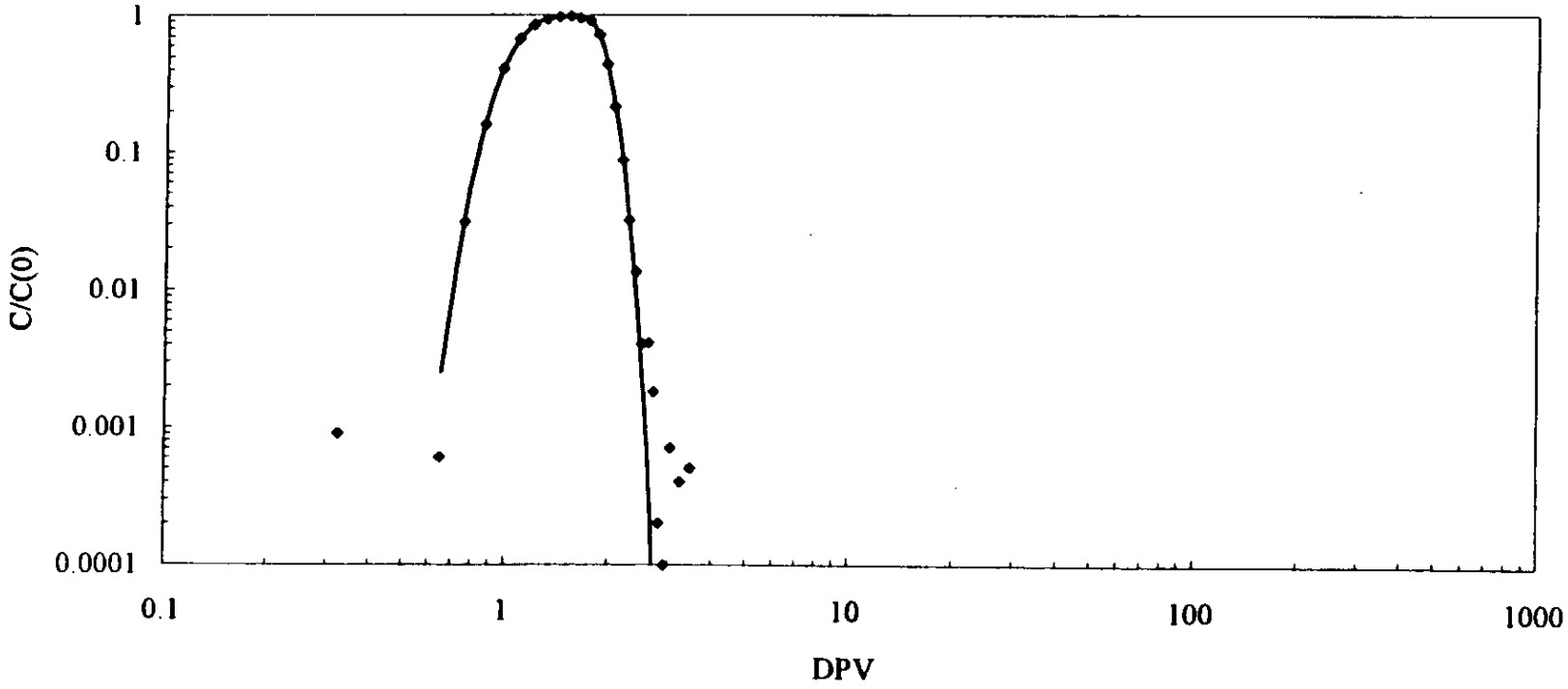

Figure E-5. Breakthrough of ^{3}H (96.2% recovery) in crushed basalt packed column B11. The diamond shapes represent data points and the line represents the CXTFIT equilibrium model fit.

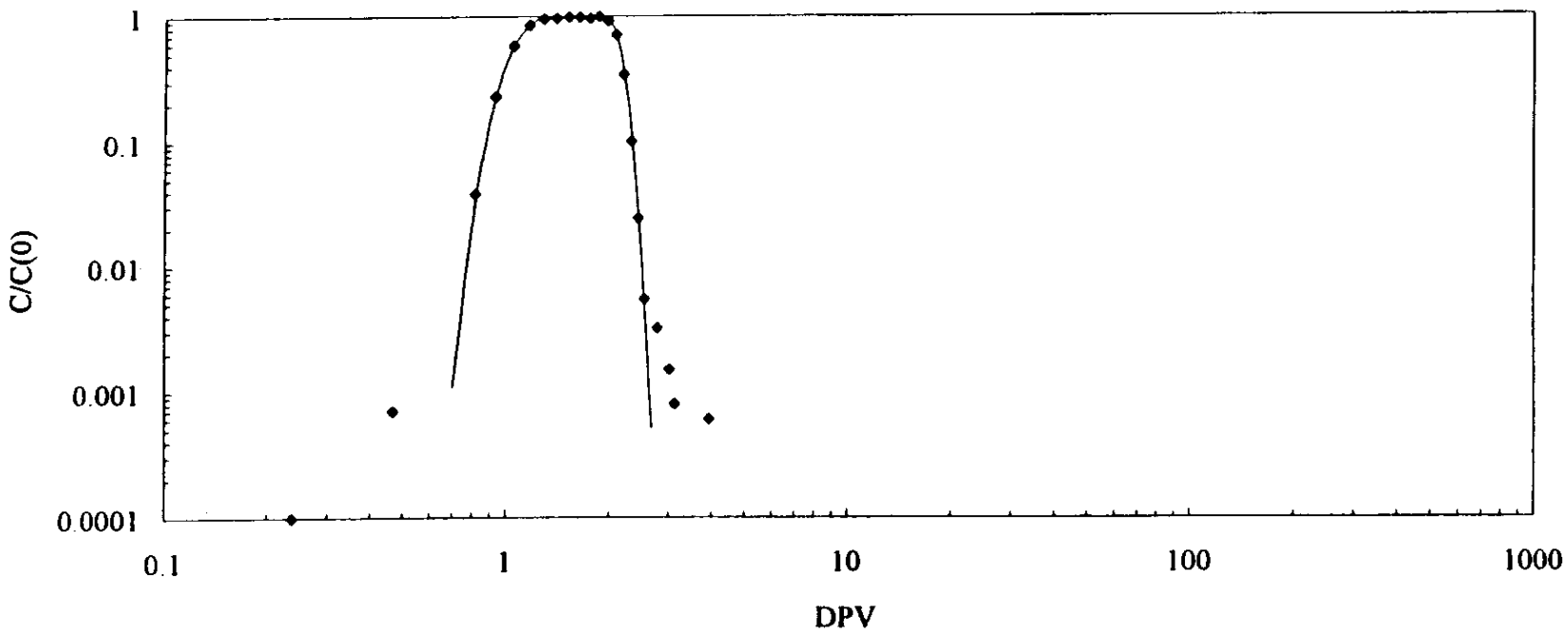

Figure E-6. Breakthrough of ^{3}H (111% recovery) in crushed basalt packed column B12. The diamond shapes represent data points and the line represents the CXTFIT equilibrium model fit.

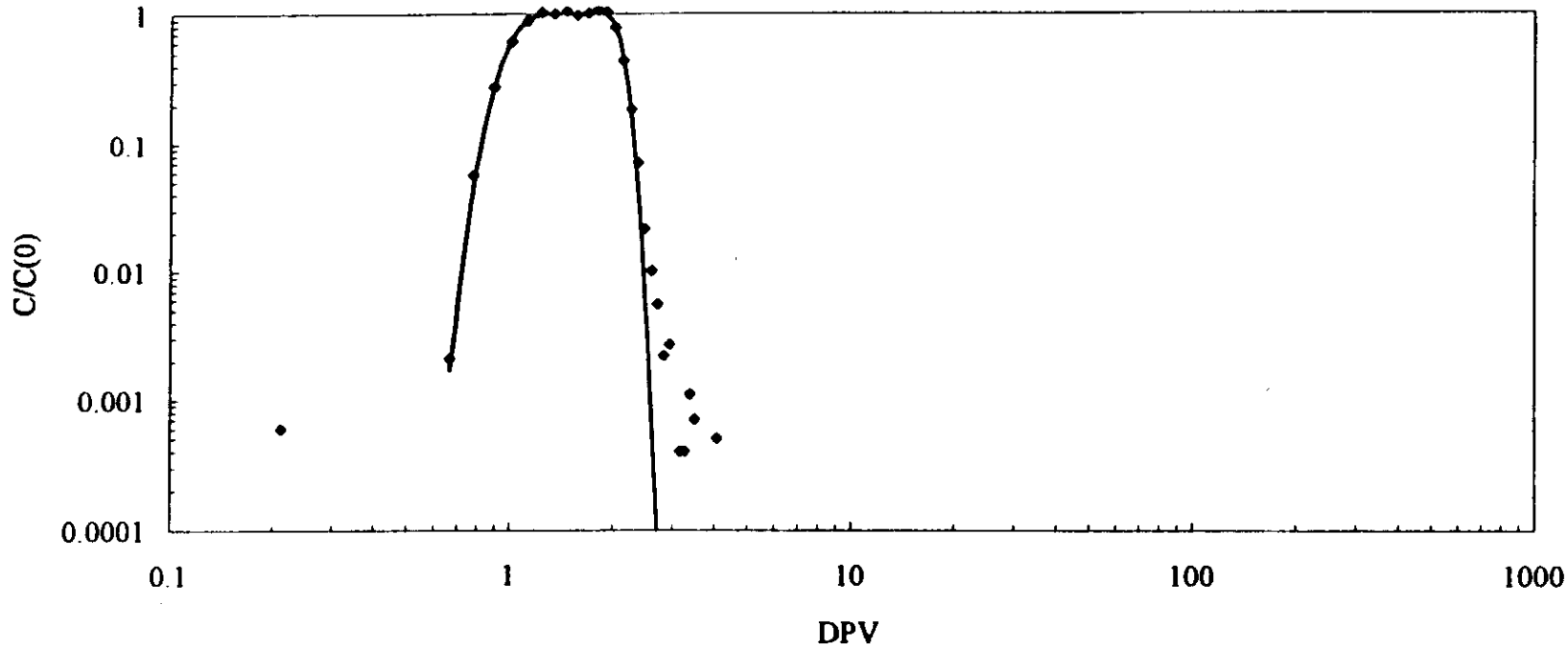

Figure E-7. Breakthrough of ^{3}H (124% recovery) in crushed basalt packed column B13. The diamond shapes represent data points and the line represents the CXTFIT equilibrium model fit.

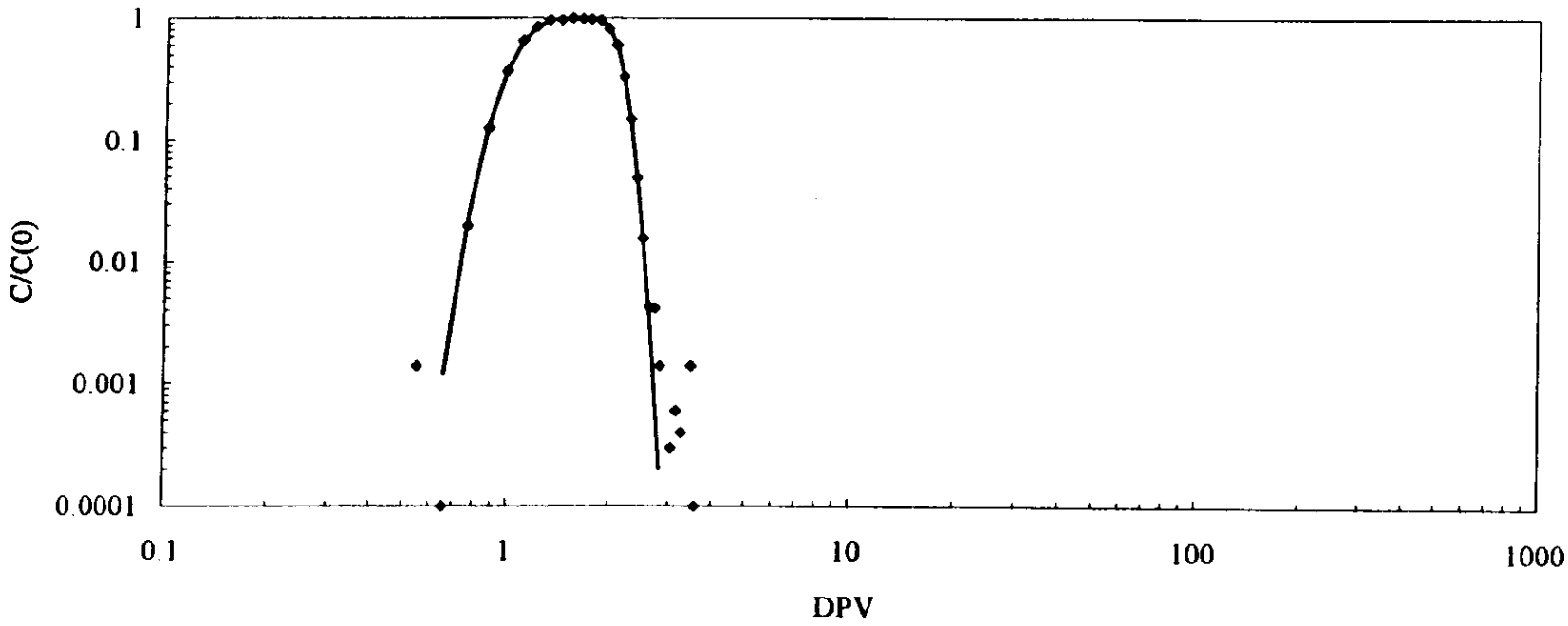

Figure E-8. Breakthrough of ^{3}H (99.3% recovery) in crushed basalt packed column B10. The diamond shapes represent data points and the line represents the CXTFIT equilibrium model fit.

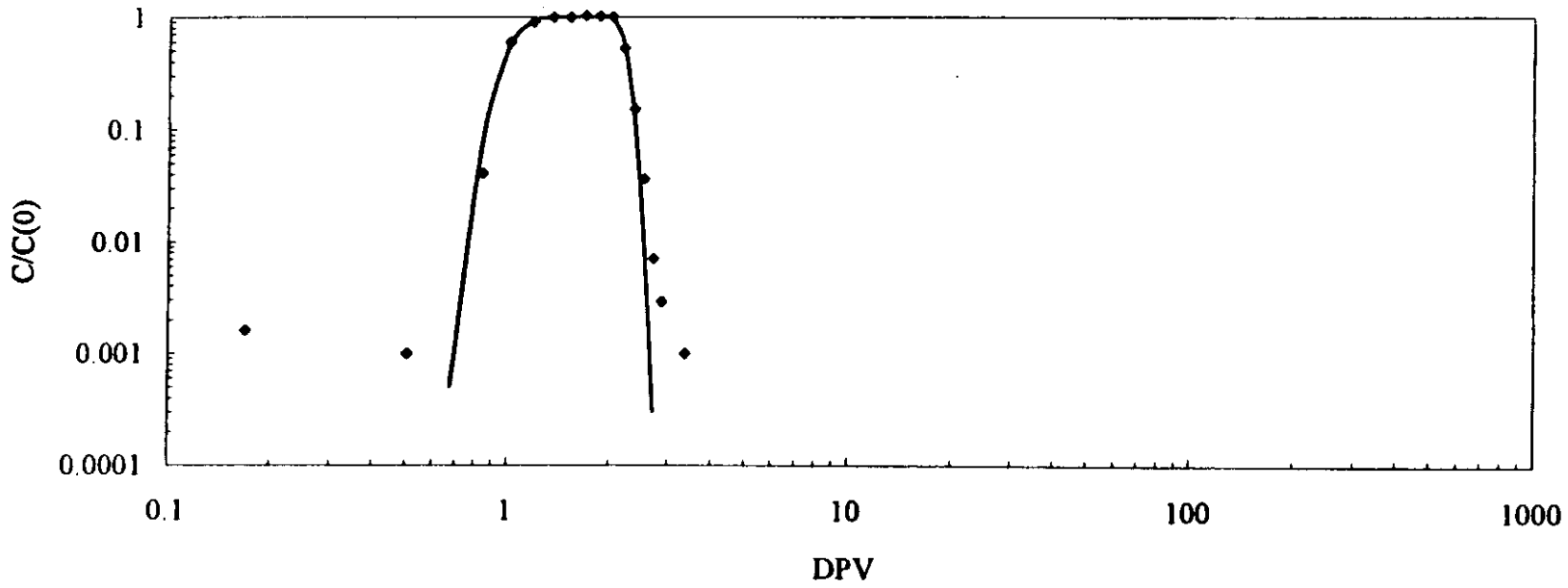

Figure E-9. Breakthrough of ^{3}H (110% recovery) in interbed material packed column IB01. The diamond shapes represent data points and the line represents the CXTFIT equilibrium model fit.

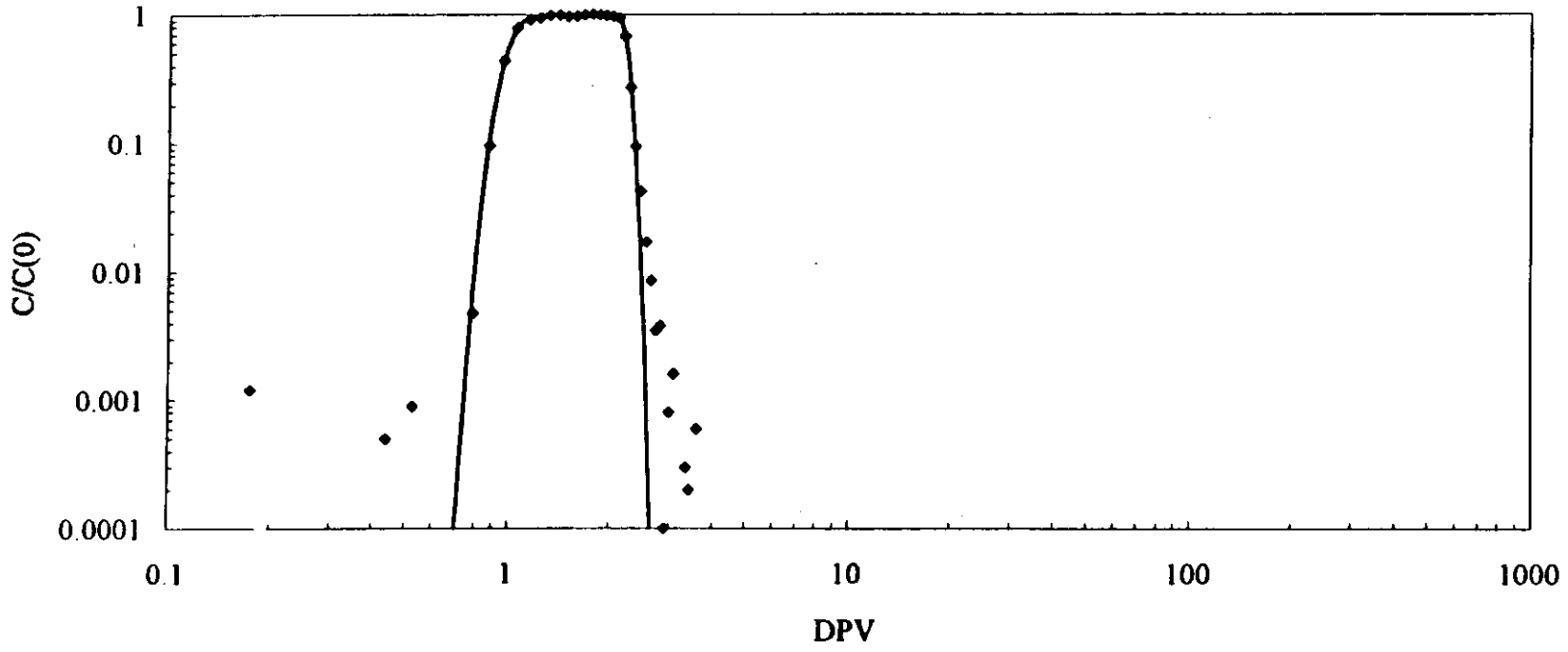

Figure E-10. Breakthrough of ^{3}H (106% recovery) in interbed material packed column IB02. The diamond shapes represent data points and the line represents the CXTFIT equilibrium model fit.

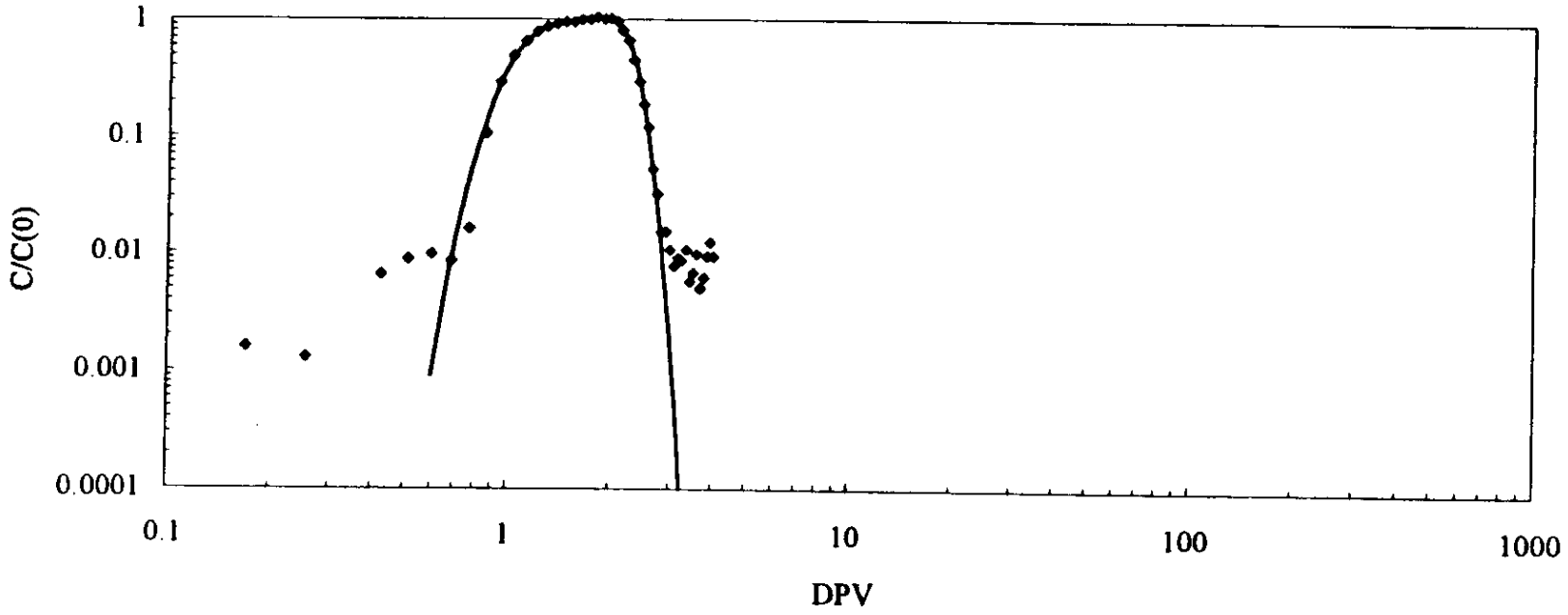

Figure E-11. Breakthrough of ^{3}H (98.2% recovery) in interbed material packed column IB05. The diamond shapes represent data points and the line represents the CXTFIT equilibrium model fit.

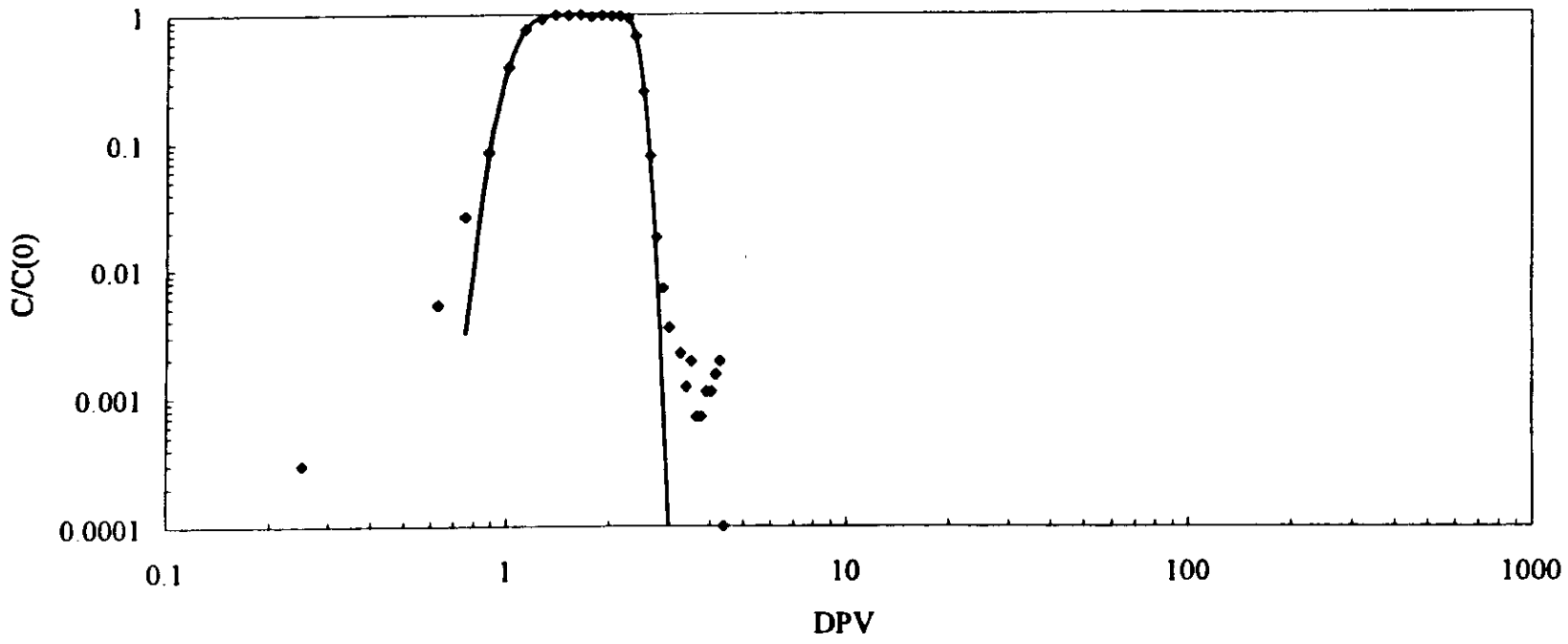

Figure E-12. Breakthrough of ^{3}H (99.4% recovery) in interbed material packed column IB06. The diamond shapes represent data points and the line represents the CXTFIT equilibrium model fit.

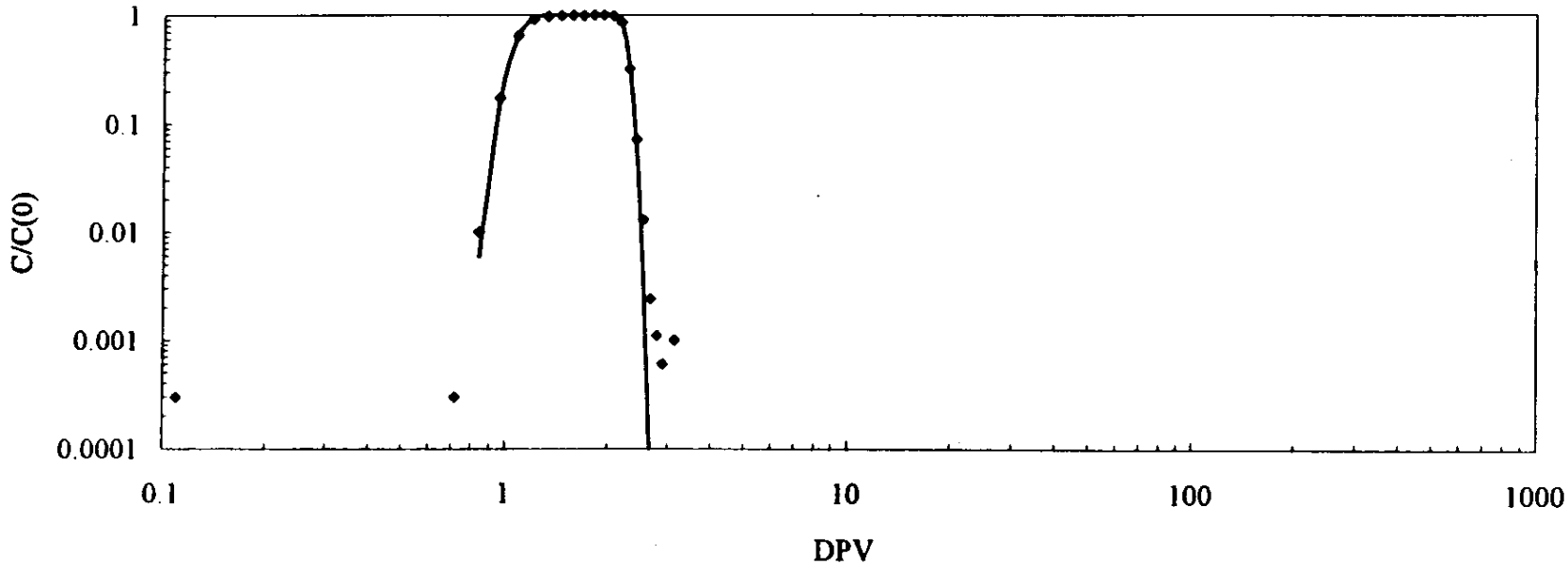

Figure E-13. Breakthrough of ^{3}H (100% recovery) in interbed material packed column IB08. The diamond shapes represent data points and the line represents the CXTFIT equilibrium model fit.

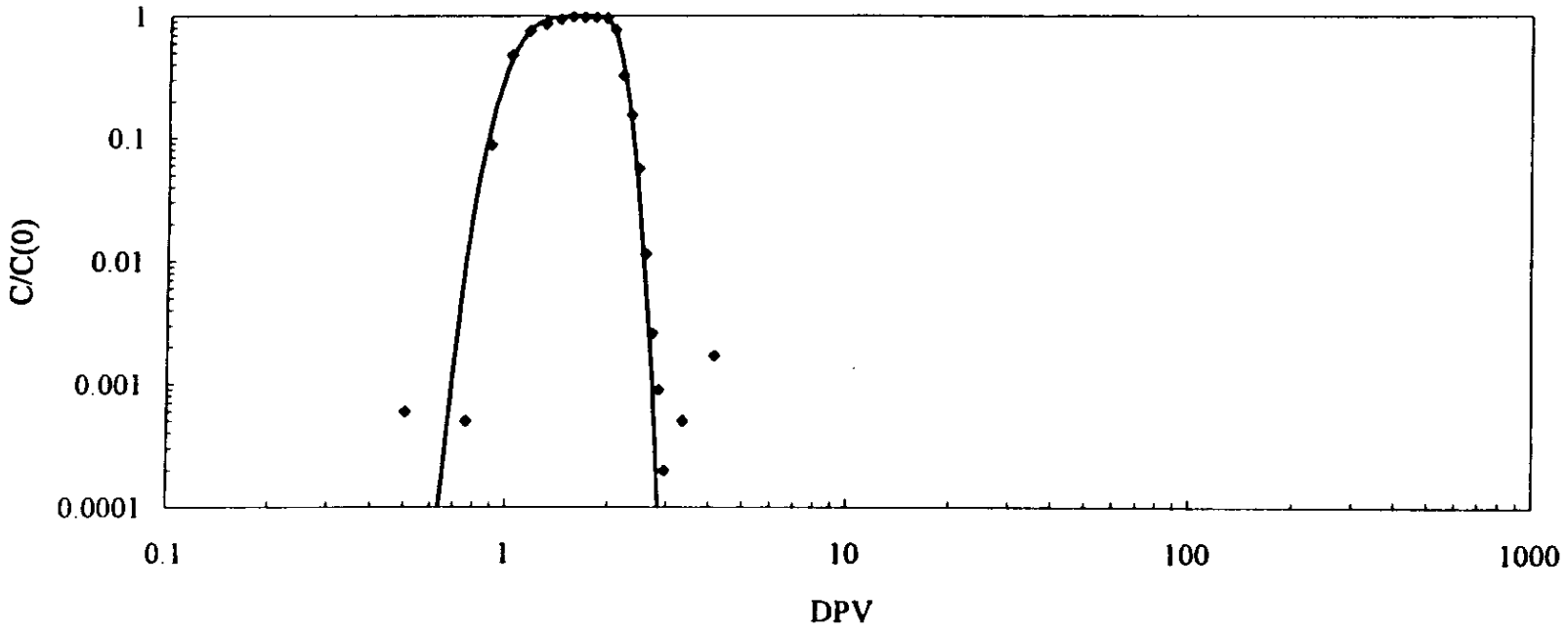

Figure E-14. Breakthrough of ^{3}H (95.7% recovery) in interbed material packed column IB09. The diamond shapes represent data points and the line represents the CXTFIT equilibrium model fit.

Appendix F

Appendix F

Breakthrough Curves for Am, Cs, Co, Pu, Sr, and U in Crushed Basalt and Interbed Material Columns at Clemson University

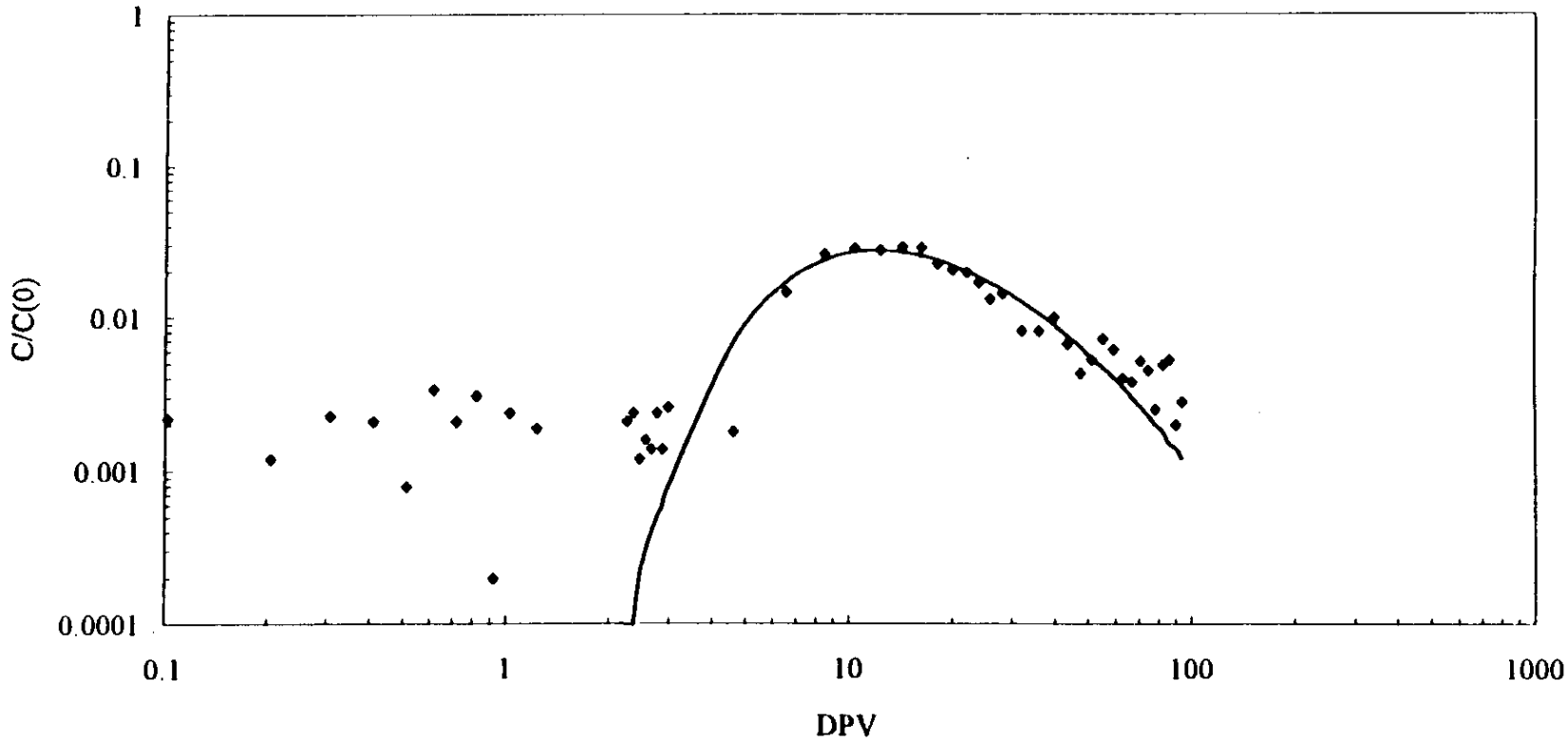

Figure F-1. Breakthrough of ^{90}Sr (43% recovery) in crushed basalt packed column B08. The diamond shapes represent data points and the line represents the CXTFIT equilibrium model fit.

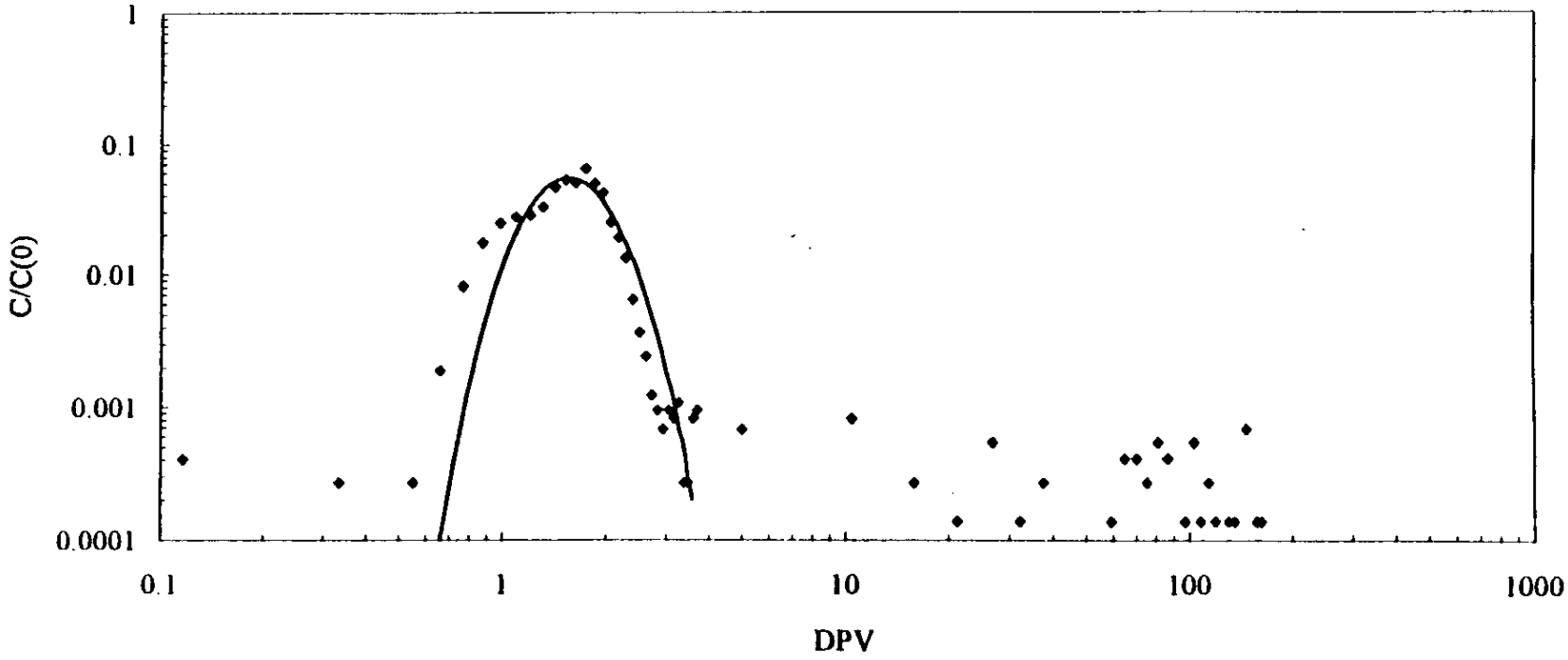

Figure F-2. Breakthrough of an enhanced mobile fraction of ^{241}Am (9% recovery) in crushed basalt packed column B10. The diamond shapes represent data points and the line represents the CXTFIT equilibrium model fit.

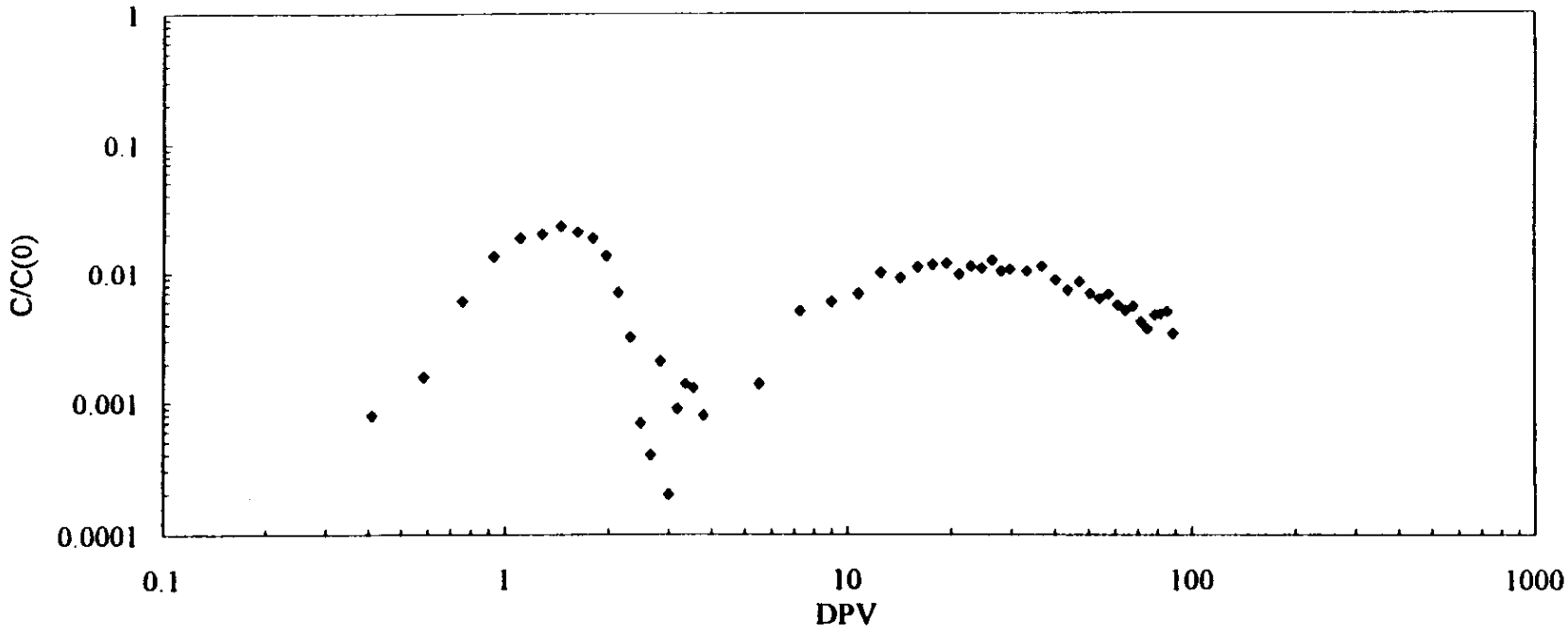

Figure F-3. Breakthrough of two distinct fractions of ^{60}Co (2.4 and 55.1 % recovery) in crushed basalt packed column B03. The diamond shapes represent data points and the line represents the CXTFIT equilibrium model fit.

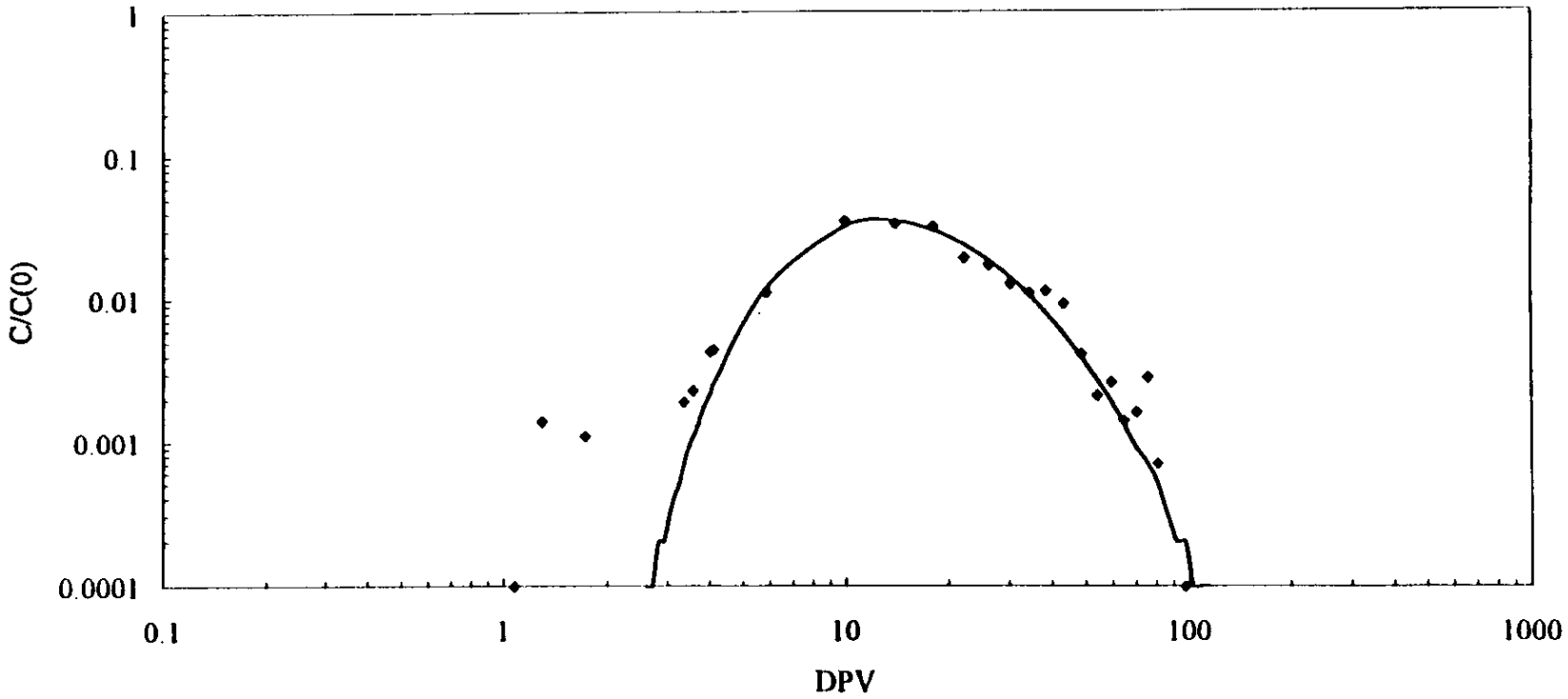

Figure F-4. Breakthrough of ^{90}Sr (43% recovery) in crushed basalt packed column B11. The diamond shapes represent data points and the line represents the CXTFIT equilibrium model fit.

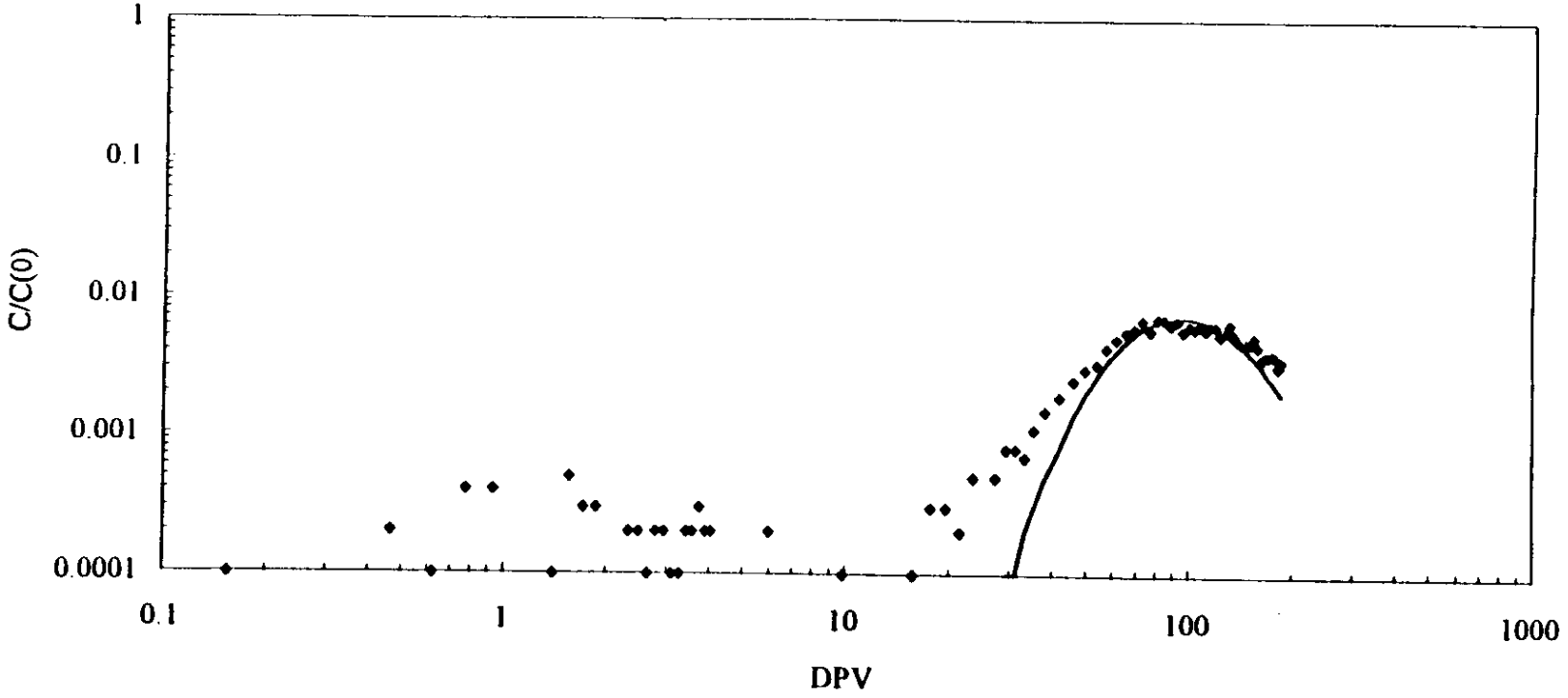

Figure F-5. Breakthrough of ^{137}Cs (67.1% recovery) in crushed basalt packed column B07. The diamond shapes represent data points and the line represents the CXTFIT equilibrium model fit.

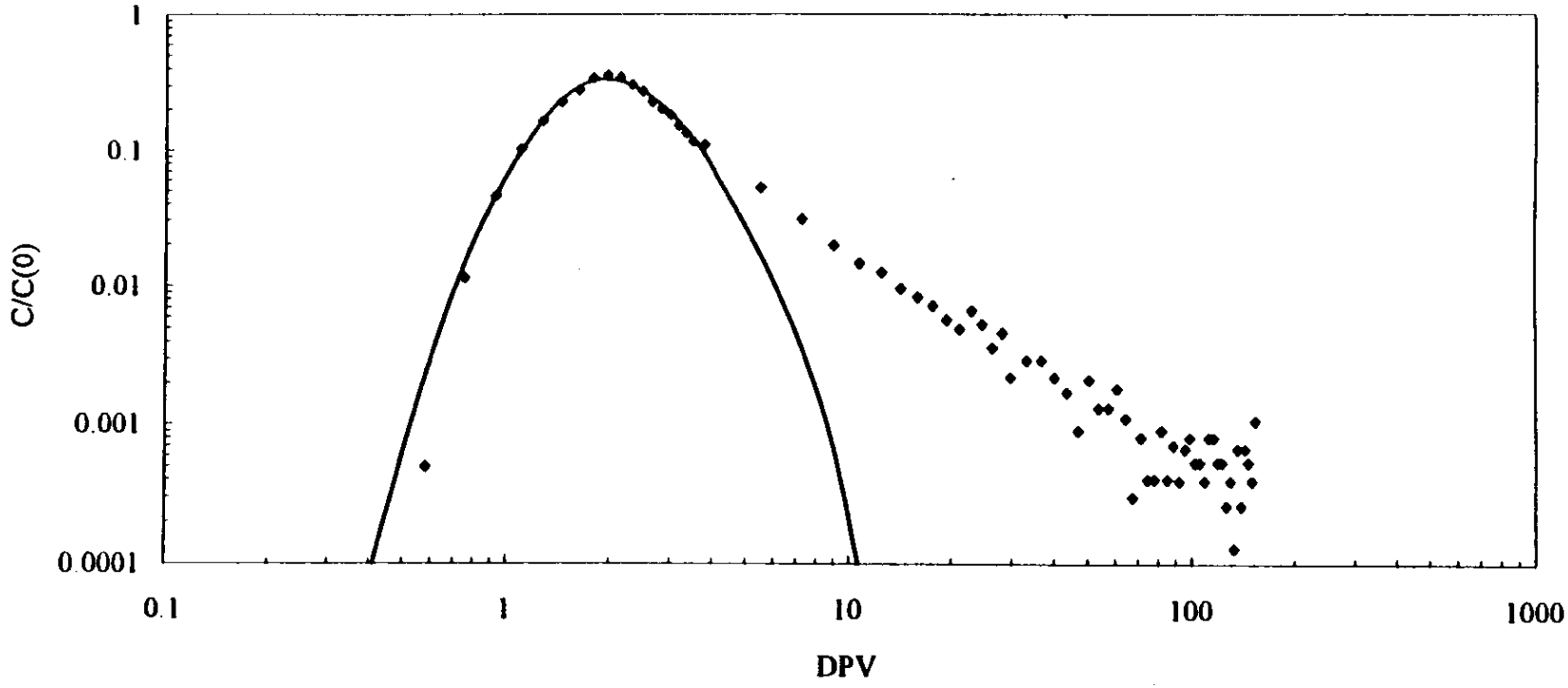

Figure F-6. Breakthrough of ^{233}U (104% recovery) in crushed basalt packed column B03. The diamond shapes represent data points and the line represents the CXTFIT equilibrium model fit.

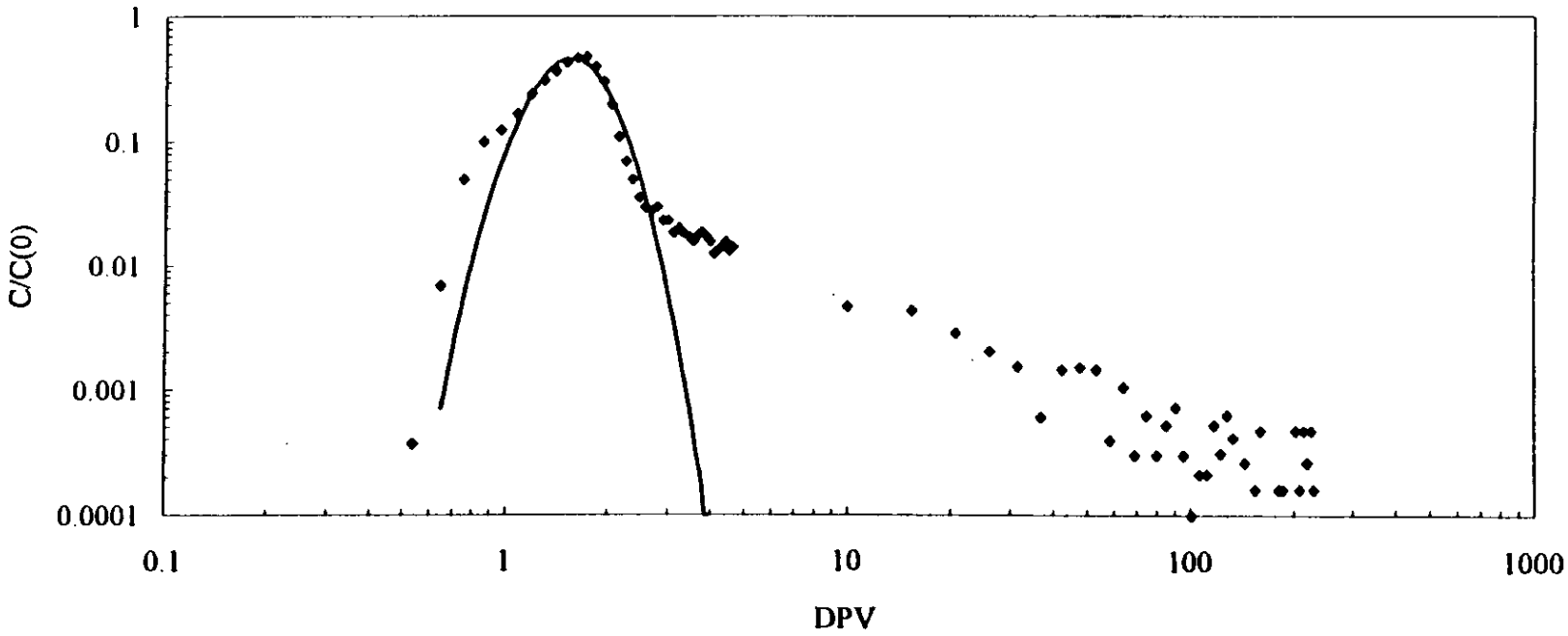

Figure F-7. Breakthrough of an enhanced mobile fraction of ^{239}Pu (57% recovery) in crushed basalt packed column B09. The diamond shapes represent data points and the line represents the CXTFIT equilibrium model fit.

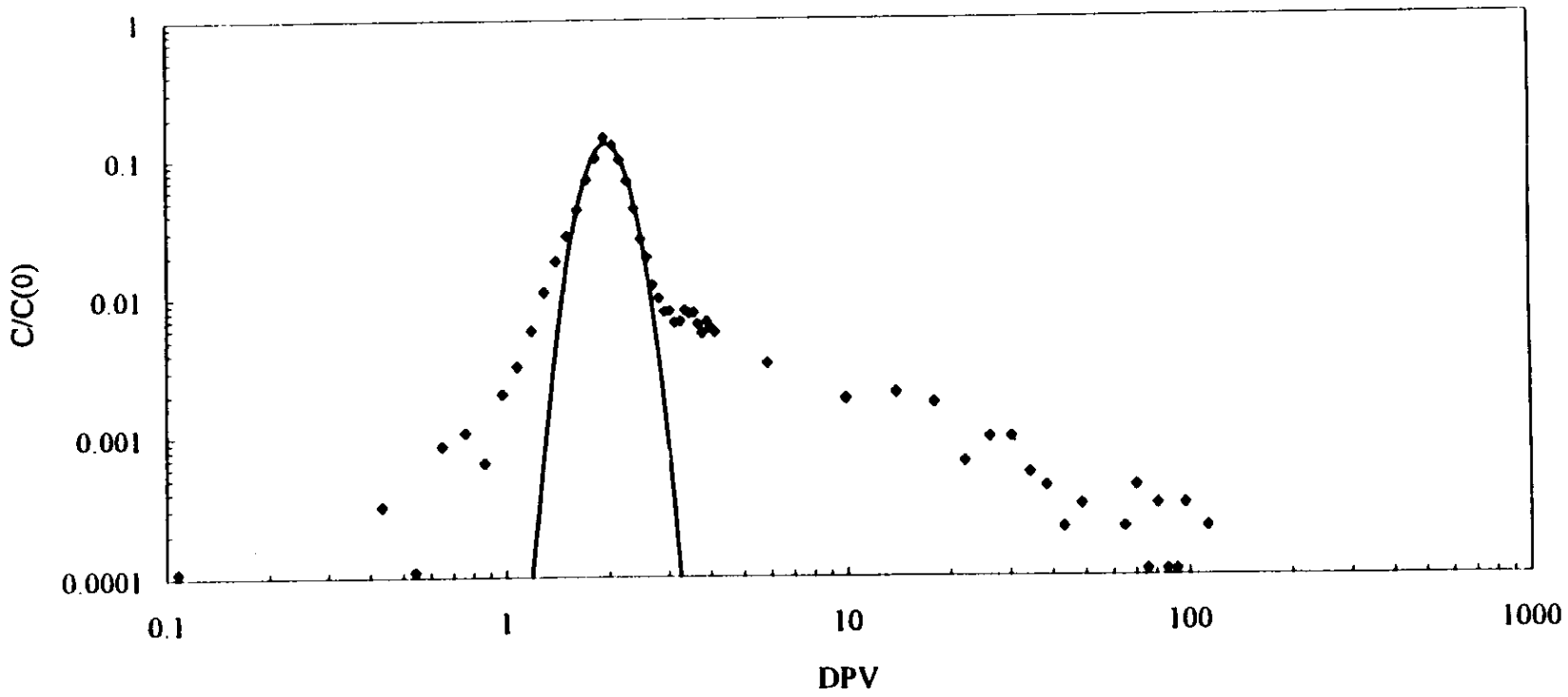

Figure F-8. Breakthrough of an enhanced mobile fraction of ^{239}Pu (10% recovery) in crushed basalt packed column B11. The diamond shapes represent data points and the line represents the CXTFIT equilibrium model fit.

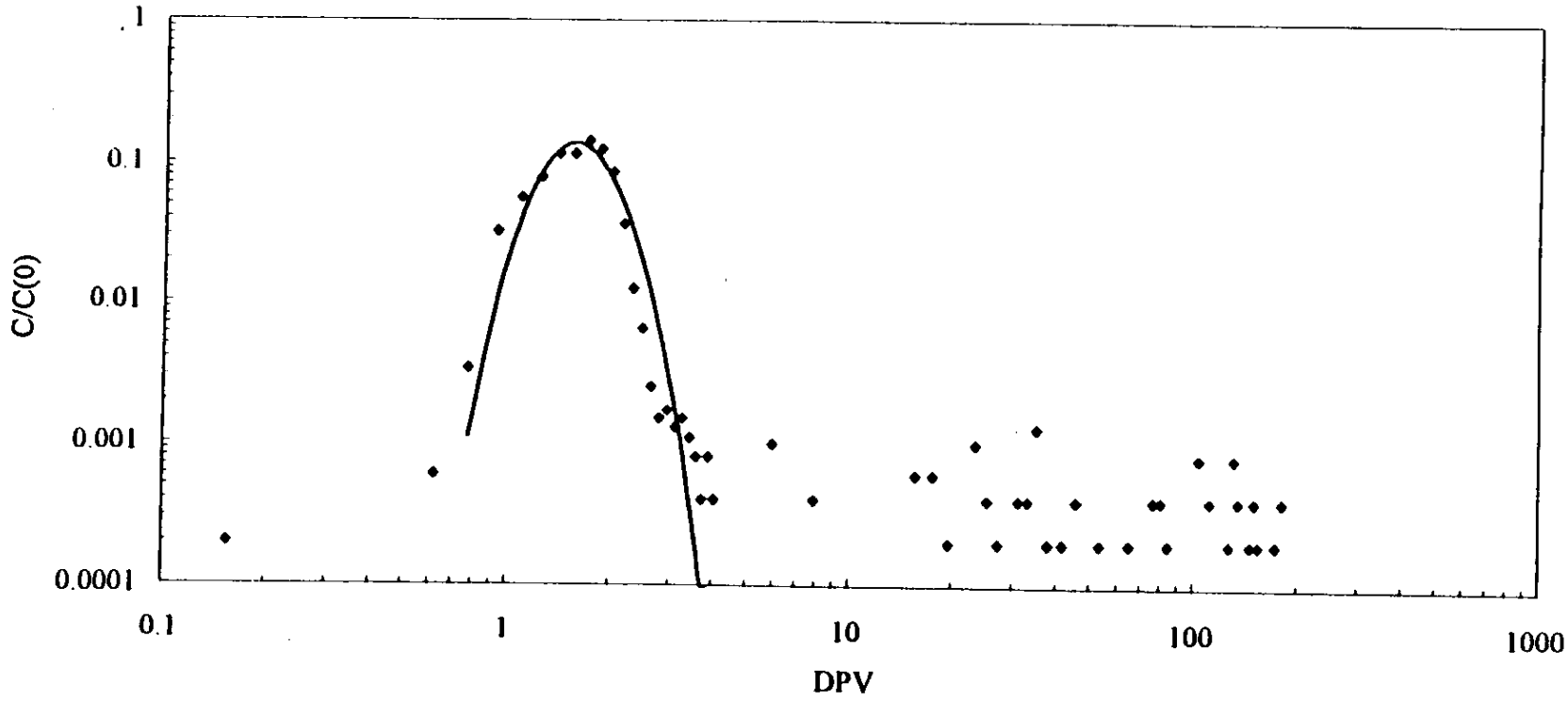

Figure F-9. Breakthrough of an enhanced mobile fraction of ^{241}Am (14% recovery) in crushed basalt packed column B07. The diamond shapes represent data points and the line represents the CXTFIT equilibrium model fit.

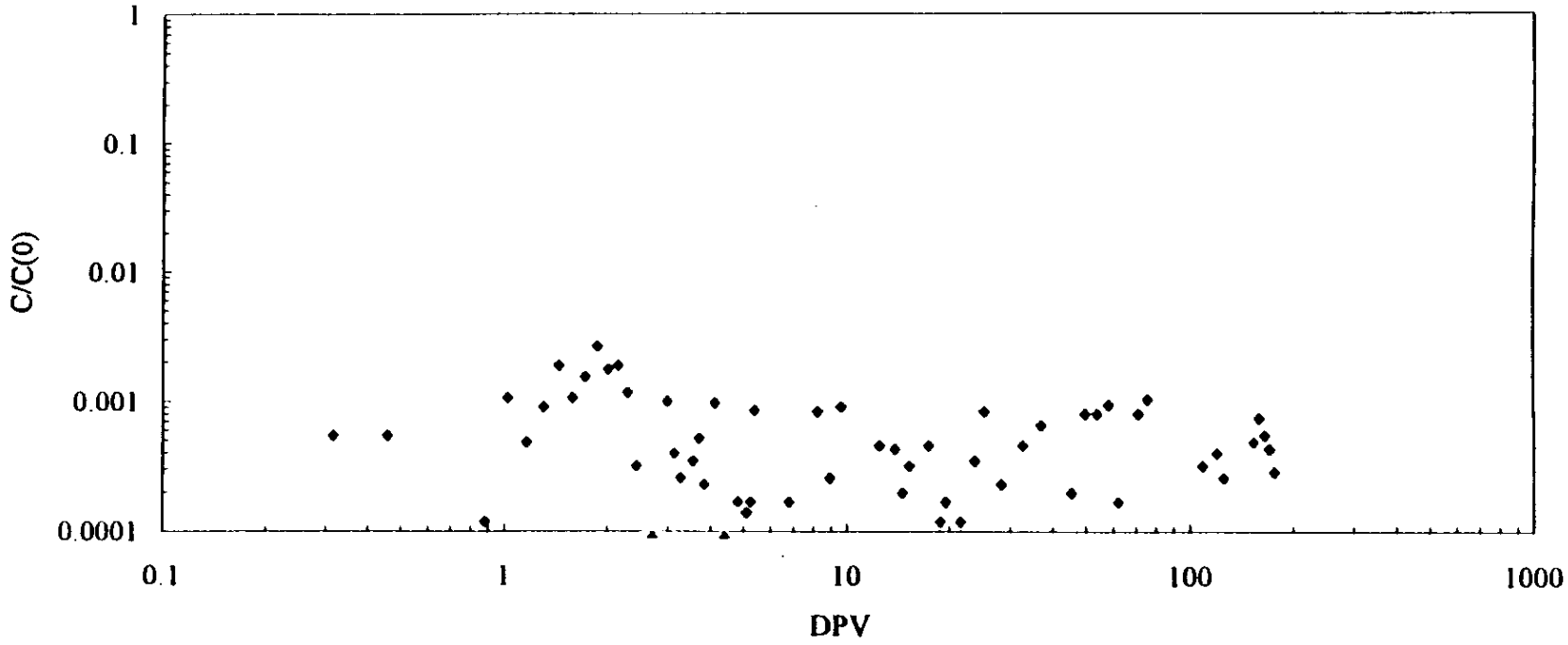

Figure F-10. Breakthrough of an enhanced mobility fraction of ^{60}Co (0.9% recovery) in interbed material packed column IB01. The diamond shapes represent data points and the line represents the CXTFIT equilibrium model fit.

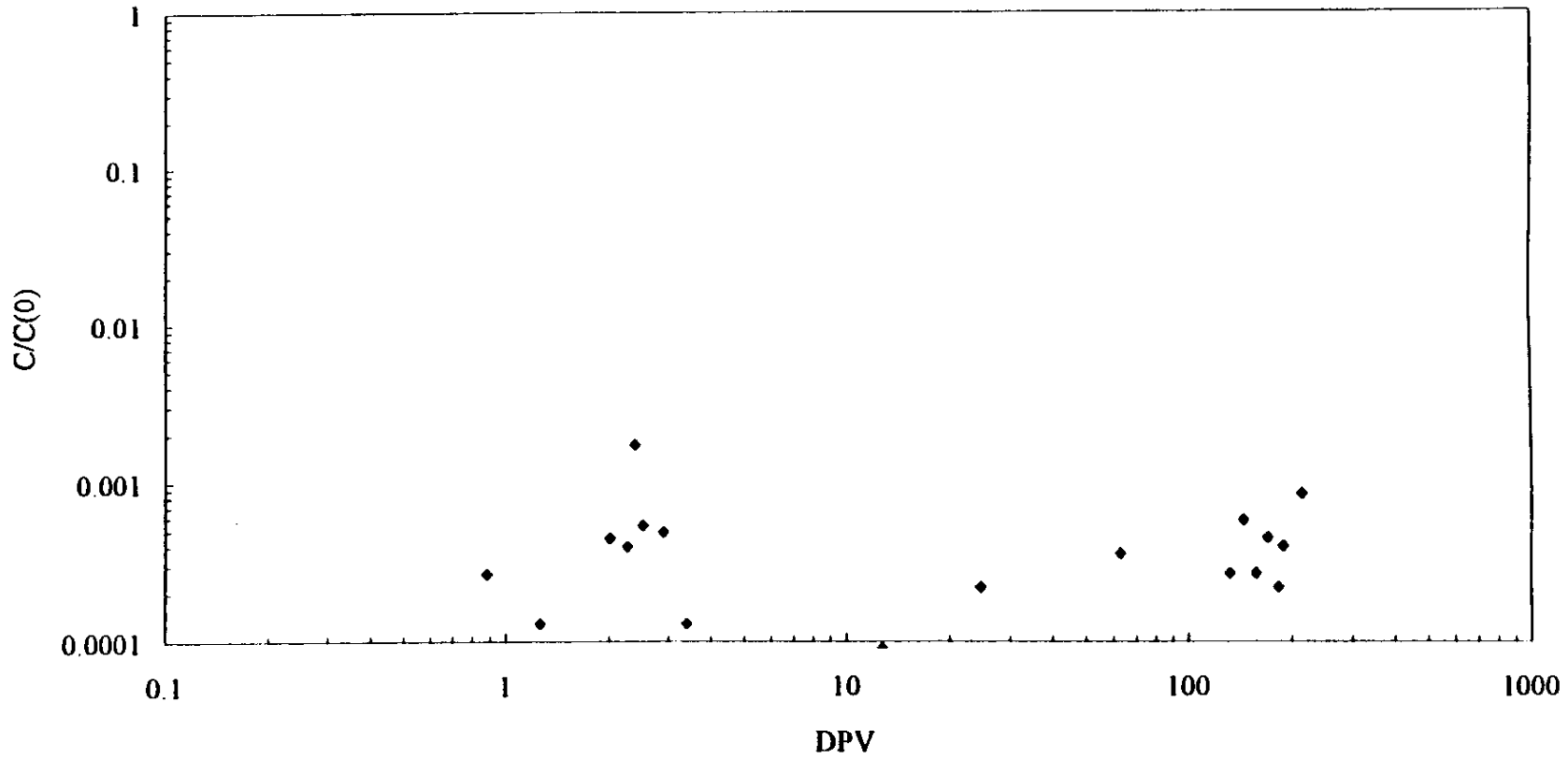

Figure F-11. Breakthrough of ^{90}Sr (0% recovery) in interbed material packed column IB06. The diamond shapes represent data points and the line represents the CXTFIT equilibrium model fit.

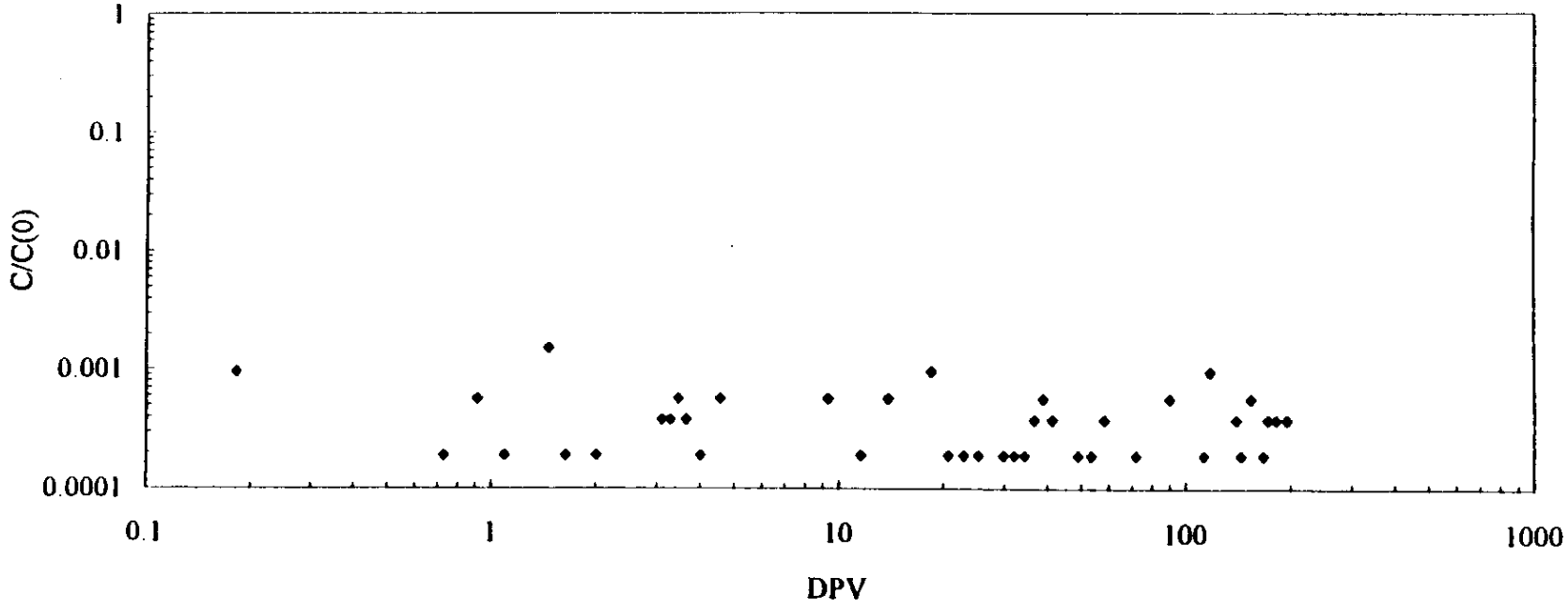

Figure F-12. Breakthrough of an enhanced mobility fraction of ^{241}Am (1.8% recovery) in interbed material packed column IB05. The diamond shapes represent data points and the line represents the CXTFIT equilibrium model fit.

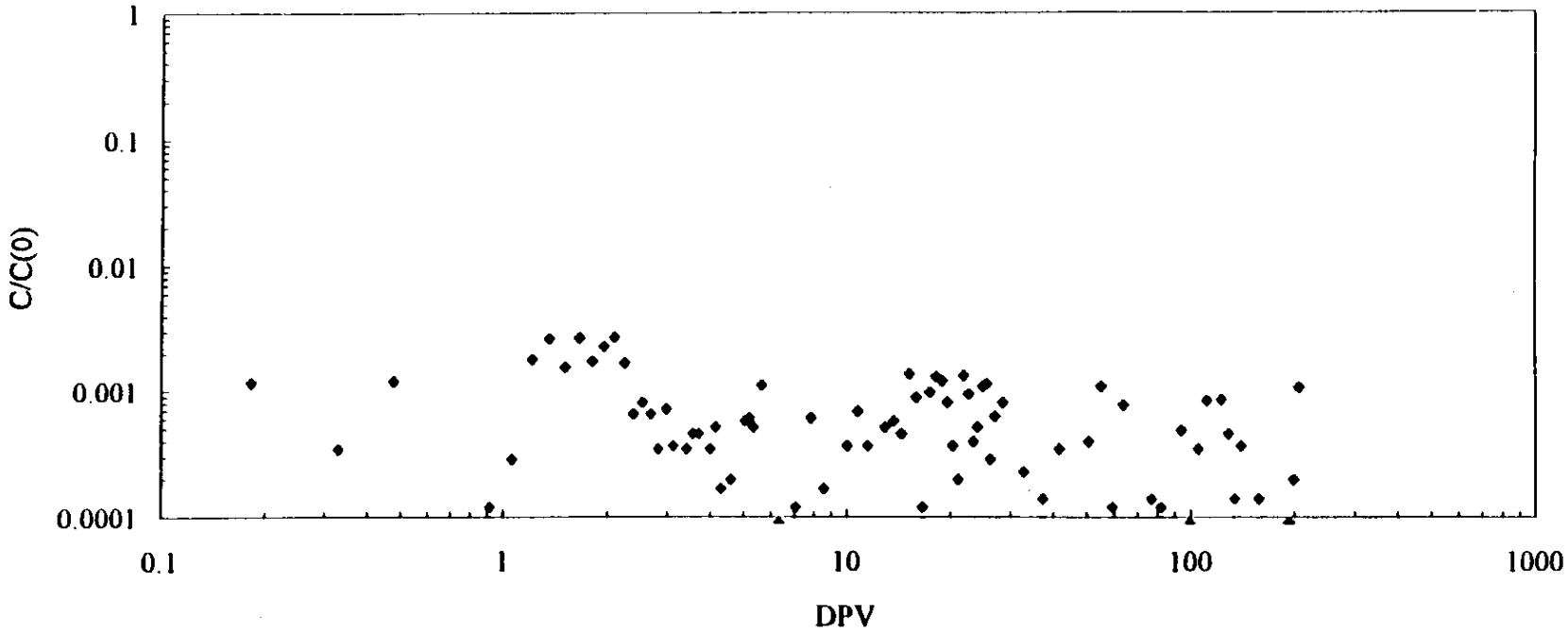

Figure F-13. Breakthrough of an enhanced mobility fraction of ^{60}Co (3.8% recovery) in interbed material packed column IB02. The diamond shapes represent data points and the line represents the CXTFIT equilibrium model fit.

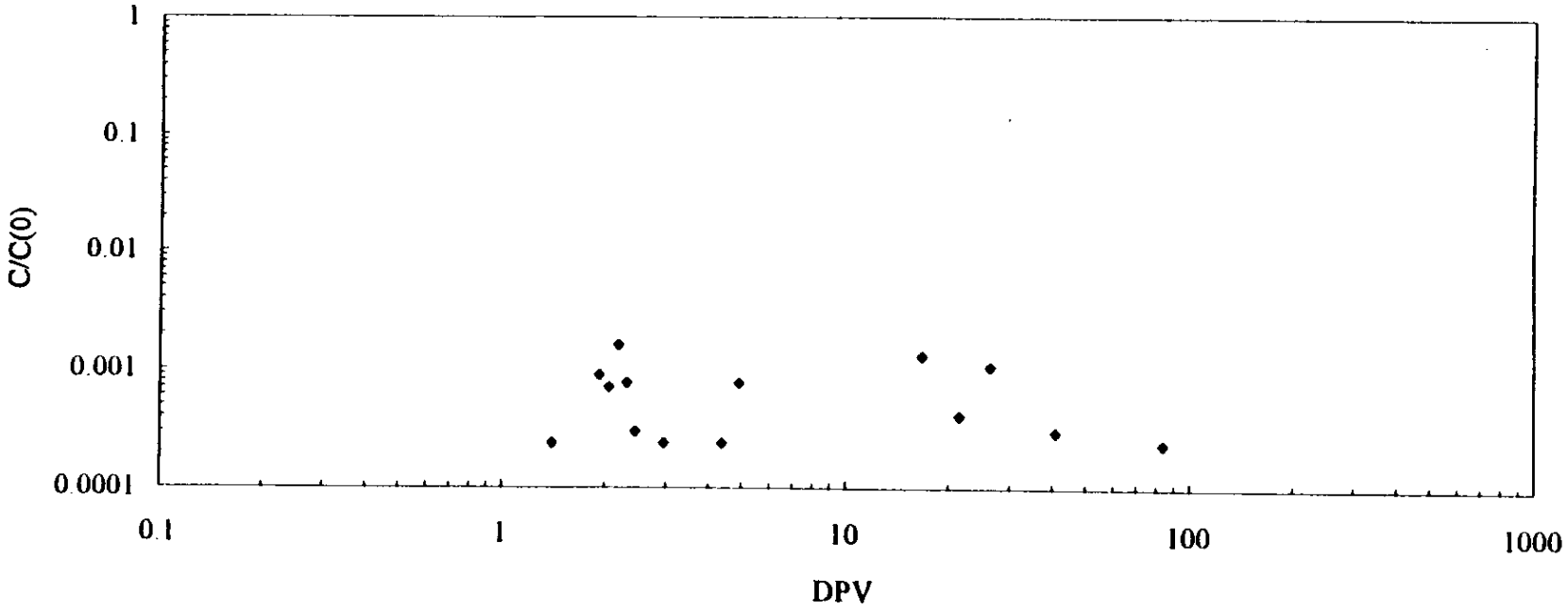

Figure F-14. Breakthrough of ^{90}Sr (0% recovery) in interbed material packed column IB09. The diamond shapes represent data points and the line represents the CXTFIT equilibrium model fit.

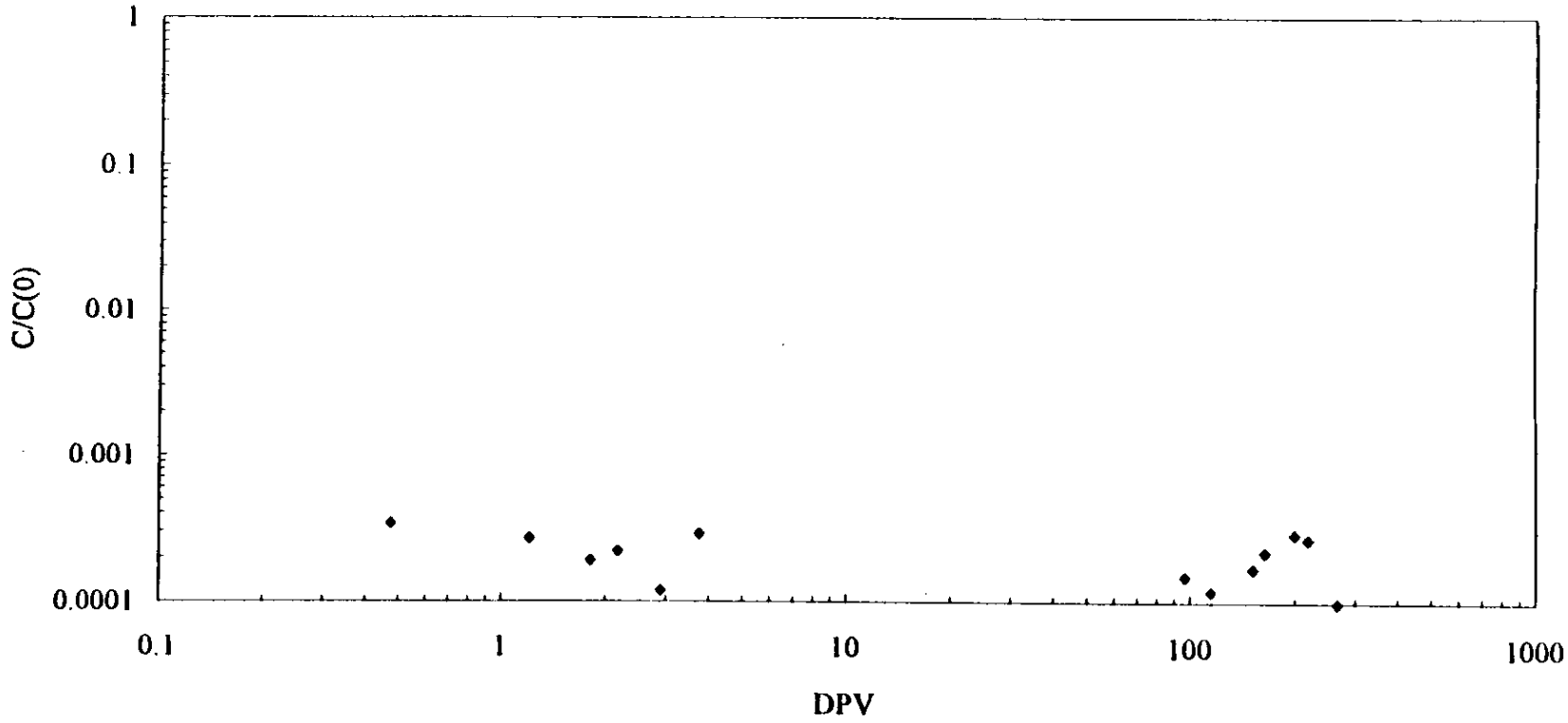

Figure F-15. Breakthrough of ^{137}Cs (0% recovery) in interbed material packed column IB08. The diamond shapes represent data points and the line represents the CXTFIT equilibrium model fit.

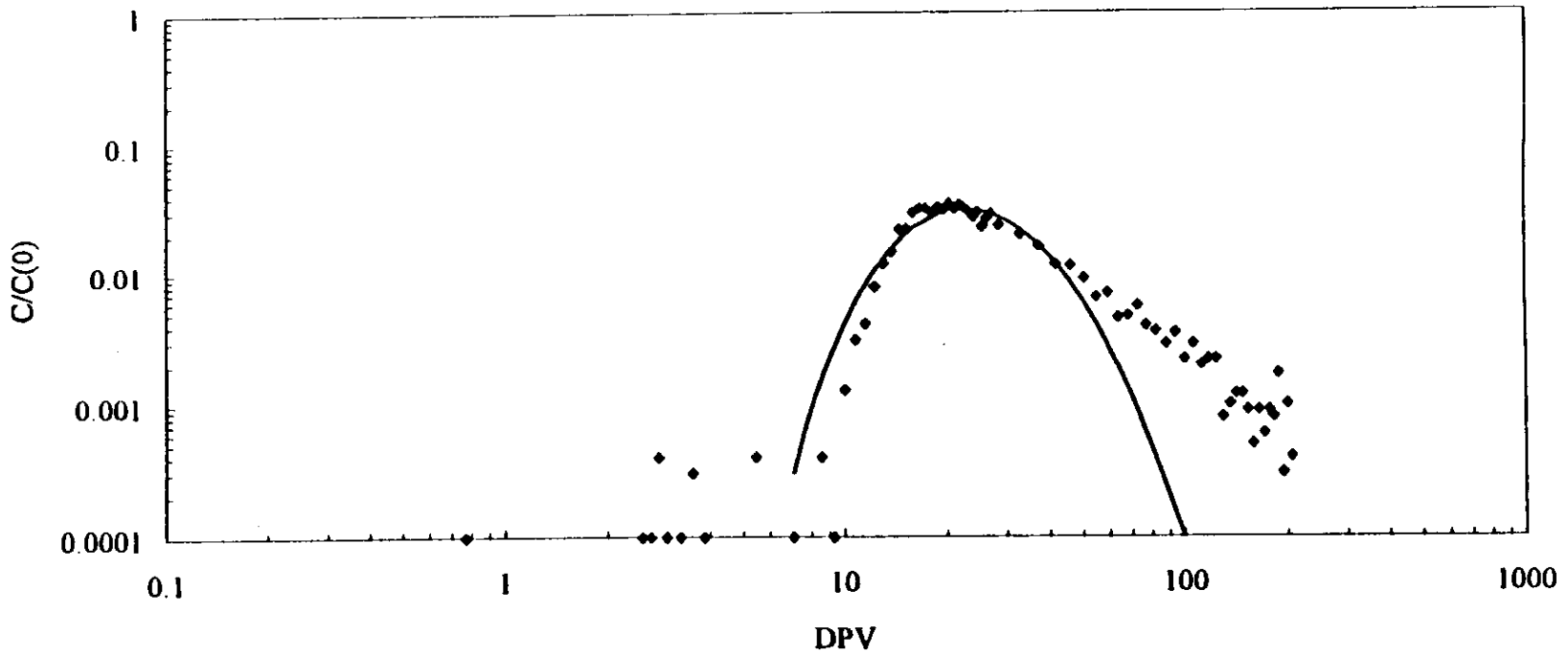

Figure F-16. Breakthrough of ^{233}U (98.3% recovery) in interbed material packed column IB02. The diamond shapes represent data points and the line represents the CXTFIT equilibrium model fit.

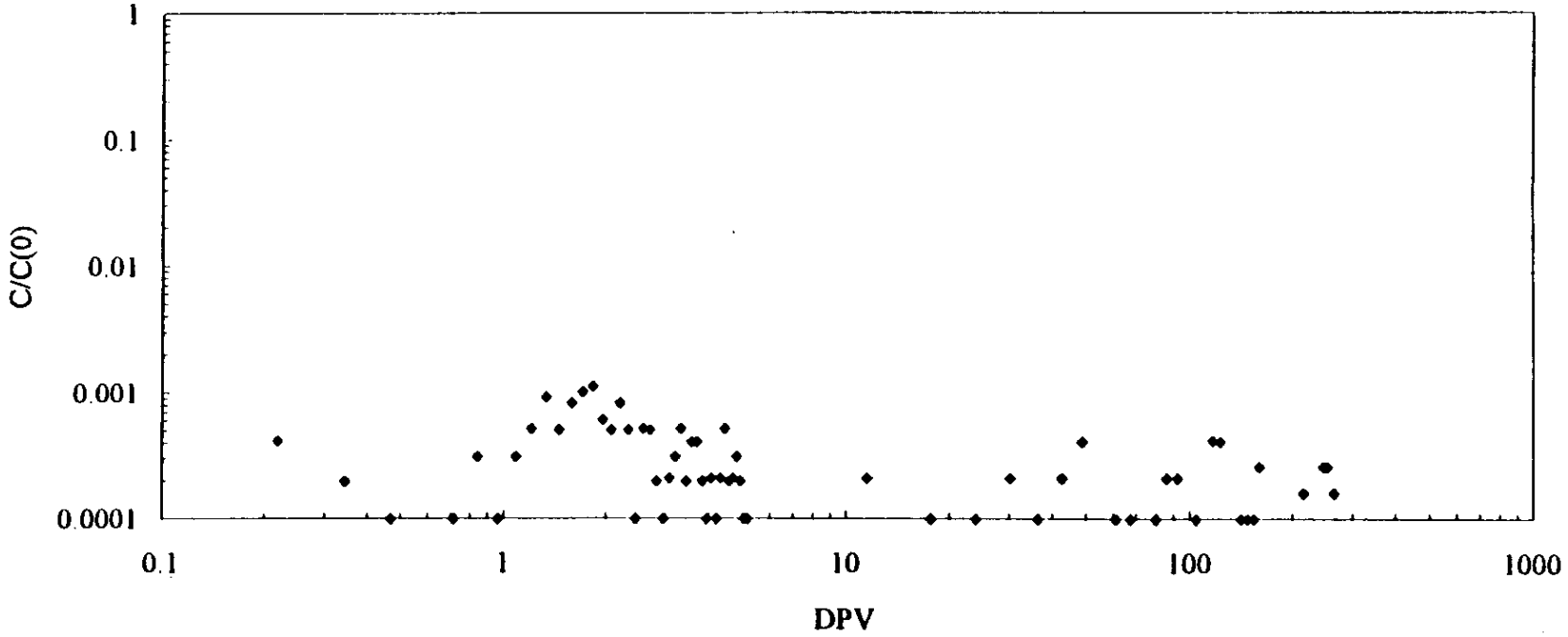

Figure F-17. Breakthrough of an enhanced mobility fraction of ^{239}Pu (0.01% recovery) in interbed material packed column IB07. The diamond shapes represent data points and the line represents the CXTFIT equilibrium model fit.

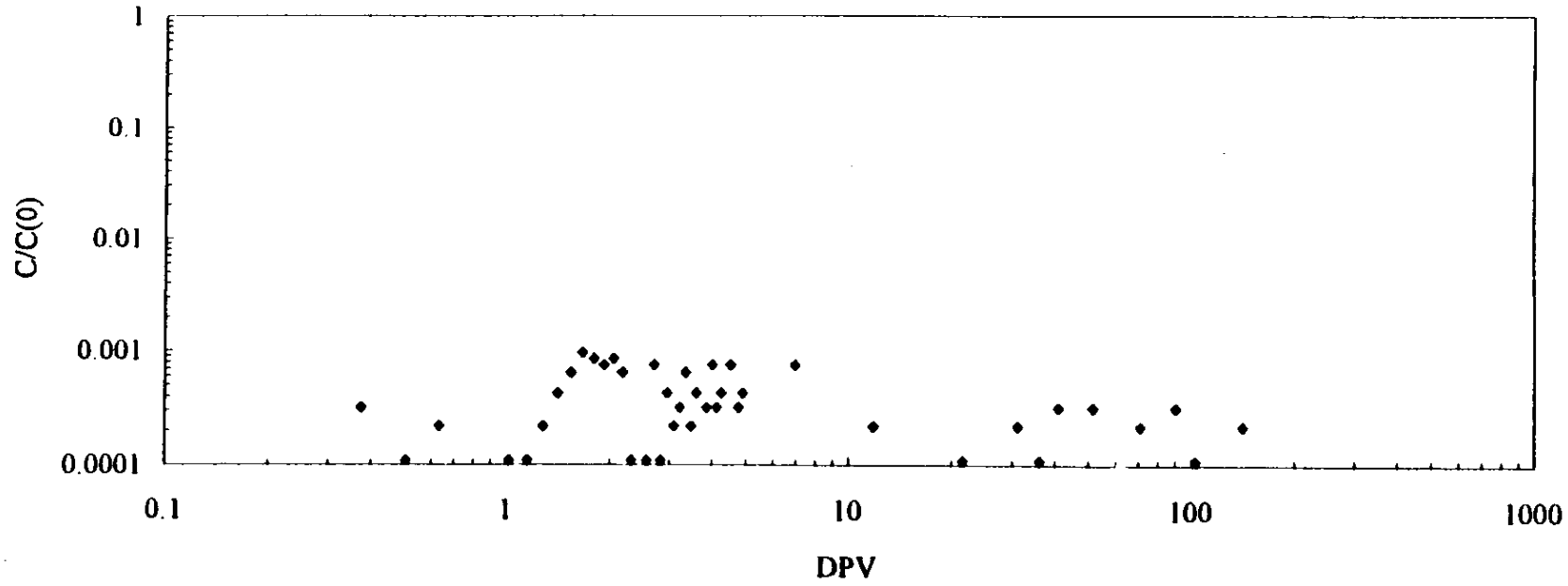

Figure F-18. Breakthrough of an enhanced mobility fraction of ^{239}Pu (0.15% recovery) in interbed material packed column IB09. The diamond shapes represent data points and the line represents the CXTFIT equilibrium model fit.

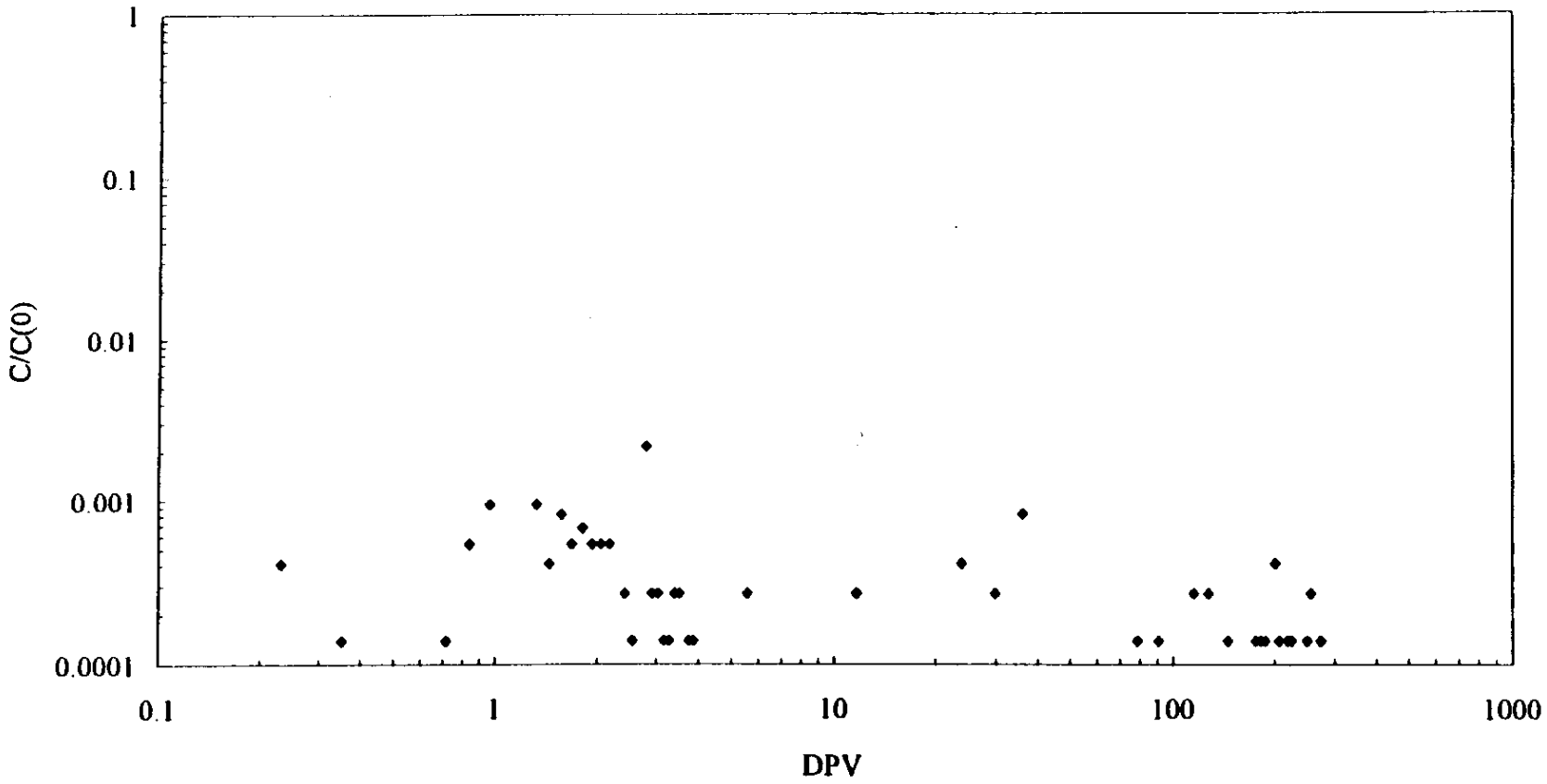

Figure F-19. Breakthrough of an enhanced mobility fraction of ^{241}Am (1.9% recovery) in interbed material packed column IB08. The diamond shapes represent data points and the line represents the CXTFIT equilibrium model fit.

Appendix G

Appendix G

Distribution of Gamma-Emitting Radionuclides in Crushed Basalt and Interbed Material Packed Columns at Clemson University

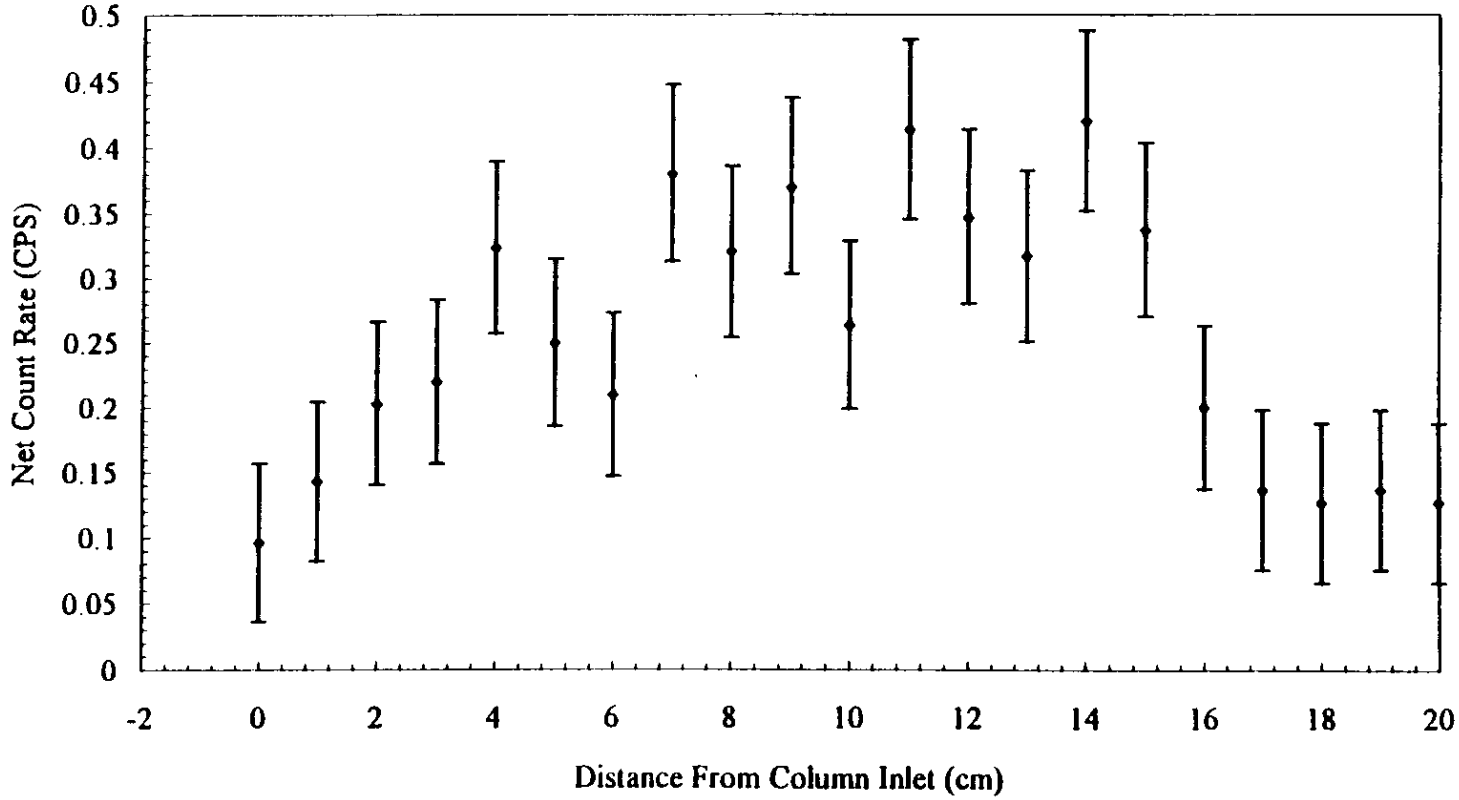

Figure G-1. Distribution of ^{60}Co activity in crushed basalt packed column B03 as determined by a gamma-scan. The error bars represent the variation in duplicate analyses.

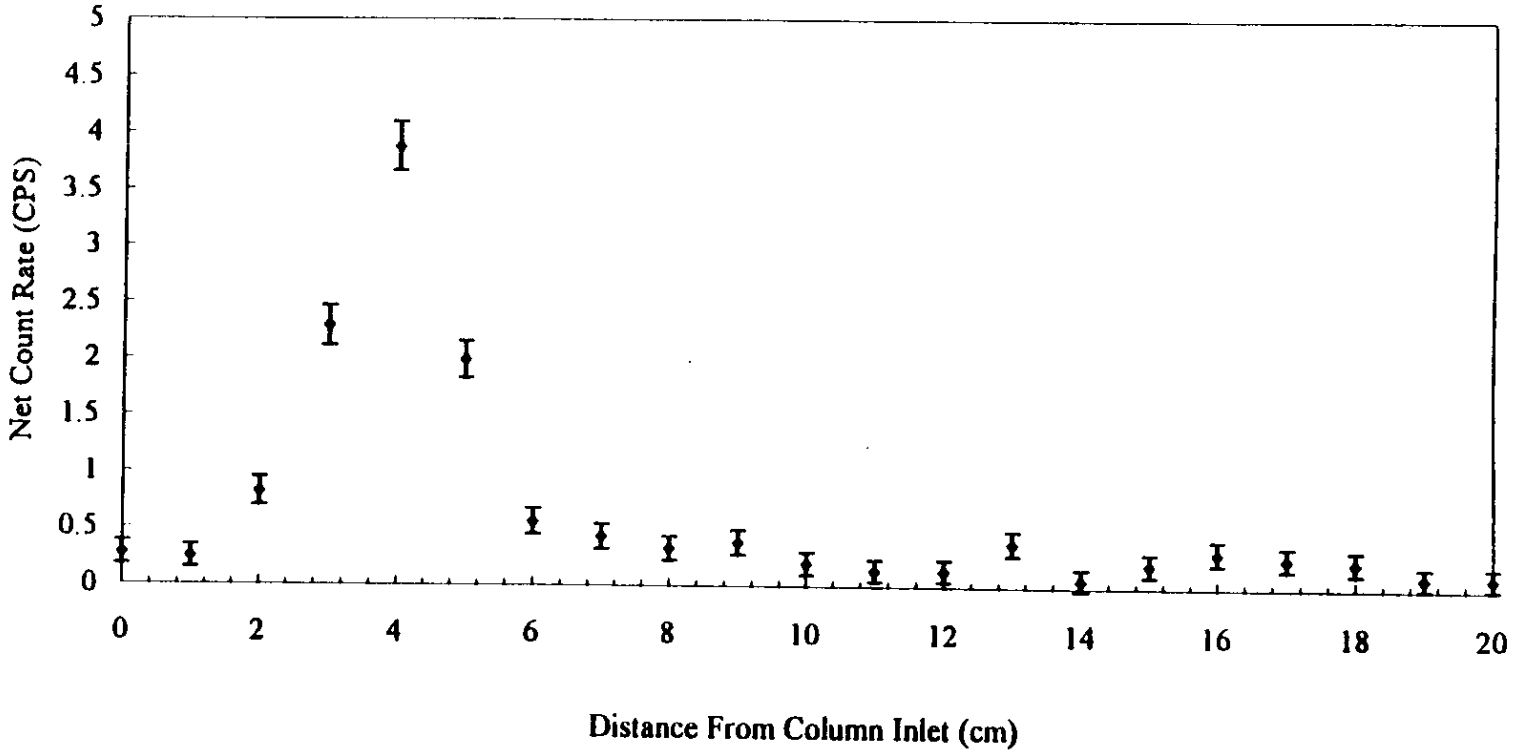

Figure G-2. Distribution of ^{60}Co activity in interbed material packed column IB02 as determined by a gamma-scan. The error bars represent the variation in duplicate analyses.

Appendix H

Appendix H

Results from Batch Tests Conducted at Clemson University Using Crushed Basalt and Interbed Materials from the INEL

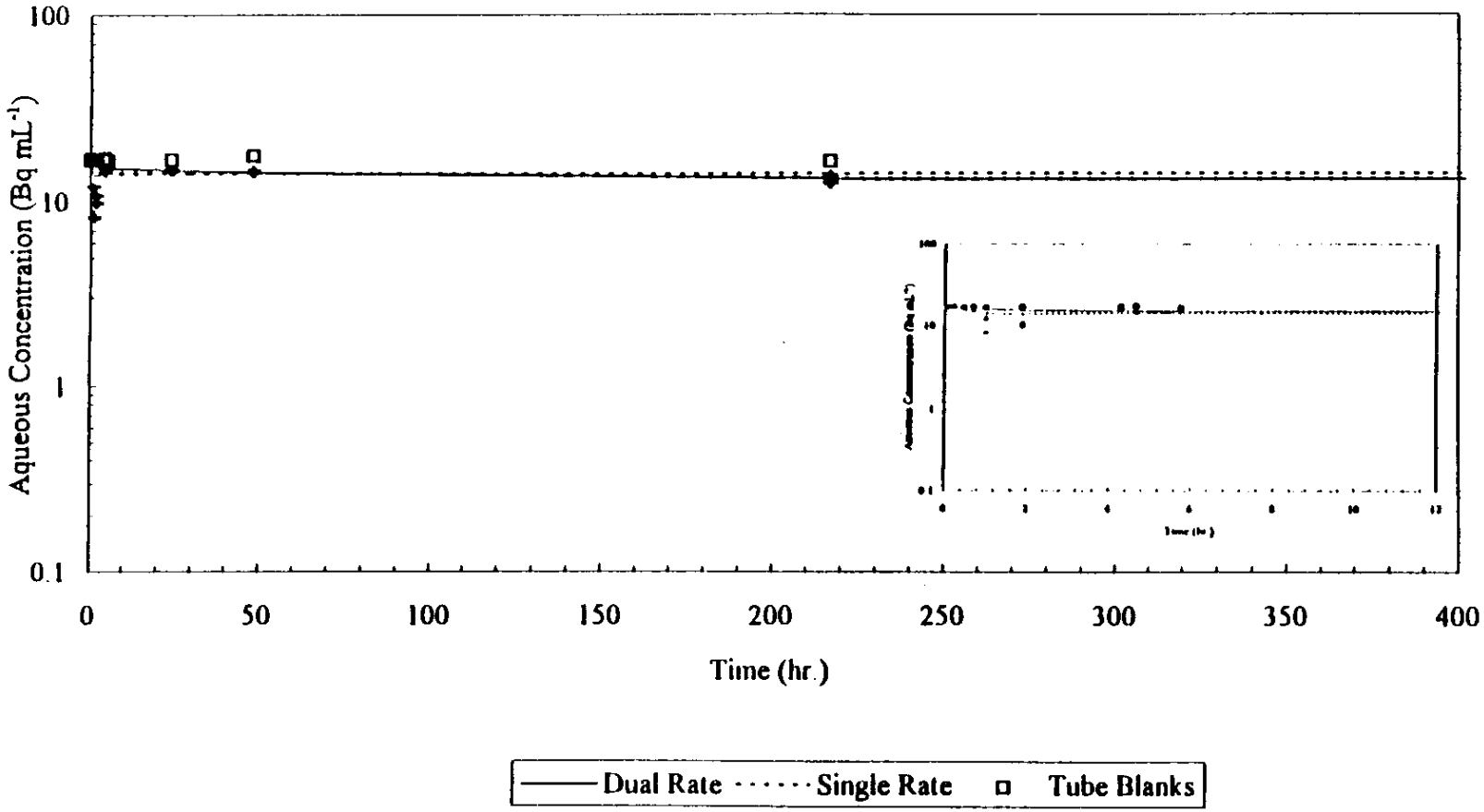

Figure H-1. Aqueous phase concentration of ^{90}Sr as a function of time in a crushed basalt batch test. The solid diamond shapes represent data points. The error bars represent the variation in duplicate analyses.

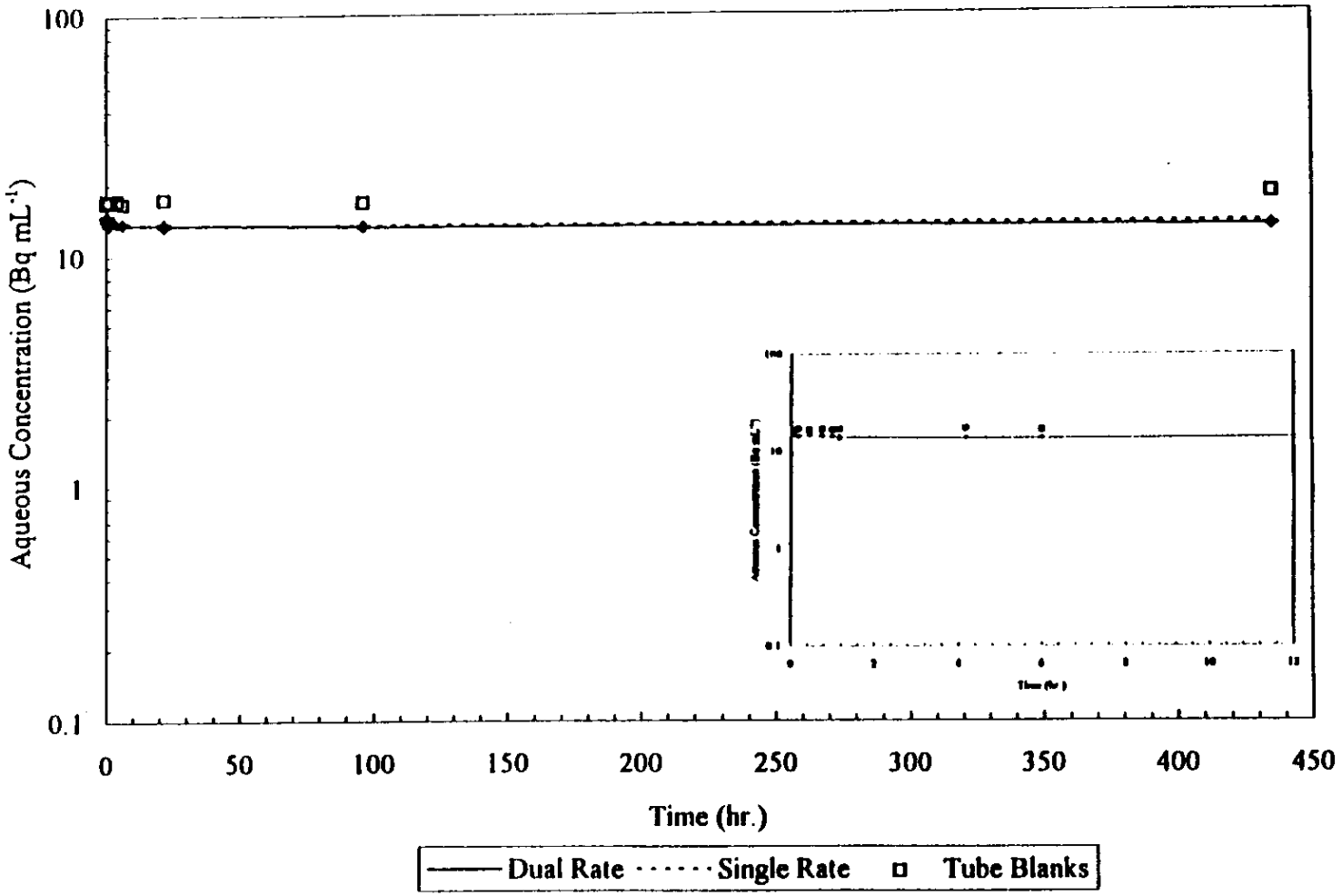

Figure H-2. Aqueous phase concentration of ^{90}Sr as a function of time in an interbed material batch test. The solid diamond shapes represent data points. The error bars represent the variation in duplicate analyses.

Appendix I

Appendix I

Results from Batch Tests Designed to Evaluate the Effects of Variations in pH and Ionic Strength on Measured Distribution Coefficients

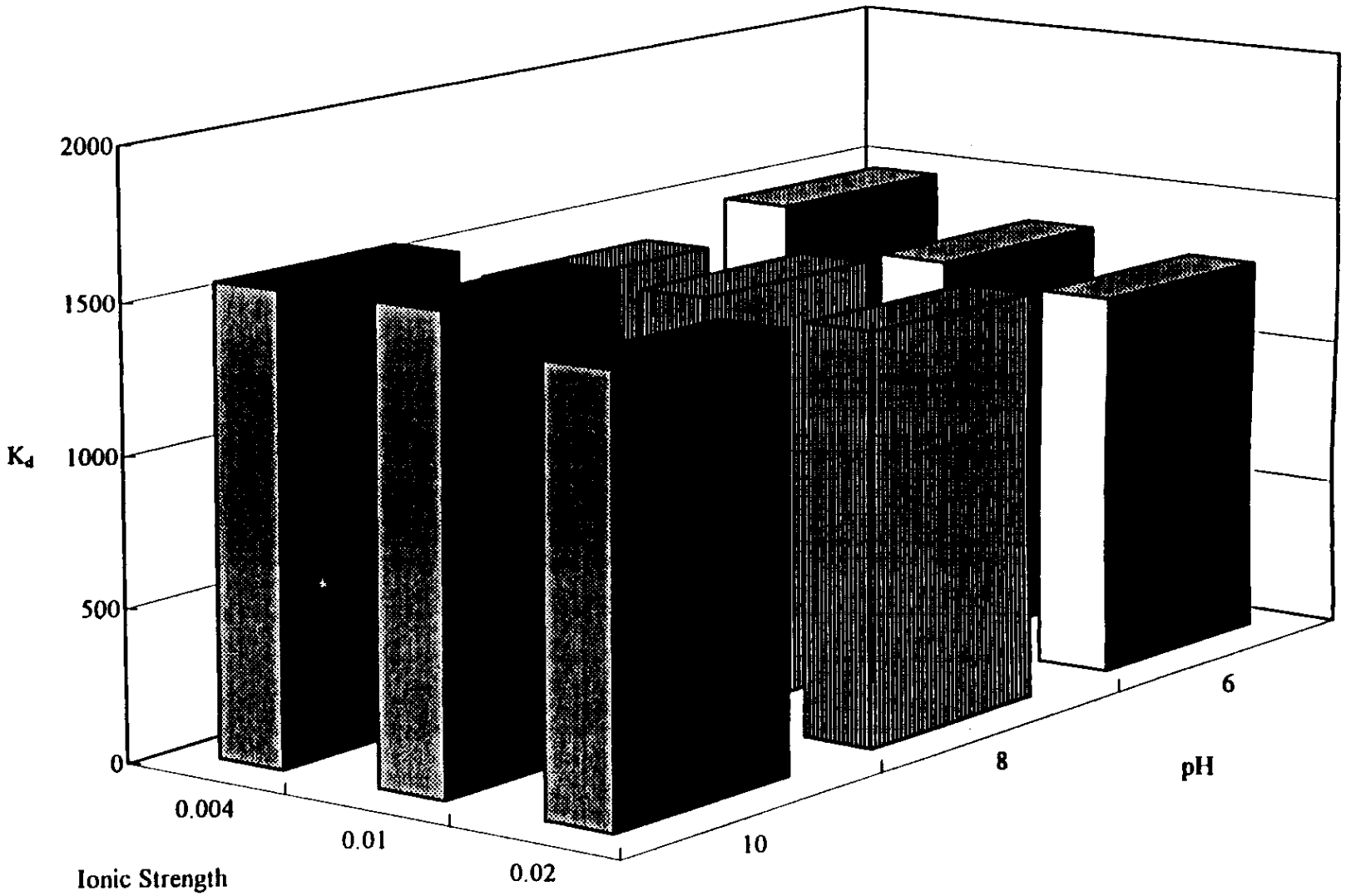

Figure I-1. Cesium K_d's versus pH and ionic strength (controlled with Ca^{2+}) with interbed material.

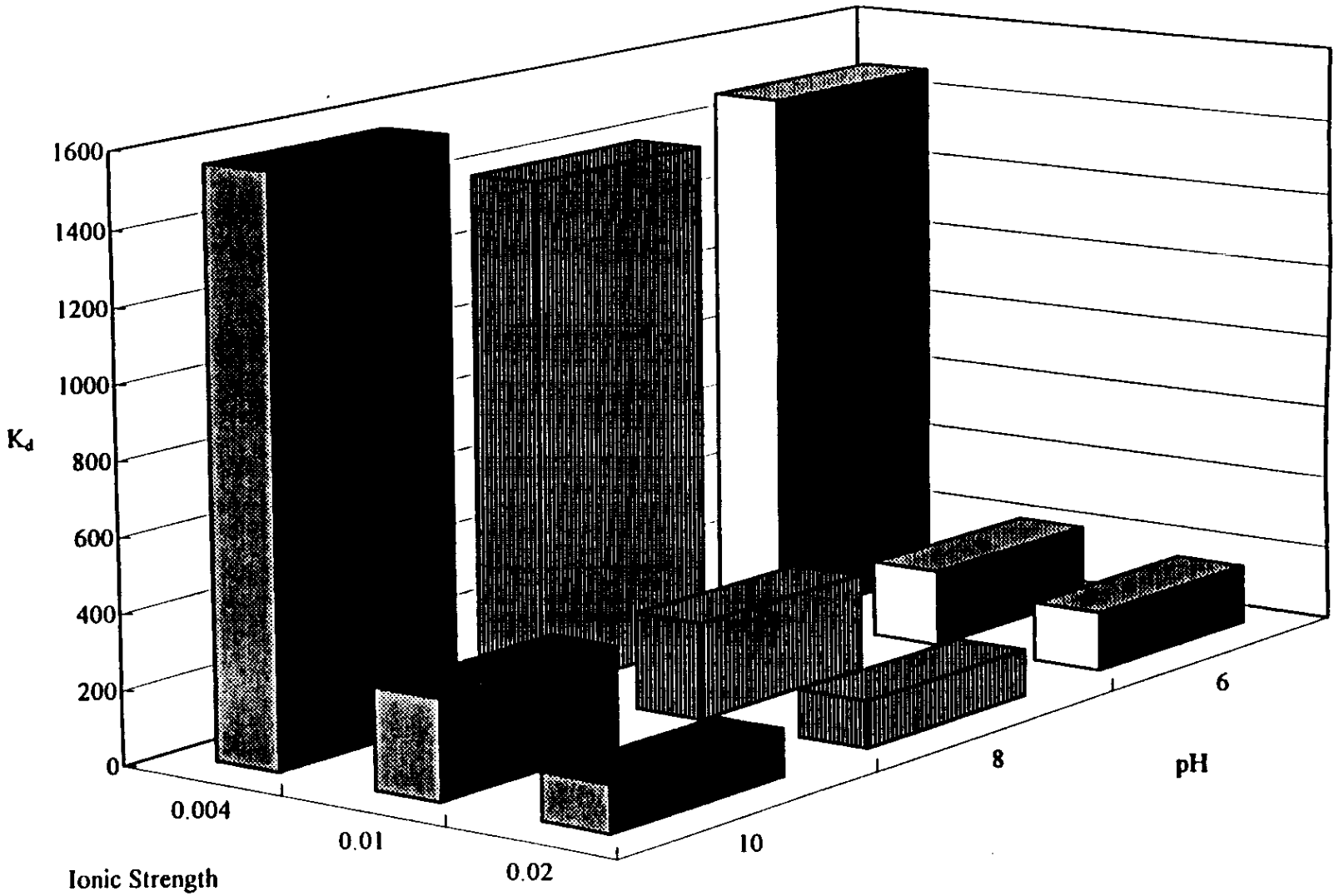

Figure I-2. Cesium K_d's versus pH and ionic strength (controlled with K^+) with interbed material.

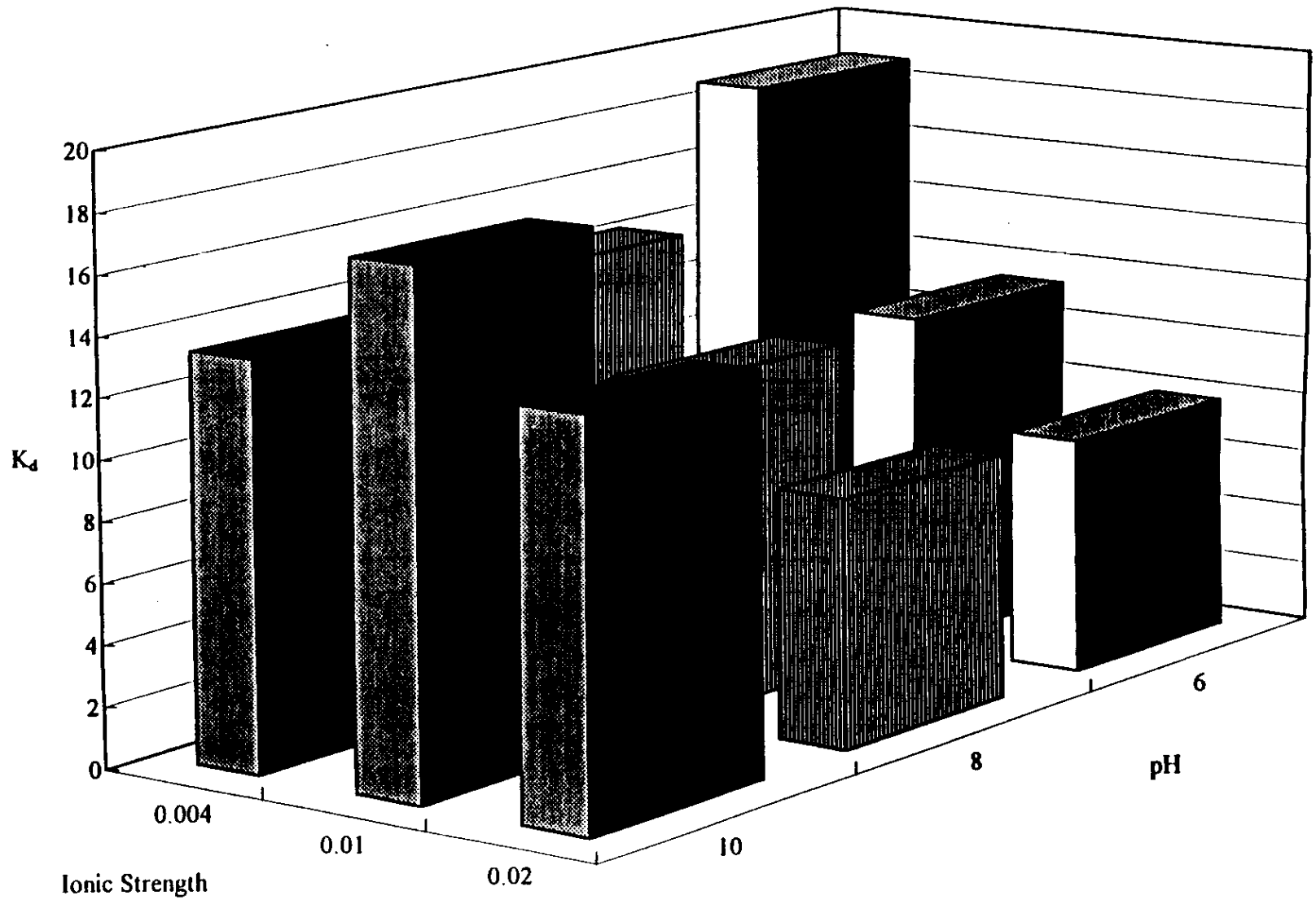

Figure I-3. Uranium K_d's versus pH and ionic strength (controlled with Ca^{2+}) with interbed material.

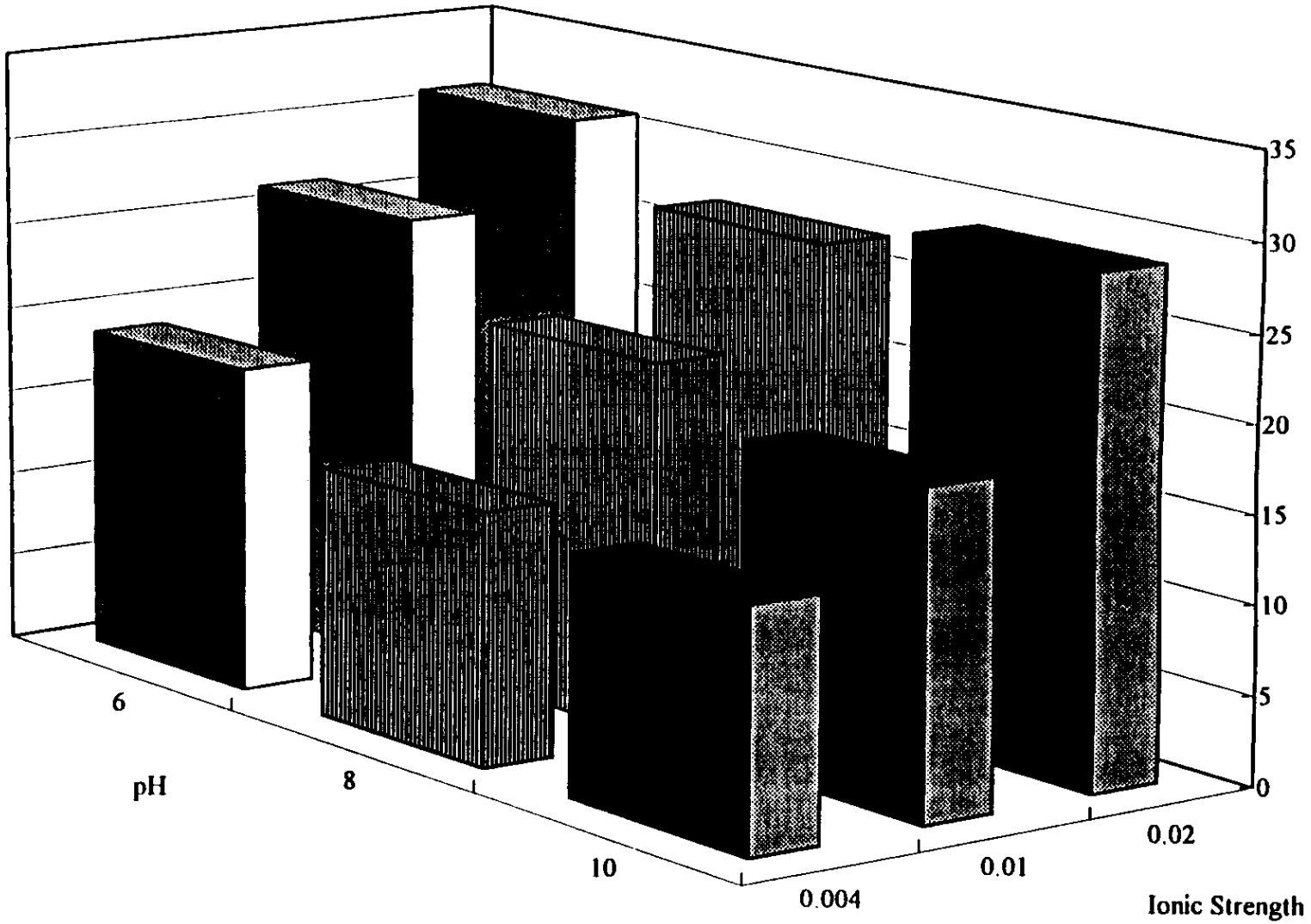

Figure I-4. Uranium K_d's versus pH and ionic strength (controlled with K^+) with interbed material.

Appendix J

Appendix J

Breakthrough Curves of Bromide and Strontium in Crushed Basalt Packed Columns and Intact Basalt Cores

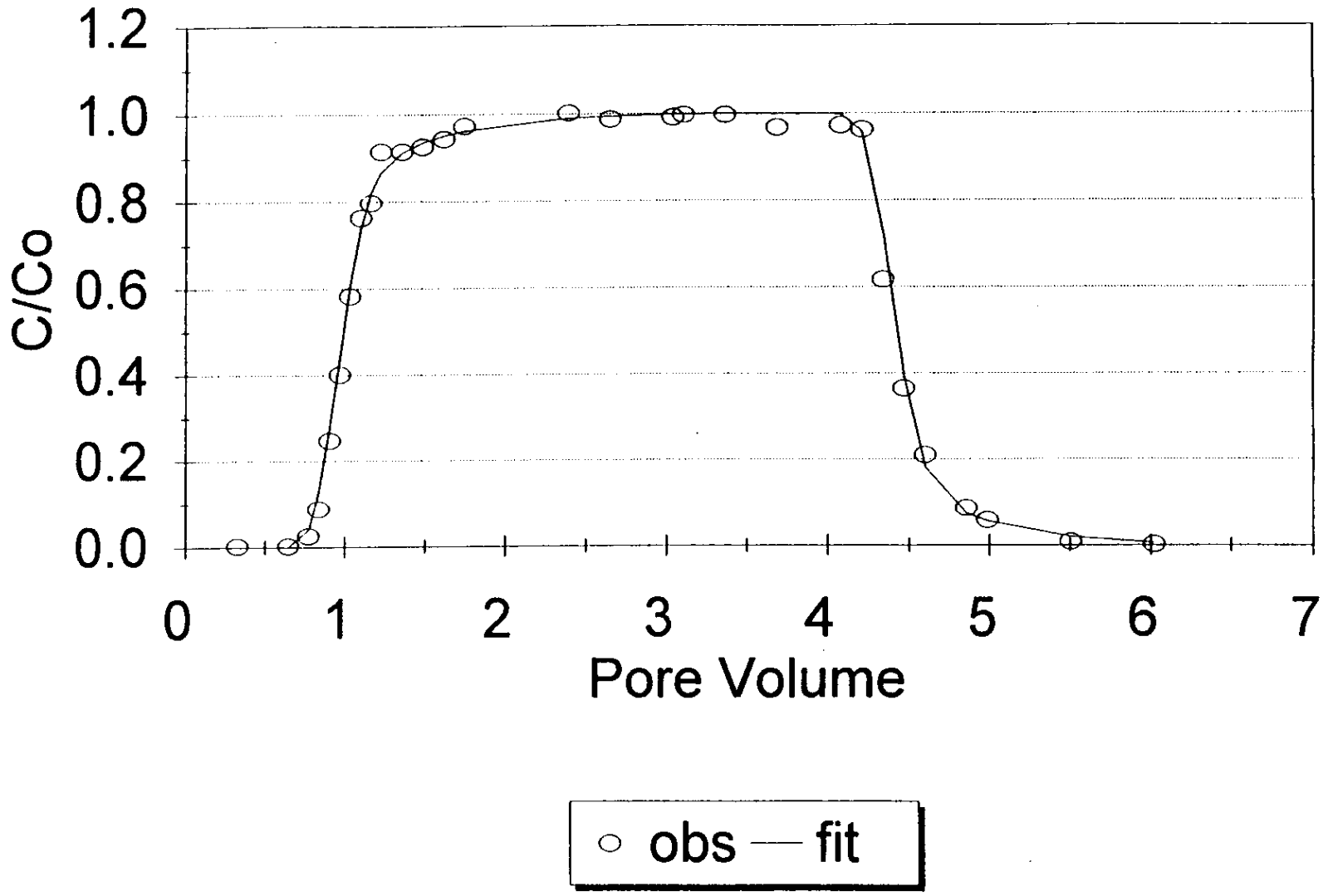

Figure J-1. Bromide breakthrough from crushed basalt packed column CB5BR1. The fit represented here is from the two-site/two region CXTFIT model.

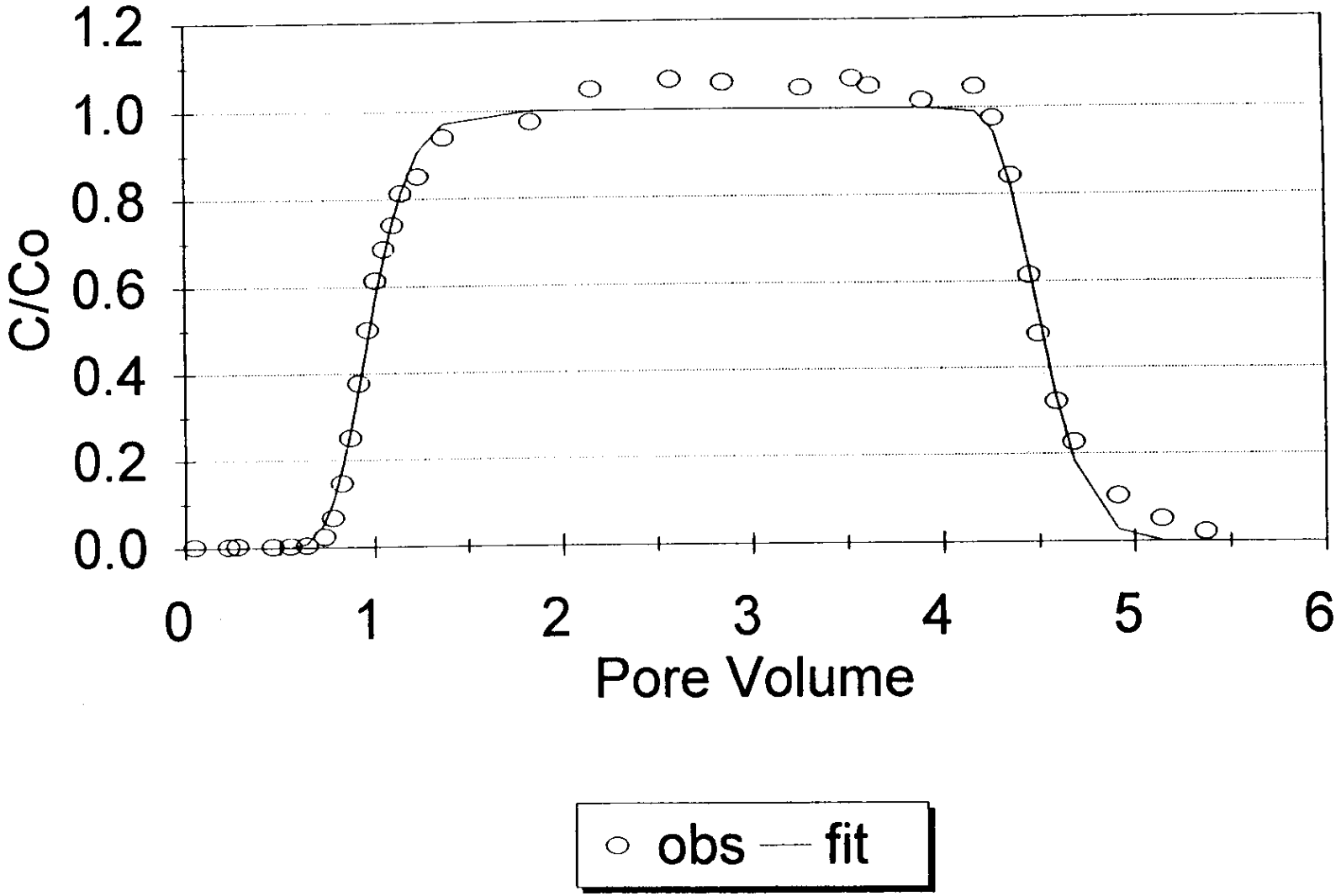

Figure J-2. Bromide breakthrough from crushed basalt packed column CB5BR2. The fit represented here is from the equilibrium CXTFIT model.

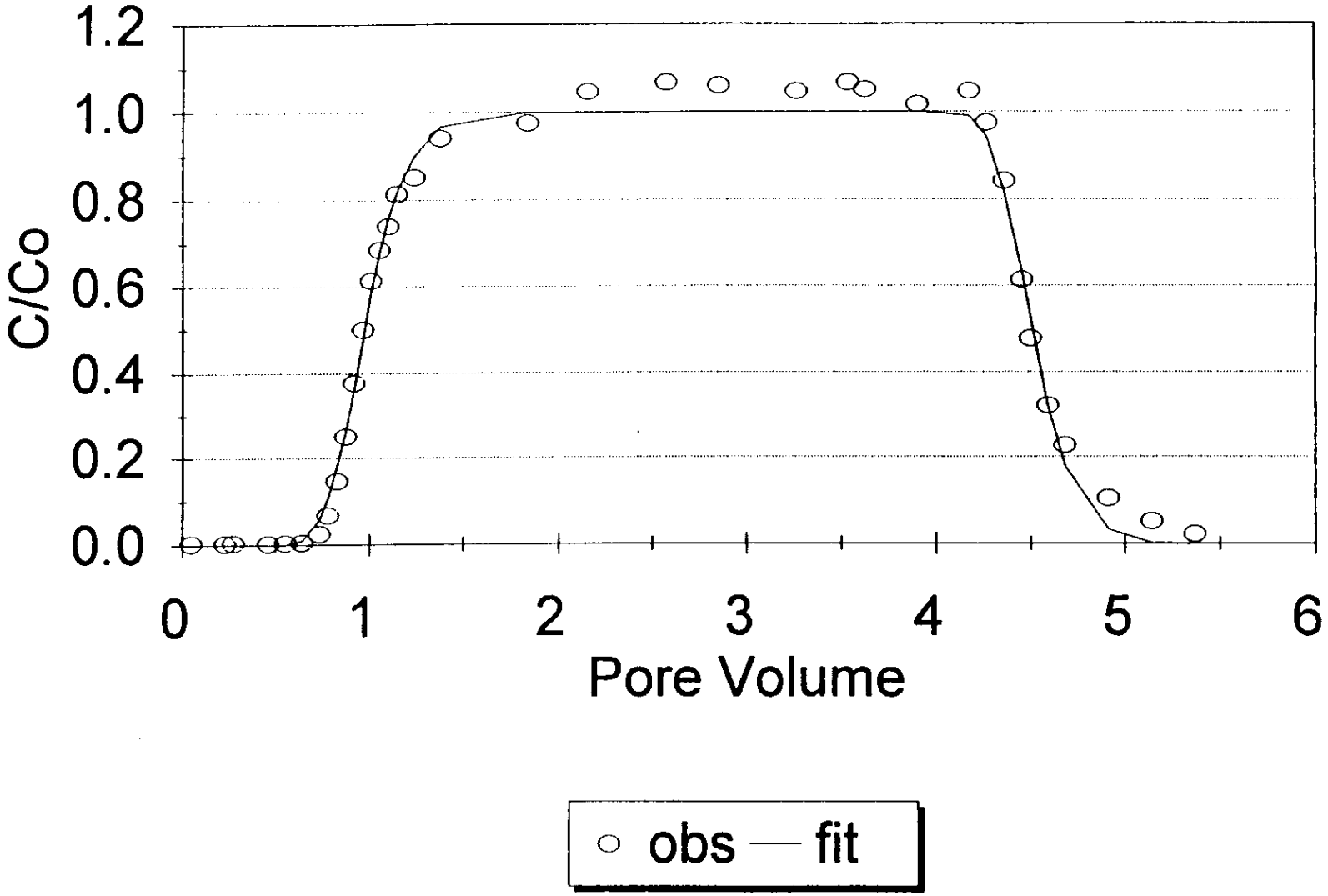

Figure J-3. Bromide breakthrough from crushed basalt packed column CB5CB2. The fit represented here is from the two-site/two region CXTFIT model.

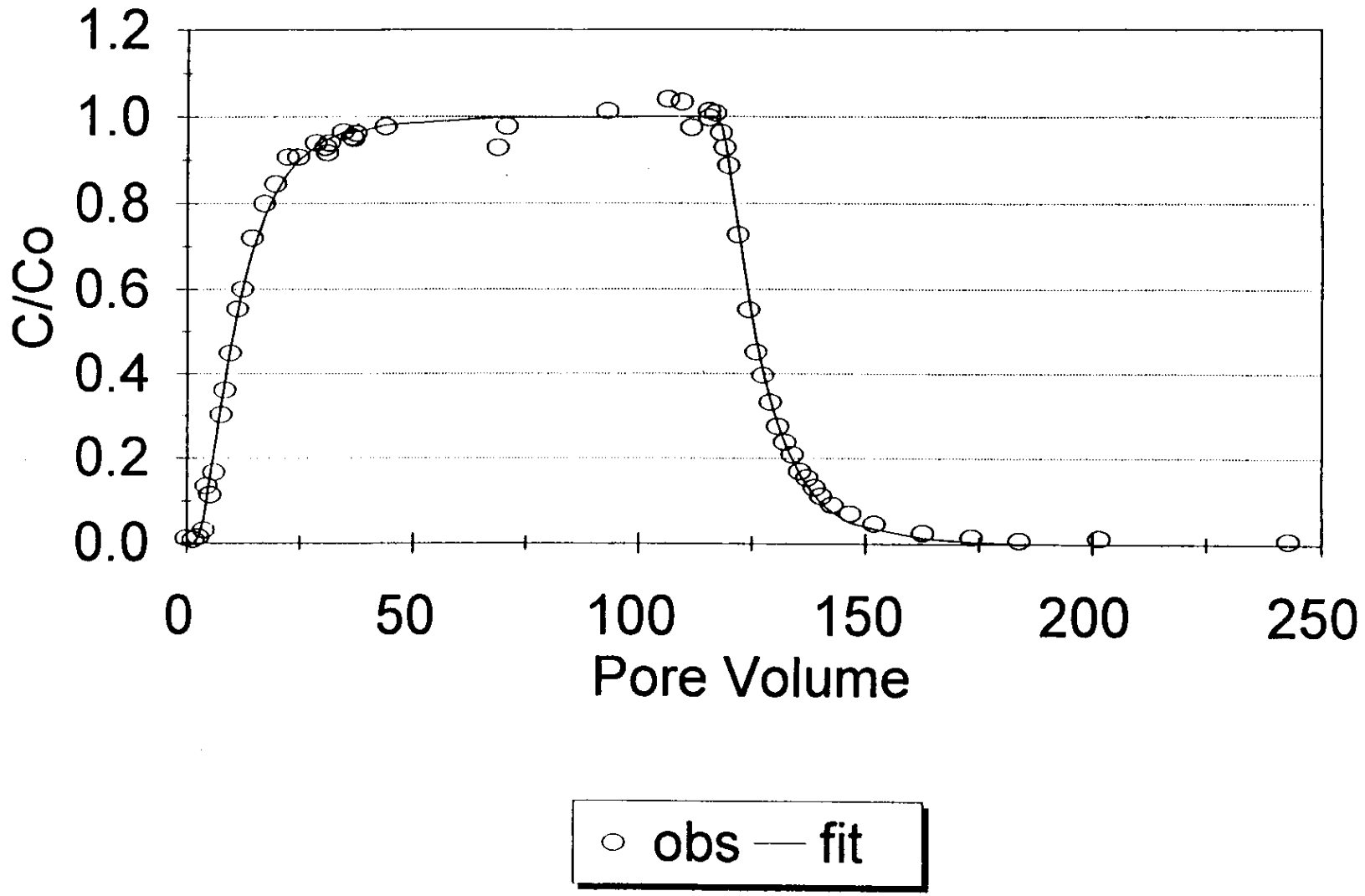

Figure J-4. Strontium breakthrough from crushed basalt packed column CB5SR1. The fit represented here is from the two-site/two region CXTFIT model.

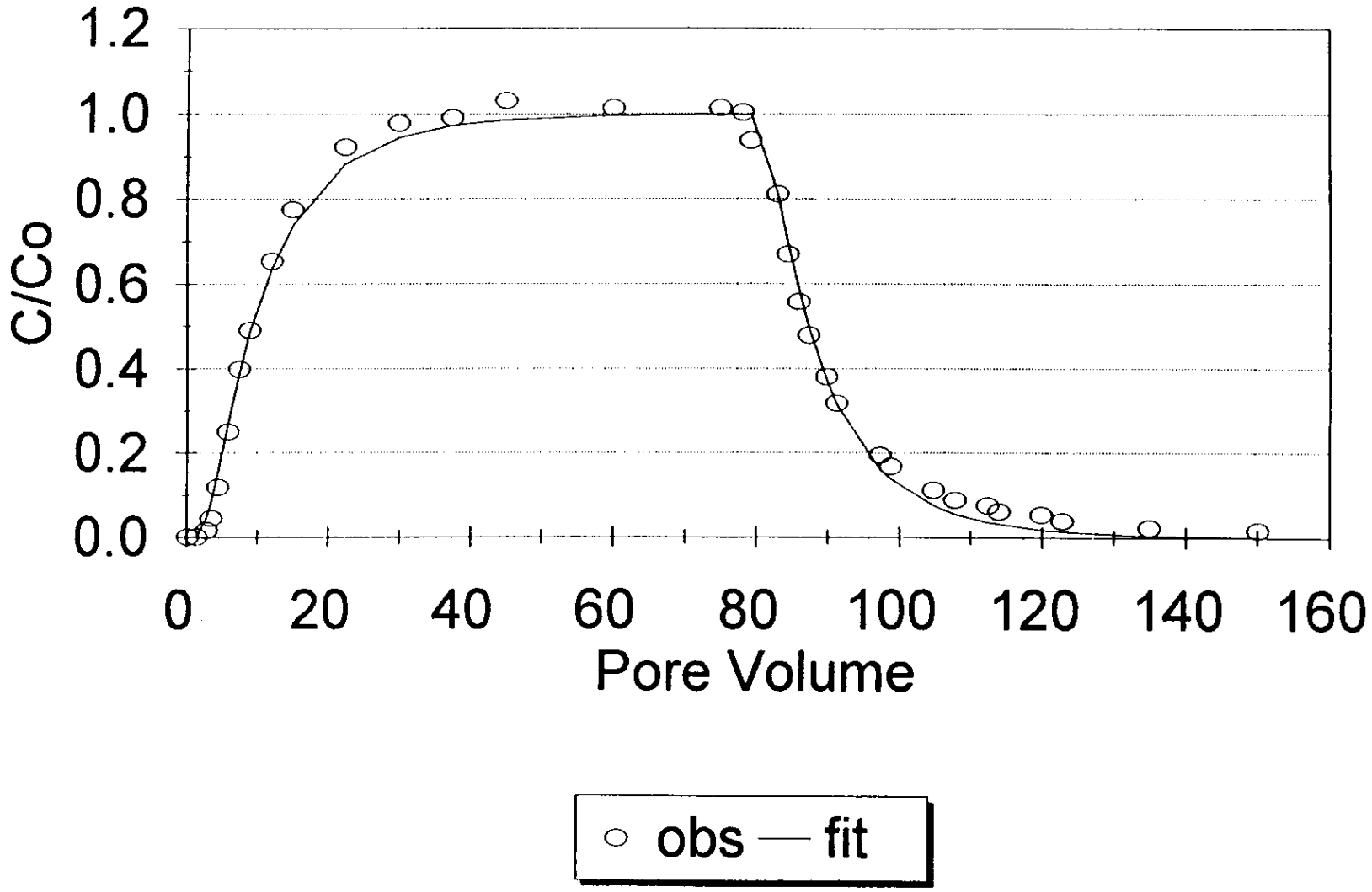

Figure J-5. Strontium breakthrough from crushed basalt packed column CB5SR2. The fit represented here is from the equilibrium region CXTFIT model.

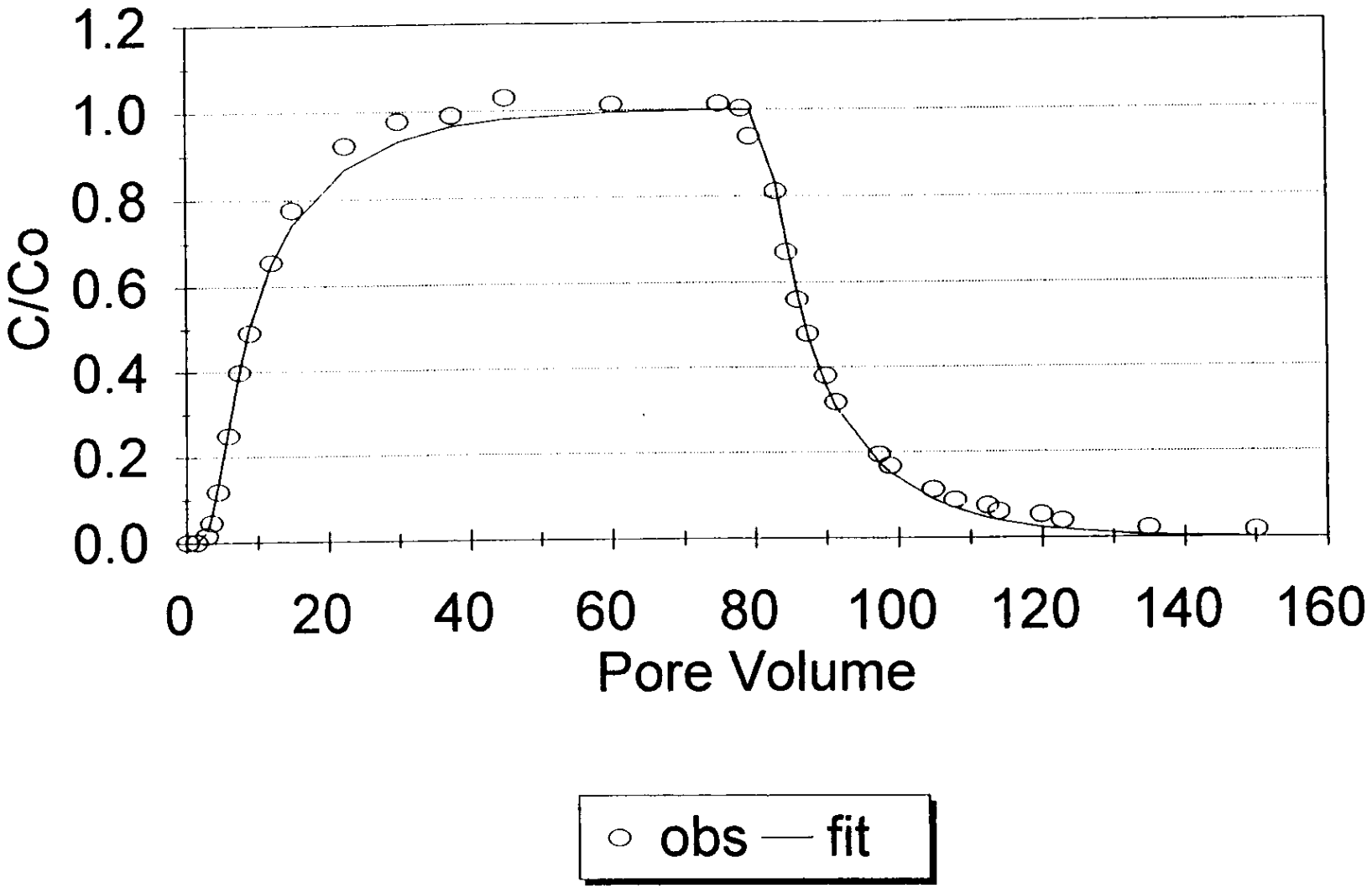

Figure J-6. Strontium breakthrough from crushed basalt packed column CB5SR2. The fit represented here is from the two-site/two region CXTFIT model.

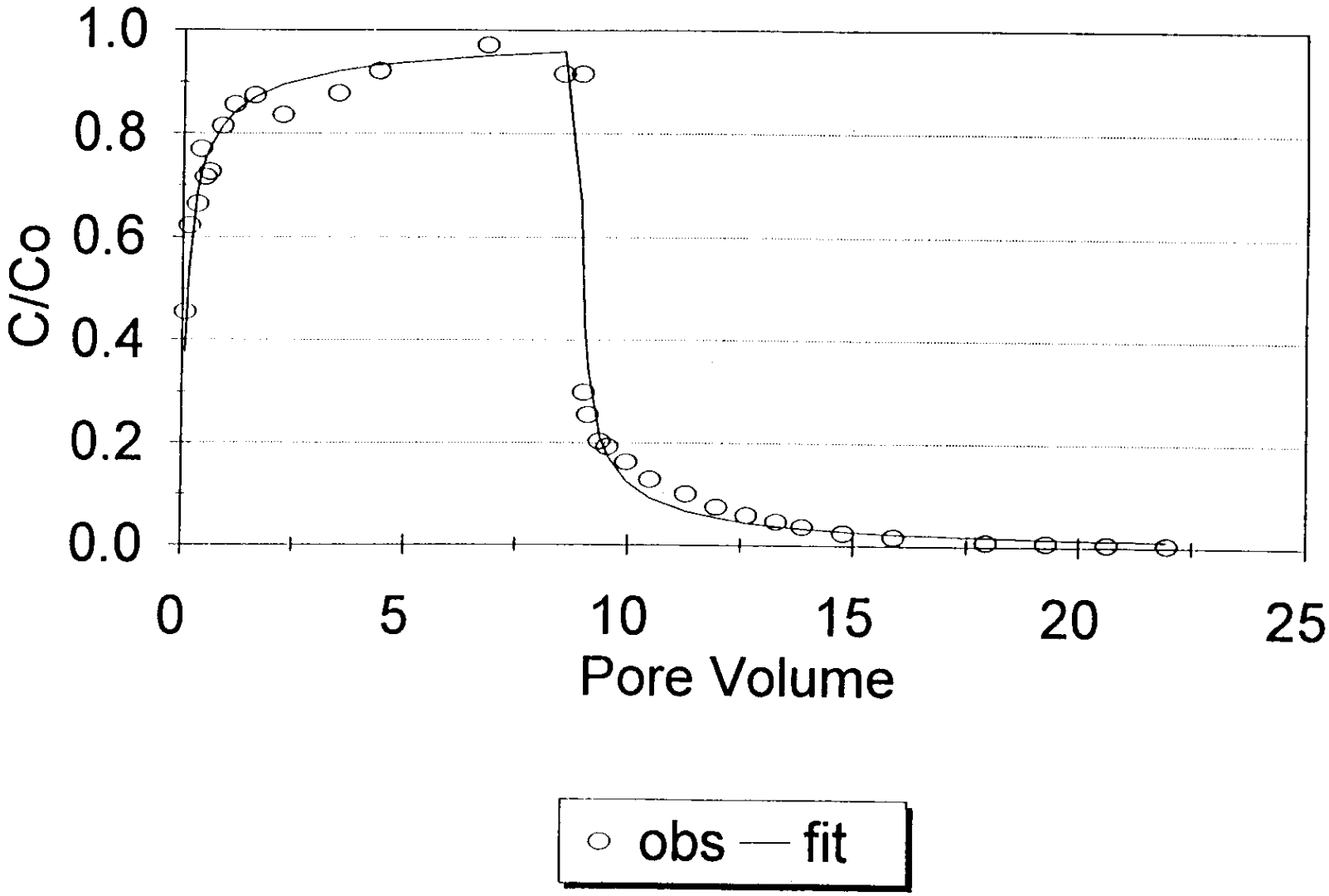

Figure J-7. Bromide breakthrough from intact basalt core 11BR1. The fit represented here is from the equilibrium CXTFIT model.

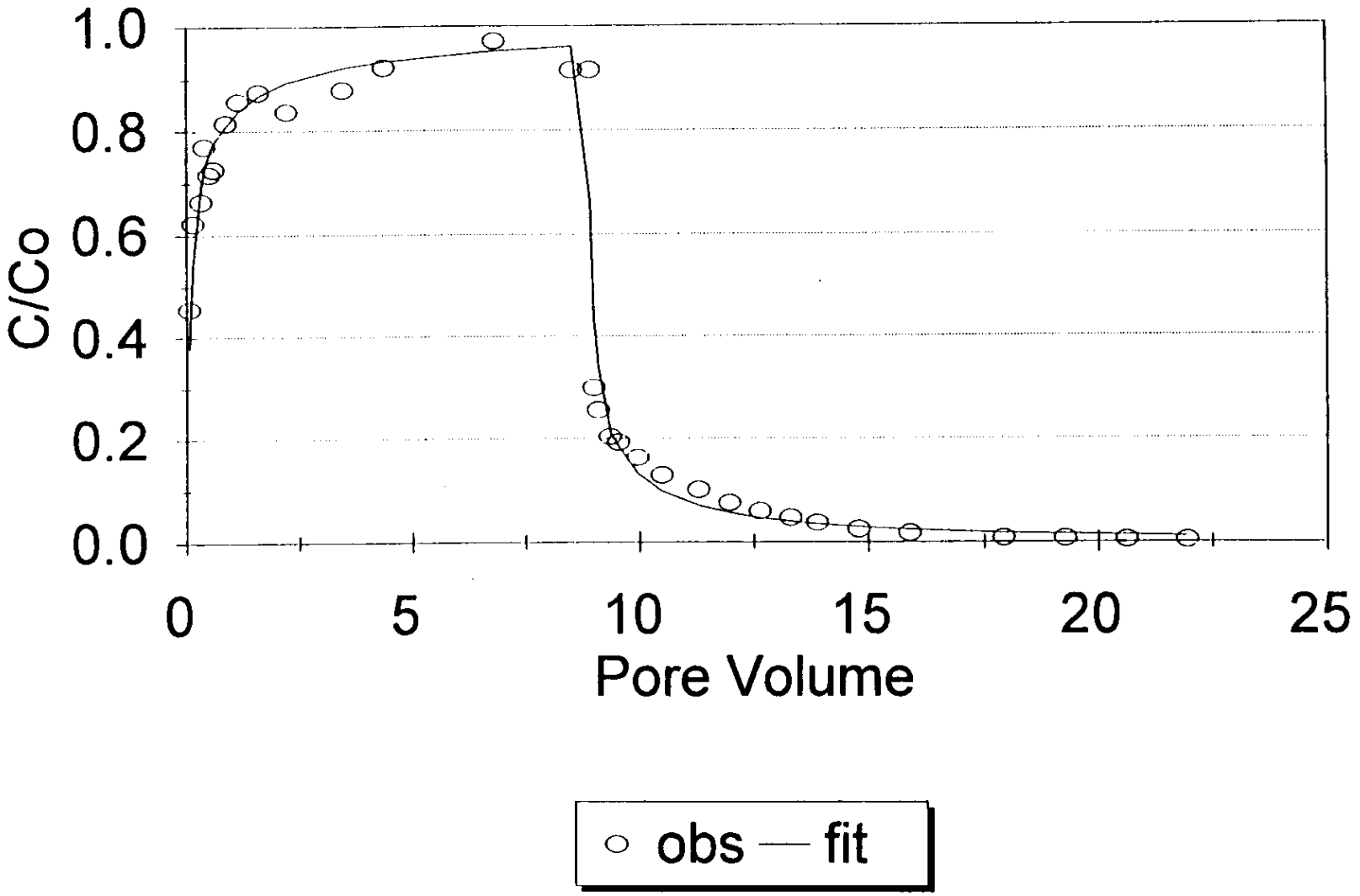

Figure J-8. Bromide breakthrough from intact basalt core I1BR1. The fit represented here is from the two-site/two region CXTFIT model.

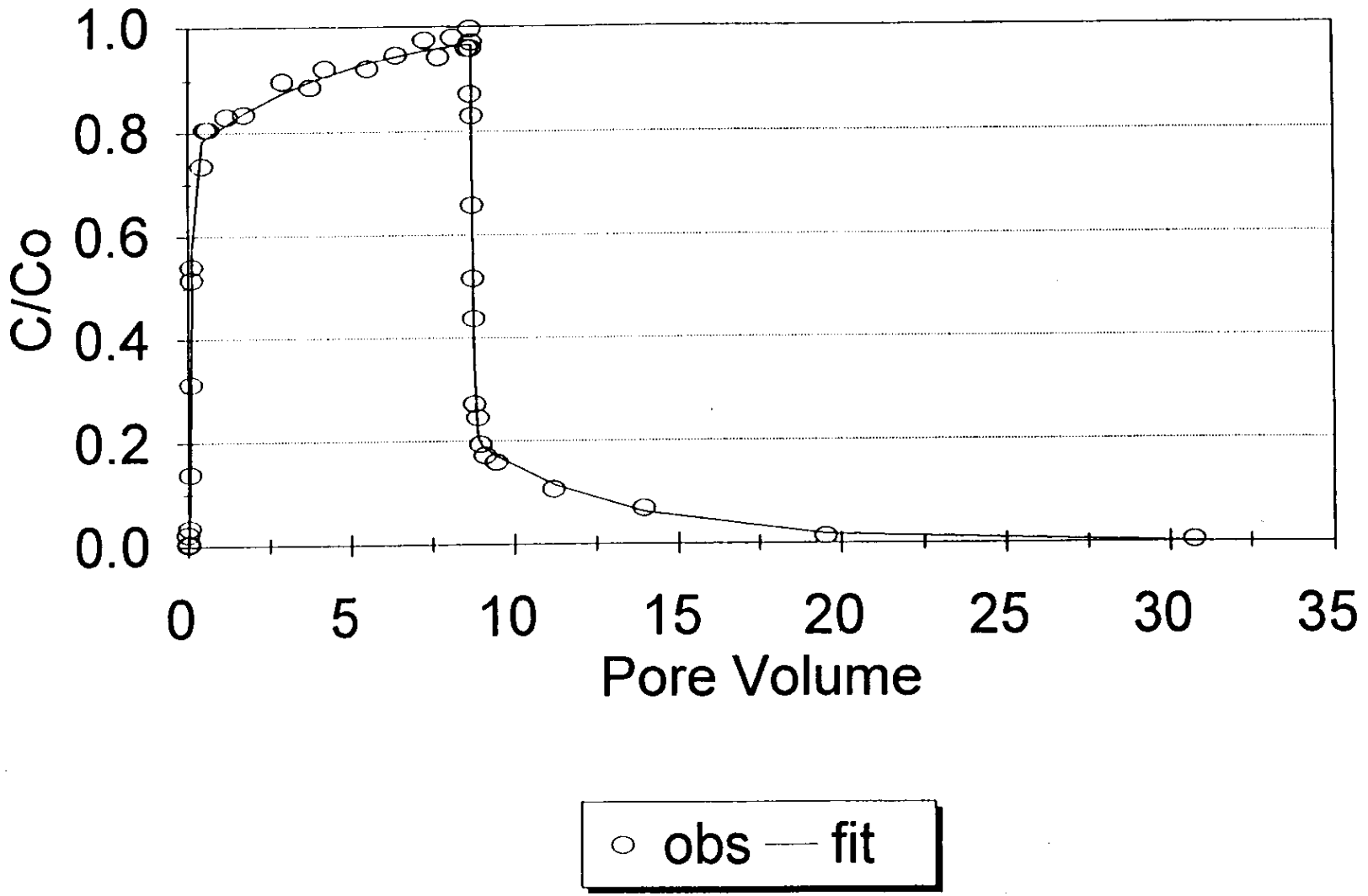

Figure J-9. Bromide breakthrough from intact basalt core I1BR2. The fit represented here is from the two-site/two region CXTFIT model.

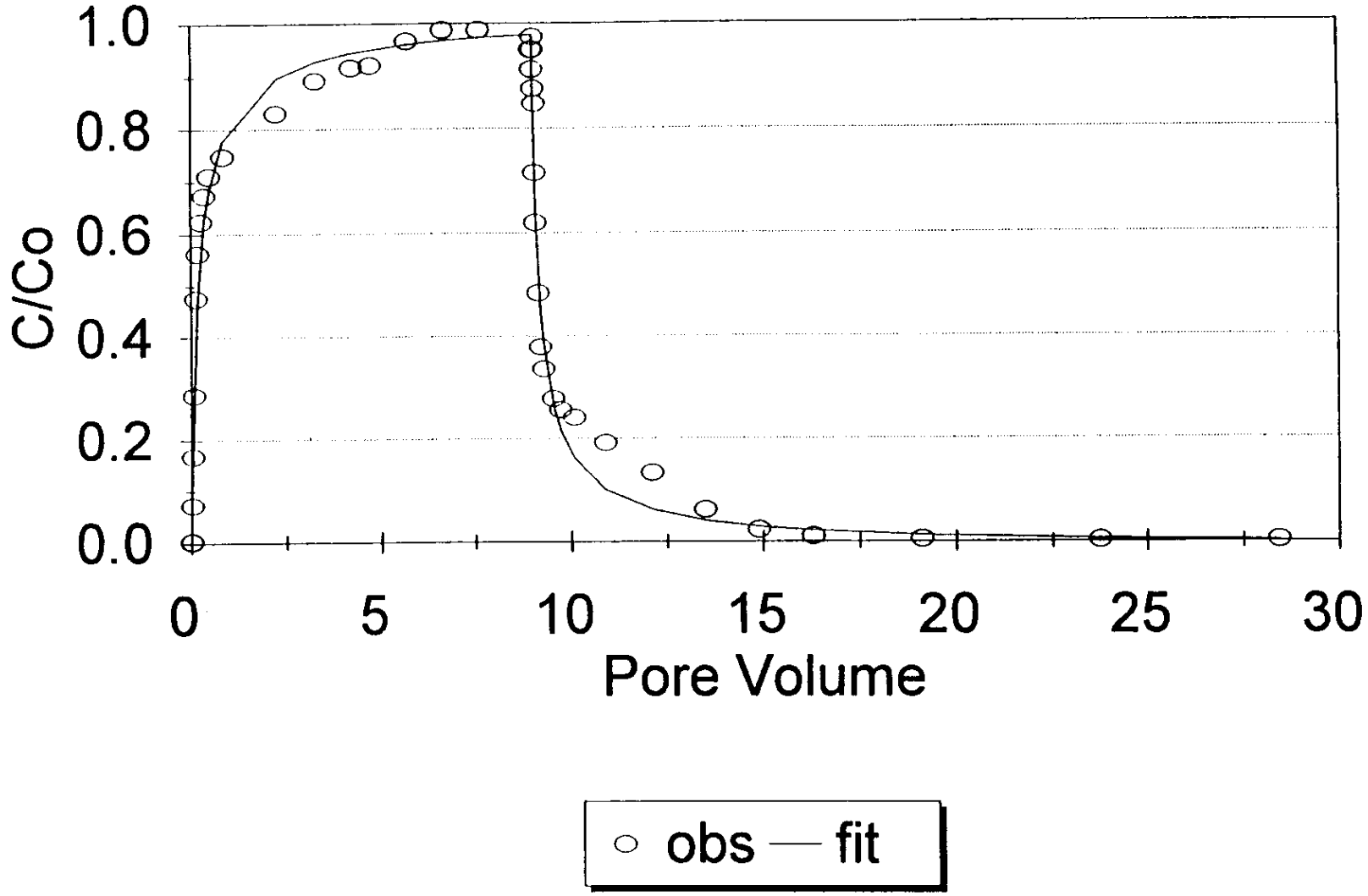

Figure J-10. Bromide breakthrough from intact basalt core 11BR3. The fit represented here is from the equilibrium region CXTFIT model.

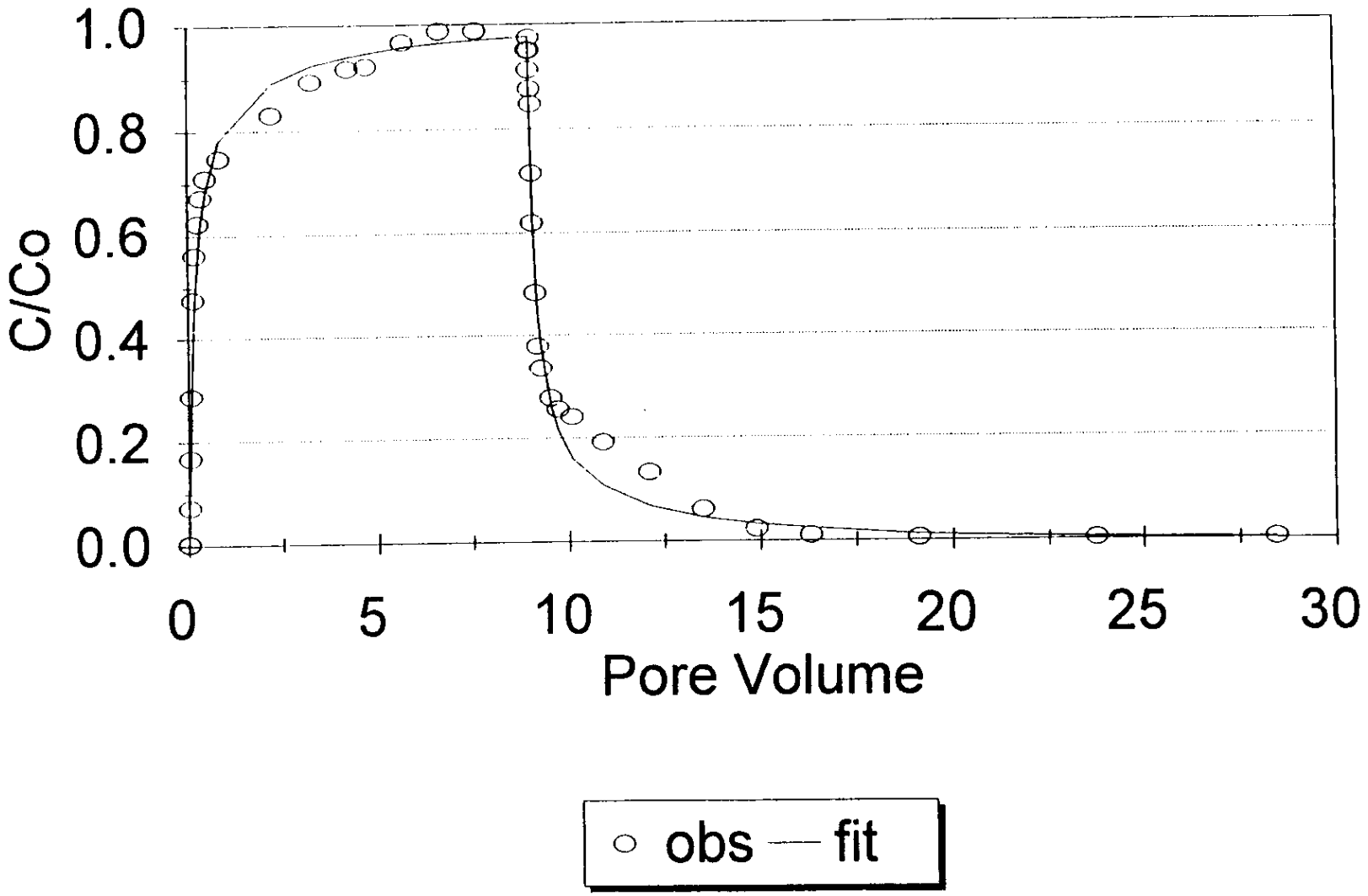

Figure J-11. Bromide breakthrough from intact basalt core I1BR3. The fit represented here is from the two-site/two region CXTFIT model.

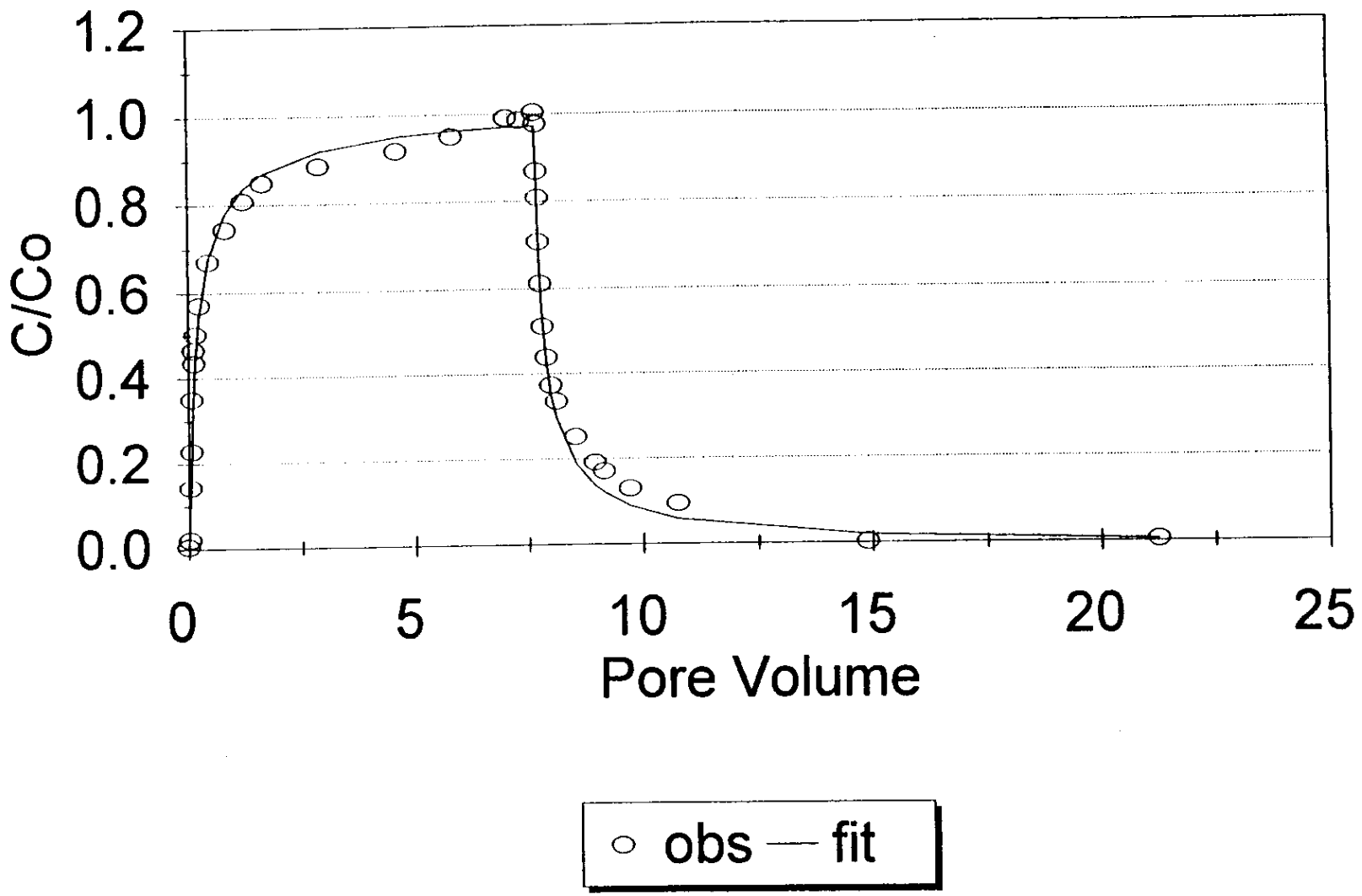

Figure J-12. Bromide breakthrough from intact basalt core I2BR1. The fit represented here is from the equilibrium region CXTFIT model.

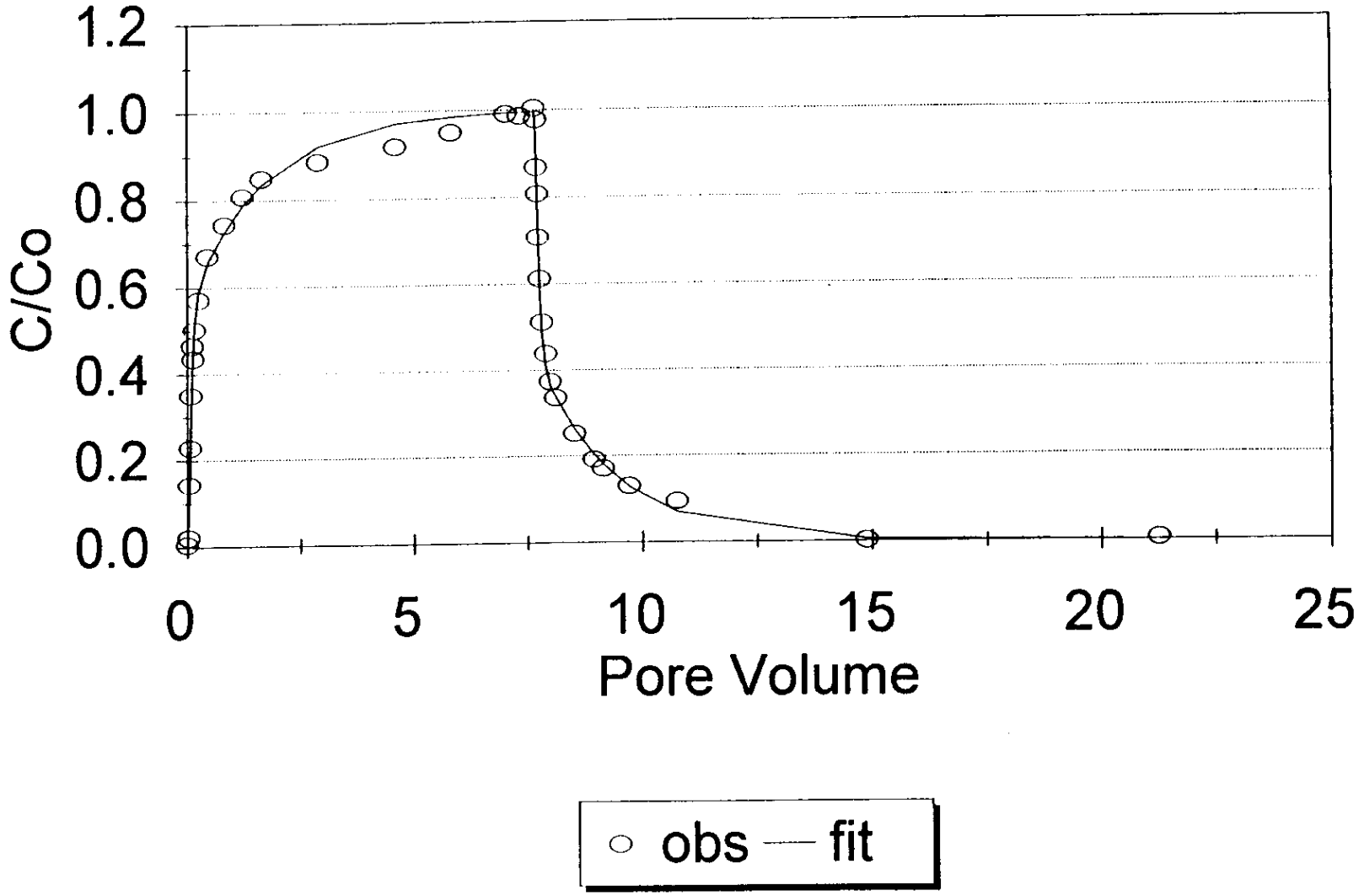

Figure J-13. Bromide breakthrough from intact basalt core I2BR1. The fit represented here is from the two-site/two region CXTFIT model.

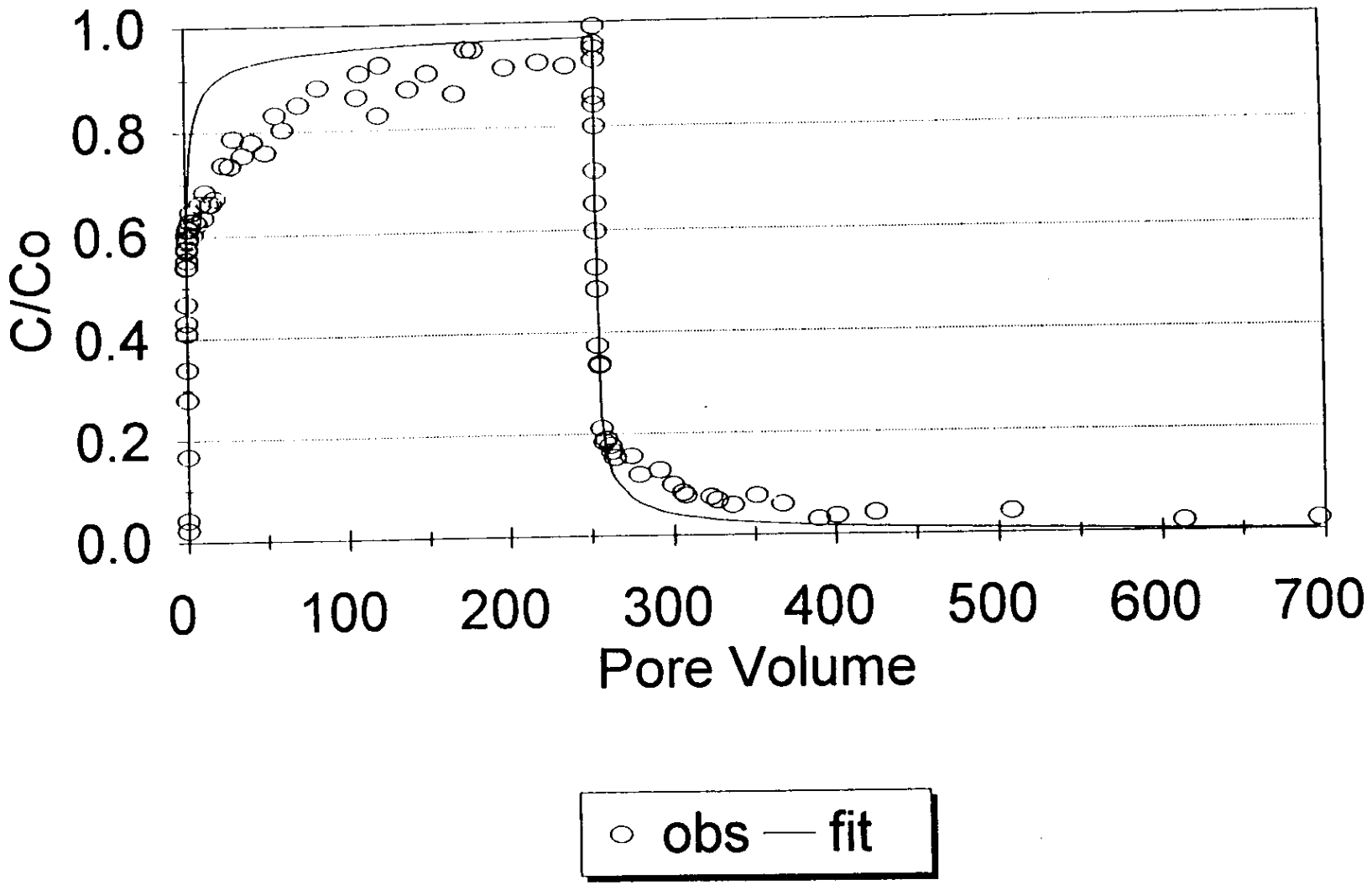

Figure J-14. Strontium breakthrough from intact basalt core 11SR1. The fit represented here is from the two-site/two region CXTFIT model.

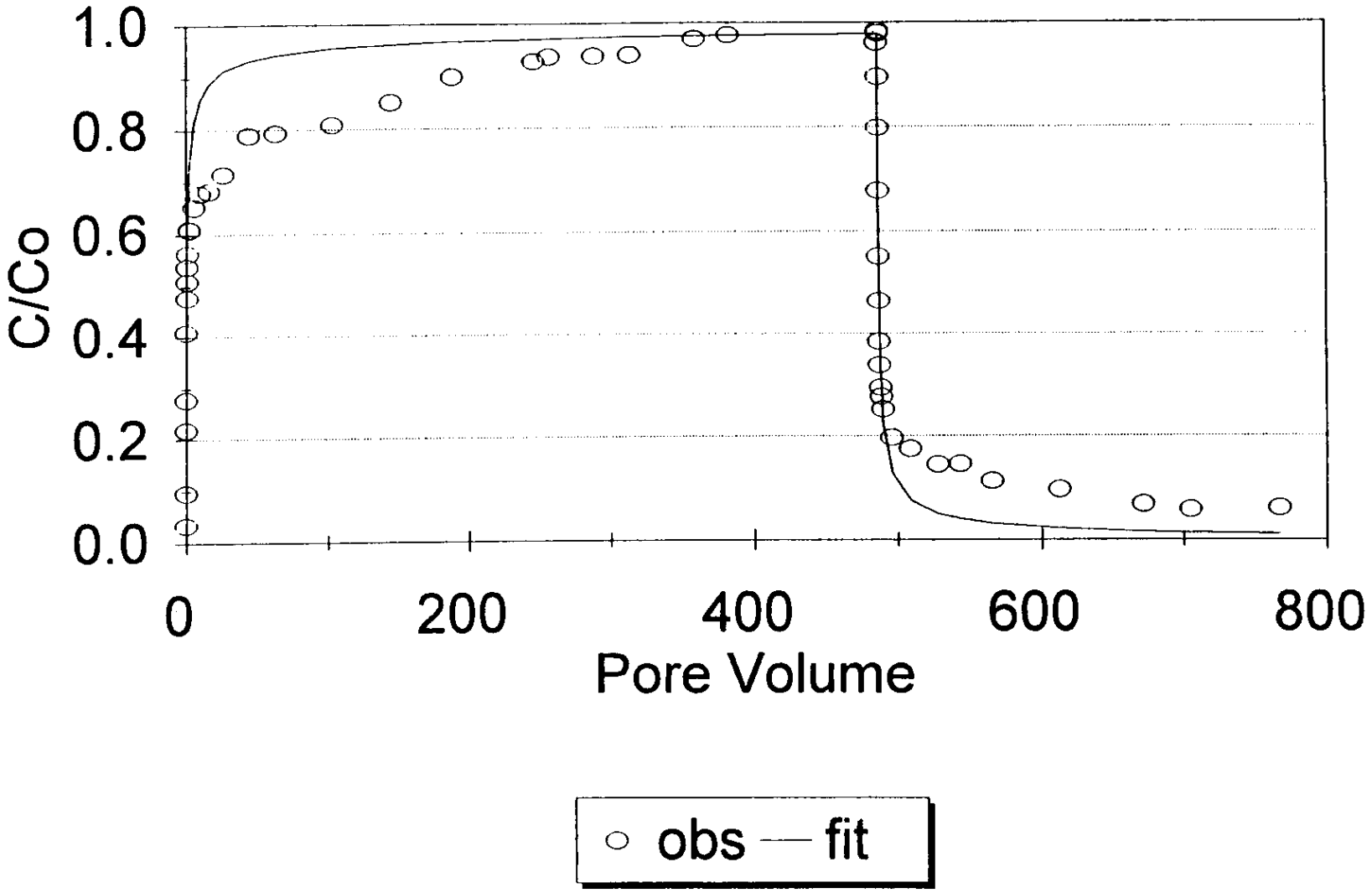

Figure J-15. Strontium breakthrough from intact basalt core 11SR2. The fit represented here is from the equilibrium CXTFIT model.

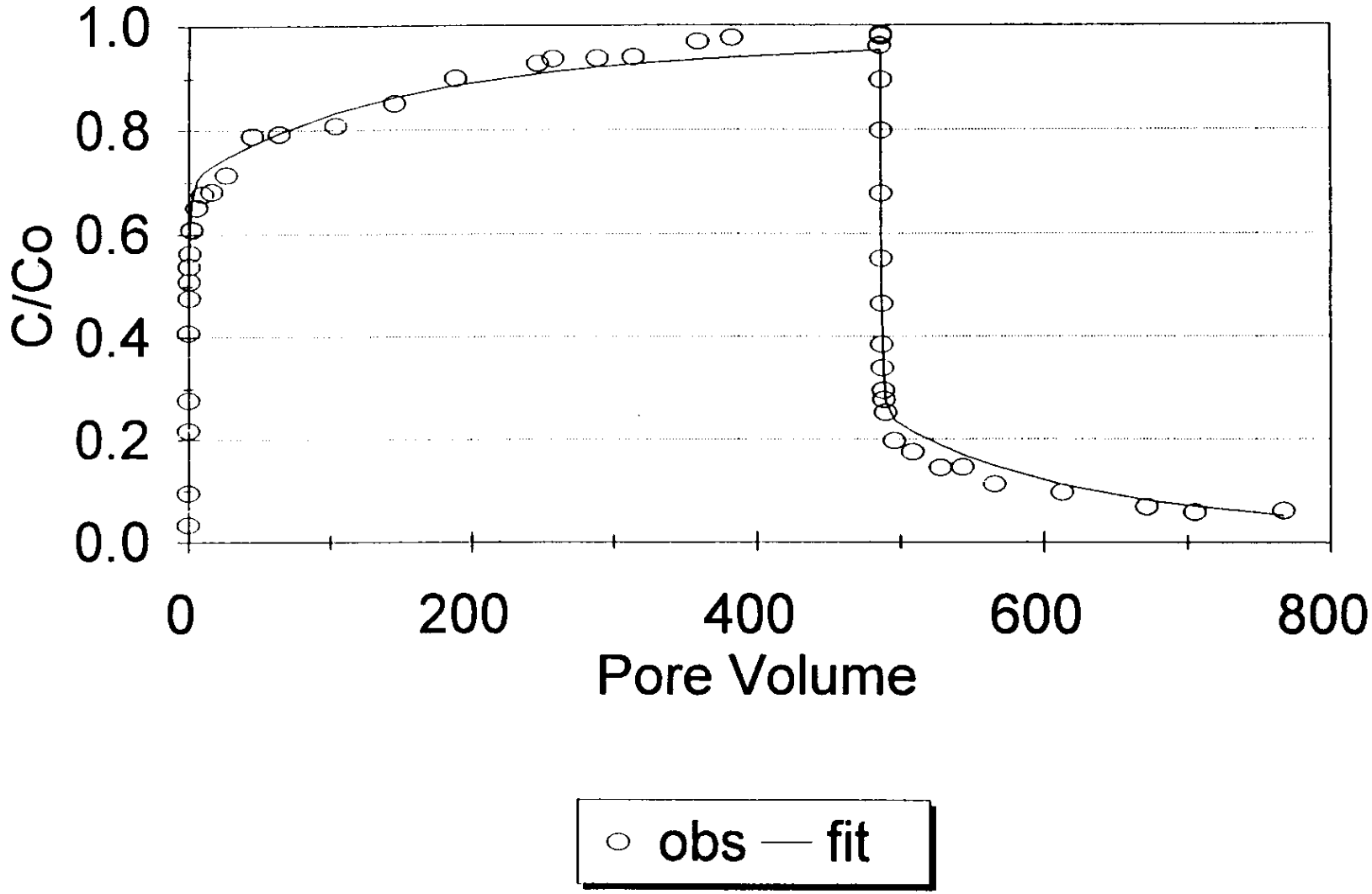

Figure J-16. Strontium breakthrough from intact basalt core I1SR2. The fit represented here is from the two-site/two region CXTFIT model.

Appendix K

Appendix K

Breakthrough of Bromide and Strontium from Crushed Basalt Packed Columns of Varying Moisture Contents

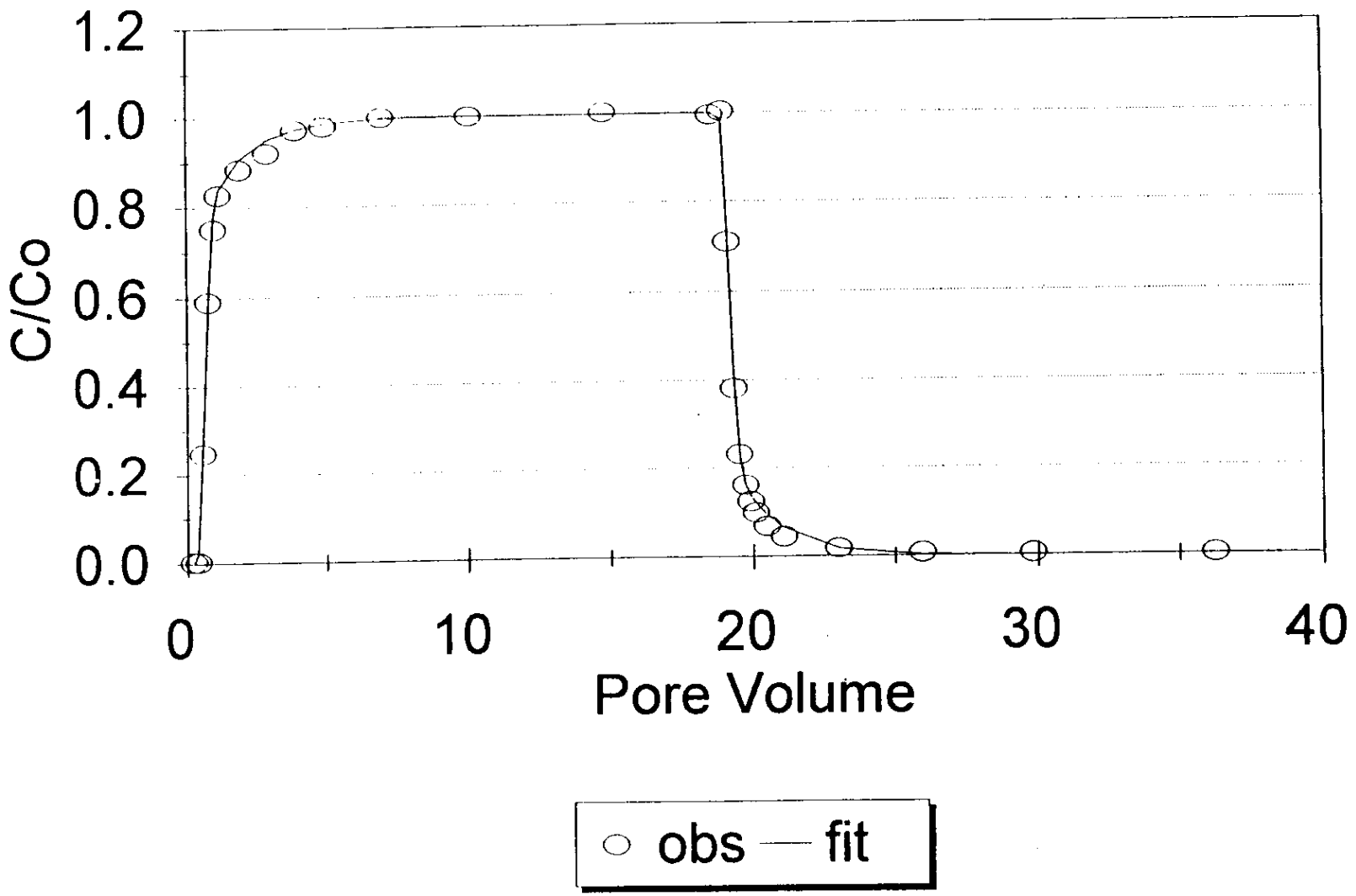

Figure K-1. Bromide breakthrough from column BR1 having a volumetric moisture content of 0..180 (33% saturation). The fit represented here is from the two-site/two-region CXTFIT model.

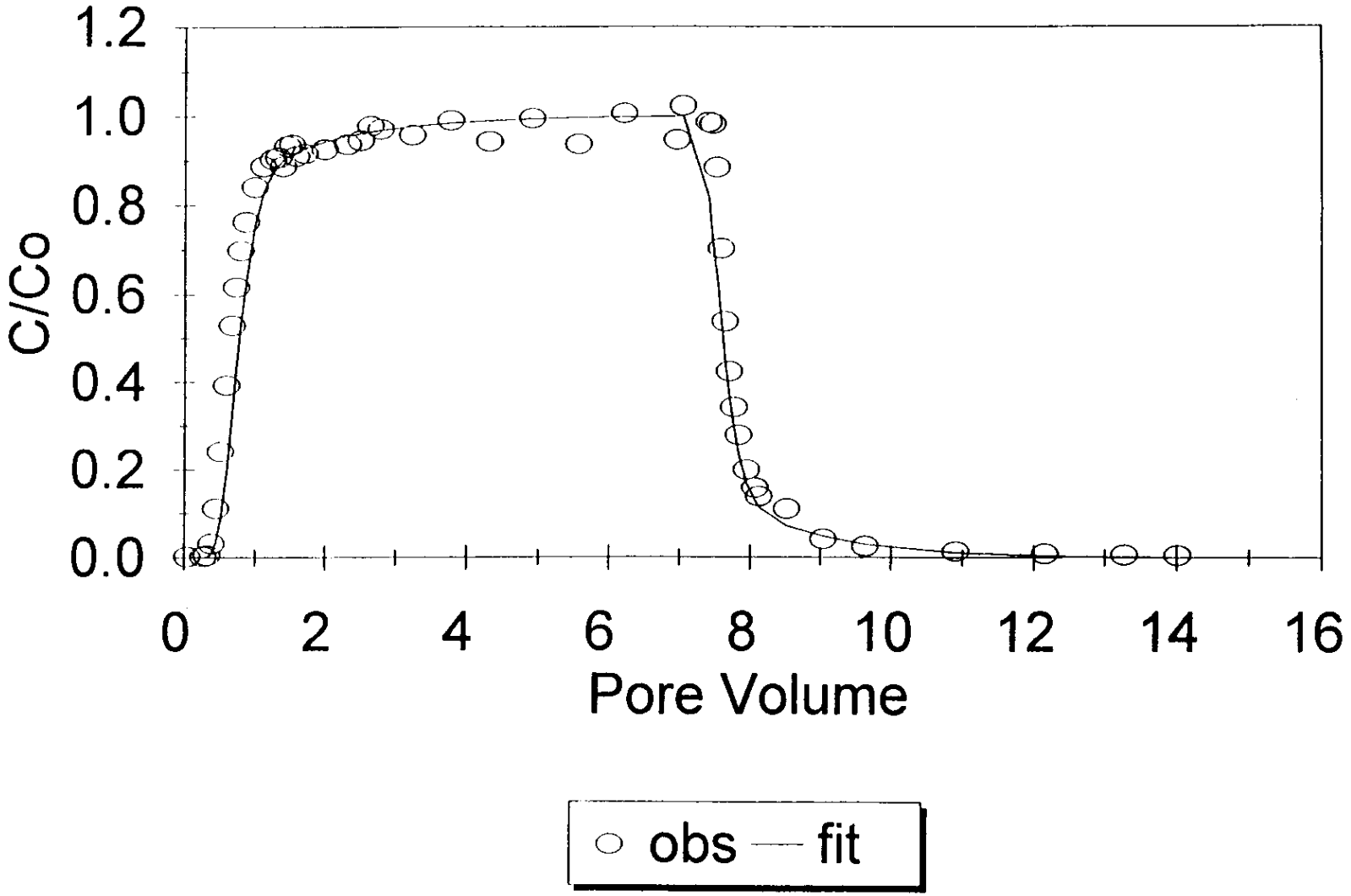

Figure K-2. Bromide breakthrough from column BR2 having a volumetric moisture content of 0.218 (40% saturation). The fit represented here is from the equilibrium region CXTFIT.

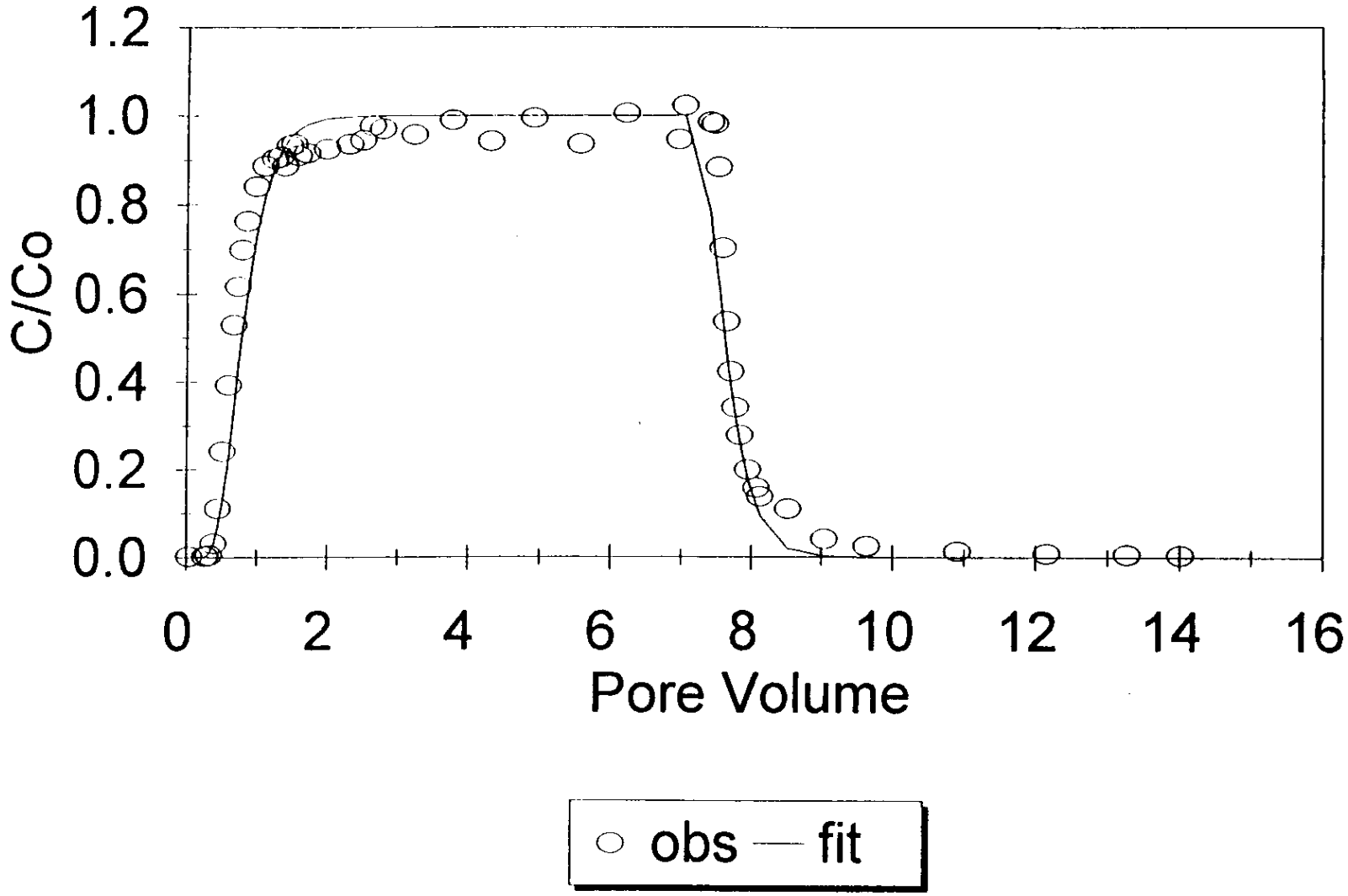

Figure K-3. Bromide breakthrough from column BR2 having a volumetric moisture content of 0.218 (40% saturation). The fit represented here is from the two-site/two region CXTFIT.

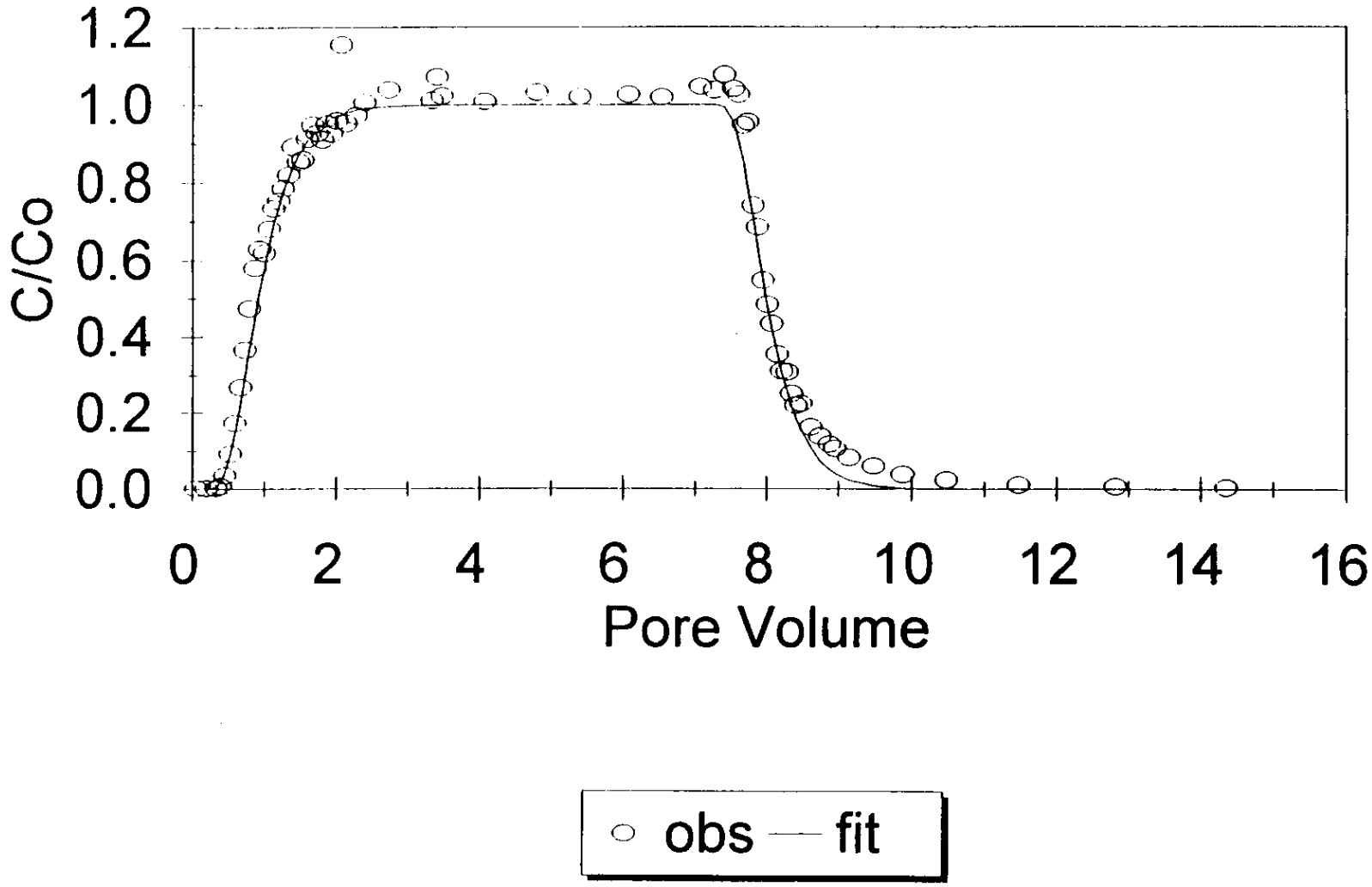

Figure K-4. Bromide breakthrough from column BR3 having a volumetric moisture content of 0.218 (29% saturation). The fit represented here is from the two-site/two region CXTFIT.

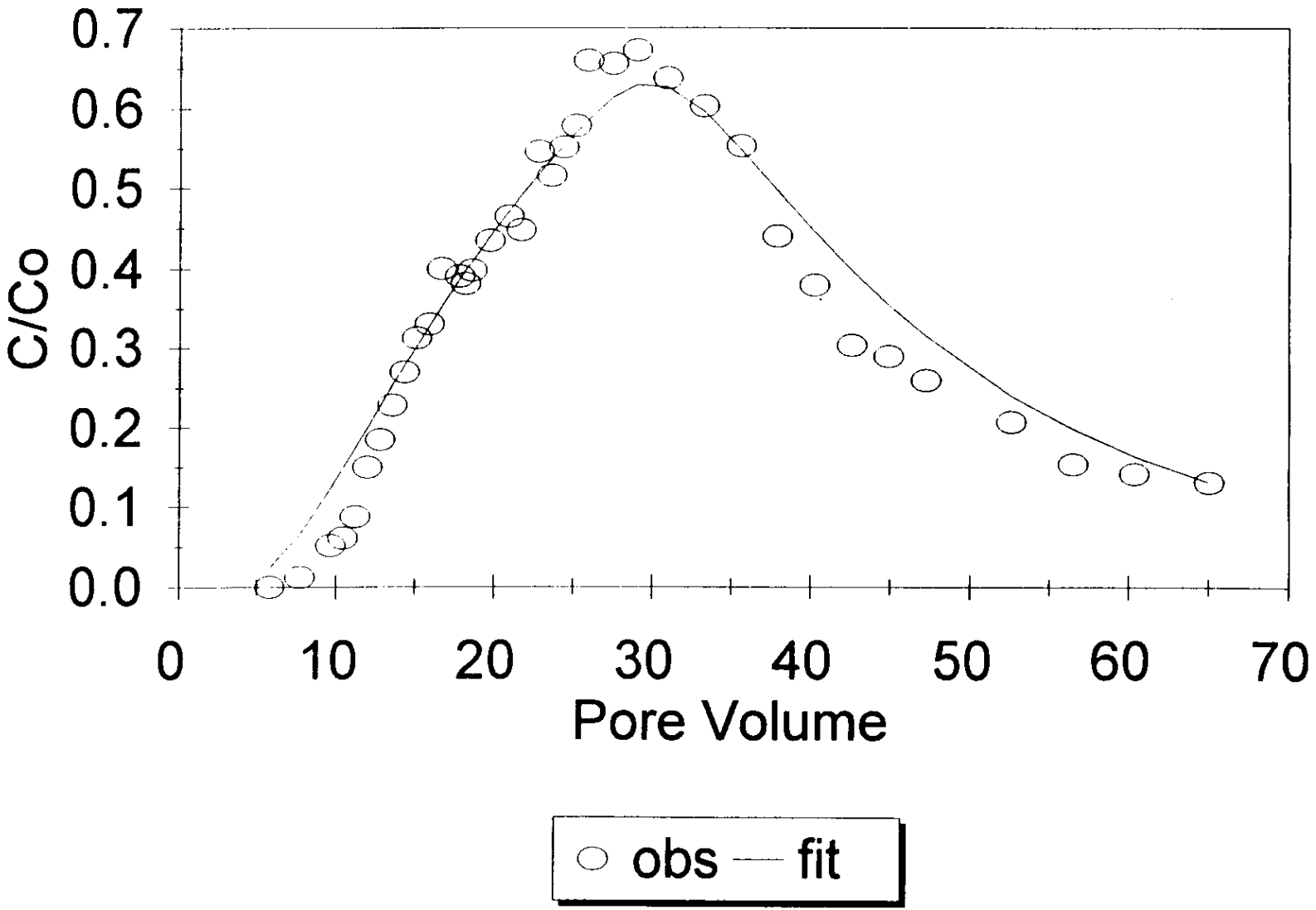

Figure K-5. Strontium breakthrough from column SR4 having a volumetric moisture content of 0.20 (36.85% saturation). The fit represented here is from the equilibrium region CXTFIT.

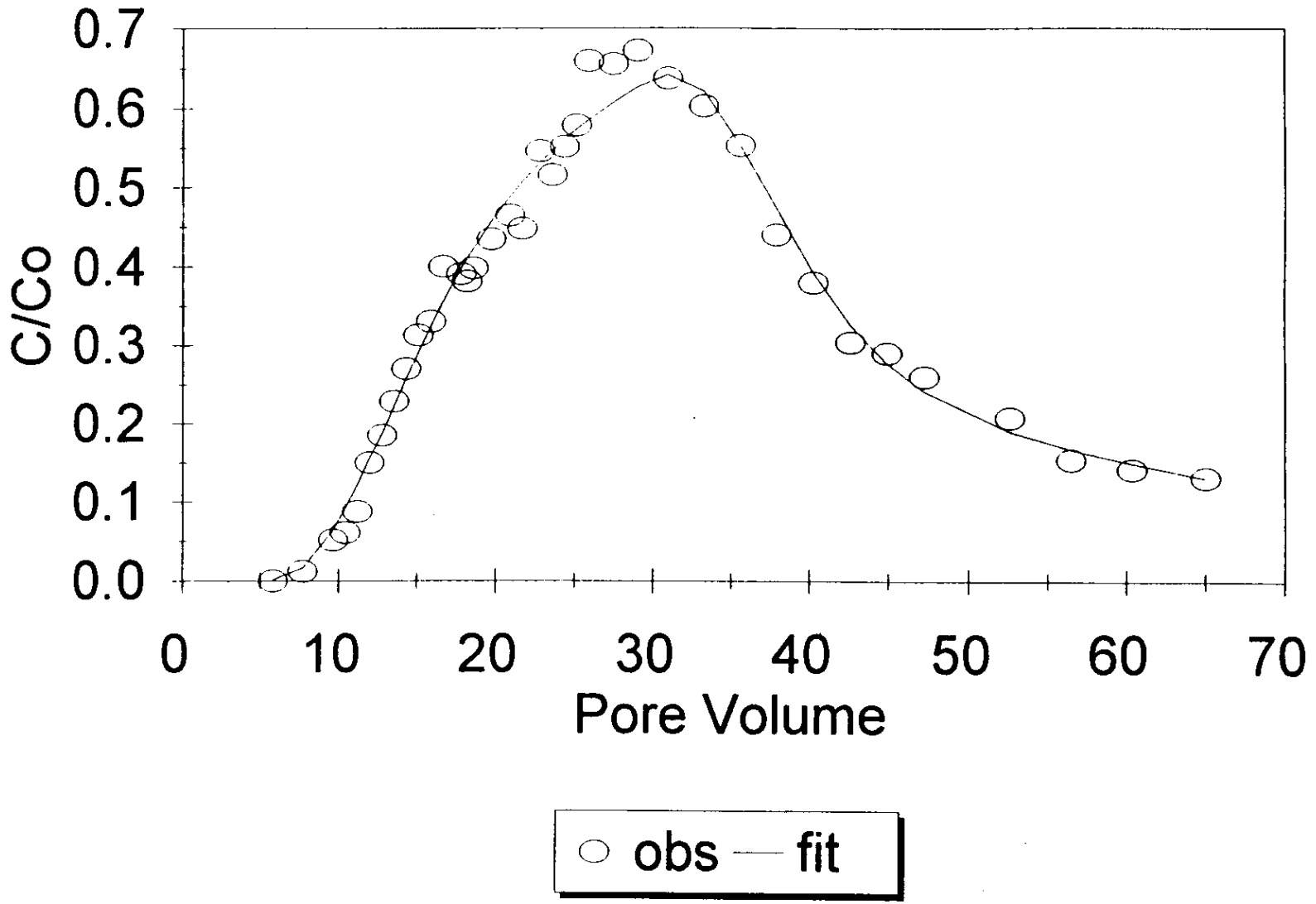

Figure K-6. Strontium breakthrough from column SR4 having a volumetric moisture content of 0.20 (36.85% saturation). The fit represented here is from the two-site/two region CXTFIT.

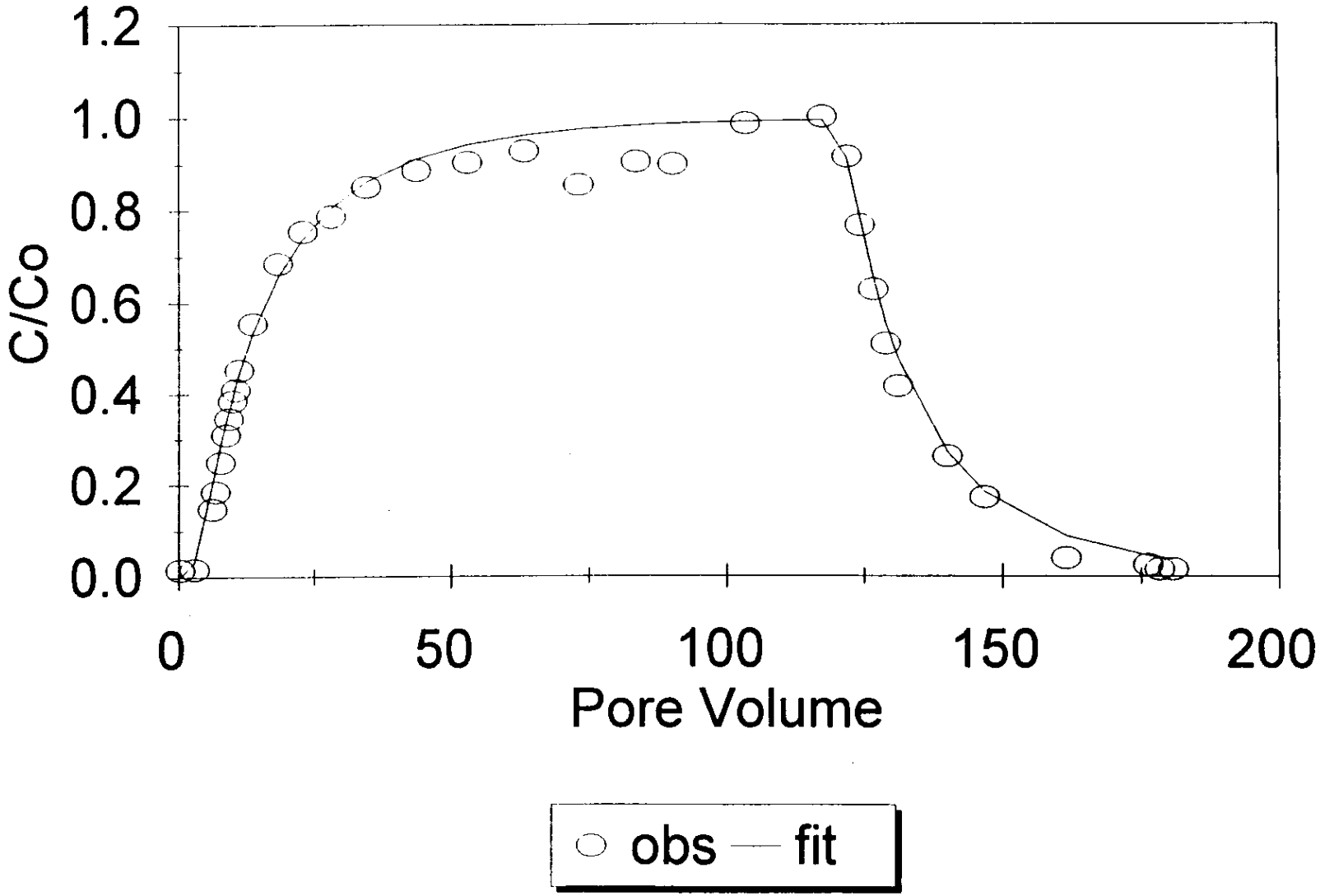

Figure K-7. Strontium breakthrough from column SR5 having a volumetric moisture content of 0.22 (40.29% saturation). The fit represented here is from the two-site/two region CXTFIT.

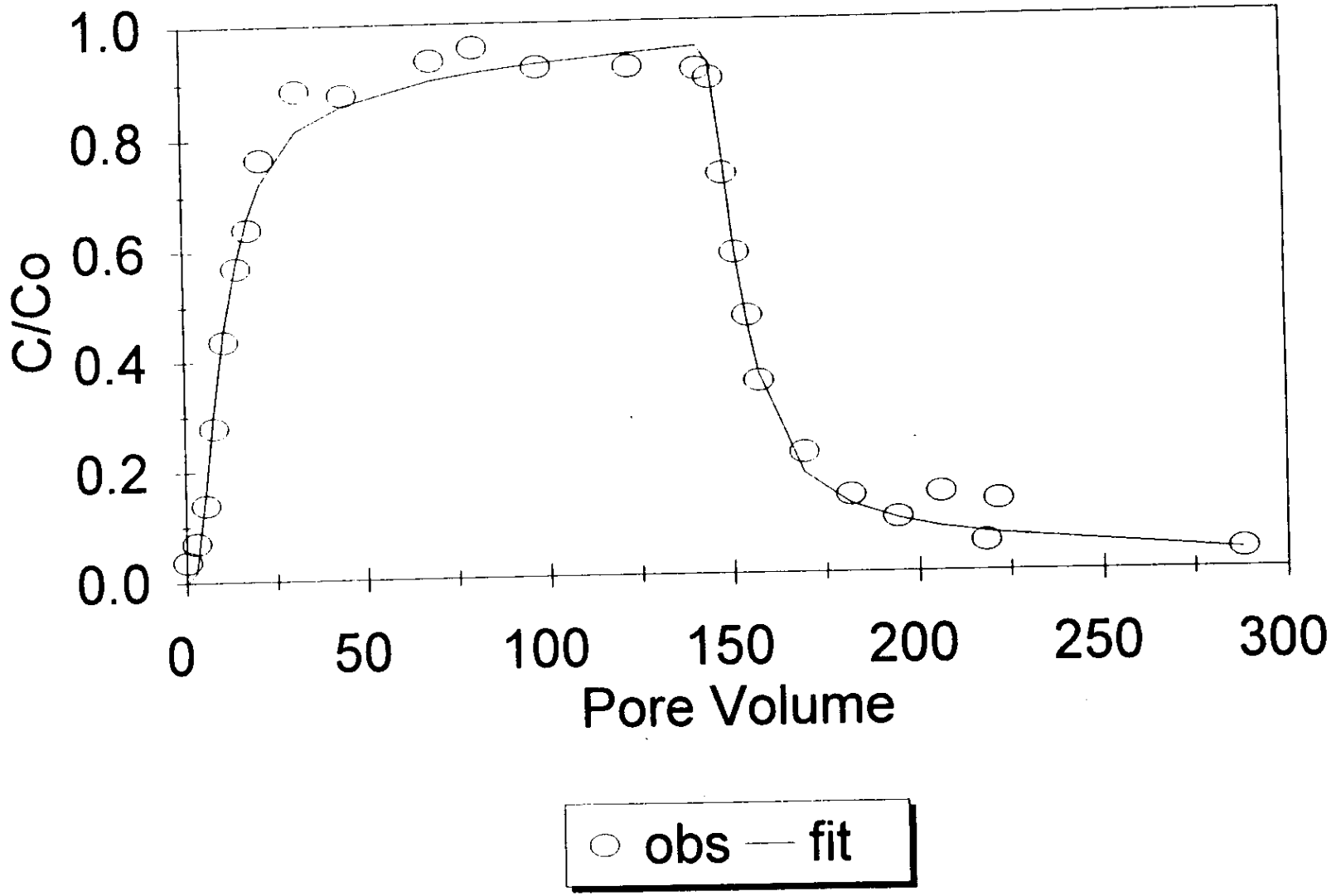

Figure K-8. Strontium breakthrough from column SR6 having a volumetric moisture content of 0.25 (45.44% saturation). The fit represented here is from the two-site/two region CXTFIT.

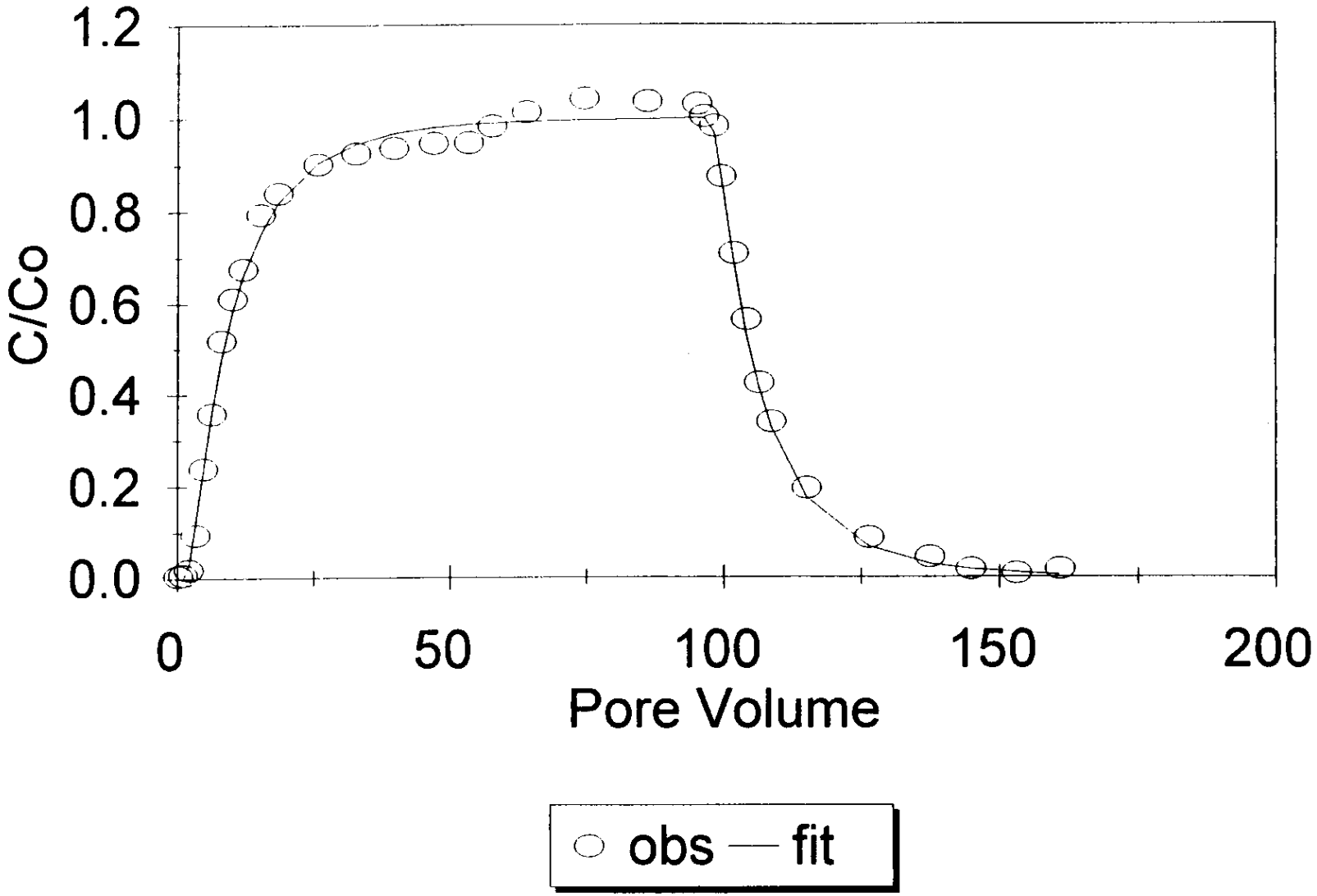

Figure K-9. Strontium breakthrough from column SR7 having a volumetric moisture content of 0.546 (100% saturation). The fit represented here is from the equilibrium region CXTFIT.

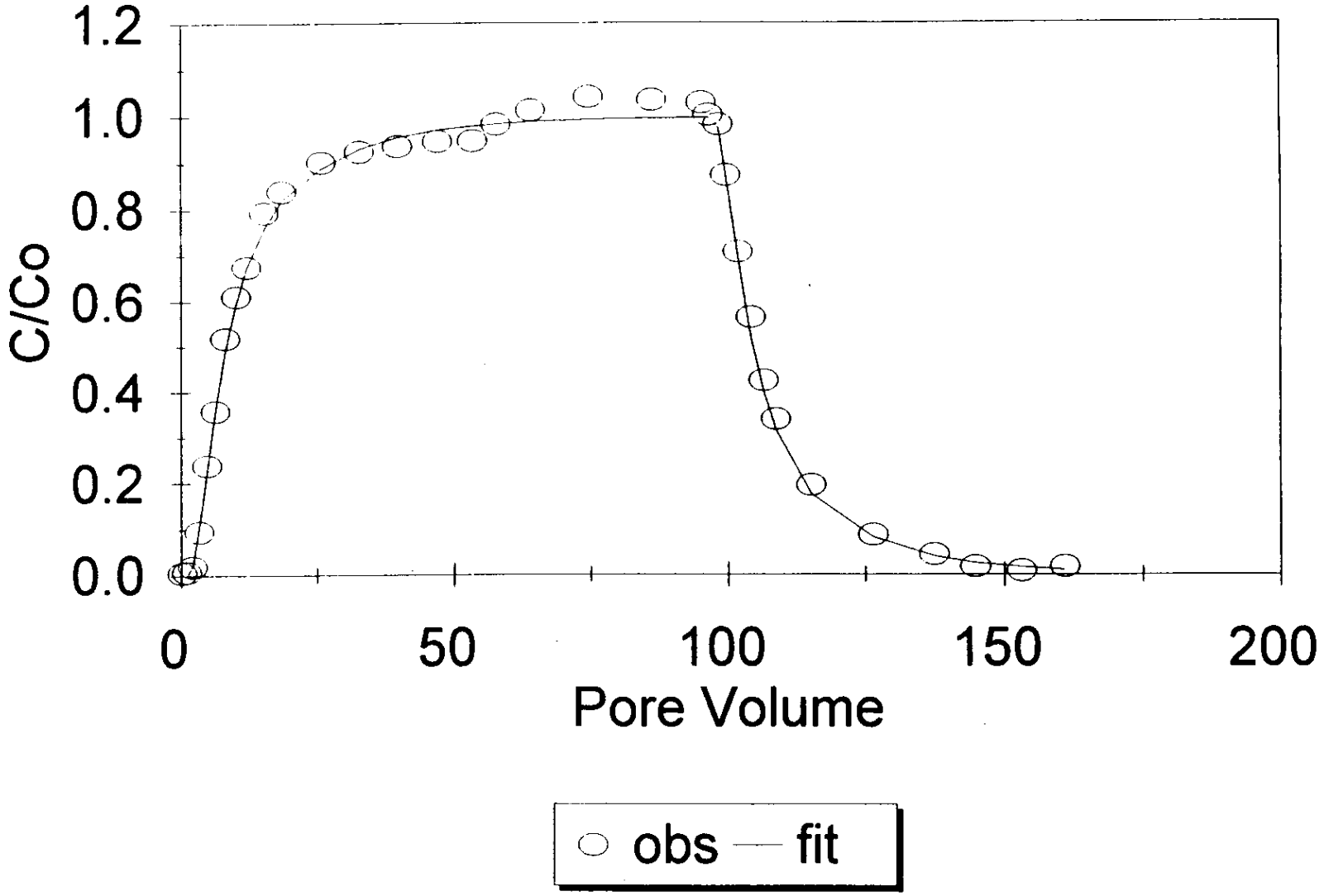

Figure K-10. Strontium breakthrough from column SR7 having a volumetric moisture content of 0.546 (100% saturation). The fit represented here is from the two-site/two region CXTFIT.